Aspects of Nonperturbative Heavy Quark Physics

by

Joshua Lin

B.A. Physics, B.A. Mathematics, University of California, Berkeley, 2020

Submitted to the Department of Physics
in partial fulfillment of the requirements for the degree of

DOCTOR OF PHILOSOPHY IN PHYSICS, STATISTICS, AND DATA SCIENCE

at the

MASSACHUSETTS INSTITUTE OF TECHNOLOGY

September 2025

Authored by:	Joshua Lin Department of Physics August 8, 2025
Certified by:	William Detmold Professor of Physics, Thesis Supervisor
Certified by:	Phiala E. Shanahan Associate Professor of Physics, Thesis Supervisor
Accepted by:	Lindley Winslow Associate Department Head of Physics Department of Physics

Aspects of Nonperturbative Heavy Quark Physics

by

Joshua Lin

Submitted to the Department of Physics
on August 15th, 2025, in partial fulfillment of the
requirements for the degree of
Doctor of Philosophy in Physics, Statistics, and Data Science

Abstract

The properties of charm and bottom quarks are an interesting corner of Quantum Chromo-Dynamics (QCD) due to the fact that their masses are much heavier than the typical QCD interaction energy Λ_{QCD}. Due to this scale separation, it is possible to describe these heavy quarks by Effective Field Theories (EFTs) that simplify their equations of motion, make explicit additional symmetries that only appear for heavier quark masses, and simplify the theoretical calculations required for predictions. By discretising these EFTs in a lattice regularisation, nonperturbative calculations of observables of interest become possible. This thesis presents progress towards systematically controlled calculations of two such observables: the Spectator Effect contributions to the inclusive decay rates of b-hadrons, and the real-time dynamics of fermions propagating in a thermal medium.

Standard EFT calculations in Lattice-QCD proceed by expressing observables as sums over perturbatively computed Wilson coefficients and nonperturbative matrix elements that can be calculated by path integral monte-carlo methods. Though it is possible to carry out this procedure within a regulator-independent renormalization scheme, in practice almost all such decompositions are computed in the modified minimal subtraction scheme $\overline{\mathrm{MS}}$ which is only defined for the dimensional regulator (DR), due to its simplicity. Computing such observables therefore requires a matching between lattice regularised operators and operators renormalized in $\overline{\mathrm{MS}}$. In Chapter 2, both the dimensional regulator (DR) and the lattice regulator are reviewed, with a particular emphasis on techniques needed for calculations carried out in later sections. An interesting subtelty in DR is the need to introduce d-dimensional counterparts to the Dirac γ-matrices, which a-priori are only well defined in integer number of dimensions. This analytic continuation is of practical importance as it introduces additional Evanescent Operators (Sec. 2.1.4) that have physical consequences. In Sec. 2.1.5, traces of d-dimensional γ-matrices were related to Tutte polynomial evaluations [4], presenting a new graph-theoretic interpretation of the dimensionally regulated γ-matrices.

One strategy of renormalizing lattice-regulated operators into $\overline{\mathrm{MS}}$ involves first renormalizing into a regulator independent scheme, before perturbatively matching between the regulator independent scheme and $\overline{\mathrm{MS}}$. In Chapter 3, regulator independent position-space (X-space) schemes for renormalizing operators defined in the leading order Heavy Quark Effective Theory (HQET) are proposed [3]. Compared to other regulator independent renormalization schemes such as RI-xMOM, X-space schemes have the benefit that they are gauge invariant. The next to leading order matching calculations between X-space and $\overline{\mathrm{MS}}$ are presented for heavy-light and heavy-light-light multiplicatively renormalizable operators, as well as $\Delta Q = 0$ and $\Delta Q = 2$ four quark operators relevant for heavy hadron decays and mixing, where Q refers to the static quark number.

Due to their heavy masses, hadrons containing heavy quarks decay via the weak nuclear force. Experimental measurements of these lifetimes provide precision determinations of the fundamental parameters of the Standard Model. The Heavy Quark Expansion expresses the inclusive lifetimes of heavy hadrons in terms of matrix elements of HQET operators of increasing dimension. The Spectator Effects are contributions due to the $\Delta Q = 0$ four-quark operators, where the light quark degrees of freedom within a heavy hadron participate in the decay. In Chapter 4, a Lattice-QCD determination of the static decay constant f_B^{HQET} and the isospin-nonsinglet portion of the Spectator Effect matrix elements for heavy-light mesons is presented. Fits of bare matrix elements were performed for three different lattice spacings, and renormalized with the schemes proposed in Chapter 3 before a continuum limit is taken.

Due to the heavy masses m_Q of the heavy quarks, it is possible to find temperatures T approximately satisfying a hierarchy $\Lambda_{\mathrm{QCD}} \ll T \ll m_Q$. At these temperatures, QCD undergoes a deconfinement transition into the Quark-Gluon-Plasma (QGP) phase where the light degrees of freedom are no longer confined, and instead screen the long-range colour forces. The heavy quarks however are not thermalised, and act as probes of the QGP. Further understanding of the QGP requires first principles simulations of the heavy quark dynamics at finite temperature, however such calculations are difficult due to the enormous size of the Hilbert space. Variational approximations of the Hilbert space encode wavefunctions within a few parameters, and provide a practical method to simulate many particle systems. As a testcase, the variational approach was applied for the first time to simulate fermions at finite temperature in a simple QFT: the $1+1d$ U(1) gauge theory known as the massive Schwinger model. Both the real-time dynamics of string like states, and the properties of the thermal state were studied, and such variational methods are shown to be promising approaches to the more difficult case of a heavy quark effective theory in QCD.

[1] : **Joshua Lin**, William Detmold, and Stefan Meinel. Lattice Study of Spectator Effects in b-hadron Decays. PoS, LATTICE2022:417, 2023. doi: 10.22323/1.430.0417.

[2] : **Joshua Lin**, Di Luo, Xiaojun Yao, and Phiala E. Shanahan. Real-time dynamics of the Schwinger model as an open quantum system with Neural Density Operators. JHEP, 06:211, 2024. doi: 10.1007/JHEP06(2024)211.

[3] : **Joshua Lin**, William Detmold, and Stefan Meinel. Position-space renormalization schemes for four-quark opera- tors in HQET. JHEP, 07:188, 2024. doi: 10.1007/JHEP07(2024)188.

[4] : **Joshua Lin.** Dirac Traces and the Tutte Polynomial. JHEP, 10 2024. doi: 10.1007/JHEP05(2025)235.

Thesis Supervisor: William Detmold
Title: Professor
Thesis Supervisor: Phiala E. Shanahan
Title: Associate Professor

ACKNOWLEDGEMENTS

I have been tremendously lucky to spend the past five years at MIT, and I owe a great deal to my advisors Will and Phiala for their constant guidance and encouragement. I have not only learnt a lot of phyiscs from both of you; but even moreso I've learnt about how to *be* a physicist. These lessons - about when to be practical and when to dream, about kindness and community, and about setting and following a standard - mold who I aspire to be. Entering into our student-advisor relationships felt quite serendipitous, but will stay with me for life: thank you for everything.

I owe many thanks to my collaborators Stefan, Xiaojun and Di for your patience and guidance, and for everything you've taught me. Also many thanks to my friends I am working with currently: Neill, Max, Stephen, Julian, Robert, Ryan, Tom, Nora, Bruno, Thomas, Jean, John, Elba; thank you for the excitement of embarking on a journey with me to places unknown. Studying physics is precious, and it tastes better shared. I also have many thanks for the current and former members of the MIT lattice group that I've learned from and shared memories with: thank you to Artur, Will Jay, Anthony, Jamie, Patrick, Dimitra, Fernando, Dan, Julian, Yin, and Cagin. And to the younger members Matías, Brian and Rosie - the group lives and thrives with you, good luck with the rest of your PhDs! Many thanks to my friends around the world for the constant support - special thanks to Zhiquan, Elba, Rahul, Keeley, Rikab, Paige, Javi, Pok, Edwin, and Jack for the adventures and for having my back.

None of this would have been possible without the support of my family; my parents that supported me through my studies and my family in New York and Boston. I'd like to say that I understood what it meant to leave home ten years ago to pursue my dreams - but the truth is that at the time I didn't. Thank you for the constant support, for taking an interest in what I do, for celebrating my successes and commiserating with me in times of trouble.

To Margo: thank you for sharing your life with me, I love you.

To the reader: I hope that something in this thesis - a figure, an explanation, a single word - helps you. I've attempted to write interesting things in this thesis that I've discovered with many collaborators, and any mistakes in presentation are mine alone.

CONTENTS

CHAPTER 1

HEAVY QUARK FLAVOR PHYSICS

Contents

1.1 FROM THE STANDARD MODEL TO HEAVY QUARKS

It is a surprising fact that the natural phenomena of the world around us occurs at so many different scales. A-priori there doesn't seem to be any principle, anthropic or otherwise, why the solar system is 10^{16} times the size of you (the reader), or why you happen to be made of 10^{27} of your constituent atoms. One could imagine an alternate reality with different fundamental particles and different physical laws, where intelligent life is embedded as overdensities in an almost-homogenous soup; instead in our universe we are left to muse at our insignificance as a part of the cosmos. As perplexing as this situation is, it offers a great opportunity for physicists as each isolated scale offers an opportunity to study an *effective* theory for the degrees of freedom at that scale, without worrying about fine grained details. This is indeed how physics has historically progressed - for example Newtonian gravity was superseded by General Relativity, which is expected to be an effective theory for some yet unknown theory of everything.

Particle physics is the study of physics at the smallest experimentally accessible scales, and deals with the interactions of particles currently thought to be fundamental. Even within particle physics, there is yet still a great range of scales across which physics occurs. This thesis presents my contributions to the corner of particle physics known as heavy flavour physics - which deals with the properties of charm and bottom quarks. These quarks are special because they are much heavier than the typical strong-force interaction strength, and can be described by effective nonrelativistic theories. To introduce the subject we start by describing the Standard Model of particle physics,

	SU(3)	SU(2)	U(1)	$\mathrm{U}(1)_{\mathrm{QED}}$
$q_L^i = \begin{pmatrix} u_L^i \\ d_L^i \end{pmatrix}$	3	2	1/6	$\begin{pmatrix} \frac{2}{3} \\ -\frac{1}{3} \end{pmatrix}$
u_R^i	3	1	2/3	2/3
d_R^i	3	1	−1/3	−1/3
$l_L^i = \begin{pmatrix} \nu_L^i \\ e_L^i \end{pmatrix}$	1	2	−1/2	$\begin{pmatrix} 0 \\ -1 \end{pmatrix}$
e_R^i	1	1	−1	−1
ϕ	1	2	1/2	$\begin{pmatrix} - \\ 0 \end{pmatrix}$

Table 1.1: Matter content of the Standard Model, and their charges under the different gauge groups. The integers in the leftmost two columns refer to the dimension of the representation, with 2, 3 referring to the fundamental representation of SU(2), SU(3) respectively. $\mathrm{U}(1)_{\mathrm{QED}}$ refers to the electromagnetic U(1) gauge group that remains after electroweak symmetry breaking as reviewed later in this section.

which is the currently accepted description of the known fundamental particles and forces (there are many reviews of this subject, see for example Ref [1]). The Standard Model is an SU(3)×SU(2)×U(1) quantum gauge theory with matter content tabulated in Table 1.1. The Standard Model Lagrangian without ghosts or counterterms is:

$$\begin{aligned}\mathcal{L}_{\mathrm{SM}} = -\frac{1}{4}\sum_G \mathrm{Tr}(F_{\mu\nu}F^{\mu\nu}) + i\sum_\psi \bar{\psi}\not{D}\psi + |D_\mu\phi|^2 + \mu^2\phi^\dagger\phi - \lambda(\phi^\dagger\phi)^2 \\ -Y^e_{ij}\bar{l}^i_L\phi e^j_R - Y^d_{ij}\bar{q}^i_L\phi d^j_R - Y^u_{ij}\epsilon^{ab}\bar{q}^i_{La}\phi^\dagger_b u^j_R + \text{h.c.},\end{aligned} \tag{1.1}$$

where $F_{\mu\nu}$ are gauge field tensors for the three different gauge groups $G \in \{\mathrm{SU}(3)_C, \mathrm{SU}(2)_L, \mathrm{U}(1)_Y\}$, ψ indexes over all the fermionic degrees of freedom, ϕ is a complex bosonic doublet, l_L are left-handed leptons, q_L are left handed quarks, u_R, d_R are right handed quarks, e_R are right handed leptons, h.c. refers to the hermitian conjugate and μ, λ, Y are free parameters. In Eq. (1.1), the Standard Model comes equipped with only a single mass scale μ. As it turns out however, physical processes in the Standard Model occur at many different scales. Firstly, the form of the Higgs potential with $\mu^2, \lambda > 0$ induces spontaneous symmetry breaking to $|\langle\phi\rangle| =: v = \frac{\mu}{\sqrt{\lambda}}$ at tree-level.[1] This spontaneous symmetry breaking in unitary gauge has the effect of giving the electroweak bosons (the W, Z and Higgs boson) masses. The massless fermions, which interacted via the Yukawa matrices Y in the

---

[1] Formally, this statement only makes sense after gauge fixing, for otherwise ϕ is not a gauge-invariant quantity and $\langle\phi\rangle$ has no meaning.

so-called flavor-basis now acquire masses:

$$-Y^d_{ij}\bar{q}^i_L \phi d^j_R - Y^u_{ij}\epsilon^{ab}\bar{q}^i_{La}\phi^\dagger_b u^j_R + \text{h.c.} \mapsto -\frac{v}{\sqrt{2}}\left(Y^d_{ij}\bar{d}^i_L d^j_R + Y^u_{ij}\bar{u}^i_L u^j_R + \text{h.c.}\right) + O(h) \tag{1.2}$$

where the term $O(h)$ denotes the interactions of the quarks and the Higgs boson. Note that the matrices $Y^{u,d}$ need not be diagonal: that is to say the *flavor*-basis used in Eq. (1.1) (which is the basis that the gauge degrees of freedom naturally act on) is not the same as the *mass* basis for the quarks. In this section, regular script u, d, q will refer to quarks in the flavor basis, and bolded $\mathbf{u}, \mathbf{d}, \mathbf{q}$ refers to quarks in the mass basis. To compute the Lagrangian in the mass basis, one can find unitary matrices U_u, U_d, K_u, K_d that perform a singular value decomposition:

$$Y^d_{ij} = U_d M_d K^\dagger_d, \quad Y^u_{ij} = U_u M_u K^\dagger_u \tag{1.3}$$

to extract diagonal mass matrices M_u, M_d so that the mass term becomes:

$$\begin{aligned} -\frac{v}{\sqrt{2}}\left(Y^d_{ij}\bar{d}^i_L d^j_R + Y^u_{ij}\bar{u}^i_L u^j_R + \text{h.c.}\right) &\mapsto -\frac{v}{\sqrt{2}}\left((\bar{d}_L U_d)M_d(K^\dagger_d d_R) + (\bar{u}_L U_u)M_u(K^\dagger_u u_R) + \text{h.c.}\right) \\ &= -\frac{v}{\sqrt{2}}\left(\bar{\mathbf{d}}_L M_d \mathbf{d}_R + \bar{\mathbf{u}}_L M_u \mathbf{u}_R + \text{h.c.}\right) \end{aligned} \tag{1.4}$$

This is the mass basis, that the QCD hadrons will be built out of. The only flavor mixing occurs in the couplings to $W^\pm_\mu$, from the term:

$$\begin{aligned} i\bar{q}\not{D}q &= \delta_{ij}\begin{pmatrix}\bar{u}^i_L & \bar{d}^i_L\end{pmatrix}\left(i\not{\partial} + \gamma_\mu\begin{pmatrix}\frac{g_Y}{6}B_\mu + \frac{g_L}{2}W^3_\mu & \frac{g_L}{\sqrt{2}}W^+_\mu \\ \frac{g_L}{\sqrt{2}}W^-_\mu & \frac{g_Y}{6}B_\mu - \frac{g_Y}{2}W^3_\mu\end{pmatrix}\right)\begin{pmatrix}u^j_L \\ d^j_L\end{pmatrix} \\ &= \frac{e}{\sqrt{2}\sin\theta_w}\left(W^+_\mu \bar{\mathbf{u}}^i_L\gamma^\mu V^{ij}\mathbf{d}^j_L + W^-_\mu \bar{\mathbf{d}}^i_L\gamma^\mu (V^\dagger)^{ij}\mathbf{u}^j_L\right) + \cdots \end{aligned} \tag{1.5}$$

so, in the mass basis the $W^\pm$ bosons couple fermions from different generations together with strengths according to $V = U^\dagger_u U_d$, the Cabibbo-Kobayashi-Maskawa (CKM) matrix [2, 3]. There is additional redundancy (in this case, the phases of the mass basis quark fields) to reduce the number of degrees of freedom of this matrix - the standard parametrisation of the remaining degrees of freedom is:

$$V = \begin{pmatrix}1 & & \\ & \cos\theta_{23} & \sin\theta_{23} \\ & -\sin\theta_{23} & \cos\theta_{23}\end{pmatrix}\begin{pmatrix}\cos\theta_{13} & & \sin\theta_{13}e^{i\delta} \\ & 1 & \\ -\sin\theta_{13}e^{i\delta} & & \cos\theta_{13}\end{pmatrix}\begin{pmatrix}\cos\theta_{12} & \sin\theta_{12} & \\ -\sin\theta_{12} & \cos\theta_{12} & \\ & & 1\end{pmatrix}$$

The experimentally determined values are $\sin(\theta_{12}) = 0.22501 \pm 0.0006$, $\sin(\theta_{23}) = 0.04183^{+0.00079}_{-0.00062}$, $\sin(\theta_{13}) = 0.003732^{+0.000090}_{-0.00008}$, $\delta = 1.147 \pm 0.026$[4]. Note that most of the mixing occurs between the first two generations, and it's a good approximation to take $\theta_{23} = \theta_{13} = 0$ (θ_{12} is also known as the Cabibbo angle).

After electroweak symmetry breaking, the particles of the Standard Model span across many orders of magnitude, as shown in Fig. 1.1. The Standard Model (along with neutrino masses and

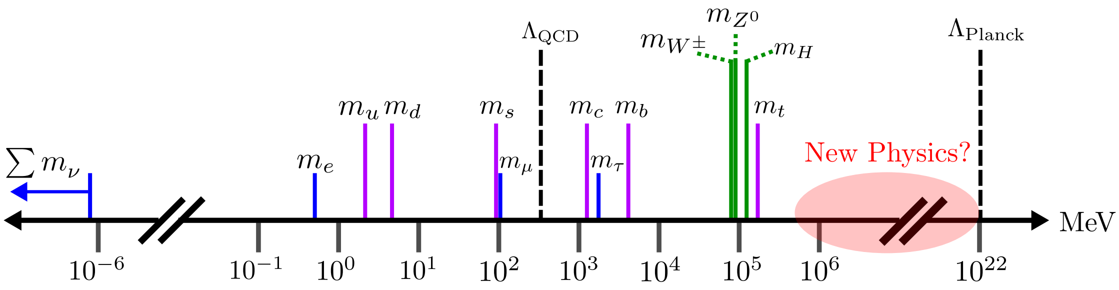

Figure 1.1: Hierarchies of energy scales appearing in the standard model, with data from Ref [4]. Lepton masses are shown in blue, quark masses are shown in purple, electroweak boson masses (after symmetry breaking) are shown in green, and some typical scales $\Lambda_{\text{QCD}} = 330^{+21}_{-63}$MeV [5] and $\Lambda_{\text{Planck}} = G_{\text{Newton}}^{-\frac{1}{2}} \sim 10^{22}$ MeV are shown.

PMNS mixing matrix) has been incredibly successful at describing the observed fundamental particles. But it is also known that the story is not complete, for example at energy scales approaching $\Lambda_{\text{Planck}} = G_{\text{Newton}}^{-\frac{1}{2}}$ quantum gravity effects become important.[2] One motivation of modern particle physics is to explore the apparent desert inbetween the electroweak scale and the Planck scale; is there yet to be discovered New Physics hiding within this desert? Aside from advancing down the precision/energy/intensity frontiers with experimental advances, theorists have the prickly job of determining which regions in phasespace would be interesting to investigate, which is guided by the following questions (among others):

- **Naturalness.**
  A strong notion of 'naturality' is presented by Dirac in Ref [8], wherein a theory is considered natural if all dimensionless constants are $O(1)$ numbers. The flavour hierarchy is unnatural in this sense because $\frac{m_u}{m_c} \sim 0.002$, $\frac{m_c}{m_t} \sim 0.007$[3]. A refined definition by 't Hooft [9] is that a theory is 'technically natural' if a given number is small only when making it zero increases the symmetry of the theory: in other words a parameter is *allowed* to be small if it cannot receive radiative corrections from Planck scale physics due to the enhanced symmetry. There are parameters in the Standard Model which are *not* natural in this sense: for instance the Higgs mass, or the parameter

---

[2] Furthermore, U(1) gauge theories coupled to fermions have a perturbative Landau-pole Λ_{QED} at which energy the renormalized coupling strength blows up to infinity, at a fixed order of perturbation theory. Nonperturbative studies of lattice-QED also seem to indicate that the theory is quantum trivial [6, 7], lending us to believe that the Standard Model is not UV complete.

[3] Quark masses are renormalisation scheme dependent, but the flavour hierarchies persist in any reasonable scheme.

θ_{QCD} which appears in front of the dimension-4 CP-violating term in the QCD Lagrangian[4].

- **Cosmology.**
  Λ-CDM (the Standard Model of cosmology) is a combination of the Standard Model of particle physics with general relavitivity as well as two additions: cold Dark Matter as well as a cosmological constant Λ. Given the success of Quantum Field Theory at describing the Standard Model of particle physics, it is natural to conjecture that these two additional components should also be described by some quantum field theory, and many such models are constructed that are consistent with current experimental cosmological constraints. There are many more unresolved cosmological problems including explaining baryogenesis [12], the lithium abundance problem [13], and the Hubble tension [14].

- **Particle Physics Tensions.**
  Out of the many theoretical predictions made by the Standard Model, a handful show tensions with experimental data. Two recent examples in particle physics are the Collider Detector at Fermilab's recent high-precision measurement of the W-boson mass [15], and the muon anomalous magnetic moment [16, 17]. These tensions have received signficant further discussion and theoretical updates in the previous few years. Other tensions include the heavy flavour physics tensions, which will be discussed in detail in Sec. 1.2.

To begin tackling the questions raised above requires precision theoretical calculations of Standard Model predictions. At experimentally accessible energies, the electroweak interactions are perturbative, and percent level results can be obtained by one-loop perturbation theory. On the other hand, the $\mathrm{SU}(3)_{\mathrm{QCD}}$ gauge theory's coupling becomes weaker at higher energies (known as asymptotic freedom [18, 19]), and perturbation theory actually becomes *less* reliable at lower energies. The running of the strong coupling α_S as a function of scale is shown in Fig. 1.2, and at fixed orders in perturbation theory has a divergence at an energy scale Λ_{QCD}. Isolating the QCD Lagrangian from the rest of the Standard Model:

$$\mathcal{L}_{\mathrm{QCD}} = -\frac{1}{4}\mathrm{Tr}(F_{\mu\nu}F_{\mu\nu}) + \sum_f \overline{\psi}_f(i\not{D} - m_f)\psi_f, \tag{1.6}$$

one is left with a vector-like theory, where electroweak couplings can be considered as external currents (as is done in the Fermi effective theory, discussed in Sec. 4.1.2). To obtain accurate predictions about the strong gauge theory requires non-perturbative methods, the most well-established of which being Lattice-QCD which is discussed in some detail in Sec. 2.2.

The flavors of the quarks have masses spanning many orders of magnitude, and are split into roughly three categories, the light quarks, the heavy quarks, and the top quark. The up, down

---

[4] Note that θ_{QCD} actually does not run under ordinary perturbative renormalisation group at all, as it is a topological term that only contributes on a nontrivial background. It does however have nonperturbative renormalisation scale dependence, and since the Standard Model is already known to be CP-violating (due to the CKM-matrix phase), it is technically unnatural that the effective parameter $\overline{\theta}_{\mathrm{QCD}}$ has been experimentally constrained to be $\overline{\theta}_{\mathrm{QCD}} \leq 10^{-10}$ [10, 11]

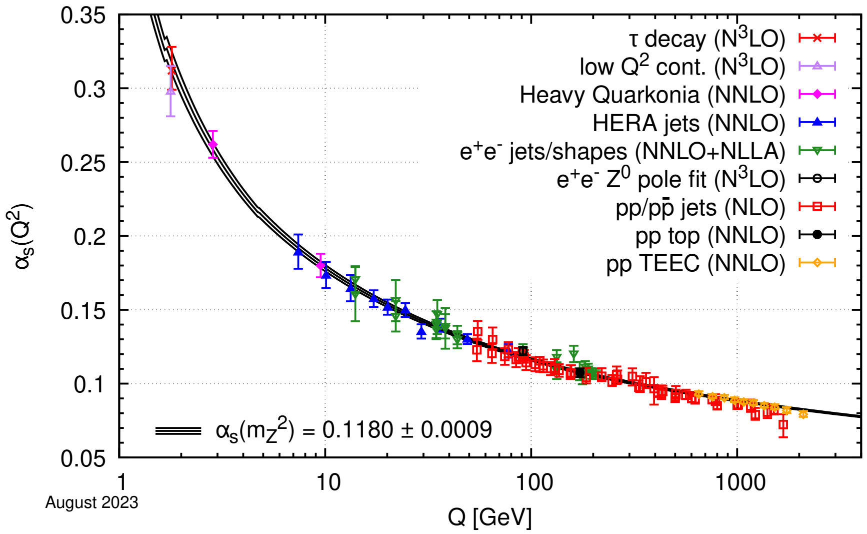

Figure 1.2: (Fig. from review [4]) Dependence of the running strong coupling $\alpha_S(Q)$ as a function of the energy scale Q, where α_S is renormalized in the $\overline{\text{MS}}$ prescription. The black lines show the 5-loop perturbative running, with a jump with jumps at $\mu^2 = m_c^2, m_b^2$ due to matching between $N_f + 1$ and N_f flavour theories. Note that the strong coupling tends to zero as $Q \to \infty$ (asymptotic freedom), and in $\overline{\text{MS}}$ for fixed orders of perturbation theory, the running coupling blows up at some finite scale.

and strange quarks are considered light quarks because $m_f \lesssim \Lambda_{\text{QCD}}$. The quark masses of light quarks do not contribute much to hadrons containing valence light quarks. In fact, due to the light masses of the up, down, and strange quarks, the theory of the light hadrons is fairly well described by Chiral Effective Field Theory. The charm and bottom quarks are considered heavy, with $\frac{m_c}{\Lambda_{\text{QCD}}} \sim 3.9$, $\frac{m_b}{\Lambda_{\text{QCD}}} \sim 12.7$[5]. They are heavier compared to typical QCD interaction energies, and hadrons containing bottom quarks and charm quarks appear as some light QCD degrees of freedom bound to the heavy quark. The top quark is often considered in it's own category, as it is so heavy that it does not form bound states. Formally, there are likely resonance poles corresponding to what would be called 'hadrons containing a top quark' [20, 21], however the corresponding poles in the S-matrix are so far off the real axis (very short lifetimes) that colloquially it is said that the top quark decays before it has time to hadronize.

One of the main reasons that studying the large m_f limit is interesting is that it gives an additional small parameter, Λ_{QCD}/m_f, to expand in, which introduces additional symmetries and simplifies many calculations. To see this in action, consider a heavy hadron containing a heavy quark bound to some number of light quarks. In the rest frame of the heavy hadron the heavy quark is approximately at rest, and interactions with the light degrees of freedom induces changes in

---

[5] These ratios depend on the renormalisation scheme used for the quark masses, and the exact definition of Λ_{QCD} used.

momentum of the order of Λ_{QCD}. In the infinite mass limit, the heavy quark becomes a nonrelativistic object and the complication in systems such as the heavy-light mesons are due to the light degrees of freedom, dubbed 'brown muck' by Nathan Isgur [22]. Inspired by this observation, an effective field theory can be described with operators having power counting parameter $\lambda := \frac{\Lambda_{\mathrm{QCD}}}{m_Q}$ where Q is a heavy flavour of quark. The heavy quark momentum is expanded as:

$$p^\mu = m_Q v^\mu + k^\mu \tag{1.7}$$

where $v^\mu \sim O(\lambda^0)$ is a fixed timelike four-vector satisfying $v^2 = 1$, and $k^\mu / m_Q \sim O(\lambda^1)$ describes the residual momenta due to interactions with the light degrees of freedom. The free heavy quark propagator in momentum space can also be expanded in powers of λ:

$$\langle Q(0)\overline{Q}(p)\rangle = \frac{i(\not{p} + m_Q)}{p^2 - m_Q^2 + i\epsilon} = \frac{i(m_Q(1+\not{v}) + \not{k})}{2m_Q v\cdot k + k^2 + i\epsilon} \tag{1.8}$$

$$= \frac{i}{v\cdot k + i\epsilon}\left(\frac{1+\not{v}}{2}\right) + \frac{i(v\cdot k)\not{k} - ik^2\left(\frac{1+\not{v}}{2}\right)}{2m_Q(v\cdot k)^2 + i\epsilon} + O\left(\frac{\lambda}{m_Q}\right) \tag{1.9}$$

To leading order, the projector $P_+ = \frac{1+\not{v}}{2}$ projects onto the particle degrees of freedom. Keeping just this piece, the antiparticle degrees of freedom are removed from the theory, in the sense that contracting the propagator against external antiparticle-like spinors will give zero because of this projector. In position space, the propagator takes the form (for details on heavy-quark integrals, see Sec. 2.1.2):

$$\langle Q(0)\overline{Q}(x)\rangle = \delta^{d-1}(\vec{x})\frac{1+\gamma_0}{2}\theta(0 > x^0) \tag{1.10}$$

where v has been chosen to be purely timelike, $v = (1,0,0,0)^T$, and d is the spacetime dimension. The $\delta^{d-1}(\vec{x})$ factor causes the heavy quark to not spatially propagate in the infinite mass limit of the quark, hence why this limit is known as the 'static quark limit'. One can also check what happens to a quark-gluon-quark type vertex:

$$\left(\frac{1+\not{v}}{2}\right)\gamma^\mu\left(\frac{1+\not{v}}{2}\right) = v^\mu\left(\frac{1+\not{v}}{2}\right), \quad -ig\gamma^\mu T^a \mapsto -igv^\mu T^a \tag{1.11}$$

The formal procedure of expanding the QCD Lagrangian in powers of λ generates the Heavy Quark Effective Theory (HQET) [23], whose leading order Lagrangian is given by:

$$\mathcal{L}_{\mathrm{HQET}} = \overline{Q}_v iv\cdot DQ_v + O(\lambda) \tag{1.12}$$

where the heavy field Q_v satisfies $P_+ Q_v = Q_v$. The power-counting is that $Q_v \sim \lambda^{-\frac{1}{2}}, v \sim \lambda^0, D \sim \lambda^1$, so that the leading term in the HQET Lagrangian is λ^0. The static nature of the heavy quark introduces new symmetries such as the heavy quark spin-symmetry, and causes the theory to drastically simplify. Effective Field Theories such as HQET and the related Non-Relativistic QCD (NRQCD) used for systems containing more than one heavy quark, allow one to study these heavy quark systems with more control, and offers greater understanding of the underlying physics.

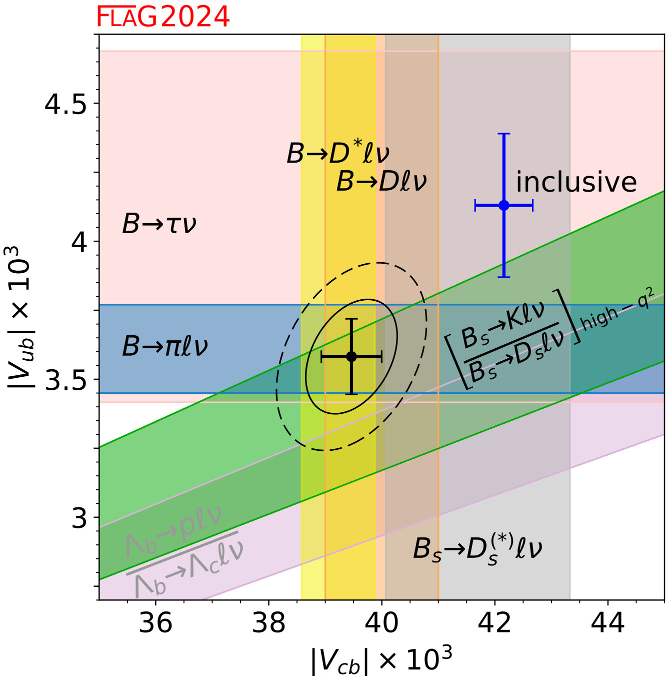

Figure 1.3: Tensions between inclusive and exclusive measurements of V_{ub} and V_{cb}, where the black datapoint is the combined constraint from exclusive determinations, and the blue datapoint is from the inclusive determination. Figure from Ref [5], with data from [24–51, 51–60].

1.2 TENSIONS IN HEAVY HADRON DECAYS

Much of what drives the heavy-flavour-physics community is the presence of tensions between theoretical and experimental predictions of various decay channels. Of the tensions, three stand out due to their persistence over time, and their roughly 3σ level of statistical significance:

- **Lepton Flavour Universality.**
  Lepton Flavour Universality is the statement that in the Standard Model the different generations of leptons all couple in the same fashion to the weak force, the only difference being their masses. This provides predictions between different branching ratios. Two quantities that can be measured quite accurately are given by ratios of branching fractions of decays of semileptonic decays of B mesons to τ, versus B mesons to either of the lighter leptons:

$$R(D) = \frac{\mathcal{B}(B \to D\tau^-\overline{\nu}_\tau)}{\mathcal{B}(B \to Dl^-\overline{\nu}_l)}, \qquad R(D^*) = \frac{\mathcal{B}(B \to D^*\tau^-\overline{\nu}_\tau)}{\mathcal{B}(B \to D^*l^-\overline{\nu}_l)}, \tag{1.13}$$

  where $l \in \{e, \mu\}$ has been averaged over in the denominators of the expressions appearing in Eq. (1.13). Due to the ratio construction, the $R(D^{(*)})$ quantities are largely independent of parameters such as V_{cb} and hadronic form factors $B \to D^{(*)}$, and instead are dominated by phasespace effects. For instance, due to the heavy mass of the τ, the phasespace of decays to τ are suppressed. These effects can be calculated quite accurately, and currently there is a 3.14σ combined tension between the experimentally observed $R(D), R(D^*)$ and the theoretically predicted ratios [61].

- **Rare b-decays.**
  The rare b-decays $b \to sl^+l^-$ are excellent processes to consider to search for new physics, because they are induced by flavor-changing-neutral-currents which are loop-suppressed in the Standard Model. Hence, these processes are proportionally much more sensitive to new physics contributions. Current tensions in the $B_s \to \phi\mu^+\mu^-$ branching rates are about 3.6σ [62].

- **Inclusive-Exclusive V_{ub}, V_{cb} tension.**
  The V_{ub} and V_{cb} CKM matrix-elements determine the tree-level decay rates of bottom quarks into up and charm quarks respectively; and hence are important factors in the decay rates of b-hadrons into light hadrons containing up quarks and charm-hadrons respectively. Measurements of the V_{ub} and V_{cb} CKM matrix-elements can be performed by exclusive analyses (analysing individual decay channels of b-hadrons) or inclusive analyses (for example, an inclusive semi-leptonic analysis sums over all semi-leptonic decay channels). Experimental determinations following these two strategies are shown in Fig. 1.3, where the bounds from each exclusive channel is a different shaded band. The tension between the two different determinations has a significance of 3σ.

Of these, the tension between the inclusive and exclusive determinations of the CKM matrix elements is particularly interesting, due to the theoretical difficulties inherent in ab-initio calculations of inclusive decay rates. As explained later in Sec. 4.1.2, one of the more straightforward approaches to predictions of inclusive decay rates of heavy hadrons is to expand the two insertions of the electroweak current appearing in the optical theorem as an Operator Product Expansion (OPE). In fact, the experimental method used in Fig. 1.3 for extracting the inclusive matrix elements relies on fits of experimental data to OPE matrix elements, in contrast to exclusive measurements which require no OPE. It is natural then to wonder whether this tension is caused by a failure of convergence in the OPE (also known as violations of quark-hadron duality). To better understand the situation, first-principles determinations of the matrix elements appearing in the OPE are needed, and this thesis presents my work towards systematically controlled determinations of these matrix elements.

In more detail, the inclusive decay rate of a heavy hadron H_b can be written as a sum [63]:

$$\begin{aligned}\Gamma(H_b) = \frac{G_F^2 m_b^5}{192\pi^3}|V_{cb}|^2\Bigg\{ c_3\frac{\langle H_b|\bar{b}b|H_b\rangle}{2M_{H_b}} + \frac{c_5}{m_b^2}\frac{\langle H_b|\bar{b}g_s\sigma_{\mu\nu}F^{\mu\nu}b|H_b\rangle}{2M_{H_b}} \\ + \frac{c_6}{m_b^3}\frac{\langle H_b|(\bar{b}\Gamma_L q)(\bar{q}\Gamma_R b)|H_b\rangle}{M_{H_b}} + O\left(\frac{1}{m_b^4}\right)\Bigg\}\end{aligned} \tag{1.14}$$

where G_F is the Fermi constant, M_{H_b} is the mass of the heavy hadron H_b, $\sigma_{\mu\nu} = \frac{i}{2}[\gamma_\mu, \gamma_\nu]$, g_s is the strong coupling constant, Γ_L, Γ_R are spin-colour matrices that are discussed in more detail in

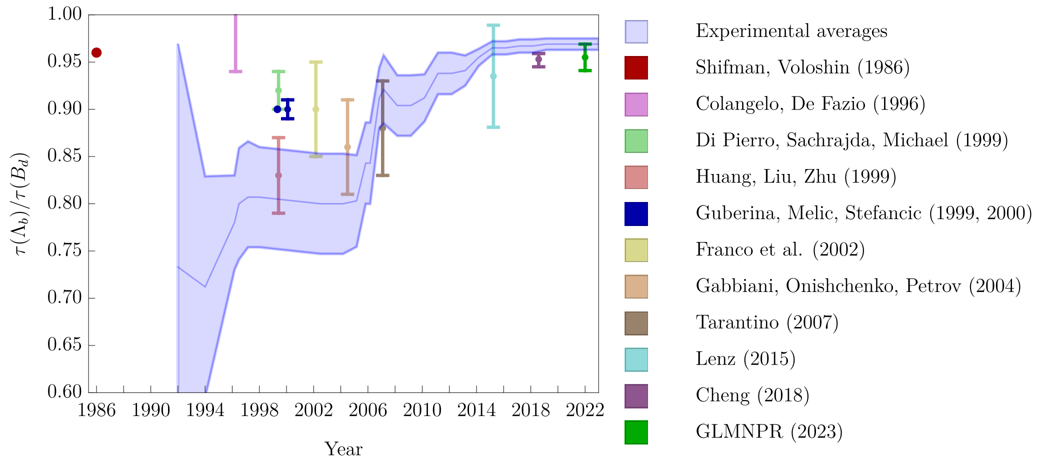

Figure 1.4: Figure from Ref [65], showing the ratio of lifetimes of the Λ_b baryon and neutral B_d meson. Theoretical predictions using various frameworks for the lifetime ratios are shown in the different scatter points [63, 66–76]. The only Lattice-QCD determination of the relevant matrix elements dates back to work from UKQCD 25 years ago with quenched ensembles (no dynamical fermions) and lattice perturbation theory renormalisation of the operators [68, 77].

Sec. 3.2, and c_n are perturbatively calculable Wilson coefficients. Note that this series relies on the heavy mass of the b quark to converge. Of these terms, matrix elements of the dimension 6 flavour-nonsinglet operators $(\bar{b}\Gamma_L q)(\bar{q}\Gamma_R b)$ are known as the spectator effects, due to the participation of the light spectator quark in the decay.[6] After matching the OPE operators to HQET, these contributions are phasespace enhanced by a factor of $16\pi^2$ relative to other $\frac{1}{m_b^3}$ corrections. As explained in Ref [64], these contributions can either be fit from experimental data with sizeable uncertainties, or the analysis can focus on regions of phasespace where these effects are relatively suppressed and can simply be treated as a systematic error on the analysis. In either strategy, they form a sizeable contribution to the total error budget of the inclusive CKM matrix element determinations.

Historically, these spectator effects were also interesting as they provided large contributions to measurements of ratios of lifetimes of b-hadrons with different light quark contents. In these ratios, the leading CKM matrix elements and other factors cancelled out, leaving only hadronic matrix element contributions. It was understood from the early days of HQET that to leading order, the decays of b-hadrons are largely determined by decays of the b-quark in isolation; and that corrections due to the 'brown-muck' describing the light degrees of freedom are subleading. This lead to the prediction that ratios of lifetimes of different b-hadrons should be $1 + O\left(\frac{\Lambda_{\text{QCD}}}{m_b}\right)$. In contrast, for about a decade the experimentally extracted value of the lifetime ratio $\tau(\Lambda_b)/\tau(B_d)$ hovered around

---

[6] These are also known as 'Weak Annihilation' terms in the literature.

0.8 ± 0.05 (Fig. 1.4), leading to speculation of enhanced contributions from the Spectator Effects [78]. This tension closed slightly in 2007 with an updated measurement of the Λ_b-lifetimes from the CDF collaboration [79] of $\tau(\Lambda_b) = 1.593^{+0.083}_{-0.078}(\text{stat}) \pm 0.033(\text{syst})$, which was 3.2σ higher than the previous world average $\tau(\Lambda_b) = 1.230 \pm 0.074$. [7] In recent years, this tension is mostly considered resolved, however the Spectator Effect matrix elements remain a large contribution to ratios of inclusive lifetimes[65].

There are various strategies to theoretical predictions of the Spectator Effect matrix elements, which are reviewed in Sec. 4.1.3. In this thesis, I present progress towards Lattice-QCD determinations of the Spectator Effect matrix elements in HQET. The QCD operators appearing in an OPE have power-divergent mixings that prevent simple extractions with Lattice-QCD, hence it is common to then match these operators to HQET, in a procedure that is collectively known as the Heavy Quark Expansion. This comes with the unique challenge of dealing with the introduced static quark self-energy divergence, which causes exponentially bad signal-to-noise problems in the continuum limit, as well as difficulties in defining renormalisation schemes. In Chapter 3, I present new gauge-invariant position-space renormalisation schemes for the four-quark operators appearing in these Spectator Effects. The $O(\alpha_S)$ matchings between the X-space scheme and $\overline{\text{MS}}$ are calculated, and these are used to provide the first unquenched Lattice-QCD measurement of the Spectator Effects in HQET. A review of all the different dimensional regularisation integrals required for the X-space to $\overline{\text{MS}}$ matchings presented here is also provided in Appendix B.

1.3 Real-time dynamics of heavy quarks

As the temperature is increased the renormalised strong coupling drops to zero by asymptotic freedom, and one expects a transition from the zero-temperature 'confined' phase of QCD (where the degrees of freedom are hadrons) to a high temperature 'deconfined' phase (where perturbative quarks and gluons become the correct degrees of freedom). In a grand canonical ensemble where all chemical potentials are set to zero it turns out that the transition between these two phases is an analytic-crossover for physical quark masses [85, 86]. The phase diagram is often extended by considering the effect of adding a positive baryon chemical potential μ_B, where the corresponding Euclidean-time partition function can be expressed as:

$$Z_E[T,\mu_B] = \int D\overline{\psi}D\psi D\mathcal{A}\, \exp\left[\int_0^\beta \mathrm{d}t \int \mathrm{d}^3x\, \sum_f \overline{\psi_f}\left(\not{\mathcal{D}} + m_f + \frac{\mu_B}{3}\gamma_0\right)\psi_f + \mathcal{L}_{\text{gauge}}\right] \tag{1.15}$$

Note that due to the γ_0 insertion, the Dirac operator no longer anticommutes with γ_5, and in fact the fermion determinant is complex-valued causing Eq. (1.15) to no longer be an integral against a probability distribution. This makes practical investigations of the phase structure using path-integral Monte Carlo (introduced in Sec. 2.2) difficult, however perturbative calculations can still be

---

[7] This and other measurements, like of B_s mixing and the properties of Ξ_b, Σ_b baryons, are largely thanks to the high luminosity run-II of the tevatron [80].

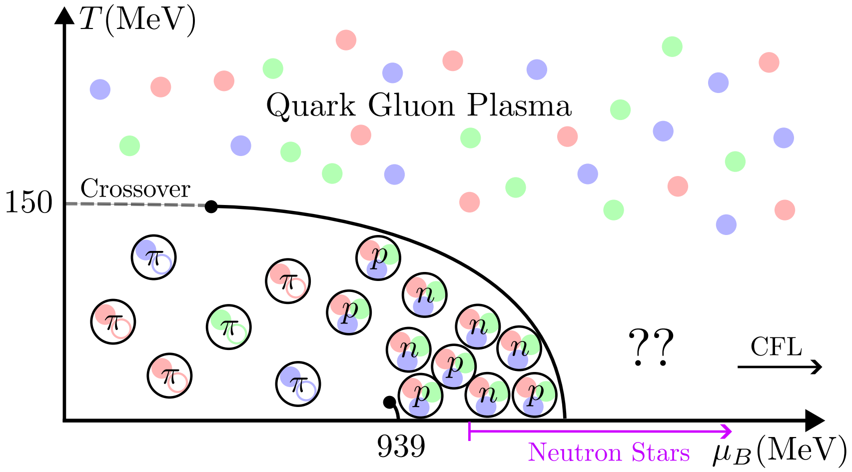

Figure 1.5: Conjectured phase diagram of QCD in the (T, μ_B) plane (not to scale). Along the $T = 0$ axis as μ_B increases, first there is a liquid-gas transition to nuclear matter at μ_B =mass of the nucleon [81, 82]. At intermediate densities the phase structure is not well understood, but at high densities where perturbative calculations become reliable there is expected to be a Colour-Flavour-Locked (CFL) phase that is colour superconducting [83, 84]. Neutron stars occupy the low T, intermediate μ_B region in this schematic, and are conjectured to contain various phases of QCD matter. The putative phase transition separating hadronic matter from the high temperature Quark-Gluon-Plasma phase ends at a critical endpoint, which is currently being searched for.

performed in certain regions of phasespace, leading to the conjectured rich phase structure shown in Fig. 1.5.

The predominant way that experimentalists attempt to create and measure properties of the quark-gluon-plasma phase is with heavy-ion colliders, such as the Large Hadron Collider (LHC) and Relativistic Heavy Ion Collider (RHIC). The behaviours of heavy quarks as they travel through the QGP and eventually hadronize offers a precious probe of the thermal QGP medium. For instance, it has long been conjectured [87] that bottomonium production is suppressed if produced within a QGP medium. Such a suppression has been observed in heavy-ion collider experiments [88–91]. The authors of the original references reason that after $\bar{b}b$ pairs are produced, they are allowed to propagate freely in the deconfined QGP medium whilst the medium is still hot as the colour-force between them is screened by the medium, and only after the medium cools down do they hadronize. This results in a greater production rate of open-heavy hadrons (hadrons containing a single heavy quark and some light degrees of freedom) than heavy quarkonia pairs as sketched in Fig. 1.6. Recent studies [92] have suggested that this interpretation is actually incorrect, as the real-

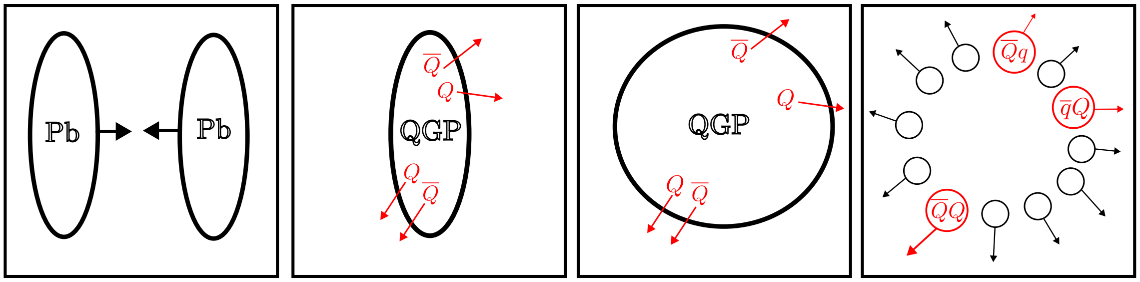

1. Initial heavy-ion Collision

2. Heavy quarks produced in a QGP fireball

3. The heavy quarks are carried along with the QGP

4. Fireball cools and quarks hadronize.

Figure 1.6: Schematic depicting a typical central collision at a heavy-ion collider.

part of the heavy quark-antiquark potential actually is not meaningfully screened at all - rather the suppression is due to the significant imaginary component of the heavy quark-antiquark potential at finite temperatures, leading to quarkonia dissolution.

To better understand the role of the imaginary potential and to extract properties of the QGP produced at heavy-ion colliders from observed bottomonium rates, one must be able to perform theoretical simulations of the real-time dynamics of heavy quarks in the medium. The general problem of real-time simulations of lattice discretised QFTs is very difficult due to the exponential growth of the size of the Hilbert space as you increase the volume or take the continuum limit. The specific problem of simulating heavy quarks in the QGP actually happens to be in an easy corner of the realtime dynamics landscape, as not only are nonrelativistic theories a good description of the heavy quark degrees of freedom, at high temperatures the effects of light quarks and gluons can be treated perturbatively and integrated out. This procedure results in an Open Quantum System description of the remaining heavy quark degrees of freedom encoded as a density matrix, whose time evolution is given by a Lindblad equation.

To solve the problem of the large Hilbert spaces, the approach advocated for in this thesis is to use a variational ansätz which parametrises the space of quantum states in terms of a few parameters that capture the essential aspects of the underlying physics. In Chapter 5, this approach was studied in a simple test-case for an open Quantum Field Theory - the open massive Schwinger Model, which is a 1+1d $U(1)$ gauge theory with a single massive fermionic degree of freedom coupled to a thermal bath. The density matrices were parametrised by a neural network ansätz known as the Neural Density Operator (NDO, introduced in Sec. 5.1), for which arbitrary initial states can be prepared and then time-evolved in the thermal bath in a systematically controllable manner. Extensions of these methods to more realistic descriptions of heavy quarkonia in the QGP are currently underway.

By preparing these variational ansätz for density matrices, there is also the attractive possibility that the thermal state can be investigated in regimes for which it is impossible to investigate using traditional path-integral Monte Carlo methods. For example, as discussed earlier introducing a chemical potential term μ_B for the QCD action introduces a sign problem, which prevents efficient sampling and evaluation of observables in Lattice-QCD. However, in the Hamiltonian formulation there is no such issue as long as one can solve the problem of the exponentially large Hilbert space. As it so happens, the steady state of the Lindblad equation is approximately the thermal state, with errors depending on the perturbative order to which the Lindbladian has been derived. In Sec. 5.2.4, the NDO ansätz is shown to be capable of parametrising the steady states of the Open Schwinger Model at large volumes, and a study is performed at different number densities. Extending this approach to QCD would be difficult due to the larger dimension, more complicated gauge group structure and matter content - however may be a possibility in the future.

BIBLIOGRAPHY

[1] Matthew D. Schwartz. *Quantum Field Theory and the Standard Model*. Cambridge University Press, 3 2014. ISBN 978-1-107-03473-0, 978-1-107-03473-0.

[2] Nicola Cabibbo. Unitary Symmetry and Leptonic Decays. *Phys. Rev. Lett.*, 10:531–533, 1963. doi: 10.1103/PhysRevLett.10.531.

[3] Makoto Kobayashi and Toshihide Maskawa. CP Violation in the Renormalizable Theory of Weak Interaction. *Prog. Theor. Phys.*, 49:652–657, 1973. doi: 10.1143/PTP.49.652.

[4] S. Navas et al. Review of particle physics. *Phys. Rev. D*, 110(3):030001, 2024. doi: 10.1103/PhysRevD.110.030001.

[5] Y. Aoki et al. FLAG Review 2021. *Eur. Phys. J. C*, 82(10):869, 2022. doi: 10.1140/epjc/s10052-022-10536-1.

[6] M. Gockeler, R. Horsley, V. Linke, Paul E. L. Rakow, G. Schierholz, and H. Stuben. Is there a Landau pole problem in QED? *Phys. Rev. Lett.*, 80:4119–4122, 1998. doi: 10.1103/PhysRevLett.80.4119.

[7] M. Gockeler, R. Horsley, V. Linke, Paul E. L. Rakow, G. Schierholz, and H. Stuben. Resolution of the Landau pole problem in QED. *Nucl. Phys. B Proc. Suppl.*, 63:694–696, 1998. doi: 10.1016/S0920-5632(97)00875-X.

[8] Paul A. M. Dirac. The Cosmological constants. *Nature*, 139:323, 1937. doi: 10.1038/139323a0.

[9] Gerard 't Hooft. Naturalness, chiral symmetry, and spontaneous chiral symmetry breaking. *NATO Sci. Ser. B*, 59:135–157, 1980. doi: 10.1007/978-1-4684-7571-5_9.

[10] Nodoka Yamanaka. Review of the electric dipole moment of light nuclei. *Int. J. Mod. Phys. E*, 26(4):1730002, 2017. doi: 10.1142/S0218301317300028.

[11] C. A. Baker et al. An Improved experimental limit on the electric dipole moment of the neutron. *Phys. Rev. Lett.*, 97:131801, 2006. doi: 10.1103/PhysRevLett.97.131801.

[12] A. D. Sakharov. Violation of CP Invariance, C asymmetry, and baryon asymmetry of the universe. *Pisma Zh. Eksp. Teor. Fiz.*, 5:32–35, 1967. doi: 10.1070/PU1991v034n05ABEH002497.

[13] Brian D. Fields. The primordial lithium problem. *Ann. Rev. Nucl. Part. Sci.*, 61:47–68, 2011. doi: 10.1146/annurev-nucl-102010-130445.

[14] Licia Verde, Nils Schöneberg, and Héctor Gil-Marín. A Tale of Many H0. *Ann. Rev. Astron. Astrophys.*, 62(1):287–331, 2024. doi: 10.1146/annurev-astro-052622-033813.

[15] T. Aaltonen et al. High-precision measurement of the W boson mass with the CDF II detector. *Science*, 376(6589):170–176, 2022. doi: 10.1126/science.abk1781.

[16] T. Aoyama et al. The anomalous magnetic moment of the muon in the Standard Model. *Phys. Rept.*, 887:1–166, 2020. doi: 10.1016/j.physrep.2020.07.006.

[17] D. P. Aguillard et al. Measurement of the Positive Muon Anomalous Magnetic Moment to 0.20 ppm. *Phys. Rev. Lett.*, 131(16):161802, 2023. doi: 10.1103/PhysRevLett.131.161802.

[18] David J. Gross and Frank Wilczek. Ultraviolet Behavior of Nonabelian Gauge Theories. *Phys. Rev. Lett.*, 30:1343–1346, 1973. doi: 10.1103/PhysRevLett.30.1343.

[19] H. David Politzer. Reliable Perturbative Results for Strong Interactions? *Phys. Rev. Lett.*, 30:1346–1349, 1973. doi: 10.1103/PhysRevLett.30.1346.

[20] Benjamin Fuks, Kaoru Hagiwara, Kai Ma, and Ya-Juan Zheng. Signatures of toponium formation in LHC run 2 data. *Phys. Rev. D*, 104(3):034023, 2021. doi: 10.1103/PhysRevD.104.034023.

[21] Aram Hayrapetyan et al. Observation of quantum entanglement in top quark pair production in proton–proton collisions at $\sqrt{s} = 13$ TeV. *Rept. Prog. Phys.*, 87(11):117801, 2024. doi: 10.1088/1361-6633/ad7e4d.

[22] Howard Georgi. Heavy quark effective field theory. In *Theoretical Advanced Study Institute in Elementary Particle Physics (TASI 91): Perspectives in the Standard Model*, 8 1991.

[23] Aneesh V. Manohar and Mark B. Wise. *Heavy quark physics*, volume 10. 2000. ISBN 978-0-521-03757-0.

[24] Jon A. Bailey et al. $|V_{ub}|$ from $B \to \pi\ell\nu$ decays and (2+1)-flavor lattice QCD. *Phys. Rev. D*, 92(1):014024, 2015. doi: 10.1103/PhysRevD.92.014024.

[25] J. M. Flynn, T. Izubuchi, T. Kawanai, C. Lehner, A. Soni, R. S. Van de Water, and O. Witzel. $B \to \pi\ell\nu$ and $B_s \to K\ell\nu$ form factors and $|V_{ub}|$ from 2+1-flavor lattice QCD with domain-wall light quarks and relativistic heavy quarks. *Phys. Rev. D*, 91(7):074510, 2015. doi: 10.1103/PhysRevD.91.074510.

[26] Brian Colquhoun, Shoji Hashimoto, Takashi Kaneko, and Jonna Koponen. Form factors of B→$\pi\ell\nu$ and a determination of —Vub— with Möbius domain-wall fermions. *Phys. Rev. D*, 106(5):054502, 2022. doi: 10.1103/PhysRevD.106.054502.

[27] P. del Amo Sanchez et al. Study of $B \to \pi\ell\nu$ and $B \to \rho\ell\nu$ Decays and Determination of $|V_{ub}|$. *Phys. Rev. D*, 83: 032007, 2011. doi: 10.1103/PhysRevD.83.032007.

[28] J. P. Lees et al. Branching fraction and form-factor shape measurements of exclusive charmless semileptonic B decays, and determination of $|V_{ub}|$. *Phys. Rev. D*, 86:092004, 2012. doi: 10.1103/PhysRevD.86.092004.

[29] H. Ha et al. Measurement of the decay $B^0 \to \pi^-\ell^+\nu$ and determination of $|V_{ub}|$. *Phys. Rev. D*, 83:071101, 2011. doi: 10.1103/PhysRevD.83.071101.

[30] A. Sibidanov et al. Study of Exclusive $B \to X_u\ell\nu$ Decays and Extraction of $\|V_{ub}\|$ using Full Reconstruction Tagging at the Belle Experiment. *Phys. Rev. D*, 88(3):032005, 2013. doi: 10.1103/PhysRevD.88.032005.

[31] Jon A. Bailey et al. B→D$\ell\nu$ form factors at nonzero recoil and —V$_{cb}$— from 2+1-flavor lattice QCD. *Phys. Rev. D*, 92(3):034506, 2015. doi: 10.1103/PhysRevD.92.034506.

[32] Heechang Na, Chris M. Bouchard, G. Peter Lepage, Chris Monahan, and Junko Shigemitsu. $B \to Dl\nu$ form factors at nonzero recoil and extraction of $|V_{cb}|$. *Phys. Rev. D*, 92(5):054510, 2015. doi: 10.1103/PhysRevD.93.119906. [Erratum: Phys.Rev.D 93, 119906 (2016)].

[33] Bernard Aubert et al. Measurement of —V(cb)— and the Form-Factor Slope in anti-B —> D l- anti-nu Decays in Events Tagged by a Fully Reconstructed B Meson. *Phys. Rev. Lett.*, 104:011802, 2010. doi: 10.1103/PhysRevLett.104.011802.

[34] R. Glattauer et al. Measurement of the decay $B \to D\ell\nu_\ell$ in fully reconstructed events and determination of the Cabibbo-Kobayashi-Maskawa matrix element $|V_{cb}|$. *Phys. Rev. D*, 93(3):032006, 2016. doi: 10.1103/PhysRevD.93.032006.

[35] A. Bazavov et al. Semileptonic form factors for $B \to D^*\ell\nu$ at nonzero recoil from 2+1-flavor lattice QCD: Fermilab Lattice and MILC Collaborations. *Eur. Phys. J. C*, 82(12):1141, 2022. doi: 10.1140/epjc/s10052-022-10984-9. [Erratum: Eur.Phys.J.C 83, 21 (2023)].

[36] Y. Aoki, B. Colquhoun, H. Fukaya, S. Hashimoto, T. Kaneko, R. Kellermann, J. Koponen, and E. Kou. B→D*$\ell\nu\ell$ semileptonic form factors from lattice QCD with Möbius domain-wall quarks. *Phys. Rev. D*, 109(7):074503, 2024. doi: 10.1103/PhysRevD.109.074503.

[37] Judd Harrison and Christine T. H. Davies. B→D* and Bs→Ds* vector, axial-vector and tensor form factors for the full q2 range from lattice QCD. *Phys. Rev. D*, 109(9):094515, 2024. doi: 10.1103/PhysRevD.109.094515.

[38] E. Waheed et al. Measurement of the CKM matrix element $|V_{cb}|$ from $B^0 \to D^{*-}\ell^+\nu_\ell$ at Belle. *Phys. Rev. D*, 100(5):052007, 2019. doi: 10.1103/PhysRevD.100.052007. [Erratum: Phys.Rev.D 103, 079901 (2021)].

[39] M. T. Prim et al. Measurement of differential distributions of B→D*$\ell\nu^-\ell$ and implications on —Vcb—. *Phys. Rev. D*, 108(1):012002, 2023. doi: 10.1103/PhysRevD.108.012002.

[40] I. Adachi et al. Determination of —Vcb— using B¯0→D*+ℓ−ν¯ℓ decays with Belle II. *Phys. Rev. D*, 108(9): 092013, 2023. doi: 10.1103/PhysRevD.108.092013.

[41] Yasmine Sara Amhis et al. Averages of b-hadron, c-hadron, and τ-lepton properties as of 2021. *Phys. Rev. D*, 107(5):052008, 2023. doi: 10.1103/PhysRevD.107.052008.

[42] R. J. Dowdall, C. T. H. Davies, R. R. Horgan, C. J. Monahan, and J. Shigemitsu. B-Meson Decay Constants from Improved Lattice Nonrelativistic QCD with Physical u, d, s, and c Quarks. *Phys. Rev. Lett.*, 110(22): 222003, 2013. doi: 10.1103/PhysRevLett.110.222003.

[43] A. Bussone et al. Mass of the b quark and B -meson decay constants from N$_f$=2+1+1 twisted-mass lattice QCD. *Phys. Rev. D*, 93(11):114505, 2016. doi: 10.1103/PhysRevD.93.114505.

[44] C. Hughes, C. T. H. Davies, and C. J. Monahan. New methods for B meson decay constants and form factors from lattice NRQCD. *Phys. Rev. D*, 97(5):054509, 2018. doi: 10.1103/PhysRevD.97.054509.

[45] A. Bazavov et al. B- and D-meson leptonic decay constants from four-flavor lattice QCD. *Phys. Rev. D*, 98(7): 074512, 2018. doi: 10.1103/PhysRevD.98.074512.

[46] B. Kronenbitter et al. Measurement of the branching fraction of $B^+ \to \tau^+\nu_\tau$ decays with the semileptonic tagging method. *Phys. Rev. D*, 92(5):051102, 2015. doi: 10.1103/PhysRevD.92.051102.

[47] J. P. Lees et al. Evidence of $B^+ \to \tau^+\nu$ decays with hadronic B tags. *Phys. Rev. D*, 88(3):031102, 2013. doi: 10.1103/PhysRevD.88.031102.

[48] C. M. Bouchard, G. Peter Lepage, Christopher Monahan, Heechang Na, and Junko Shigemitsu. $B_s \to K\ell\nu$ form factors from lattice QCD. *Phys. Rev. D*, 90:054506, 2014. doi: 10.1103/PhysRevD.90.054506.

[49] J. M. Flynn, R. C. Hill, A. Jüttner, A. Soni, J. T. Tsang, and O. Witzel. Exclusive semileptonic Bs→K$\ell\nu$ decays on the lattice. *Phys. Rev. D*, 107(11):114512, 2023. doi: 10.1103/PhysRevD.107.114512.

[50] Alexei Bazavov et al. $B_s \to K\ell\nu$ decay from lattice QCD. *Phys. Rev. D*, 100(3):034501, 2019. doi: 10.1103/PhysRevD.100.034501.

[51] E. McLean, C. T. H. Davies, J. Koponen, and A. T. Lytle. $B_s \to D_s\ell\nu$ Form Factors for the full q^2 range from Lattice QCD with non-perturbatively normalized currents. *Phys. Rev. D*, 101(7):074513, 2020. doi: 10.1103/PhysRevD.101.074513.

[52] R. Aaij et al. First observation of the decay $B_s^0 \to K^-\mu^+\nu_\mu$ and Measurement of $|V_{ub}|/|V_{cb}|$. *Phys. Rev. Lett.*, 126(8):081804, 2021. doi: 10.1103/PhysRevLett.126.081804.

[53] William Detmold, Christoph Lehner, and Stefan Meinel. $\Lambda_b \to p\ell^-\bar{\nu}_\ell$ and $\Lambda_b \to \Lambda_c\ell^-\bar{\nu}_\ell$ form factors from lattice QCD with relativistic heavy quarks. *Phys. Rev. D*, 92(3):034503, 2015. doi: 10.1103/PhysRevD.92.034503.

[54] Roel Aaij et al. Determination of the quark coupling strength $|V_{ub}|$ using baryonic decays. *Nature Phys.*, 11: 743–747, 2015. doi: 10.1038/nphys3415.

[55] E. McLean, C. T. H. Davies, A. T. Lytle, and J. Koponen. Lattice QCD form factor for $B_s \to D_s^* l\nu$ at zero recoil with non-perturbative current renormalisation. *Phys. Rev. D*, 99(11):114512, 2019. doi: 10.1103/PhysRevD.99.114512.

[56] Roel Aaij et al. Measurement of $|V_{cb}|$ with $B_s^0 \to D_s^{(*)-}\mu^+\nu_\mu$ decays. *Phys. Rev. D*, 101(7):072004, 2020. doi: 10.1103/PhysRevD.101.072004.

[57] Roel Aaij et al. Precise measurement of the f_s/f_d ratio of fragmentation fractions and of B_s^0 decay branching fractions. *Phys. Rev. D*, 104(3):032005, 2021. doi: 10.1103/PhysRevD.104.032005.

[58] Marzia Bordone, Bernat Capdevila, and Paolo Gambino. Three loop calculations and inclusive Vcb. *Phys. Lett. B*, 822:136679, 2021. doi: 10.1016/j.physletb.2021.136679.

[59] Yasmine Sara Amhis et al. Averages of b-hadron, c-hadron, and τ-lepton properties as of 2018. *Eur. Phys. J. C*, 81(3):226, 2021. doi: 10.1140/epjc/s10052-020-8156-7.

[60] P. A. Zyla et al. Review of Particle Physics. *PTEP*, 2020(8):083C01, 2020. doi: 10.1093/ptep/ptaa104.

[61] Swagato Banerjee et al. Averages of b-hadron, c-hadron, and τ-lepton properties as of 2023. 11 2024.

[62] Roel Aaij et al. Branching Fraction Measurements of the Rare $B_s^0 \to \phi\mu^+\mu^-$ and $B_s^0 \to f_2'(1525)\mu^+\mu^-$- Decays. *Phys. Rev. Lett.*, 127(15):151801, 2021. doi: 10.1103/PhysRevLett.127.151801.

[63] Alexander Lenz. Lifetimes and heavy quark expansion. *Int. J. Mod. Phys. A*, 30(10):1543005, 2015. doi: 10.1142/S0217751X15430058.

[64] Bjorn O. Lange, Matthias Neubert, and Gil Paz. Theory of charmless inclusive B decays and the extraction of V(ub). *Phys. Rev. D*, 72:073006, 2005. doi: 10.1103/PhysRevD.72.073006.

[65] Johannes Albrecht, Florian Bernlochner, Alexander Lenz, and Aleksey Rusov. Lifetimes of b-hadrons and mixing of neutral B-mesons: theoretical and experimental status. *Eur. Phys. J. ST*, 233(2):359–390, 2024. doi: 10.1140/epjs/s11734-024-01124-3.

[66] Mikhail A. Shifman and M. B. Voloshin. Hierarchy of Lifetimes of Charmed and Beautiful Hadrons. *Sov. Phys. JETP*, 64:698, 1986.

[67] P. Colangelo and F. De Fazio. Role of four quark operators in the inclusive Lambda(b) decays. *Phys. Lett. B*, 387:371–378, 1996. doi: 10.1016/0370-2693(96)01049-0.

[68] Massimo Di Pierro, Christopher T Sachrajda, and Christopher Michael. An Exploratory lattice study of spectator effects in inclusive decays of the Λ_b baryon. *Phys. Lett. B*, 468:143, 1999. doi: 10.1016/S0370-2693(99)01166-1. [Erratum: Phys.Lett.B 525, 360–360 (2002)].

[69] Chao-Shang Huang, Chun Liu, and Shi-Lin Zhu. Reanalysis of the four-quark operators relevant to Lambda(b) lifetime from QCD sum rule. *Phys. Rev. D*, 61:054004, 2000. doi: 10.1103/PhysRevD.61.054004.

[70] B. Guberina, B. Melic, and H. Stefancic. Enhancement of preasymptotic effects in inclusive beauty decays. *Phys. Lett. B*, 469:253–258, 1999. doi: 10.1016/S0370-2693(99)01198-3.

[71] B. Guberina, B. Melic, and H. Stefancic. Preasymptotic effects in beauty decays. In *3rd International Conference on B Physics and CP Violation (BCONF99)*, pages 156–159, 12 1999. doi: 10.1142/9789812791870_0024.

[72] E. Franco, V. Lubicz, F. Mescia, and C. Tarantino. Lifetime ratios of beauty hadrons at the next-to-leading order in QCD. *Nucl. Phys. B*, 633:212–236, 2002. doi: 10.1016/S0550-3213(02)00262-6.

[73] Fabrizio Gabbiani, Andrei I. Onishchenko, and Alexey A. Petrov. Spectator effects and lifetimes of heavy hadrons. *Phys. Rev. D*, 70:094031, 2004. doi: 10.1103/PhysRevD.70.094031.

[74] Cecilia Tarantino. B^- hadron lifetimes, width differences and semileptonic CP-asymmetries. In *4th International Workshop on the CKM Unitarity Triangle (CKM 2006)*, 2 2007.

[75] Hai-Yang Cheng. Phenomenological Study of Heavy Hadron Lifetimes. *JHEP*, 11:014, 2018. doi: 10.1007/JHEP11(2018)014.

[76] James Gratrex, Alexander Lenz, Blaženka Melić, Ivan Nišandžić, Maria Laura Piscopo, and Aleksey V. Rusov. Quark-hadron duality at work: lifetimes of bottom baryons. *JHEP*, 04:034, 2023. doi: 10.1007/JHEP04(2023)034.

[77] Massimo Di Pierro and Christopher T. Sachrajda. A Lattice study of spectator effects in inclusive decays of B mesons. *Nucl. Phys. B*, 534:373–391, 1998. doi: 10.1016/S0550-3213(98)00580-X.

[78] M. Neubert and Christopher T. Sachrajda. Spectator effects in inclusive decays of beauty hadrons. *Nucl. Phys. B*, 483:339–370, 1997. doi: 10.1016/S0550-3213(96)00559-7.

[79] A. Abulencia et al. Measurement of the Λ_b^0 Lifetime in $\Lambda_b^0 \to J/\psi\Lambda^0$ in $p\bar{p}$ Collisions at $\sqrt{s} = 1.96$-TeV. *Phys. Rev. Lett.*, 98:122001, 2007. doi: 10.1103/PhysRevLett.98.122001.

[80] Dmitri Denisov and Jacobo Konigsberg. The tevatron legacy: a luminosity story. *CERN Courier*, 2016.

[81] S. Das Gupta, A. Z. Mekjian, and M. B. Tsang. Liquid-gas phase transition in nuclear multifragmentation. *Avd. Nucl. Phys.*, 26:89–166, 2001.

[82] J. B. Kogut and D. K. Sinclair. Applying Complex Langevin Simulations to Lattice QCD at Finite Density. *Phys. Rev. D*, 100(5):054512, 2019. doi: 10.1103/PhysRevD.100.054512.

[83] Mark G. Alford, Krishna Rajagopal, and Frank Wilczek. QCD at finite baryon density: Nucleon droplets and color superconductivity. *Phys. Lett. B*, 422:247–256, 1998. doi: 10.1016/S0370-2693(98)00051-3.

[84] Mark G. Alford, Andreas Schmitt, Krishna Rajagopal, and Thomas Schäfer. Color superconductivity in dense quark matter. *Rev. Mod. Phys.*, 80:1455–1515, 2008. doi: 10.1103/RevModPhys.80.1455.

[85] Y. Aoki, G. Endrodi, Z. Fodor, S. D. Katz, and K. K. Szabo. The Order of the quantum chromodynamics transition predicted by the standard model of particle physics. *Nature*, 443:675–678, 2006. doi: 10.1038/nature05120.

[86] Tanmoy Bhattacharya et al. QCD Phase Transition with Chiral Quarks and Physical Quark Masses. *Phys. Rev. Lett.*, 113(8):082001, 2014. doi: 10.1103/PhysRevLett.113.082001.

[87] T. Matsui and H. Satz. J/ψ Suppression by Quark-Gluon Plasma Formation. *Phys. Lett. B*, 178:416–422, 1986. doi: 10.1016/0370-2693(86)91404-8.

[88] Shreyasi Acharya et al. Υ production and nuclear modification at forward rapidity in Pb–Pb collisions at sNN=5.02TeV. *Phys. Lett. B*, 822:136579, 2021. doi: 10.1016/j.physletb.2021.136579.

[89] Georges Aad et al. Production of Υ(nS) mesons in Pb+Pb and pp collisions at 5.02 TeV. *Phys. Rev. C*, 107(5): 054912, 2023. doi: 10.1103/PhysRevC.107.054912.

[90] Albert M Sirunyan et al. Measurement of nuclear modification factors of Υ(1S), Υ(2S), and Υ(3S) mesons in PbPb collisions at $\sqrt{s_{\mathrm{NN}}}$ = 5.02 TeV. *Phys. Lett. B*, 790:270–293, 2019. doi: 10.1016/j.physletb.2019.01.006.

[91] Armen Tumasyan et al. Observation of the $\Upsilon(3S)$ Meson and Suppression of Υ States in Pb-Pb Collisions at sNN=5.02 TeV. *Phys. Rev. Lett.*, 133(2):022302, 2024. doi: 10.1103/PhysRevLett.133.022302.

[92] Alexei Bazavov, Daniel Hoying, Rasmus N. Larsen, Swagato Mukherjee, Peter Petreczky, Alexander Rothkopf, and Johannes Heinrich Weber. Unscreened forces in the quark-gluon plasma? *Phys. Rev. D*, 109(7):074504, 2024. doi: 10.1103/PhysRevD.109.074504.

CHAPTER 2

REGULARISATION AND RENORMALISATION OF QUANTUM FIELD THEORIES

Some content in this section adapted with permission from the following references:

Joshua Lin, William Detmold, and Stefan Meinel. Position-space renormalization schemes for four-quark opera- tors in HQET. JHEP, 07:188, 2024. doi: 10.1007/JHEP07(2024)188.

Joshua Lin. Dirac Traces and the Tutte Polynomial. JHEP, 10 2024. doi: 10.1007/JHEP05(2025)235.

Contents

Our modern understanding of particle physics is formulated within a framework known as Quantum Field Theory (QFT). There a number of difficult questions that arise in practical QFT calculations: for instance how to formalise the path integral, and how to make sense out of the ultraviolet (UV) and infrared (IR) divergences that naively appear. ‘Regularisation’ amounts to a controlled deformation of a QFT of interest such that all divergences are made finite. Different regulators come with their own benefits and disadvantages, but each offers a unique *understanding* of QFTs - and along the way allow us to perform useful phenomenological calculations.

The dimensional regulator is an example of a regulator where the dimensions of spacetime are formally analytically continued to an arbitrary complex number d. Divergences can be analysed as d approaches the spacetime dimension of interest (in the physical world, this is $d = 4$), and systematically subtracted in a process known as 'renormalisation'. The dimensional regulator is convenient for computing perturbative weak-coupling calculations, which for QCD are most accurate and systematically controllable for high energy processes where the typical energies in the process are much larger than Λ_{QCD}. In Sec. 2.1.1, a review is given of UV divergences and how they are made finite by dimensional regularisation. Performing high order perturbative calculations in dimensional regularisation is made difficult by the complicated structure of the relevant loop integrals, however many tools have been developed to deal with this difficulty. The necessary techniques to compute dimensionally-regulated HQET diagrams are covered in Sec. 2.1.2.

Though it has been used to great success and is a mainstay of modern perturbative calculations, it is perplexing that Dimensional Regularisation is actually consistent at all. Naively the idea of analytically continuing the integer-valued *dimension* of a theory is a strange thing to do - and it is fairly shocking that divergences as you approach an integer number of dimensions can be systematically cancelled. One particular source of confusion that arises in theories including fermions is the need to dimensionally regulate Dirac matrices, which a-priori are a strictly 4-dimensional construction. This procedure leads to mixing with operators which vanish as the regulator is removed, known as 'Evanescent Operators'. In Sec. 2.1.4, an introduction to evanescent operators is given, and we discuss how to deal with them when matching between $\overline{\text{MS}}$ and schemes designed for Lattice-QCD. One might also wonder whether or not there is a more intuitive understanding of 'what is actually happening to the Dirac matrices' as they are analytically continued - which until recently has just been a formal prescription. In Ref. [1] I proved that dimensionally-regulated Dirac traces have a graph-theoretic interpretation as a Tutte polynomial evaluation, and this newly found connection is summarised in Sec. 2.1.5 (with formal mathematical details of the proof left to Appendix A).

Though Dimensional Regularisation is the simplest regulator for performing perturbative calculations, there is no known way of extending it to be nonperturbative. There is also the practical problem of computing any but the first few orders of perturbation theory in dimensional regularisation, as there is a combinatorial exponential explosion of number of diagrams needed to compute as well as an increasing complexity in evaluating multiloop diagrams.[1] Instead, nonperturbative calculations of QCD properties can be carried out in Lattice-QCD. The lattice regulator used in this approach is a regulator of QFTs where spacetime is discretised onto a (usually hypercubic) lattice with finitely many vertices. This regulator falls into a class of 'hard-cutoff' regulators that remove high-momenta modes from the theory (another prototypical example being Wilson's hard-edge cut-off regulator). One benefit of utilising a lattice cutoff for gauge theories is that it is possible to construct manifestly gauge-invariant actions and operators by using the correct degrees of freedom. A brief introduction to the aspects of Lattice-QCD needed for the calculations performed in later sections is given in Sec. 2.2. An interesting consequence of discretising the leading order HQET action is that the static-quark self-energy divergence which manifests as a pole at $d = 3$ in dimensional regularisation, becomes physically important and leads to divergences and signal-to-noise problems in the continuum limit, as discussed in Sec. 2.2.5. Finally, for various physical processes, it is also important to consider Wilson lines which are *not* exactly parallel to one of the four spacetime axes. These applications and their associated divergences are discussed in Sec. 2.2.6.

2.1 Dimensional Regularisation

2.1.1 Taming UV divergences with dimensional regularisation

The divergences of a perturbative QFT calculation are split into two classes, the Infrared (IR) divergences associated with low-momenta modes and massless particles, and the Ultraviolet (UV) divergences. In any physically measurable observable, the IR divergences should cancel when all perturbative diagrams are summed - though this cancellation is often complicated and subtle. For this thesis IR divergences will not play a signficant role - and instead we focus on UV divergences, which are treated by renormalisation. When utilising bare perturbation theory, UV divergences appear generically for nearly all operators[2] in QCD and HQET. As an example, consider a four-quark operator in HQET of the form $(\overline{Q}\Gamma_L q)(q\Gamma_R Q)$, where Γ_L, Γ_R are spin-color matrices. These operators will become important later in the discussion of Spectator Effects in Chapters 3 and 4. For now, all that will be used about the heavy quark field is that its bare propagator takes the form derived in Eq. (1.10), the details of the renormalisation of HQET is covered in more detail in Sec. 2.1.2. For this four-quark operator, there are six different $O(\alpha_S)$ diagrams to compute for it's momentum-space Green's function, shown in Fig. 2.1.

As an example of where UV-divergences can arise when doing bare 4-dimensional perturbation

---

[1] Even if this procedure was possible, there remains the intrinsic issue that the perturbative series is expected to be asymptotic (not convergent) [2]. Attempting to Borel resum this series for a given physical quantity, in general one finds a discrete series of poles - some of which correspond to instanton effects (which approximately enter as a contribution like $e^{-S_I} \sim e^{-\frac{1}{\alpha_S}}$ where S_I is the action of the instanton), and some of which correspond to renormalon effects [3]. Modern research into Resurgence Theory (see Ref. [4] and references contained within) offers a glimpse of a dream that perturbative asymptotic series contain enough information to reconstruct the full nonperturbative effects; however this program has not yet yielded a solution of nonperturbative QCD.

[2] Except those associated to a conserved current.

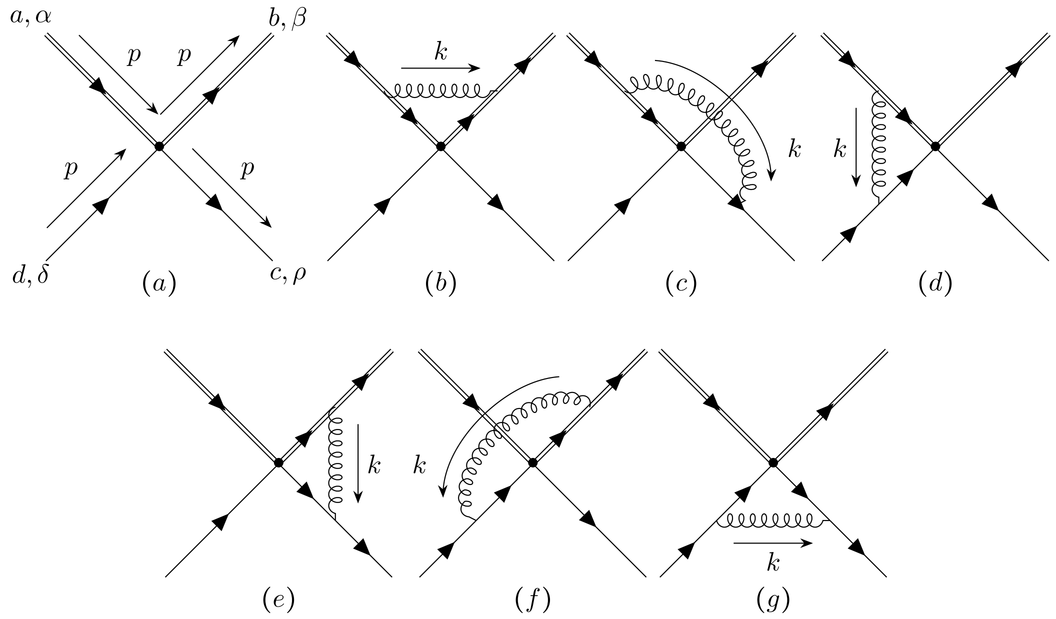

Figure 2.1: Tree level and $O(\alpha_S)$ diagrams needed for renormalising the four-quark operators of interest. Diagrams (b) - (g) are understood to have the same external quark momenta and color-spin indices as shown in the tree-level diagram (a), where latin indices a, b, c, d are color indices and greek indices $\alpha, \beta, \rho, \delta$ are spin indices. Double-lines represent static heavy quark propagators.

theory, consider diagram (g):

$$\begin{aligned} i\mathcal{M}^{abcd}_{\alpha\beta\gamma\delta} = \int \frac{\mathrm{d}^4k}{(2\pi)^4}\frac{-i}{k^2+i\epsilon} & \left(\frac{1+\slashed{v}}{2}\Gamma_L\frac{i}{(\slashed{p}-\slashed{k})+i\epsilon}(ig\gamma^\mu T^A)\right)^{bd}_{\beta\delta} \\ & \left((ig\gamma^\mu T^A)\frac{i}{(\slashed{p}-\slashed{k})+i\epsilon}\Gamma_R\frac{1+\slashed{v}}{2}\right)^{ca}_{\gamma\alpha} \\ = -ig^2\int \frac{\mathrm{d}^4k}{(2\pi)^4}\frac{k^\mu k^\nu}{k^6} & \left(\frac{1+\slashed{v}}{2}\Gamma_L\gamma^\mu\gamma^\rho T^A\right)^{bd}_{\beta\delta}\left(T^A\gamma^\rho\gamma^\nu\Gamma_R\frac{1+\slashed{v}}{2}\right)^{ca}_{\gamma\alpha} + O\left(\frac{p^2}{k^2}\right) \end{aligned} \tag{2.1}$$

To simplify the expression and isolate only the UV-structure, the integral has been expanded in $\frac{p^2}{k^2}$ as it is being investigated in the limit that $k \to \infty$. Once all the spin-colour structure has been removed, this simplified integral has the form:

$$\int \frac{\mathrm{d}^4k}{(2\pi)^4}\frac{k^\mu k^\nu}{k^6} = \frac{g^{\mu\nu}}{4}\int \frac{\mathrm{d}^4k}{(2\pi)^4}\frac{1}{k^4} = \frac{g^{\mu\nu}}{4}\frac{\frac{4}{3}\pi}{(2\pi)^4}\lim_{\Lambda_{\mathrm{IR}}\to 0, \Lambda_{\mathrm{UV}}\to\infty}\int_{\Lambda_{IR}}^{\Lambda_{\mathrm{UV}}}\mathrm{d}k\ \frac{1}{k} \tag{2.2}$$

which *logarithmically* diverges as the UV-cutoff $\Lambda_{\mathrm{UV}} \to \infty$. Note that one of the tricks used in deriving Eq. (2.2) is that with no external scales available in the integral, the only available tensors for the integral to be proportional to is the metric tensor $g_{\mu\nu}$. Also, note that the momentum scale p in Fig. 2.1 regulates the infrared divergence as $\Lambda_{\text{IR}} \to 0$ (in other words, p plays the role of the infrared cutoff Λ_{IR} for these Greens-function calculations). As such, the IR divergences have been left out, and there is a remnant UV-divergence from the diagram. Even though this analysis was only performed on one of the diagrams appearing in Fig. 2.1, after summing over all the diagrams there is a residual UV-divergence.

One particular regulator for these divergences is the dimensional regulator, which analytically continues the dimension of spacetime from $d = 4$ to an arbitrary complex parameter d. Heuristically, logarithmic divergences will show up as simple poles at $d = 4$, and power divergences (which make an appearance later in this chapter) will appear as poles at integer values of $d < 4$. To formalise the procedure of dimensional regularisation, first we will discuss the dimensional regularization of scalar functions, $\int \frac{\mathrm{d}^d k}{(2\pi)^d} f(k)$. The function $f(k)$ may also depend on some external (fixed) momenta $p_1, \cdots, p_n$, some of which may live in $d = 4$, some of which may be other loop momenta that live in a continuous-valued dimension. A common prescription is that all d-dimensional momenta such as k lives in the infinite dimensional vector space, where the first 4 dimensions are the same subspace as the external momenta. Then, a parallel subspace (denoted $k_{\|}$) that is spanned by the p_i (of dimension d_0) and a perpendicular complement (denoted $k_\perp$) can be defined. The dimensionally regulated integral is defined by [5]:

$$\begin{aligned} \int \mathrm{d}^d k f(k) &:= \int_{-\infty}^{\infty} \mathrm{d}^{d_0} k_{\|} \int_{-\infty}^{\infty} \mathrm{d}^{d-d_0} k_\perp \; f(k_{\|}, k_\perp) \\ &= \int_{-\infty}^{\infty} \mathrm{d}^{d_0} k_{\|} \int_0^{\infty} \mathrm{d}k_\perp \frac{2\pi^{(d-d_0)/2}}{\Gamma\left(\frac{d-d_0}{2}\right)} k_\perp^{d-d_0-1} f(k_{\|}, k_\perp). \end{aligned} \tag{2.3}$$

If this integral is defined for some finite d, then it is defined for all d by analytic continuation in d (meromorphic continuations are unique). If the integral happens to not be defined for any d due to the presence of both IR and UV divergences, the function can be split up and analysed separately, which will be shown in the examples section. An important relation that can be used to simplify integrals is integration by parts, which asserts that $\int \mathrm{d}^d k \partial f(k)/\partial k = 0$. To extract recurrence relations, one can apply the operator $\partial_k \cdot p$ to integrals, where p can be an external momenta, but may also be k itself.

When dimensionally regulating, it is important to note that the whole theory has been analytically continued to be d-dimensional. For example the QCD action is modified to:

$$S = \int d^d x \left(-\frac{1}{4} F_{\mu\nu} F^{\mu\nu} + \overline{\psi}(i(\partial_\mu + i\mu^{\frac{4-d}{2}} g A_\mu)\gamma^\mu - m)\psi \right) \tag{2.4}$$

where a mass-dimension 1 parameter μ has been introduced to absorb the dimensions of g, which is traditionally kept dimensionless. The field dimensions of the various parameters are modified to be:

$$[\partial_\mu] = 1, \quad [A_\mu] = \frac{d-2}{2}, \quad [\psi] = \frac{d-1}{2}, \quad [g] = 1. \tag{2.5}$$

Thus, the bare momentum integral Eq. (2.2) becomes:

$$g^2 \int \frac{\mathrm{d}^4 k}{(2\pi)^4} \frac{1}{k^4} \mapsto \mu^{4-d} g^2 \int \frac{\mathrm{d}^d k}{(2\pi)^d} \frac{1}{k^4} \tag{2.6}$$

In formal dimensional regularisation, this integral is zero. The reason is that it is scale-less (involves no external scales) - by dimensional analysis Eq. (2.2) must scale as $\mu^{4-d}\Lambda^{d-4}$ for some mass scale Λ, however there are no such scale available. So for $d \neq 4$ the integral is zero, and by analytic continuation must also be zero at $d = 4$.

However, recall that the integrand actually contains overlapping IR and UV divergences, where the IR divergences are regulated by external momenta. To focus just on the UV divergences, the integral can be split up as follows:

$$\begin{aligned} i \int \frac{\mathrm{d}^d k}{(2\pi)^d} \frac{1}{k^4} &= i \int \frac{\mathrm{d}^d k_E}{(2\pi)^d} \frac{\theta(k^2 < \Lambda_{\mathrm{IR}}^2)}{k^4} + i \int \frac{\mathrm{d}^d k_E}{(2\pi)^d} \frac{\theta(k^2 > \Lambda_{\mathrm{UV}}^2)}{k^4} + \text{finite} \\ &= \frac{i}{8\pi^2 \epsilon} \left(\Lambda_{\mathrm{UV}}^{d-4} - \Lambda_{\mathrm{IR}}^{d-4}\right) \left(\frac{2^\epsilon \pi^{\epsilon/2}}{\Gamma\left(2 - \frac{\epsilon}{2}\right)} \right) + \text{finite} =_{(\mathrm{UV})} \frac{i}{8\pi^2 \epsilon_{\mathrm{UV}}} + \frac{i}{16\pi^2} \left(\ln \left(\frac{4\pi e^{-\gamma_E}}{\Lambda_{\mathrm{UV}}^2} \right) \right) + \text{finite} \end{aligned} \tag{2.7}$$

where $d = 4 - \epsilon$[3], and in the final equality only the piece that diverges due to UV-divergences has been written explicitly (ϵ_{UV} has been decorated with a subscript to emphasize this point). Thus correlation functions of bare operators in QFTs will have divergences which can be regulated by dimensional regularisation, and will manifest as poles in powers of $\frac{1}{\epsilon_{\mathrm{UV}}}$.

2.1.2 Static Heavy Quarks

For hadrons containing a heavy quark Q ($Q = c, b$), the heavy quark mass is much larger than the scale of QCD-dynamics $m_Q \gg \Lambda_{\mathrm{QCD}}$. In the rest frame of the heavy hadron the heavy quark is approximately at rest, and interactions with the light degrees of freedom induces changes in momentum of the order of Λ_{QCD}. In the infinite mass limit, the heavy quark becomes a nonrelativistic object and the complications of systems such as heavy-light mesons such as the B-meson are due to the light degrees of freedom, dubbed 'brown muck' by Nathan Isgur [6]. To demonstrate that the leading order position-space propagator of HQET is static in space, a d-dimensional Fourier transform is needed. As a reminder, the momentum space static propagator is given by:

$$\langle Q(0)\overline{Q}(k)\rangle = \frac{i}{v \cdot k + i\epsilon} \left(\frac{1 + \not{v}}{2} \right) \tag{2.8}$$

To leading order, the projector $P_+ = \frac{1+\not{v}}{2}$ projects onto the particle degrees of freedom in the sense that attaching antiparticle-like spinors will give zero when multiplying this projector. To derive the corresponding propagator in position space, the $+i\epsilon$ factor will be important for keeping track of the time-ordering. In the general case where $v = (\sqrt{1 + \vec{v}^2}, \vec{v})$ is timelike and the momentum space propagator is raised to the n-th power, a Fourier transform to position-space can be calculated as:

---

[3] Note that some conventions use $d = 4 - 2\epsilon$ instead.

$$
\begin{aligned}
D_H^{-1}(x;n) := \int \frac{d^dk}{(2\pi)^d}\left(\frac{1}{v\cdot k + i\epsilon}\right)^n e^{-ik\cdot x} &= \int \frac{dk' d^{d-1}k_\perp}{(2\pi)^d}\left(\frac{1}{v_0 k' + i\epsilon}\right)^n e^{-ik't - \vec{k}\cdot\left(t\frac{\vec{v}}{v_0} - \vec{x}\right)} \\
&= \delta^{d-1}\left(\vec{x} - \frac{\vec{v}t}{\sqrt{1+\vec{v}^2}}\right)\int \frac{dk'}{2\pi}\frac{e^{-ik't}}{(v_0 k' + i\epsilon)^n}
\end{aligned}
\tag{2.9}
$$

where the change of variables $k' = k_0 - \frac{\vec{v}\cdot\vec{k}}{\sqrt{1+\vec{v}^2}}$ was performed, which does not give any jacobian factor. Note that if $t < 0$, then the function is suppressed in the upper half plane. The red contour n the figure below can then be closed in the upper-half plane and the resulting integral is zero (no residue).

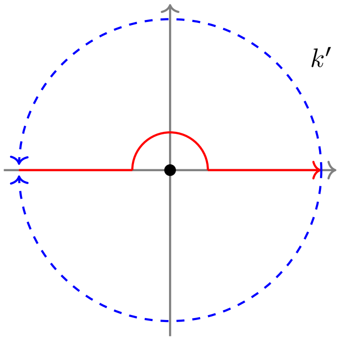

If however $t > 0$ the integrand is suppressed in the lower half plane, and closing the contour in the lower half plane picks up the residue from the pole at $k' = 0$. The integral is thus evaluated as:

$$
D_H^{-1}(x;n) = \delta^{d-1}\left(\vec{x} - \frac{\vec{v}t}{\sqrt{1+\vec{v}^2}}\right)\frac{(-i)^n t^{n-1}}{\Gamma(n) v_0^n}\theta(t > 0)
\tag{2.10}
$$

In the approach above, the $m_Q \to \infty$ limit was taken in momentum space, before Fourier transforming to position-space. Performing the procedure the other way around is not as straightforward - as the position space propagator only converges to the static δ function in a distributional sense. For much of this thesis, $v = (1,0,0,0)$ will be chosen to be purely timelike, in which case the $n = 1$ case recovers the usual position-space heavy-quark propagator:

$$
\langle T\{Q(y)\overline{Q}(x)\}\rangle = -\delta^{d-1}(\vec{x} - \vec{y})\frac{1 + \not{v}}{2}\theta(y^0 > x^0).
\tag{2.11}
$$

For completeness, the analogous Fourier transform for a power of a massive scalar propagator can be calculated as:

$$
D_S^{-1}(x;n) := \int \frac{d^dp}{(2\pi)^d}\frac{e^{ipx}}{(p^2 + i\epsilon)^n} = \frac{i\Gamma(\frac{d}{2} - n)}{e^{i\pi\frac{d}{2}}4^n\pi^{\frac{d}{2}}\Gamma(n)}(x^2 - i\epsilon)^{n-\frac{d}{2}}.
\tag{2.12}
$$

The position-space propagator for a massless fermion can be derived from Eq. (2.12) by differentiating

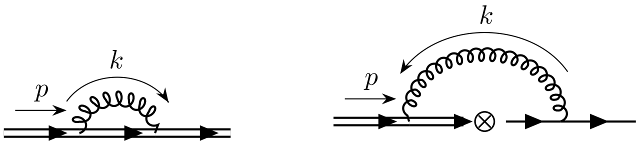

Figure 2.2: The two diagrams needed for $O(\alpha_S)$ renormalisation of the static field renormalisation, and the static-light bilinear operator renormalisation.

against x:

$$\begin{aligned} D_L^{-1}(x) &:= \langle T\{\psi(0)\overline{\psi}(x)\}\rangle = \int \frac{d^dp}{(2\pi)^4}\frac{i(\not{p}+m)}{p^2-m^2+i\epsilon}e^{ipx} = -i\not{\partial}^{(x)}\int\frac{d^dp}{(2\pi)^4}\frac{i}{p^2+i\epsilon}e^{ipx} \\ &= \frac{i\Gamma(\frac{d}{2})}{2e^{i\pi\frac{d}{2}}\pi^{\frac{d}{2}}}\frac{-\not{x}}{(x^2-i\epsilon)^{\frac{d}{2}}} =_{\text{d=4}} \frac{i}{2\pi^2}\left(\frac{-\not{x}}{(x^2-i\epsilon)^2}\right) \end{aligned} \tag{2.13}$$

At $O(\alpha_S)$, divergences start appearing in static HQET due to UV divergences appearing in loop integrals. For example, the interacting heavy-quark propagator has a diagram where it has been dressed by a gluon, as shown on the left of Fig. 2.2. Operators such as $(\overline{Q}\Gamma q)$ where q is a massless quark, and Γ is an arbitrary spin matrix, also have $O(\alpha_S)$ divergences associated with the right diagram of Fig. 2.2. The left diagram has the following expression:

$$\begin{aligned} i\mathcal{M}_Q = \mu^{4-d}&\int\frac{d^dk}{(2\pi)^d}\frac{-i}{k^2+i\epsilon}(igv^\mu T^A)\frac{1+\not{v}}{2}\frac{i}{v\cdot(p-k)+i\epsilon}\frac{1+\not{v}}{2}(igv^\mu T^A)\frac{1+\not{v}}{2} \\ &= -C_Fg^2\mu^{4-d}\int\frac{d^dk}{(2\pi)^d}\frac{1}{(k^2+i\epsilon)(v\cdot(p-k)+i\epsilon)}\frac{1+\not{v}}{2} \end{aligned} \tag{2.14}$$

where C_F is the fundamental casimir (reviewed in Appendix B.0.1). The right diagram has the following expression:

$$\begin{aligned} i\mathcal{M}_{\overline{Q}\Gamma q} &= \mu^{4-d}\int\frac{d^dk}{(2\pi)^d}(ig\gamma_\mu T^A)\frac{i}{\not{k}+\not{p}+i\epsilon}\Gamma^\mu\frac{i}{v\cdot(k+p)+i\epsilon}(igv^\mu T^A)\frac{1+\not{v}}{2}\frac{-i}{k^2+i\epsilon} \\ &= -ig^2\mu^{4-d}C_F\int\frac{d^dk}{(2\pi)^d}\frac{1}{(k^2+i\epsilon)(k+p+i\epsilon)^2}\Gamma^\mu\frac{1+\not{v}}{2} \end{aligned} \tag{2.15}$$

The general strategy used in this thesis to solve these (and more complicated) loop calculations is to use integration-by-parts relations to relate the integral of interest to base cases known as 'master integrals', and solve those by hand. For Eq. (2.14), the master integral is defined as:

$$I_{HL}(n_1,n_2) := (-v\cdot p)^{d-n_1-2n_2}\overline{I}_{HL}(n_1,n_2) = \int\frac{\mathrm{d}^dk}{(2\pi)^d}\frac{1}{(v\cdot(k+p)+i\epsilon)^{n_1}(-k^2-i\epsilon)^{n_2}}, \tag{2.16}$$

where the HL subscript is a rough notation to denote that the integral has a heavy-type propagator and a light-type propagator, and $\overline{I}_{HL}$ has the leading dimensionful parameters removed. These notations follow Ref. [7] closely. This integral can be computed by Fourier transforming the relevant propagators into position-space, and using the formulas already derived:

$$
\begin{aligned}
\overline{I}_{\mathrm{HL}}(n_1,n_2) &= \int \frac{\mathrm{d}^d k}{(2\pi)^d} \frac{1}{(v\cdot(k+p)+i\epsilon)^{n_1}(k^2+i\epsilon)^{n_2}} \\
&= \int \frac{d^d k_1 d^d k_2}{(2\pi)^{2d}} \left(\frac{1}{v\cdot k_1 + i\epsilon}\right)^{n_1} \left(\frac{1}{k_2^2+i\epsilon}\right)^{n_2} \delta^d(k_1-p-k_2) \\
&= \int \frac{d^d k_1 d^d k_2}{(2\pi)^{2d}} \left(\int d^d x_1 e^{-ik_1x_1} \int \frac{d^d \tilde{k}_1}{(2\pi)^d} e^{i\tilde{k}_1 x_1} \left(\frac{1}{v\cdot \tilde{k}_1 + i\epsilon}\right)^{n_1}\right) \times \\
&\quad \left(\int d^d x_2 e^{-ik_2x_2} \int \frac{d^d \tilde{k}_2}{(2\pi)^d} e^{i\tilde{k}_2 x_2} \left(\frac{1}{\tilde{k}_2^2 + i\epsilon}\right)^{n_2}\right) \delta^d(k_1-p-k_2).
\end{aligned}
\tag{2.17}
$$

Using the Fourier transform of powers of the scalar propagator calculated in Eq. (2.12), the outside integral can be performed with respect to k_1, k_2 against the phase and delta functions to see that:

$$
\int \frac{d^d k_1 d^d k_2}{(2\pi)^{2d}} e^{-ik_1x_1} e^{-ik_2x_2} \delta^d(k_1-p-k_2) = e^{-ipx_1}\delta^d(x_1+x_2).
\tag{2.18}
$$

Relabelling $x := x_1$ and integrating out x_2 against the delta function:

$$
\begin{aligned}
&\int d^d x e^{ipx} \left(\frac{(-1)^{n_1} i 2^{-2n_1}\Gamma(\frac{d}{2}-n_1)}{\pi^{\frac{d}{2}}\Gamma(n_1)}(-x^2+i\epsilon)^{n_1-\frac{d}{2}}\right)\left(-\delta^{d-1}(x_\perp)\frac{i^{n_2}(-x_0)^{n_2-1}}{\Gamma(n_2)}\theta(x_0>0)\right) \\
&= (v\cdot p)^{d-2n_1-n_2} \frac{(-1)^{n_1+d} i 2^{d-2n_1}}{(4\pi)^{d/2}} \frac{\Gamma(2n_1+n_2-d)\Gamma(\frac{d}{2}-n_1)}{\Gamma(n_1)\Gamma(n_2)}
\end{aligned}
\tag{2.19}
$$

which gives the result:

$$
\overline{I}_{\mathrm{HL}}(n_1,n_2) = \frac{i 2^{d-2n_2}(-1)^{-n_1-n_2}}{(4\pi)^{d/2}} \frac{\Gamma(2n_2+n_1-d)\Gamma(\frac{d}{2}-n_2)}{\Gamma(n_1)\Gamma(n_2)} (-v\cdot p)^{d-2n_2-n_1}.
\tag{2.20}
$$

For example, for $d = 4-\epsilon$ and small n_1, n_2, the master integral simplifies to the expressions:

$$
\begin{aligned}
I_{\mathrm{HL}}(2,1) &= \int \frac{\mathrm{d}^d k}{(2\pi)^d} \frac{1}{(v\cdot(k+p))^2 k^2} = \frac{-i}{4\pi^2\epsilon} - \frac{i}{8\pi^2}\left(\ln(\pi e^{-\gamma_E}) - 2\ln(-v\cdot p)\right)) \\
I_{\mathrm{HL}}(1,1) &= \int \frac{\mathrm{d}^d k}{(2\pi)^d} \frac{1}{(v\cdot(k+p))k^2} = (-v\cdot p)\cdot\left(\frac{-i}{4\pi^2\epsilon} - \frac{i}{8\pi^2}\left(2+\ln(\pi e^{-\gamma_E}) - 2\ln(-v\cdot p)\right)\right)
\end{aligned}
\tag{2.21}
$$

The light-light master integral calculation can be done similarly:

$$
\begin{aligned}
I_{LL}(n_1,n_2) &= (-p^2)^{\frac{d}{2}-n_1-n_2}\overline{I}_{LL}(n_1,n_2) = \int \frac{\mathrm{d}^d k}{(2\pi)^d} \frac{1}{(k^2+i\epsilon)^{n_1}((k+p)^2+i\epsilon)^{n_2}} \\
\overline{I}_{LL}(n_1,n_2) &= \frac{\Gamma(\frac{d}{2}-n_1)\Gamma(\frac{d}{2}-n_2)\Gamma(-d+2n_1+2n_2)}{2^{2n_1+2n_2}\pi^{\frac{d}{2}}\Gamma(n_1)\Gamma(n_2)}
\end{aligned}
\tag{2.22}
$$

The integrals I_{HL}, I_{LL} are used as base cases for more complicated master integrals calculated in Chapter 3. This result can be now be used to calculate the divergences appearing in the two diagrams appearing in Fig. 2.2:

$$i\mathcal{M}_Q = i(v\cdot p)\left(\frac{-C_F\alpha_S}{\pi\epsilon} - \frac{C_F\alpha_S}{2\pi}\left(2+\ln\left(\frac{\pi e^{-\gamma_E}\mu^2}{(-v\cdot p)^2}\right)\right)\right)\frac{1+\not{v}}{2} \tag{2.23}$$

$$i\mathcal{M}_{\overline{Q}\Gamma q} = \left(\frac{C_F\alpha_S}{2\pi\epsilon} + \frac{C_F\alpha_S}{4\pi}\left(2+\ln\left(\frac{4\pi e^{-\gamma_E}\mu^2}{-p^2}\right)\right)\right)\Gamma^\mu\frac{1+\not{v}}{2} \tag{2.24}$$

The renormalisation procedure is the procedure of adding counterterms to the theory to cancel these divergences, such that all correlation functions of the remaining, renormalised fields are finite. For the heavy quark field renormalisation, define the wavefunction renormalization Z_Q such that $Q^{(0)} = \sqrt{Z_Q}Q^{\mathrm{MS}}$, where the MS (Minimal Subtraction) scheme is constructed such that counterterms cancel only the $\frac{1}{\epsilon^n}$ poles, and the superscript (0) refers to the bare heavy quark field. Then, examining Eq. (2.23) the wavefunction renormalisation is given to $O(\alpha_S)$ as:

$$Z_Q^{\mathrm{MS}} = 1 + \frac{C_F\alpha_S}{\pi\epsilon} + O(\alpha_S^2) \tag{2.25}$$

Many, but not all, one-loop momentum-space integrals come with factor of $\ln\left(4\pi e^{-\gamma_E}\right)$ directly proportional to $\frac{1}{2}$ of the $\frac{1}{\epsilon}$ pole. It is common to use a *modified* Minimal Subtraction scheme known as $\overline{\mathrm{MS}}$ which relabels the μ parameter as:

$$(\mu^2)^{\overline{\mathrm{MS}}} = 4\pi e^{-\gamma_E}\mu^2 \tag{2.26}$$

which has the effect of cancelling these finite logarithmic pieces.

The divergences appearing in the heavy-light operator are *not* just an addition of the divergences from each of the bare fields that make it up, there are *additional* UV divergences when operators are placed on top of each other. To clarify this difference, the notation $\phi_1^R\phi_2^R$ will be used for a product of two fields ϕ_1, ϕ_2 renormalised in some scheme R, whereas the notation $(\phi_1\phi_2)^R$ denotes the composite operator renormalised in the scheme R. For the renormalisation of composite operators, there are various conventions that are used. Unless otherwise specified, the convention used in this thesis ('operator renormalisation') is that $Z^R\mathcal{O}^{(0)} = \mathcal{O}^R$ where R is an arbitrary renormalisation scheme, to be consistent with Ref. [8]. In the literature, it is commonly written the other way around, as $\mathcal{O}^{(0)} = Z^R\mathcal{O}^R$. It is also sometimes written such that the renormalisation constants of the fields have been factored out ('coefficient renormalisation'), so that for the heavy-light operator $\overline{Q}^{(0)}\Gamma q^{(0)} = Z^R_{\overline{Q}\Gamma q}\overline{Q}^R\Gamma q^R$. Using the operator renormalisation convention:

$$O^{\overline{\mathrm{MS}}}_{\overline{Q}\Gamma q} = Z_{\overline{Q}\Gamma q}\overline{Q}^{(0)}\Gamma q^0 = Z_{\overline{Q}\Gamma q}\sqrt{Z_Q Z_2}\,\overline{Q}^{\overline{\mathrm{MS}}}\Gamma^\mu q^{\overline{\mathrm{MS}}} = \left(1+\frac{1}{2}\delta_Q+\frac{1}{2}\delta_2+\delta_{\overline{Q}\Gamma q}+O(\alpha_S^2)\right)\overline{Q}^{\overline{\mathrm{MS}}}\Gamma^\mu q^{\overline{\mathrm{MS}}} \tag{2.27}$$

where Z_X is expanded as $1+\delta_X$ for any X, and where $\delta_2 = -\frac{C_F\alpha_S}{2\pi\epsilon}$ is the wavefunction renormalisation of the massless quark field. Such a decomposition is needed because $i\mathcal{M}_{\overline{Q}\Gamma q}$ was computed with amputated external quark lines, equivalently it was computed with all fields being renormalised. Using this relation, the operator renormalisation can be derived as:

$$Z_{\overline{Q}\Gamma q} = 1 - \frac{3C_F\alpha_S}{4\pi\epsilon} + O(\alpha_S^2). \tag{2.28}$$

2.1.3 Infinite-dimensional representations of the d-dimensional Clifford Algebra

Some text in this subsection reproduced with coauthors' permission from Ref. [8].

Along with specifying a procedure for analytically continuing the momentum integrals to d-dimensions, similar continuations must be chosen for the other objects appearing in typical calculations. In any QFT calculation involving fermions, fermion loops come with associated traces of strings of Dirac matrices which must be consistently treated. There are various different schemes suited to different purposes. The simplest kind of regularisation is to require the γ-matrices to satisfy

$$\{\gamma_\mu, \gamma_\nu\} = 2g_{\mu\nu}, \quad g_{\mu\mu} = d, \quad \mathrm{Tr}_d(\mathbb{1}) = 4 \tag{2.29}$$

The base case $\mathrm{Tr}_d(\mathbb{1}) = 4$ is the conventional choice used in most calculations involving dimensional regularisation, but this condition can be changed, for instance to $\mathrm{Tr}_d(\mathbb{1}) = 2^{\frac{d}{2}}$. This latter choice may seem more natural given that in even spacetime dimensions d, the standard representation of the Clifford Algebra has dimension $2^{\frac{d}{2}}$. However, such modifications to the base case do not affect the renormalisation procedure in any meaningful way, and simply amount to a shift in the renormalisation constants [5].

Note that since all momenta formally live in an infinite-dimensional space due to the dimensional regularisation procedure, finding a representation of the defining equations Eq. (2.29) requires an infinite-dimensional space as well. An explicit construction provided in Ref. [5] for the Minkowski-signature gamma matrices is to make the following inductive definitions: (up to a trivial reordering that enforces $(\gamma^\mu)^T = (-1)^\mu \gamma^\mu$)

1) Define:

$$\gamma^0_{(1)} := \begin{bmatrix} 1 & 0 \\ 0 & -1 \end{bmatrix}, \quad \gamma^1_{(1)} := \begin{bmatrix} 0 & 1 \\ -1 & 0 \end{bmatrix}. \tag{2.30}$$

2) For any positive integer $\omega \in \mathbb{Z}_{\geq 1}$, define:

$$\hat{\gamma}_{(\omega)} := i^{\omega-1} \gamma^0_{(\omega)} \cdots \gamma^{2\omega-1}_{(\omega)}, \tag{2.31}$$

$$\gamma^\mu_{(\omega+1)} := \begin{bmatrix} \gamma^\mu_{(\omega)} & 0 \\ 0 & \gamma^\mu_{(\omega)} \end{bmatrix} \quad \text{for} \quad 0 \leq \mu < 2\omega, \tag{2.32}$$

$$\gamma^{2\omega}_{(\omega+1)} := \begin{bmatrix} 0 & i\hat{\gamma}_{(\omega)} \\ i\hat{\gamma}_{(\omega)} & 0 \end{bmatrix}, \quad \gamma^{2\omega+1}_{(\omega+1)} := \begin{bmatrix} 0 & \hat{\gamma}_\omega \\ -\hat{\gamma}_{(\omega)} & 0 \end{bmatrix}. \tag{2.33}$$

3) The infinite-dimensional γ-matrices are defined by block-diagonal copies of the finite-dimensional construction, so that for $\mu \in \mathbb{Z}_{\geq 0}$, choosing any $\omega \geq \lfloor \frac{\mu}{2} \rfloor + 1$,

$$\gamma^\mu := \begin{bmatrix} \gamma^\mu_{(\omega)} & & \\ & \gamma^\mu_{(\omega)} & \\ & & \ddots \end{bmatrix}. \tag{2.34}$$

The γ matrices defined here satisfy

$$\{\gamma_\mu, \gamma_\nu\} = 2g_{\mu\nu}, \quad \gamma_\mu^\dagger = \gamma_0\gamma_\mu\gamma_0, \tag{2.35}$$

where the metric is written in the mostly-negative convention, $g_{\mu\nu} = \mathrm{diag}(+1, -1, -1, \cdots)$. Note that the γ^5 constructed by the inductive process above does *not* refer to the chiral $\gamma_5^{\mathrm{ch.}}$ (which for this subsection only has a superscript of ch. to distinguish it), and is simply a part of the infinite-dimensional representation of the d-dimensional Clifford algebra. Euclidean γ-matrices are obtained by defining $\gamma_0^{\mathrm{E}} := \gamma_0, \gamma_i^{\mathrm{E}} := -i\gamma_i$ such that $\{\gamma_\mu^E, \gamma_\nu^E\} = 2\delta_{\mu\nu}$.

There are two additional complications to discuss, the appropriate analytic continuation of the charge operator C, and a continuation of the chiral $\gamma_5^{\mathrm{ch.}}$. First we deal with C, as a treatment is needed even for vector-like theories like QCD. Having explicit charge matrices C will be useful later, as charge-conjugation matrices C are used in the construction of the baryonic operators such as $\epsilon^{abc}[q^{aT} C\Gamma q^b]Q^c$ (where Γ is a Dirac matrix). It is natural to assume that the defining relation in 4-dimensions, $C\gamma_\mu C^{-1} = -\gamma_\mu^T$, also holds in dimensional regularization. However, to my knowledge, an explicit charge-conjugation matrix satisfying the defining relations for an explicit basis of infinite-dimensional γ-matrices had not been constructed previously in the literature for dimensional regularization until our work in Ref. [8] (a construction was presented for dimensional reduction in Ref. [9]). The explicit construction presented below demonstrates that enforcing $C\gamma_\mu C^{-1} = -\gamma_\mu^T$ does not lead to inconsistencies in Dirac traces. This is in contrast to naively enforcing the anticommuting relation $\{\gamma_5^{\mathrm{ch.}}, \gamma_\mu\} = 0$, which leads to inconsistencies in certain Dirac traces as shown later in this section.

With the inductive construction defined in Eqs. (2.30) to (2.34), no finite product of γ matrices will satisfy the charge-conjugation matrix condition $C\gamma_\mu C^{-1} = -\gamma_\mu^T$. Modifying the basis of γ-matrices by eliminating $\gamma_4, \gamma_6, \gamma_8 \ldots$ from the basis, such that the new basis $\tilde{\gamma}_\mu$ is given by the relabelling

$$\{\tilde{\gamma}_0, \tilde{\gamma}_1, \tilde{\gamma}_2, \tilde{\gamma}_3, \tilde{\gamma}_4, \tilde{\gamma}_5, \tilde{\gamma}_6, \cdots\}, = \{\gamma_0, \gamma_1, \gamma_2, \gamma_3, \gamma_5, \gamma_7, \gamma_9, \cdots\} \tag{2.36}$$

a charge-conjugation matrix can be defined. These $\tilde{\gamma}$ matrices still satisfy Eq. (2.35), but now we can define $C = i\tilde{\gamma}_0\tilde{\gamma}_2$, which satisfies

$$C\tilde{\gamma}_\mu^T C^{-1} = -\tilde{\gamma}_\mu^T, \quad C^{-1} = C^T = C^\dagger = -C. \tag{2.37}$$

Similarly, one might attempt to naively enforce the 4-dimensional identity $\{\gamma_5^{\mathrm{ch.}}, \gamma_\mu\} = 0$ to create a d-dimensional $\gamma_5^{\mathrm{ch.}}$. This is known as Naive Dimensional Regularisation (NDR), but this famously leads to inconsistencies. To see this, assume that you *could* construct such a $\gamma_5^{\mathrm{ch.}}$, and consider the following set of identities:

$$\mathrm{Tr}_d\left(\gamma_5^{\mathrm{ch.}}\gamma_\alpha\gamma_\beta\gamma_\mu\gamma_\nu\right) = \frac{1}{d}\mathrm{Tr}_d\left(\gamma_5^{\mathrm{ch.}}\gamma_\alpha\gamma_\beta\gamma_\mu\gamma_\nu\gamma_\lambda\gamma_\lambda\right) = \frac{8-d}{d}\mathrm{Tr}_d\left(\gamma_5^{\mathrm{ch.}}\gamma_\alpha\gamma_\beta\gamma_\mu\gamma_\nu\right) \tag{2.38}$$

where importantly, trace-cyclicity has been used. By analytic continuation in d, Eq. (2.38) implies that $\mathrm{Tr}_d\left(\gamma_5^{\mathrm{ch.}}\gamma_\alpha\gamma_\beta\gamma_\mu\gamma_\nu\right) = 0$, but it is known by explicit computation that in 4-dimensions $\mathrm{Tr}_4\left(\gamma_5^{\mathrm{ch.}}\gamma_\alpha\gamma_\beta\gamma_\mu\gamma_\nu\right) = 4i\epsilon_{\alpha\beta\mu\nu}$ where $\epsilon_{\alpha\beta\mu\nu}$ is the Levi-civita tensor, hence there is a contradiction.

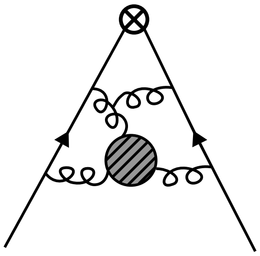

Figure 2.3: Schematic drawing of a correction to a bilinear current $\overline{q}\Gamma q$. Such corrections do not give rise to any evanescent operators, as the Dirac structure associated to radiative corrections can be simplified.

To solve this problem, the 't Hooft-Veltman (HV) scheme [10] proposes to set $\gamma_5^{\text{ch.}} := i\gamma_0\gamma_1\gamma_2\gamma_3$ (in Minkowski signature), which has been shown to be internally consistent (and consistent with the definition of C above, as $C\gamma_5^{\text{ch.}}C^{-1} = \gamma_5^{\text{ch.}}$) This explicitly breaks d-dimensional ($\mathrm{SO}(d-1,1)$) covariance, and causes the first four-dimensions to become 'special'. In practical calculations, using the HV scheme requires all d-dimensional quantities (momenta, γ-matrices, spinors, etc.) to be split into their four-dimensional, and $(d-4)$ dimensional components, which are then treated separately. Aside from NDR and HV, there are many other schemes each with their own benefits and quirks [11] - however this thesis will primarily use the HV scheme for $\gamma_5^{\text{ch.}}$ regularisation.

2.1.4 Evanescent Operators

Depending on the UV-regulator used, additional spurious operators can emerge that mix with physical operators, but vanish as the regulator is removed. These operators are known as evanescent operators, though this name is mainly used to refer to the operators appearing due to the d-dimensional Dirac structure introduced in dimensional regularisation[4]. In vector-like theories such as QCD (where no γ_5 insertions will be considered), there are no bilinear evanescent operators because any diagram contributing to the green's function involving a bilinear current $\overline{\psi}\Gamma\psi$ such as shown in Fig. 2.3 takes the form of $\overline{\psi}\Gamma_1\Gamma\Gamma_2\psi$, where Γ_1, Γ_2 are strings of Dirac matrices with all their indices contracted. Such strings can however be simplified by repeated use of the defining anticommutation relations, implying that bilinear operators are multiplicatively renormalisable.

Evanescent operators generically occur for four-quark operators of the form $(\overline{\psi}\Gamma_L\psi)(\overline{\psi}\Gamma_R\psi)$, due to the breakdown of four-dimensional Fierz identities that would allow one to simplify expressions such as $(\overline{\psi}\gamma_\mu\Gamma_1\psi)(\overline{\psi}\gamma_\mu\Gamma_2\psi)$. An example of particular importance for Chapter 3 are four-quark

---

[4] In some older references, these operators were also known as 'effervescent' operators [12]. In a sense, one can also consider higher-dimensional 'lattice artifacts' appearing in a Symanzik Effective theory[13] to be evanescent operators, though this terminology seems to never be used in the literature.

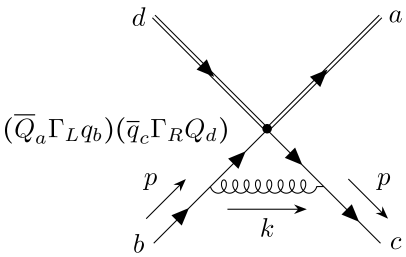

$$\begin{aligned} &= \int \frac{d^dk}{(2\pi)^d}\frac{-i}{k^2+i\epsilon}\left(\frac{1+\not{v}}{2}\Gamma_L\frac{i}{(\not{p}-\not{k})+i\epsilon}(ig\gamma_\mu T^A)\right)_{ab} \\ &\qquad\times\left((ig\gamma_\mu T^A)\frac{i}{(\not{p}-\not{k})+i\epsilon}\Gamma_R\frac{1+\not{v}}{2}\right)_{cd} \\ &= \frac{\alpha_S}{8\pi\epsilon}\left(\frac{1+\not{v}}{2}\Gamma_L\gamma^\mu\gamma^\nu T^A\right)_{ab}\left(T^A\gamma^\nu\gamma^\mu\Gamma_R\frac{1+\not{v}}{2}\right)_{cd}+O(\epsilon^0)\end{aligned}$$

Figure 2.4: The one-loop diagram in Minkowski space for the $\Delta Q = 0$ operators that generates the evanescent structures shown in Eq. (2.40). The indices a, b, c, d are combined Dirac-color indices.

operators appearing in the operator-product-expansion for b-hadron lifetimes:

$$\begin{aligned} O_1^f &:= (\overline{Q}\gamma_\mu P_L q_f)(\overline{q}_f\gamma_\mu P_L Q), & O_2^f &:= (\overline{Q}P_L q_f)(\overline{q}_f P_R Q), \\ O_3^f &:= (\overline{Q}\gamma_\mu P_L T^A q_f)(\overline{q}_f\gamma_\mu P_L T^A Q), & O_4^f &:= (\overline{Q}P_L T^A q_f)(\overline{q}_f P_R T^A Q), \end{aligned} \tag{2.39}$$

where $\{P_L, P_R\} = \{\frac{1-\gamma_5}{2}, \frac{1+\gamma_5}{2}\}$ are left/right handed projectors, T^A are colour matrices as reviewed in Appendix B.0.1, and the adjoint A index is summed over. By one-loop diagrams such as shown in Fig. 2.4, evanescent operators are generated with the structures:

$$\begin{aligned} E_1 &:= (\overline{Q}\gamma_\mu P_L\gamma_\alpha\gamma_\beta q)(\overline{q}\gamma_\beta\gamma_\alpha\gamma_\mu P_L Q) - 4O_1, \\ E_2 &:= (\overline{Q}P_L\gamma_\alpha\gamma_\beta q)(\overline{q}\gamma_\beta\gamma_\alpha P_R Q) - 4O_2, \\ E_3 &:= (\overline{Q}\gamma_\mu P_L\gamma_\alpha\gamma_\beta T^A q)(\overline{q}\gamma_\beta\gamma_\alpha\gamma_\mu P_L T^A Q) - 4O_3, \\ E_4 &:= (\overline{Q}P_L\gamma_\alpha\gamma_\beta T^A q)(\overline{q}\gamma_\beta\gamma_\alpha P_R T^A Q) - 4O_4. \end{aligned} \tag{2.40}$$

Note that these operators are chosen such that in the naive $d \to 4$ limit, each of the E_i vanishes due to four-dimensional Fierz identities. Even though evanescent operators naively vanish in $d = 4$, they have consequences for practical calculations. For example, different choices of bases for evanescent operators give rise to finite shifts in renormalised $\overline{\text{MS}}$ matrix elements, and give rise to different anomalous dimensions (at two-loop order) [14].

To see this in action, consider the infinite-dimensional vector space V given by all four-quark operators of the form $(\overline{\psi}_{f_1}\Gamma_L\psi_{f_2})(\overline{\psi}_{f_3}\Gamma_R\psi_{f_4})$ for fixed but not necessarily distinct flavours f_1, f_2, f_3, f_4 and arbitrary spin-colour matrix Γ_L, Γ_R. It is assumed that all operators in V have the same quantum numbers, hence mix under renormalization. This space has a natural decomposition $V = V_0 \oplus V_1 \oplus V_2 \ldots$ where V_0 are physical operators, and evanescent operators in V_n first appear at n-loop order.Computing the renormalization of these operators requires calculating the bare (unamputated) Green's functions with some fixed external kinematics (represnted by $\langle\cdot\rangle$):

$$\langle V_m\rangle^{(0)} = \sum_{m,i\in\mathbb{Z}_{\geq 0}}\sum_{j\in\mathbb{Z}} b_{m,n,i,j}\frac{(\alpha_S^{\overline{\text{MS}}})^i}{\epsilon^j}\langle V_n\rangle^{(\text{Tree})} \tag{2.41}$$

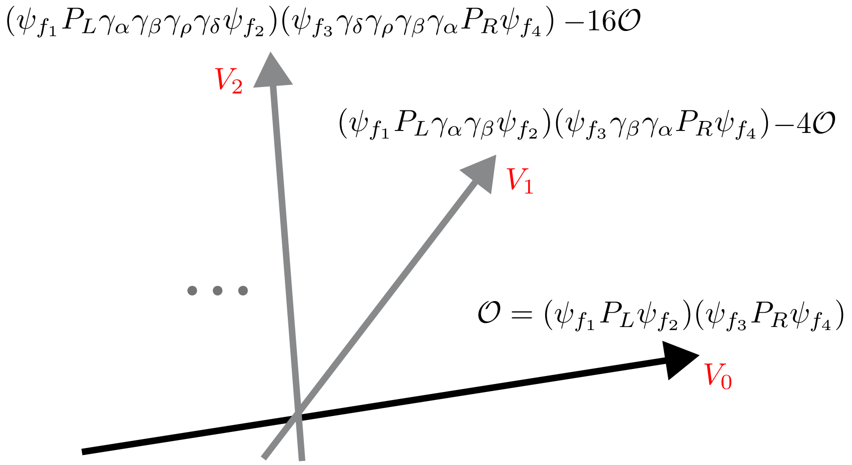

Figure 2.5: Example of operators that appear in decomposition of the total space $(V_0 \oplus V_1 \oplus V_2 \dots)$ of four-quark operators.

[5]where (0) refers to the bare Green's function, (Tree) refers to the tree-level evaluation, and $b_{m,n,i,j}$ are coefficients. For the above formula and what follows in this section, we will consider a simple situation where $\dim(V_n) = 1$ for all n, so that the operators are multiplicatively renormalizable up to mixing with evanescent operators. In this case, $b_{m,n,i,j}$ are fixed real numbers, if operator mixing is allowed then these coefficients are promoted to matrices. $\overline{\text{MS}}$ renormalization usually simply dictates that the $\frac{1}{\epsilon^n}$ poles are removed by the renormalization constants, such that at $O(\alpha_S)$ the renormalization condition is given by:

$$\begin{pmatrix} V_0^{(0)} \\ V_1^{(0)} \end{pmatrix} = \left[\mathbb{1} + \frac{\alpha_S}{\epsilon} \begin{pmatrix} b_{0,0,1,-1} & b_{0,1,1,-1} \\ 0 & b_{1,1,1,-1} \end{pmatrix} \right] \begin{pmatrix} V_0^{(\overline{\text{MS}})} \\ V_1^{(\overline{\text{MS}})} \end{pmatrix} \tag{2.42}$$

where only the mixing between V_0 and V_1 has been shown. However, this renormalization condition is slightly undesirable because the $\overline{\text{MS}}$-renormalized evanescent operator can have a finite residual matrix element in the limit that $d \to 4$:

$$\langle V_1^{(\overline{\text{MS}})} \rangle = \alpha_S b_{1,0,1,0} \langle V_0 \rangle^{\text{Tree}} \tag{2.43}$$

The origin of this $b_{1,0,1,0}$ term comes from an $\frac{\alpha_S}{\epsilon}$ loop integral contribution *cancelling* the $O(\epsilon)$ nature of the Dirac structure of V_1. When mixing with evanescent operators, the $\overline{\text{MS}}$ scheme is extended to require that the renormalized evanescent operators satisfy $\langle V_n^{(\overline{\text{MS}})} \rangle = 0$ as $d \to 4$. This has multiple effects:

---

[5] Note that the perturbative expansion parameter is usually written as $\frac{\alpha_S}{4\pi}$; here it is shortened to α_S simply because the numerical factors do not matter.

- Enforcing that renormalized evanescent operators at a scale μ are zero enforces that they are zero at all scales.
- Regularization-independent renormalization schemes such as RI-MOM schemes or X-space schemes used to connect continuum operators with those used in lattice-regularisations require setting renormalized evanescent contributions to zero, as they only contribute on the continuum side of the matching and have no corresponding operator in the lattice regulator.

The renormalization matrix is thus modified as:

$$\begin{pmatrix} V_0^{(0)} \\ V_1^{(0)} \end{pmatrix} = \left[\mathbb{1} + \frac{\alpha_S}{\epsilon} \begin{pmatrix} b_{0,0,1,-1} & b_{0,1,1,-1} \\ \epsilon b_{1,0,1,0} & b_{1,1,1,-1} \end{pmatrix} \right] \begin{pmatrix} V_0^{(\overline{\text{MS}})} \\ V_1^{(\overline{\text{MS}})} \end{pmatrix} \tag{2.44}$$

Notice however that there is a freedom to redefine what the bare evanescent operators are, given by a redefinition:

$$V_1^{(0)\prime} = V_1^{(0)} + a\epsilon V_0^{(0)} \tag{2.45}$$

for an arbitrary real constant a. The new V_1' operator still naively vanishes as $d \to 4$, and is still generated at one-loop order. However, introducing this shift introduces a shift of the renormalization matrix:

$$\begin{pmatrix} V_0^{(0)} \\ V_1^{(0)\prime} \end{pmatrix} = \left[\mathbb{1} + \frac{\alpha_S}{\epsilon} \begin{pmatrix} b_{0,0,1,-1} & b_{0,1,1,-1} \\ \epsilon(a + b_{1,0,1,0}) & b_{1,1,1,-1} \end{pmatrix} \right] \begin{pmatrix} V_0^{(\overline{\text{MS}})\prime} \\ V_1^{(\overline{\text{MS}})\prime} \end{pmatrix} \tag{2.46}$$

which crucially introduces a shift of the *renormalized* physical operators:

$$\langle V_0^{(\overline{\text{MS}})\prime} \rangle = \langle V_0^{(\overline{\text{MS}})} \rangle - \alpha_S b_{0,1,1,-1} a \langle V_0 \rangle^{\text{Tree}} \tag{2.47}$$

Thus, the choice of evanescent operators influences the physical matrix elements. In the following sections involving four-quark operators mixing with evanescent operators, an explicit basis will always be chosen so as to resolve this ambiguity.

2.1.5 DIRAC TRACES AND THE TUTTE POLYNOMIAL

Some text in this subsection reproduced from my work Ref. [1].

The fact that the 't Hooft-Veltman prescription of dimensional regularisation gives a self-consistent regulator which can be proven to renormalize the standard model to all orders is truly miraculous. One small part of the mystery is the regularisation of Dirac Traces - the explicit construction presented in Sec. 2.1.3 provides a formalisation of the system, and yet does not provide much intuition of 'what is actually happening'. One might wonder if there is a different, more geometric explanation for what the dimensional regulator actually does to Dirac Traces. The main observation made in Ref. [1] is that the defining relations for gamma matrices in d-dimensions given in Eq. (2.29) can be formulated as a 'deletion-contraction relation' on an appropriately constructed graph, relating the value of Tr_d on one graph to its value on a graph where an edge has been deleted, and a graph where the same edge has been contracted. Such a recurrence relation is very common among polynomial graph invariants, and was initially observed for the chromatic polynomial [15] and number of spanning trees [16]. This was later generalised to a two-variable polynomial known as the Tutte polynomial [17], which contains many other graph invariants which satisfy deletion-contraction relations as special cases (as shown in Fig. 2.6) such as the reliability polynomial [18], Jones polynomial of alternating knots represented as graphs [19], and the partition function of the q-state Potts models [20] ($q = 2, 3$ shown on Fig. 2.6).

All the formal statements of the theorems and their proofs are relegated to Appendix A, this subsection contains only a review of the main results. The main theorem I derived in Ref [1] relates the d-dimensional trace of a string of Dirac matrices contracted in an arbitrary way to an evaluation of the Tutte polynomial of a corresponding graph along the line $y = -1$, as depicted in Fig. 2.6.

Theorem A.1.0.8 (reworded)**.** *Suppose the $2n$-ple $x = (x_1, x_2, \dots, x_{2n})$ contains the integers $1, \dots, n$ each repeated twice in some order. Then*

$$\mathrm{Tr}_d(\gamma_{\mu_{x_1}} \cdots \gamma_{\mu_{x_{2n}}}) = 4(-1)^{|E|}(-2)^{n-c(\mathrm{Gr}(x))}\ d^{\,c(\mathrm{Gr}(x))}\ T\left(\mathrm{Gr}(x); 1-\tfrac{d}{2}, -1\right) \tag{2.48}$$

where if $x_1, \dots, x_{2n}$ are placed in order around the circumference of a circle, with straight chords connecting the repeated integers, then $\mathrm{Gr}(x)$ is the graph with a vertex for each chord and an edge connecting pairs of chords that intersect, $c(\mathrm{Gr}(x))$ is the number of connected components of $\mathrm{Gr}(x)$, $|E|$ is the number of edges of $\mathrm{Gr}(x)$, and $T(\mathrm{Gr}(x); x, y)$ is the Tutte polynomial of $\mathrm{Gr}(x)$ in the variables x and y.

Specialising to $d = 4$, the 4-dimensional trace operation Tr_4 corresponds to evaluations of the Tutte polynomial at $(x, y) = (-1, -1)$. As it turns out, this is a special point in the Tutte plane, and corresponds to evaluations of the bicycle number [21] (reviewed in Appendix A.1):

Theorem A.1.0.10 (reworded)**.** *Suppose the tuple $x = (x_1, x_2, \dots, x_{2n})$ contains the integers $1, \dots, n$ each repeated twice in some order. Then*

$$\mathrm{Tr}_4(\gamma_{\mu_{x_1}} \cdots \gamma_{\mu_{x_{2n}}}) = 4(-2)^{n+c(\mathrm{Gr}(x))+\dim(B(\mathrm{Gr}(x)))} \tag{2.49}$$

where $c(\mathrm{Gr}(x))$ is the number of connected components of $\mathrm{Gr}(x)$, and $\dim(B(\mathrm{Gr}(x)))$ is the dimension of the bicycle space of $\mathrm{Gr}(x)$.

Definitions and details of the proofs of these theorems are presented in Appendix A.1. As an example application, in Quantum Electro-Dynamics (QED) with a single massless fermion, the two-loop photon vacuum polarization (contracted against the metric tensor for simplicity) contains the

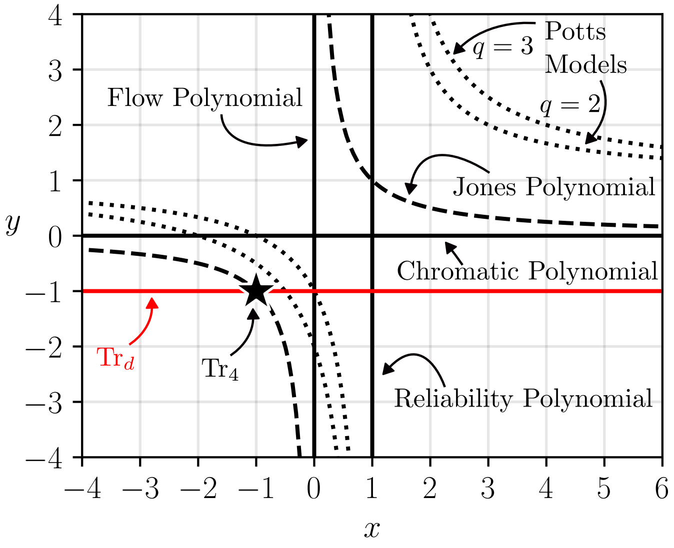

Figure 2.6: Plot of the various restrictions of the Tutte polynomial $T(x,y)$ in the Tutte plane spanned by the two variables x and y. The dimensionally regulated trace Tr_d arises from evaluations along the line $y=-1$, with the point $(x,y)=(-1,-1)$ corresponding to the four dimensional trace Tr_4.

following diagram as one of the contributions:

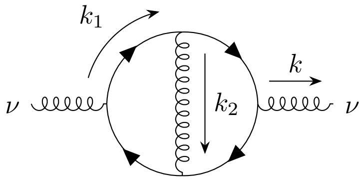

$$= e^4\,\mathrm{Tr}_d\left(\gamma_\nu\gamma_{\mu_1}\gamma_{\mu_5}\gamma_{\mu_2}\gamma_\nu\gamma_{\mu_3}\gamma_{\mu_5}\gamma_{\mu_4}\right) \times\int\frac{\mathrm{d}^dk_1\mathrm{d}^dk_2}{(2\pi)^{2d}}\frac{(k_1-k)^{\mu_1}(k_1-k_2-k)^{\mu_2}(k_1-k_2)^{\mu_3}k_1^{\mu_4}}{(k_1-k)^2(k_1-k_2-k)^2(k_1-k_2)^2k_1^2k_2^2} \tag{2.50}$$

where e is the electromagnetic charge. Eq. (2.48) can be used to compute the d-dimensional Dirac traces required for the two-loop QED diagram shown in Eq. (2.50):

$$g_{\mu_1\mu_2}g_{\mu_3\mu_4}\mathrm{Tr}_d\left(\gamma_\nu\gamma_{\mu_1}\gamma_{\mu_5}\gamma_{\mu_2}\gamma_\nu\gamma_{\mu_3}\gamma_{\mu_5}\gamma_{\mu_4}\right) = \mathrm{Tr}_d\left(\gamma_{\alpha_1}\gamma_{\alpha_2}\gamma_{\alpha_3}\gamma_{\alpha_2}\gamma_{\alpha_1}\gamma_{\alpha_4}\gamma_{\alpha_3}\gamma_{\alpha_4}\right)$$

$= \mathrm{Tr}_d\Bigg($ 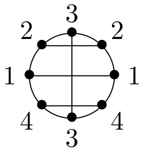 $\Bigg) = 32d\; T\Bigg($ 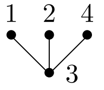 $;1-\frac{d}{2},-1\Bigg) = -4d^4+24d^3-48d^2+32d$ (2.51)

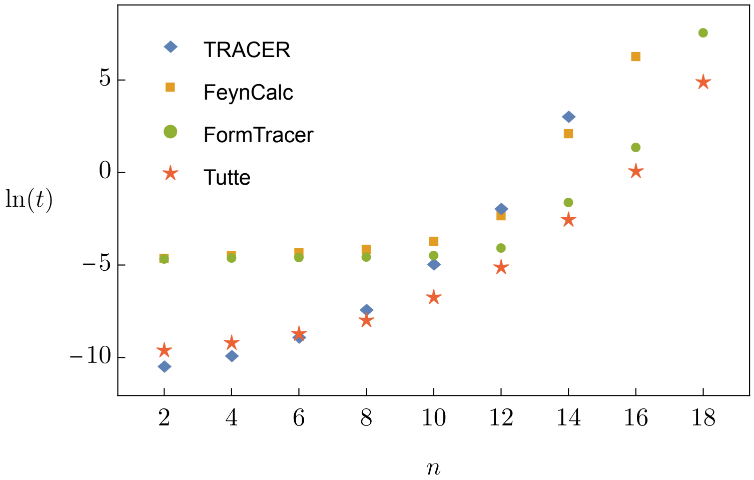

Figure 2.7: Average runtime (in seconds) of computing d-dimensional Dirac traces of $2n$ γ-matrices contracted randomly. Runtime in seconds is plotted on a log-scale using various code packages available in Mathematica [27] (TRACER [22], FeynCalc [23, 24] and FormTracer [25, 26]) averaged over 128 different examples for each n. The red star datapoints labelled 'Tutte' refers to a naive implementation of Eq. (2.48) with Mathematica's inbuilt TuttePolynomial function.

$$g_{\mu_1\mu_3}g_{\mu_2\mu_4}\mathrm{Tr}_d\left(\gamma_\nu\gamma_{\mu_1}\gamma_{\mu_5}\gamma_{\mu_2}\gamma_\nu\gamma_{\mu_3}\gamma_{\mu_5}\gamma_{\mu_4}\right) = \mathrm{Tr}_d\left(\gamma_{\alpha_1}\gamma_{\alpha_2}\gamma_{\alpha_3}\gamma_{\alpha_4}\gamma_{\alpha_1}\gamma_{\alpha_2}\gamma_{\alpha_3}\gamma_{\alpha_4}\right)$$

$$= \mathrm{Tr}_d\Bigg($$

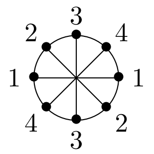

$$\Bigg) = -32d\,T\Bigg($$

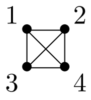

$$;1-\tfrac{d}{2},-1\Bigg) = 4d^4-48d^3+112d^2-64d \qquad (2.52)$$

The third possible contraction $g_{\mu_1\mu_4}g_{\mu_2\mu_3}$ gives the same graph up to isomorphism as in Eq. (2.51). Eqs. (2.51) and (2.52) can be verified by various computer-algebra codes available that perform Dirac traces [22–26]. In Appendix A.2, the formulas traditionally used in these computer-algebra codes to simplify traces of Dirac matrices are re-interpreted as relations on Tutte polynomials of graphs. Furthermore, the relationship to Tutte polynomials also provides *new* relationships for Dirac traces, which can provide computational benefits when calculating long traces. Comparisons between different code packages capable of performing d-dimensional Dirac traces in Mathematica [27] and computing the Dirac trace with the Tutte polynomial are shown in Fig. 2.7, where traces of strings of Dirac matrices contracted randomly. The observed performance improvement by using specialised Tutte polynomial algorithms suggests that rewriting Dirac traces as Tutte polynomials may be computationally useful.

The complexity of computing Dirac traces is explored via the connection to Tutte polynomials in Appendix A.3, which also provides a review of the relevant complexity classes discussed in this section. The problem of computing Tr_d on strings of $2n$ Dirac matrices contracted in some arbitrary fashion is equivalent to the problem of computing the Tutte polynomial of circle graphs with n vertices along the line $y = -1$ in the Tutte plane (where a circle graph is a graph obtained by drawing straight chords on a common circle, with a vertex for each chord and an edge between chords that intersect). In the more general case of evaluating the Tutte polynomial for arbitrary graphs G, it is known for example that evaluating $T(G; 1-n, 0)$ for some $n \in \mathbb{Z}, n \geq 4$ is #P-complete by parsimonious reduction from n-colouring to 3SAT [28]. By utilising some general interpolation theorems proven in Ref. [28] a corollary is that evaluating $T(G; x, y)$ along the line $\{y = -1\}$ is also #P-hard. It might be hoped that a similar strategy would apply to the restricted class of circle graphs, and that Dirac traces are #P-hard to compute. In the case where G is restricted to circle graphs, it is only known that evaluating $T(G; 1-n, 0)$ for $n \in \mathbb{Z}, n \geq 4$ is NP-hard [29] (due to lack of a parsimonious reduction), and we prove the statement:

Theorem A.3.0.9 (reworded)**.** *Let the class* **Circle*** *be the class of circle graphs and all k-stretchings of circle graphs, where a k-stretched graph (for $k \in \mathbb{N}, k \geq 2$) is obtained by subdividing each of the edges into k-segments. Computing* $\{T(G; x, -1) : x \in \mathbb{R}\}$ *(expressed as a polynomial in x) on* **Circle*** *is* NP*-hard.*

This falls short of the goal of proving that dimensionally regulated Dirac traces are #P-hard to compute, but the strategy may still be salvageable in future investigations. For the special case of evaluating the 4-dimensional trace Tr_4 however, this corresponds to evaluating $T(G; -1, -1)$, which happens to be an exceptional point in the Tutte plane, as there is a polynomial-time algorithm that solves this problem:

Theorem A.3.0.10 (reworded)**.** *The bicycle number* $\dim(B(G))$ *can be computed in polynomial time by gaussian elimination, and the 4-dimensional trace is in* FP*.*

where FP is the class of functions computable in polynomial time. Note that fixed-order perturbative QFT calculations will only require the Dirac trace to some finite power of $(d-4)$, in other words, the taylor-series coefficients of the Tutte polynomial about the point $(-1, -1)$ along the line $y = -1$. These taylor-series coefficients might have graph theoretic interpretations that allow for polynomial-time evaluations, but this is not explored in this work. Details, definitions and proofs of Theorems A.3.0.9 and A.3.0.10 are located in Appendix A.3. Finally, it is well understood that Dirac traces with open (uncontracted) indices can be reduced to Dirac traces with all indices contracted. This allows for products of Dirac traces to be computed, as well as traces including 't Hooft Veltman γ_5. As these extensions mostly rely on connection to Tutte polynomials for single traces and other formulas known in the literature, a brief perspective on this topic is presented in Appendix A.4.

2.2 Lattice QCD

Two sources of divergences in Quantum Field Theory calculations are infrared and ultraviolet divergences, associated with low and high energy cutoffs respectively. The conceptually simplest way to regulate these divergences is to place hard cutoffs on both the IR and UV degrees of freedom, as is suggested by the Wilsonian picture of renormalization [30]. As the regulator is removed, renormalized correlation functions should converge ideally as smoothly as possible. To this end, it is crucial to design regulators in a way to preserve as large a subgroup of the continuum symmetry-group as possible.

Lattice-QCD is an approach to discretising either the full four-dimensional spacetime or just three-dimensional space such that the infinitely many degrees of freedom present in the continuum are truncated to only finitely many degrees of freedom in the regulated theory. When discretising the full four-dimensional spacetime, the standard approach approximates the continuum Euclidean-time path integral formulation of QCD with a finite dimensional path integral:

$$Z[T,a] = \int D\overline{\psi} D\psi DU \ \exp[-S_{\text{gauge}}(U) + S_{\text{fermion}}(\overline{\psi},\psi,U)] \tag{2.53}$$

where T is the temperature, a is the lattice spacing, fermionic matter fields ψ live on vertices of a toroidal lattice, gauge degrees of freedom $U \in \text{SU}(3)$ are represented by parallel transporters of the SU(3) gauge group, DU represents the haar measure, and other parameters of the action (such as the fermion masses, coefficients of improvement terms, etc.) have been suppressed. Discretisation of the gauge action is discussed in Sec. 2.2.1, and discretisation of the fermion action (with an emphasis on preservation of the continuum chiral symmetry) is discussed in Sec. 2.2.2. These discretisations are predominantly considered in Euclidean spacetime for QCD as the resulting finite-dimensional path integral weighting factor $\exp[-S(\overline{\psi},\psi,U)]$ is *real*, meaning that it can be treated as a probability distribution which one can draw configurations from to calculate physical properties of QCD. In practice, for any given choice of parameters a collection of configurations is drawn from the probability distribution with Monte Carlo, and this collection is known as an ‘ensemble’. On any given ensemble, correlation functions can be measured and fitted to extract physical quantities such as the spectrum of the theory, matrix elements, decay rates, and more (see Sec. 4.2.3).

Alternatively, it is possible to only discretise space and leave the (Minkowski) time t continuous, which is known as the Hamiltonian formulation of QCD. Investigating the real-time dynamics of QCD becomes directly possible in this formulation, as opposed to attempting to analytically continue Euclidean-time correlation functions to recover real-time information. This formulation comes with its own difficulties: for example the exponentially large dimension of the Hilbert space as a function of the volume of the lattice, and the need to truncate the Hilbert space associated with gauge links. A review of the Hamiltonian formulation of Lattice-QCD is provided in Sec. 2.2.4.

	Spacetime	Gauge	Chiral	Discrete
Continuum	$\mathbb{R}^4 \rtimes O(4)$	$\{f \vert f : \mathbb{R}^4 \to \mathfrak{g}\}$	$\{D, \gamma_5\} = 0$	C, P
Hypercubic Lattice	$\mathbb{Z}_L^4 \rtimes H(4)$	G^{L^4}	$\{D, \gamma_5\} = aD\gamma_5 D$	C, P

Table 2.1: Overview of how different continuum symmetries are broken to their lattice counterparts for Euclidean time QCD. The lattice is assumed to be length L in each direction, $\mathbb{R}^4$ refers to both spacetime translations and the underlying space itself, $O(4)$ is the orthogonal group, $H(4)$ is the hypercubic group, G is the gauge group, a is the lattice spacing, and D is the Dirac operator (note that D is assumed to satisfy the Ginsparg-Wilson equation, for further discussion of chiral symmetry, see Sec. 2.2.2). The continuum gauge group is written as a collection of sufficiently nicely behaved functions from Euclidean spacetime to the Lie Algebra $\mathfrak{g}$.

2.2.1 WILSON GAUGE ACTION

There are many different ways to discretise a continuum action. A standard choice used for Yang-Mills gauge theories with gauge Lie group G is known as the Wilson gauge action, which for a hypercubic lattice means introducing a G degree of freedom per link in the lattice, and using the action:

$$S_W = \frac{a^4}{(g^{(0)})^2} \sum_{x,\mu,\nu} -\mathrm{Tr}\left[U_\mu(x) U_\nu(x + a\hat{\mu}) U_\mu^\dagger(x + a\hat{\nu}) U_\nu^\dagger(x)\right] \tag{2.54}$$

where a is the lattice spacing, $U_\mu(x) = \exp(ig^{(0)} T^A \int_x^{x+a\hat{\mu}} \mathrm{d}x_\mu \; A_\mu^{(0)A}(y))$ is the Wilson line (parallel transporter) starting at the lattice vertex x and ending at the vertex shifted by one lattice unit in the μ direction. The (0) superscript emphasizes that both the couplings and fields are bare. Note that μ, ν are indepedently summed over from $1, \cdots, 4$ which corresponds to summing over both orientations of the plaquette, ensuring that the action is always real. The action can be expanded in the continuum limit $a \to 0$ as:

$$S_W = a^8 \sum_{x,\mu,\nu} \frac{1}{4} F_{\mu\nu}^A(x) F_{\mu\nu}^A(x) + S_{\text{artifacts}}, \quad F_{\mu\nu}^A = \partial_\mu A_\nu^A - \partial_\nu A_\mu^A + g_0 f^{ABC} A_\mu^B A_\nu^C \tag{2.55}$$

where $S_{\text{artifacts}}$ corresponds to operators with mass dimensions greater than 4 - these are irrelevant operators in the continuum limit. Note that the form of the expansion can be predicted simply by listing all operators compatible with gauge symmetry and the hypercubic symmetry of the lattice. On the hypercubic lattice, a basis for the dimension-6 lattice artifacts can be given as [31]:

$$\begin{aligned} S_1 &= \frac{1}{2} \sum_{\mu,\nu,\rho} \mathrm{Tr}[D_\mu, F_{\nu\rho}^A][D_\mu, F_{\nu\rho}^A] \\ S_2 &= \sum_{\mu,\nu,\rho} \mathrm{Tr}[D_\mu, F_{\mu\rho}^A][D_\nu, F_{\nu\rho}^A] \\ S_3 &= \sum_{\mu,\nu} \mathrm{Tr}[D_\mu, F_{\mu\nu}^A][D_\mu, F_{\mu\nu}^A] \end{aligned} \tag{2.56}$$

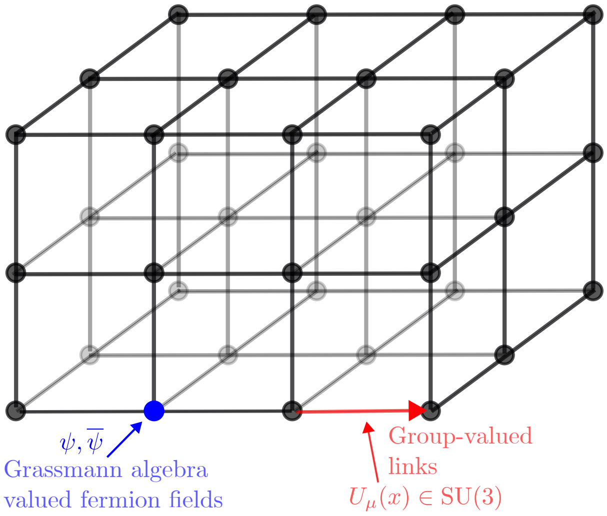

Figure 2.8: Diagram of a typically used hypercubic discretisation of spacetime.

Note that the sums have been explicitly written out, as the usual Einstein-summation convention to create Lorentz singlets breaks down when restricting to the hypercubic subgroup. For Yang-Mills theories there is one other superficially marginal operator:

$$S_\theta = -i\theta \frac{1}{64\pi^2} \epsilon_{\alpha\beta\mu\nu} \int \mathrm{d}^4 x \; F^A_{\alpha\beta}(x) F^A_{\mu\nu}(x) \tag{2.57}$$

which is CP-violating, where θ is a real number and $\epsilon_{\alpha\beta\mu\nu}$ is the Levi-Civita tensor. Because QCD itself is CP-preserving, there is exactly zero mixing between CP-conserving actions (such as the Wilson action) and such a theta term. The effect of including this term into the continuum path integral is to introduce a factor $e^{-S_{\mathrm{QCD}}} \mapsto e^{iN\theta} e^{-S_{\mathrm{QCD}}}$ where N is an integer counting the number of instantons in a given configuration[6]. Note that this term gives a sign problem where the action is no longer real, and traditional Monte-Carlo approaches can no longer sample configurations from the path integral.

2.2.2 FERMION ACTIONS AND CHIRAL SYMMETRY

Isolating the fermionic part of the QCD lagrangian:

$$\mathcal{L} = \sum_f \overline{\psi}_f (i\partial\!\!\!/ + g A\!\!\!/^A T^A - m_f) \psi_f \tag{2.58}$$

---

[6] Mathematically, an instanton corresponds to a smooth configuration with finite action (its curvature vanishes sufficiently quickly at spatial infinity) that is topologically twisted. Given a sphere with sufficiently large radius centered at the origin, and a basepoint x on the sphere, one can define a function $f(y) \in \mathrm{SU}(3)$ for y on the sphere given by the gauge transporter $U(x \to y)$. The condition that the curvature vanishes at infinity causes $f(y)$ to be well-defined (in the sense that it is independent of the choice of path connecting x to y). f furshishes a map from $S^3 \to \mathrm{SU}(3)$, which is topologically characterized by the homotopy group $\pi_3(\mathrm{SU}(3)) \simeq \mathbb{Z}$: this is the instanton number.

one notices that in the limit as $m_f \to 0$, additional symmetries known as chiral symmetries become manifest. Explicitly, supposing that there are N_f massless flavours of quarks (and ignoring all massive quarks), the Lagrangian can be written as:

$$\mathcal{L}_{\text{chiral}} = \sum_f \overline{\psi}_f (i\partial\!\!\!/ + g A\!\!\!/^A T^A) P_L \psi_f + \overline{\psi}_f (i\partial\!\!\!/ + g A\!\!\!/^A T^A) P_R \psi_f \tag{2.59}$$

where $P_L = \frac{1-\gamma_5}{2}$ and $P_R = \frac{1+\gamma_5}{2}$ are projectors onto left/right handed degrees of freedom respectively (the notation $\psi_L \coloneqq P_L\psi, \psi_R \coloneqq P_R\psi$ is also used to denote the separate chiralities). This lagrangian is invariant under a $\mathrm{U}(N_f)_L \times \mathrm{U}(N_f)_R = \mathrm{SU}(N_f)_L \times \mathrm{SU}(N_f)_R \times \mathrm{U}(1)_L \times \mathrm{U}(1)_R$ symmetry, where the actions are given by:

$$G \in \mathrm{su}(N_f)_L \text{ maps } \psi_{f,L} \to \left(e^{i\theta G}\right)_{fg} \psi_{g,L}, \quad G \in \mathrm{su}(N_f)_R \text{ maps } \psi_{f,R} \to \left(e^{i\theta G}\right)_{fg} \psi_{g,R}, \tag{2.60}$$

$$\theta \in \mathrm{u}(1)_L \text{ maps } \psi_{f,L} \to e^{i\theta}\psi_{f,L} \quad \theta \in \mathrm{u}(1)_R \text{ maps } \psi_{f,R} \to e^{i\theta}\psi_{f,R} \tag{2.61}$$

The corresponding Lie Algebra can be factored into vector and axial contributions, $\mathrm{su}(N_f)_V \oplus \mathrm{su}(N_f)_A \oplus \mathrm{u}(1)_V \oplus \mathrm{u}(1)_A$ where the vector contributions act the same on left/right-handed degrees of freedom, and the axial contributions act in opposite ways on the left/right degrees of freedom. Note that it is often written that the Lie *Group* can be similarly decomposed as $\mathrm{SU}(N_f)_V \times \mathrm{SU}(N_f)_A \times \mathrm{U}(1)_V \times \mathrm{U}(1)_A$, however this is not strictly true because exponentiating the axial lie-algebras does not give a well defined Lie group. We will however similarly abuse notations at points during this thesis, sometimes writing such Lie-group decompositions when we really are referring to Lie algebra decompositions.

For QCD, these chiral symmetry properties become important for flavours of quarks where $m_f \lesssim \Lambda_{\text{QCD}}$, in particular the up, down and strange quarks. Each factor in the chiral symmetry decomposition has a different story:

- Sometimes symmetries of the action that hold classically are broken by quantum effects, known as an *anomaly.* The $\mathrm{U}(1)_V$ symmetry is known as the baryon-number symmetry, and in QCD has no anomaly and is a true symmetry of the quantum theory. However, when including the electroweak sector of the Standard Model, there is a mixed $\mathrm{SU}_L(2)^2 \times \mathrm{U}(1)_V$ anomaly, meaning that baryon-number violations are mediated by spharelons (instantons of the $\mathrm{SU}_L(2)$ gauge field). However, $B - L$ is not anomalous, where L is the lepton number, and B the baryon number is the $\mathrm{U}(1)_V$ current normalised such that each quark contributes a factor of $\frac{1}{3}$, as their anomalies cancel.

- The $\mathrm{SU}(N_f)_L \times \mathrm{SU}(N_f)_R$ symmetry spontaneously breaks to a $\mathrm{SU}(N_f)_V$ symmetry, where the order parameter is given by a nonvanishing chiral condensate $\langle \overline{\psi}_{fs}\psi_{gt} \rangle = v\delta_{fg}\delta_{st}$, where f, g are flavour indices, s, t are spin indices, and v is the vacuum expectation value of mass dimension 3. Such spontaneous symmetry breaking can be predicted by matching the infrared anomalies appearing in a low-energy effective theory of QCD with the ultraviolet perturbative theory of quarks [32]. Due to this breaking, there are Goldstone-bosons associated with each of the generators of $\mathrm{su}(N_f)_A$, which give massless degrees of freedom. In the case that the quark masses are finite but small, these are instead referred to as pseudo-Goldstone bosons, and have masses that scale with the square-root of the quark masses.

- The $\mathrm{U}(1)_A$ symmetry is anomalous even just within QCD itself (the $\mathrm{SU}(3)^2 \times \mathrm{U}(1)_A$ anomaly), where chiral symmetry violations are mediated by SU(3)-instantons. This has various ramifications, for instance if the $\mathrm{U}(1)_A$ were not anomalous, the symmetry breaking pattern of QCD would be $\mathrm{U}(N_f)_L \times \mathrm{U}(N_f)_R \to \mathrm{U}(N_f)_V$ and there would be light η' pseudo-Goldstone boson meson. Instead, the η' is measured to have a parametrically larger mass due to this axial anomaly[7].

One use of chiral symmetries is to constrain the types of mixings that can occur between different operators of the theory, for example the four-quark operators appearing in Chapters 3 and 4. Note that if a symmetry is spontaneously broken, this is a property of the vacuum of the theory - and the symmetry still splits operators into different representations that do not mix with each other. Furthermore, if a symmetry G is anomalous, operators living in different G-representations cannot *perturbatively* mix, because all violations of the symmetry are mediated by nonperturbative instanton effects in the corresponding gauge degrees of freedom.

It turns out that implementing chiral symmetry in Lattice-QCD is difficult. For example, naively discretising derivatives appearing in the continuum action in a symmetric way gives the action[8]:

$$\overline{\psi} D_{\text{naive}} \psi = a^4 \sum_{n \in \Lambda} \overline{\psi}(n) \left(\sum_{\mu=1}^{4} \gamma_\mu \frac{U_\mu(n)\psi(n+\hat{\mu}) - U_{-\mu}(n)\psi(n-\hat{\mu})}{2a} + m\psi(n) \right) \tag{2.62}$$

where Λ is the lattice, n are vertices in the lattice, and $U_{-\mu}(n) = U(n - a\hat{\mu})^\dagger$. Examining the free massless limit $U_\mu(n) = \mathbb{1}, m = 0$, the Dirac operator can be diagonalized in momentum space to find:

$$D_{\text{naive}}(p)^{-1} = \frac{-ia \sum_\mu \gamma_\mu \sin(ap_\mu)}{\sum_\mu \sin(ap_\mu)^2} = \frac{-i\not{p}}{p^2} + O(a) \tag{2.63}$$

This has the correct dispersion relation for a massless fermion about $p = (0,0,0,0)$, however it also has spurious poles showing up at the edges of the Brillouin zone, at $p \in \{\left(\frac{\pi}{a},0,0,0\right), \left(0,\frac{\pi}{a},0,0\right), \ldots, \left(\frac{\pi}{a},\frac{\pi}{a},\frac{\pi}{a},\frac{\pi}{a}\right)\}$. Physically, this means that in the continuum limit if the naive discretisation is used, instead of having one fermion there would be 15 additional ‘doubler’ modes included in the theory. A solution proposed by Wilson in Ref. [33] that dates back to the creation of Lattice-QCD is to introduce a term into the acion which gaps the doubler modes by a mass that scales inversely with the lattice spacing, so that in the continuum limit only the mode about $p = (0,0,0,0)$ survives.

---

[7] The large difference in masses between the η and η' mesons is known as the $\eta - \eta'$ puzzle.

[8] Note that in the continuum, the Dirac matrix is usually denoted $\not{D}$ to emphasize that a covariant derivative has been contracted against γ-matrices, however in the lattice-QCD literature it is often just written as D.

Concretely, the Wilson discretisation is given by:

$$\overline{\psi} D_{\text{Wilson}} \psi = \overline{\psi} D_{\text{naive}} \psi + a^4 \sum_{n \in \Lambda} \sum_{\mu=1}^{4} \overline{\psi}(n) \left(- \frac{U_\mu(n)\psi(n+\hat{\mu}) - 2\delta_{nm} + U_{-\mu}(n)\psi(n-\hat{\mu})}{2a} \right) \psi(m) \quad (2.64)$$

This additional term provides a shift of $\mathbb{1}\frac{1}{a}\sum_\mu (1 - \cos(p_\mu a))$ to the momentum space Dirac operator, which gaps the doubler modes so that they vanish in the continuum limit. Note however that this additional term explicitly breaks the $U(1)_A$ chiral symmetry, which can be written as the condition $\{D, \gamma_5\} = 0$. Consequently, the Wilson action allows operators that transform under different chiral symmetry representations to mix, an immediate example being the power-divergent mixing between the kinetic-like terms and the mass term of the Wilson action. Practically this means that to achieve precise renormalized masses requires fine-tuning the bare lattice mass against $O(\alpha_S/a)$ type divergences.

This tradeoff between gapping the doubler modes but losing chiral symmetry is more general than just the Wilson action. In fact Nielsen and Ninomiya proved a 'no-go' theorem [34] for lattice fermions. The theorem states that a translationally invariant, hermitian, and sufficiently local (the momentum space Dirac matrix exists and is analytic) Dirac matrix D such that $\{D, \gamma_5\} = 0$ *necessarily* contains doubler modes [9]. Instead of the exact continuum chiral symmetry, it was realised by Ginsparg and Wilson [35] that the relation should be relaxed in a lattice discretisation. By considering a chirally symmetric continuum action and performing a block-spin type integration procedure to derive the corresponding action on lattice degrees of freedom, they found that the Dirac operator should instead satisfy:

$$D\gamma_5 + \gamma_5 D = aD\gamma_5 D \quad (2.65)$$

where intuitively since the right-hand-side vanishes in the continuum limit $a \to 0$, the chiral symmetry is restored. Such a Dirac operator has two very attractive features [36]:

- Lüscher proved that any Dirac matrix satisfying the Ginsparg-Wilson relation Eq. (2.65), the action is exactly symmetric under the following modified $U(1)$ chiral symmetry [37]:

$$\psi \mapsto \exp\left(i\alpha\gamma_5\left(\mathbb{1} - \frac{a}{2}D\right)\right)\psi, \quad \overline{\psi} \mapsto \overline{\psi}\, \exp\left(i\alpha\left(\mathbb{1} - \frac{a}{2}D\right)\gamma_5\right) \quad (2.66)$$

  In fact, by defining a new lattice γ_5 as:

$$\hat{\gamma}_5 = \gamma_5(\mathbb{1} - aD) \quad (2.67)$$

---

[9] There are two distinct problems, both sometimes referred to as the 'lattice chiral fermion problem'. The first is the 'easy' version, of constructing a discretisation of QCD without doubler modes that retains some amount of chiral symmetry; the solutions to this problem following Ginsparg and Wilson's approach are explained in this section. The second is the 'hard' problem, of constructing *chiral gauge theories*, where left/right handed modes are charged differently under the gauge group. For example, in the Standard Model only left-handed fermions couple to the weak gauge theory. This latter problem is an active field of research, and it is not clear that there have been any successful demonstrations for $3+1$d nonabelian chiral gauge theories.

one notices that the Dirac matrix splits into left and right handed components:

$$P_L = \frac{1-\hat{\gamma}_5}{2}, \quad P_R = \frac{1+\hat{\gamma}_5}{2}, \quad \overline{\psi} D \psi = \overline{\psi}_L D \psi_L + \overline{\psi}_R D \psi_R \tag{2.68}$$

where $\psi_{L/R} = P_{L/R}\psi$ are the chirality projected operators.

- Fujikawa [38] demonstrated that the chiral anomaly can be understood in the continuum as a non-preservation of the path-integral measure by chiral rotations. From this reasoning, one should have never expected exact chiral symmetry $\{D, \gamma_5\} = 0$ to be implementable in a lattice discretisation, as this would forbid the appearance of an appropriate lattice axial anomaly. Note that Ginsparg-Wilson fermions *do* have the correct axial anomaly. Consider an infinitessimal chiral rotation (for a single flavour theory):

  $$\psi \mapsto \left(\mathbb{1} + i\epsilon\gamma_5\left(\mathbb{1} - \frac{a}{2}D\right)\right), \quad \overline{\psi} \mapsto \overline{\psi}\left(\mathbb{1} + i\epsilon\left(\mathbb{1} - \frac{a}{2}D\right)\gamma_5\right) \tag{2.69}$$

  where terms of $O(\epsilon^2)$ are discarded, and ϵ is a small parameter. The fermionic integration measure picks up a factor:

  $$D\psi D\overline{\psi} \mapsto D\psi D\overline{\psi}\left(1 - 2i\epsilon Q_{\text{top}} + O(\epsilon^2)\right) \tag{2.70}$$

  where Q_{top} is the integer lattice topological charge [36] (discretisation of Eq. (2.57)) as expected.

An example of a lattice fermion action that satisfies the Ginsparg-Wilson relation is the Domain Wall fermion [39]. The construction begins by extending the four-dimensional lattice to a fifth dimension with extent N_5, such that the lattice is $\Lambda \times \{1, 2, \dots, N_5\}$. There are now fermionic degrees of freedom at every five-dimensional lattice site, though the gauge fields are kept four-dimensional. There are variations on the domain-wall fermion action - one that will be relevant for the ensembles used in Chapter 4 is the Möbius action [40]:

$$S_{\text{DW}} = \sum_{r,s=1}^{N_5} \sum_{m,n\in\Lambda} \overline{\psi}(n,s) D_{\text{DW}}(n,s|m,r)\psi(m,r) \tag{2.71}$$

where the five-dimensional Dirac matrix is given in block-form as a $N_5 \times N_5$ matrix as:

$$D_{\text{DW}} = \begin{pmatrix} D_+^{(1)} & D_-^{(1)}P_- & 0 & 0 & \cdots & 0 & -mD_-^{(1)}P_+ \\ D_-^{(2)}P_+ & D_+^{(2)} & D_-^{(2)}P_- & 0 & \cdots & 0 & 0 \\ 0 & D_-^{(3)}P_+ & D_+^{(3)} & D_-^{(3)}P_- & \cdots & 0 & 0 \\ 0 & 0 & D_-^{(4)}P_+ & D_+^{(4)} & \cdots & 0 & 0 \\ \vdots & \vdots & \vdots & \vdots & \ddots & \vdots & \vdots \\ 0 & 0 & 0 & 0 & \cdots & D_+^{(N_5-1)} & D_-^{(N_5-1)}P_- \\ -mD_-^{(N_5)}P_- & 0 & 0 & 0 & \cdots & D_-^{(N_5)}P_+ & D_+^{(N_5)} \end{pmatrix} \tag{2.72}$$

where

$$D_+^{(s)} = b_s D_w(M) + 1, \qquad D_-^{(s)} = c_s D_w - 1, \qquad P_\pm = \frac{1 \pm \gamma_5}{2} \tag{2.73}$$

and $D_w(M)$ is the Wilson Dirac-matrix with mass M:

$$D_w(M) = (4+M)\delta_{m,n} - \frac{1}{2}\sum_{\mu=0}^{3}\left[(1-\gamma_\mu)U_\mu(m)\delta_{m+\hat{\mu},n} + (1+\gamma_\mu)U_\mu^\dagger(r)\delta_{m,n+\hat{\mu}}\right] \tag{2.74}$$

The real coefficients b_s, c_s for $s \in \{1,\dots,N_5\}$ are constrained such that $b_s - c_s$ is a constant in s. In practice, the propagators used in Chapter 4 are all such that b_s, c_s are constants in s. Four-dimensional fermionic fields are constructed by combinations of the degrees of freedom on the first and last sites:

$$\psi_{4D}(m) = P_-\psi(m,1) + P_+\psi(m,N_5), \qquad \overline{\psi}_{4D}(m) = \overline{\psi}(m,N_5)P_- + \overline{\psi}(m,1)P_+ \tag{2.75}$$

Integrating out the fifth dimension, one can rewrite the domain-wall fermion action as a nonlocal Dirac matrix acting on the four-dimensional degrees of freedom. This effective action satisfies the Ginsparg-Wilson relation in the limit as $N_5 \to \infty$; for finite N_5, the violations of chiral symmetry are exponentially suppressed in N_5. In practice, this small chiral violation is ignored in the analysis performed in Chapter 4, as they constitute a much smaller systematic error than from statistical uncertainties.

2.2.3 Smearing and Gradient flow

A practical problem that occurs in measurements of correlation functions in Lattice-QCD is finding appropriate operators that have high overlap onto states of interest. Without high-quality operators, much higher statistics are needed to resolve states; in fact states can be completely missed if operators of the right structure are not used [41]. There is a rich history of trying to improve operators; a highly successful method has been through the concept of *smearing* operators. Smearing an operator has the consequence of taking a point-like gauge-invariant operator to a non-local gauge-invariant operator, that may have higher overlap onto states of interest which are inherently nonlocal. For the case of quark fields, the idea is to perform a replacement:

$$\psi(x) \to \sum_\gamma c_\gamma W_\gamma(x,y)\psi(y) \tag{2.76}$$

where the sum is performed over Wilson lines γ starting at x and ending at y, weighted by some factors c_γ. The Wilson lines are needed to preserve the gauge properties of the smeared operator to be the same as the original operator. A simple and effective choice is to iterate a hopping-like smearing [42]

$$\psi(x) \mapsto \psi(x) + \kappa \sum_{\hat{\mu}\in\{(\pm a,\pm a,\pm a,\pm a)\}} U(x,x+\hat{\mu})\psi(x+\hat{\mu}) \tag{2.77}$$

where the sum is sometimes restricted to μ being nonzero only in spatial directions, in order to construct smeared operators that are still time-local. In the case that the gauge fields are all set to identity, iterating Eq. (2.77) N times has the effect of building a gaussian profile. Such operators are utilised later in Chapter 4 to construct interpolating operators for heavy-light and heavy-light-light hadronic states.

Smearing of gauge-links is important for any observable that uses the gauge links directly, which includes the static heavy-quark propagators used in HQET calculations. There are various smearing procedures:

- Some smearing procedures replace links with sums over close-by Wilson lines that transform in the same way under the gauge group, before projecting back to SU(3). The projection step is important, as general sums over SU(3) elements will not remain in the group. For instance, APE smearing [43] of a link in the ν direction takes the form:

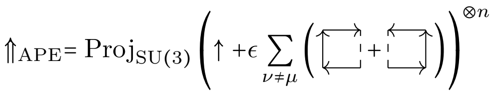

(2.78)

  where $\epsilon > 0$ is a small number, single lines such as $\uparrow$ represent the original gauge link, and double lines $\Uparrow$ represent the smeared link. The sum is performed over directions $\mu \neq \nu$, where the link is displaced ± 1 units in the μ-th direction (sometimes μ is restricted to be spacelike if a time-local correlator is desired). Note that there are various different algorithms to project generic matrices to SU(3), but they are equivalent in the small ϵ limit. The $\otimes n$ means that the operation is repeated n times (similarly to Gaussian smearing of quark fields). This has the effect of causing the smeared links to be nonlocal combinations of the unsmeared links. Alternatively, the HYP smearing [44] is a similar procedure, but only uses links within adjacent hypercubies to construct the smeared links.

- Wilson flow [45] (also known as Gradient flow) is a smearing scheme that takes initial gauge fields $U_\mu(x)$ and evolves them under the differential equation:

$$\frac{\mathrm{d}}{\mathrm{d}t} U_\mu(x;t) = -g_0^2(\partial_{x,\mu} S_W(U_t)) U_\mu(x;t), \quad U_\mu(x;0) = U_\mu(x) \tag{2.79}$$

  where $\partial_{x,\mu}$ is the $\mathfrak{su}(3)$-valued derivative of the action with respect to $U_{x,\mu}$, and the right-hand factor of $U_t(x,\mu)$ transports this to the tangent space at $U_t(x,\mu)$. Wilson flow is incredibly useful because the theory at a fixed flow-time t also serves as a well-defined regulator of UV-divergences of composite operators in the continuum limit. Wilson flow alternatively can be described as integrating infinitessimally small steps of stout smearing [46], which in the small-ϵ limit takes the form:

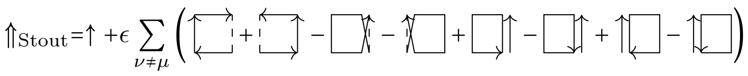

(2.80)

  where closed loops denote taking the trace of those loops, and dividing by N_c. Note that Eq. (2.80) does not require an explicit projection to SU(3) as the last 6 diagrams in the equation are an implementation of a projection to SU(3) to $O(\epsilon^2)$. Operators are smeared over a radius $\sim \sqrt{8t}$ after applying Wilson flow for time t (in lattice units).

When using Wilson flow to smear gauge links for use in HQET calculations, it has the additional benefit of replacing power-divergences (such as those appering in an Operator Product Expansion),

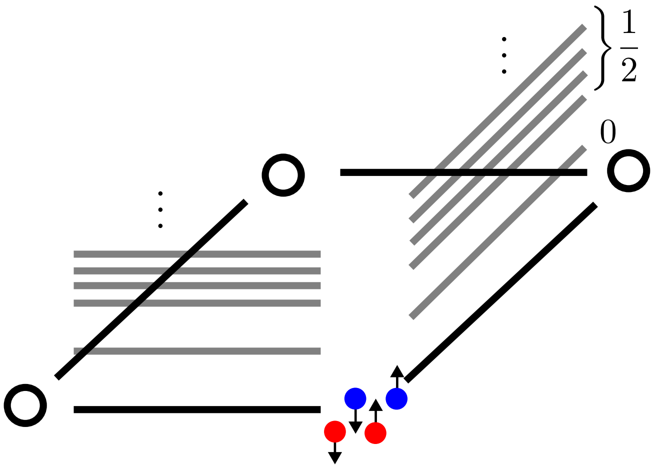

Figure 2.9: Schematic drawing of the Hilbert-space in a Kogut-susskind discretisation, for an SU(2) gauge theory. On each link, the Hilbert space is $L^2(\mathrm{SU}(2))$, which by the Peter-Weyl theorem is also given by the matrix elements of the irreducible representations. For SU(2), these irreducible representation are indexed by the spin, $0, \frac{1}{2}, 1, \ldots$. On the vertices, there are fermionic degrees of freedom associated to each colour-spin combination.

with finite mixings that are perturbatively calculable. Essentially, by using a fixed physical flow time t, the relevant UV scale changes from a^{-1} to $t^{-1/2}$. For the purposes of this thesis however, Wilson flow was used in Chapter 4 primarily to improve the signal-to-noise properties of the resulting correlators, and not as a regulator of OPE power-divergences.

2.2.4 HAMILTONIAN FORMULATION

Lattice-QCD works well in Euclidean time, as the Euclidean QCD action is real, and defines a probability distribution that one can integrate with importance sampling. It is formally possible to consider discretising spacetime *without* Wick rotating giving a regularisation of real-time QCD; however due to the sign problem importance sampling Monte Carlo computations are practically impossible to perform. Alternatively it is possible to leave time continuous and discretise the spatial degrees of freedom of the QCD Hamiltonian, the first example of which was described by Kogut and Susskind in Ref. [47]. On a spatial lattice, the local Hilbert space on each edge of the lattice (where there is some canonical order to the edge) is given by $L^2(G)$, the space of square-normalisable functions from the Lie group to $\mathbb{C}$ under the inner product:

$$\langle f, g\rangle = \int \mathrm{d}\mu_{\mathrm{Haar}}(x) f^*(x) g(x) \tag{2.81}$$

where μ_{Haar} is the Haar measure over the group G. Due to the Peter-Weyl theorem[48], this space has a orthonormal basis given by:

$$\{\sqrt{d_\rho}\rho_{ij}|\rho : G \to U(d_\rho), 1 \leq i, j \leq d_\rho\} \tag{2.82}$$

where ρ indexes over inequivalent unitary representations of G, ρ_{ij} are the matrix entries of the representation, and d_ρ is the dimension of the representation. Gauge transformations at a vertex act on the right/left of each of the local Hilbert spaces associated to the edges incoming/outgoing to the vertex. To restrict to the gauge-invariant subspace of the theory, one must impose Gauss Law conditions at each vertex, restricting to the gauge invariant subspace of the gauge-action at that vertex. Note that one can also impose that at a given vertex, the group representations corresponding to the adjacent edges must contract into a representation other than a singlet, for example the fundamental representation of an SU(N) gauge theory. This would correspond to physically placing a fundamental static charge into the system.

The Kogut-Susskind Hamiltonian can be written as[47, 49]:

$$\begin{aligned} H = \frac{g^2}{2}\sum_{\vec{x},\mu} E_\mu(\vec{x})^2 - \frac{1}{2g^2}\sum_{\vec{x},\mu>\nu}\left(\mathrm{Tr}U_\mu^{(F)}(\vec{x})U_\nu^{(F)}(\vec{x}+\hat{\mu})U_\mu^{(F)\dagger}(\vec{x}+\hat{\nu})U_\nu^{(F)\dagger}(\vec{x}) + \text{h.c.}\right) \\ + \sum_{\vec{x},\mu}\left(\psi^\dagger(\vec{x})\frac{\vec{\sigma}\cdot\vec{n}}{i}U_\mu^{(F)}(\vec{x})\psi(\vec{x}+\hat{\mu}) + \text{h.c.}\right) + m\sum_{x}(-1)^{\sum_i \vec{x}_i}\psi^\dagger(\vec{x})\psi(\vec{x}) \end{aligned} \tag{2.83}$$

To describe the gauge part of the Hamiltonian shown in Eq. (2.83), label the states of the Peter-Weyl orthonormal decomposition of each link as $|j, kl\rangle$ where j indexes the representations, and kl are the indices for the matrix element. Then, $E_\mu(\vec{x})$ is an electric field operator defined on each link, where $E^2|j, kl\rangle = C_2(j)|j, kl\rangle$, where C_2 is the quadratic casimir. For SU(2) where $j \in \left\{0, \frac{1}{2}, 1, \ldots\right\}$ indexes over spin choices, $C_2(j) = J^2 = j(j+1)$ (this is discussed in the original reference [47]). For SU(3) the irreps can be described by two numbers $j = (j_1, j_2)$ where j_1 is the number of single-box columns in the corresponding Young tableaux, and j_2 is the number of double-box columns. In this case, $C_2((j_1, j_2)) = \frac{j_1^2+j_2^2+3j_1+3j_2+j_1j_2}{3}$. The physical effect of the electric-field operator is to cause the larger representations to have higher energies.

The next term in the gauge part of the Hamiltonian is the magnetic field term, which involves a sum over all unoriented plaquettes and incentivizes the gauge field to be smooth. Operators of the form $U^{(j)}$ for some representation j act on arbitrary functions $f \in L^2(G)$ in the following natural manner:

$$(U_{kl}^{(j)}f)(x) = f(x)\rho^{(j)}(x)_{kl} \tag{2.84}$$

where $\rho^{(j)} : G \to \mathbb{C}$ is the corresponding representation, and k, l are matrix indices. The (F) superscripts in Eq. (2.83) indicate that the operators are in the fundamental representation. Finally, there are two-component fermionic fields introduced on all lattice vertices, such that the fermionic operators satisfy canonical anticommutation relations:

$$\{\psi_\alpha(x), \psi^\dagger_\beta(y)\} = \delta_{\alpha,\beta}\delta_{x,y}, \tag{2.85}$$

where α, β are the spin indices, and the σ in Eq. (2.83) are Pauli matrices coupling the spins on different sites. Note that this discretisation is known as a 'staggered' discretisation, due to splitting up the four-component spinor into two-component spinors that live on even and odd sublattices. This only fully removes the fermion-doublers in a $1+1$d discretisation, and in higher discretisations, fermion doublers remain. This type of discretisation is used for a $U(1)$ gauge theory in $1+1$-dimensions in Chapter 5 as a toy model for full QCD-dynamics. $1+1$d is also special because it is possible to completely remove all the gauge degrees of freedom from the system (in one sense, the gauge sector is trivial), and the fermionic operators can be converted to spin operators via the Jordan-Wigner transformation (explained in Sec. 5.2.1).

2.2.5 Static Quark energy power divergence

Recall that the full calculation of the $O(\alpha_S)$ contribution to the bare heavy-quark propagator (Eq. (2.14)) is given by:

$$\begin{aligned} i\mathcal{M}_Q &= -iC_F g^2 \mu^{4-d} \frac{1+\not{v}}{2} \frac{2^{d-2}\Gamma(3-d)\Gamma\left(\frac{d}{2}-1\right)}{(4\pi)^{\frac{d}{2}}} (-v\cdot p)^{d-3} \\ &= i\mu C_F g^2 \frac{1+\not{v}}{2}\left(\frac{1}{4\pi(d-3)} + O((d-3)^0)\right). \end{aligned} \tag{2.86}$$

In the second line of Eq. (2.86), the expression has been expanded around $d=3$, where the divergence as $d \to 3$ arises due to the $\Gamma(3-d)$ factor. In a pure $\overline{\text{MS}}$ renormalization scheme, these poles at values of $d < 4$ are ignored, and only poles at $d = 4$ are subtracted by counterterms. However in a lattice regularisation, these poles become power divergences $\sim \frac{\alpha_S}{a}$, which is further explored in this section.

Before calculating the self-energy divergence, a brief review of pure gauge lattice perturbation theory following Ref. [50] is given. As the continuum limit $a \to 0$ is taken, if a physical quantity is kept fixed, the renormalization-group equation can be derived as:

$$a\frac{dg^{(0)}}{da} = -\beta(g^{(0)}), \quad \beta(g^{(0)}) = -(g^{(0)})^3(b_0 + b_1(g^{(0)})^2 + b_2(g^{(0)})^4 + \cdots) \tag{2.87}$$

where the first two coefficients are universal:

$$b_0 = \frac{1}{(4\pi)^2}\left(\frac{11}{3}N_c - \frac{2}{3}N_f\right), \quad b_1 = \frac{1}{(4\pi)^4}\left(102 - \frac{38}{3}N_f\right) \tag{2.88}$$

Note that as the continuum limit $a \to 0$ is taken, the bare coupling $g^{(0)} \to 0$, which is a signature of asymptotic freedom. This behaviour is qualitatively different than what occurs in dimensional-regularisation, where there are divergences of the form $(g^{(0)})^2 \sim \frac{1}{\epsilon}(g^{(R)})^2$. These divergences don't appear in lattice regularisations, because $\frac{1}{a}$ divergences cannot appear just by counting mass dimensions - thus all lattice regularisation divergences in the coupling constant manifest as logarithms.

In principle, one can perform perturbation theory in the bare coupling $g^{(0)}$, however the a-dependence becomes obscured due to the RG-running of $g^{(0)}$. Instead, from the β function Eq. (2.87) one can derive:

$$g^{(0)} = g^R + \frac{11N_c}{48\pi^2}(g^R)^3 \log\left(\frac{\mu}{a}\right) + O((g^R)^5) \tag{2.89}$$

where the renormalized coupling $g^R(\mu)$ has *no* a-dependence, and R refers to a 'minimal' scheme with no finite piece and only the leading logarithmic contribution. Defining lattice Fourier transforms [10]:

$$A_\mu(x) = \int_{-\frac{\pi}{a}}^{\frac{\pi}{a}} \frac{d^4k}{(2\pi)^4} e^{i(x+a\hat{\mu}/2)k} A_\mu(k), \quad A_\mu(k) = a^4 \sum_x e^{-i(x+a\hat{\mu}/2)k} A_\mu(x), \tag{2.90}$$

the propagator in position space for the gauge field can be calculated as:

$$\langle A_\mu^a(x) A_\nu^b(y)\rangle = \delta^{ab}\delta^{\mu\nu} \int_{-\frac{\pi}{a}}^{\frac{\pi}{a}} \frac{d^4k}{(2\pi)^4} \frac{e^{ik(x-y)}}{\frac{4}{a^2}\sum_\lambda \sin^2\left(\frac{ak_\lambda}{2}\right)} =: \frac{1}{a^2} G\left(\frac{x-y}{a}\right) \tag{2.91}$$

Here $G(x)$ is the dimensionless coordinate-space propagator [51] which takes integer lattice points as arguments. There is an asymptotic expansion for $G(x)$:

$$G(x) \sim \frac{1}{4\pi^2 x^2}\left(1 - \frac{1}{x^2} + 2\frac{x^4}{(x^2)^3} - 4\frac{1}{(x^2)^2} + 16\frac{x^4}{(x^2)^4} - 48\frac{x^6}{(x^2)^5} + 40\frac{(x^4)^2}{(x^2)^6} + O((x^2)^{-3})\right) \tag{2.92}$$

where $x^{2n} := \sum_\mu x_\mu^{2n}$. From this, it is evident that the standard continuum propagator is reproduced as $x \to \infty$. When performing calculations involving Wilson lines, often sums of the form:

$$G_m(x) = \sum_{n=0}^{x} n^m G(n) \tag{2.93}$$

appear. Some values that are useful are listed below:

$$G_0(n) = G_0' - \frac{1}{4\pi^2 n} - \frac{1}{8\pi^2 n^2} + O\left(n^{-3}\right), \qquad G_0' = G_0(\infty) = 0.20383\ldots \tag{2.94}$$

$$G_1(n) = \frac{\log(n)}{4\pi^2} + G_1' + \frac{1}{8\pi^2 n} + O(n^{-2}), \qquad G_1' = 0.025723\ldots \tag{2.95}$$

$$G_2(n) = \frac{n}{4\pi^2} + G_2' - \frac{1}{4\pi^2 n} - \frac{1}{8\pi^2 n^2} + O(n^{-3}), \qquad G_2' = 0.0248\ldots \tag{2.96}$$

$$G_3(n) = \frac{n^2}{8\pi^2} + \frac{n}{8\pi^2} + \frac{\log(n)}{4\pi^2} + G_3' + \frac{1}{8\pi^2 n} + O(n^{-2}), \qquad G_3' = 0.0066\ldots \tag{2.97}$$

Using this information, one can compute the $O((g^R)^2)$ correction to a straight wilson line, with physical length L that starts at $(0,0,0,0)$ and ends at $\left(\frac{L}{a},0,0,0\right)$ in lattice coordinates (assume that a divides L evenly). For example, using the diagrams sketched in Fig. 2.10, the contribution can be

---

[10] Note that in the Fourier transforms, the position is shifted to the middle of the link (this is a convention).

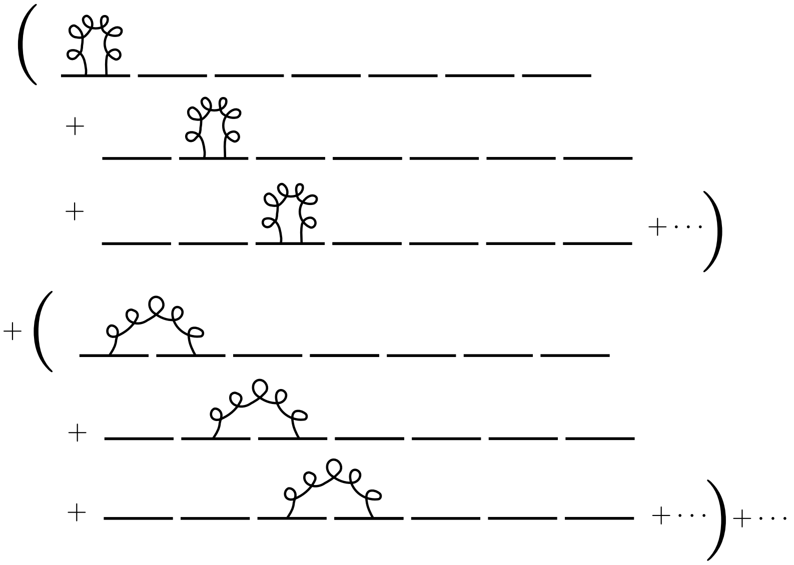

Figure 2.10: Schematic drawing of the $O(\alpha_S)$ contribution to the linear divergence. Note that if there are L links in the Wilson line, then there are L tadpole terms of a gluon attaching to itself, $(L-1)$ terms with a gluon hopping from a link to it's neighbor, and so on. The deviation from being directly proportional to L is what gives rise to the logarithmic endpoint divergences, corresponding to field renormalizations in the auxiliary field formalism [52].

written as:

$$\begin{aligned}\langle W(L)\rangle &= \mathbb{1} + C_F(g^R)^2\left[\left(-\frac{L}{a}\frac{G(0)}{2} - \left(\frac{L}{a}-1\right)G(1) - \cdots - 1\cdot G\left(\frac{L}{a}-1\right)\right)\right] \\ &= \mathbb{1} + C_F(g^R)^2\left(\frac{L}{2a}G(0) - \frac{L}{a}G_0\left(\frac{L}{a}\right) + G_1\left(\frac{L}{a}\right)\right) \\ &= \mathbb{1} + C_F(g^R)^2\left[\frac{L}{a}\left(\frac{G(0)}{2} - G_0'\right) + \frac{\log\left(\frac{L}{a}\right)}{4\pi^2} + \left(\frac{1}{4\pi^2} + G_1'\right) + \frac{a}{L}\frac{1}{4\pi^2} + O(a^2)\right] \qquad (2.98)\end{aligned}$$

The $\frac{L}{a}$ term generates the linear divergence of the static-quark propagator. This power divergence is intimately related to the corresponding renormalon in the pole-mass [3]. For a concrete interpretation of this term, consider taking the induced measure on SU(3) obtained by isolating a Wilson line of physical length L in a Lattice-QCD path integral with lattice spacing a. Instead of approaching a fixed distribution on SU(3) like one might expect from analogies to discretised quantum mechanical path integrals, the linear divergence term causes the distribution to limit towards the Haar-uniform distribution. A practical consequence is that the signal-to-noise ratio for two-point correlation functions containing a static heavy quark vanishes exponentially in the continuum limit [53, 54]. The argument (colloquially referred to as the Parisi-Lepage argument) for a heavy-light correlation function is that the signal correlator is:

$$\text{Signal} = \langle (\overline{Q}\gamma_5 q)(0)(\overline{q}\gamma_5 Q)(t)\rangle = \langle \mathrm{Tr}\left(G_q^\dagger(t)G_{\mathrm{st}}(t)\right)\rangle \approx Z^2_{\overline{Q}\Gamma q} e^{-E_{\mathrm{stat}}t} \tag{2.99}$$

where $G_q(t)$ is the light quark propagator, and G_{st} is the static quark propagator. From Eq. (2.98), E_{stat} has a power divergence which dominates the energy in the continuum limit. Now, one notices that the variance of this correlator can actually be given a physical interpretation:

$$\begin{aligned}\text{Noise}^2 &= \langle |(\overline{Q}\gamma_5 q)(0)(\overline{q}\gamma_5 Q)(t)|^2\rangle \\ &= \langle \mathrm{Tr}\left(G_q^\dagger(t)G_{\mathrm{st}}(t)\right)\mathrm{Tr}\left(G_q(t)G^\dagger_{\mathrm{st}}(t)\right)\rangle \approx Z_* e^{-m_\pi t}\end{aligned} \tag{2.100}$$

where the crucial observation is that the Wilson line propagating in the forward time direction is compensated by a Wilson line propagating in the backward time direction, and the overall quantum numbers of the contraction is given by the pion[11]. Note that Z_* is not given by the overlap of the usual $\overline{q}q$ operator onto the pion state, because the contractions used in Eq. (2.100) don't correspond to the conventional contractions. Due to this difference, the ratio Signal/Noise vanishes either in the continuum limit, or when the distance t between the operators is taken to infinity.

In practice, by smearing the gauge configurations this problem is ameliorated. For example, by Wilson flowing to a physical time t, the $O(\alpha_S/a)$ divergence in the static quark energy is replaced by an $O(\alpha_S/\sqrt{t})$-type behaviour, where for t large enough the signal to noise problem can be avoided. This is the strategy utilised in Chapter 4.

2.2.6 Bent Wilson lines

There are various situations in Lattice-QCD calculations where 'bent' Wilson lines are required. As they come in different flavours, we catalogue some situations below, along with some observations:

- For example, when discretising the light-cone operators required for Parton Distribution Function measurements into a Hamiltonian formulation, where space is discretised and time is continuous, amounts to the replacement [55]:

  $$\begin{aligned}&\overline{\psi}((0,0,0,0))\Gamma W((0,0,0,0),(Na,Na,0,0))\psi((Na,Na,0,0)) \mapsto \\ &\quad \left(\overline{\psi}((0,0,0,0))W((0,0,0,0),(a,a,0,0))Q((a,a,0,0))\right)e^{iaH} \\ &\quad \left(\overline{Q}((a,a,0,0))W((a,a,0,0),(a,2a,0,0))Q((a,2a,0,0))\right)e^{iaH}\cdots \\ &\quad e^{iaH}\left(\overline{Q}(((N-1)a,Na,0,0))W(((N-1)a,Na,0,0),(Na,Na,0,0))\psi((Na,Na,0,0))\right)\end{aligned} \tag{2.101}$$

  where Q is the static heavy quark field propagating in the purely timelike direction, as shown in Fig. 2.11. To my knowledge, there have been no proposals of renormalization schemes for such a discretisation in QCD, though various numerical studies using this scheme have been performed in superrenormalizable theories such as the Schwinger model.

---

[11] The argument is only heuristic, as the variance correlator shown in Eq. (2.100) doesn't *actually* correspond to a valid two-point correlation function. In particular, the conventional two-point correlation function for the pion interpolating operator $\overline{q}\gamma_5 q$ is $\mathrm{Tr}(G_q^\dagger(t)G_q(t))$ which differs from Eq. (2.100).

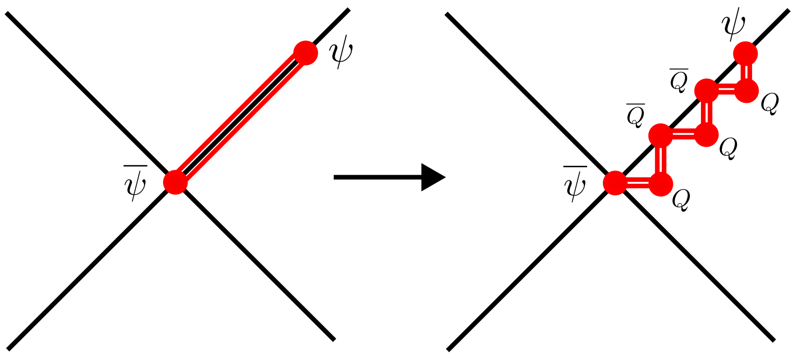

Figure 2.11: An example of a discretisation of a lightcone operator used in defining Parton Distribution Functions in the continuum to a lattice-discretised version of the operator, which utilises an auxiliary heavy quark field Q. Note that the usual Kogut-Susskind discretisation of gauge theories is performed in axial gauge, so the vertical Wilson lines in the figure on the right are all set to unity.

- In the limit of infinite masses for *two* flavours of quarks (taking the approximation that $m_c, m_b \gg \Lambda_{\text{QCD}}$), the weak decay of a B-meson to a D-meson can be described by the Isgur-Wise function ξ [56]:

$$\langle D(v')|\overline{Q}_{c,v'}\gamma_\mu Q_{b,v}|\overline{B}(v)\rangle \sim \xi(v \cdot v')(v_\mu + v'_\mu) \tag{2.102}$$

Calculating the Isgur-Wise function in Lattice-QCD requires setting up HQET with two different time-like velocity sectors, v and v'. The traditional Eichten-Hill static action [57] covers only the case where there is a single sector corresponding to $v = (1,0,0,0)$, in which the Euclidean action is given by a Wilson line propagating in the Euclidean time direction. As discussed by Aglietti [58], it is formally possible to construct Euclidean theories where the spatial velocities of the heavy quark are nonzero by analytic continuation. The proposed analytic continuation was utilised in Ref. [59] to provide a lattice calculation of the Isgur-Wise function, and has been explored in Ref. [60] as a method of calculating the Transverse-Momentum-Dependent (TMD) soft function. To be precise, the proposal is to analytically continue the heavy-quark velocity as:

$$v_E = (iv_0, \vec{v}), \qquad \text{where} \qquad v_0 = \sqrt{1+\vec{v}^2} \text{ because } v^2 = 1 \tag{2.103}$$

The lattice-propagator is given by:

$$-i(v_E)_\mu D_\mu S_v(x) = -i(v_E)_\mu(\partial_\mu - igA_\mu(x))\delta^4(x) \tag{2.104}$$

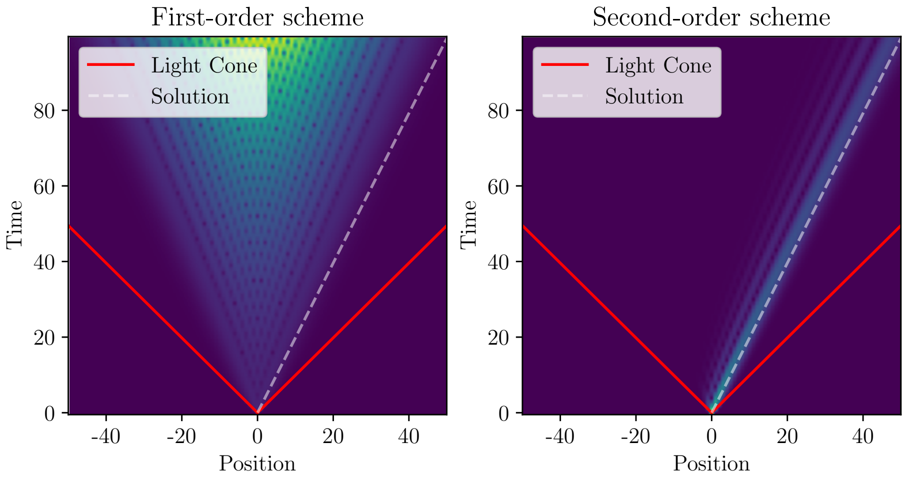

Figure 2.12: Time evolution using first or second-order schemes in Minkowski time of the Heavy Quark static propagator in the free limit with $v = (\sqrt{1+v_x^2}, v_x, 0, 0)$ and $v_x = 0.5$. The colour shown is proportional to the norm of the propagator, and both position and time are written in lattice units. The true solution is given by the white dashed line - with the delta function being transported at the corresponding velocity. The first-order scheme shows significant artifacts due to the large spatial derivatives, including the fact that the norm of the propagator is symmetric about $x = 0$. The second-order scheme solution shows much better behaviour.

with the lattice equation:

$$\begin{aligned}&(v_E)_0(U_4(x,x+\hat{t})S_{v_E}(x+\hat{t},y) - S_v(x,y))+\\&\sum_{\mu=1}^{3}\frac{-i(v_E)_\mu}{2}\left[U_\mu(x,x+\hat{\mu})S_v(x+\hat{\mu},y) - U_\mu(x,x-\hat{\mu})S_v(x-\hat{\mu},y)\right] = \delta_{x,y}\end{aligned} \tag{2.105}$$

There is, however, a potential sickness to utilising this equation - apparent already in the free Minkowski theory ($U_\mu(x) = \mathbb{1}$) in $1+1$-dimensions. In this situation, the partial differential equation (PDE) to be solved is essentially a linear-transport equation with a Dirac-delta initial state:

$$\frac{\mathrm{d}S_v(x,t)}{\mathrm{d}t} + \frac{v_x}{\sqrt{1+v_x^2}}\frac{\mathrm{d}S(x,t)}{\mathrm{d}x} = 0, \quad S_v(x,0) = \delta(x) \tag{2.106}$$

There are various discretisations of this PDE, with Eq. (2.105) being known as an upwind first order scheme. Improved schemes, such as the second-order Lax-Wendroff scheme [61] exist, and for the linear-transport equation in Eq. (2.106) are given by:

$$\begin{aligned}S_v(x,t+1) = S_v(x,t) - \frac{1}{2}\frac{v_x}{\sqrt{1+v_x^2}}\left(S_v(x+1,t) - S_v(x-1,t)\right) \\ + \frac{1}{2}\left(\frac{v_x}{\sqrt{1+v_x^2}}\right)^2\left(S_v(x+1,t) - 2S_v(x,t) + S_v(x-1,t)\right)\end{aligned} \tag{2.107}$$

(the upwind-scheme corresponds to dropping the second-order term). By comparing the two schemes behaviours on the Dirac-delta initial state, one notices that the second-order scheme is much better behaved, as shown in Fig. 2.12. This suggests that a correct discretisation of the nonzero spatial velocity heavy quark action may require using second or higher order schemes, instead of the first-order schemes that have been tested in the literature.

The situation is perhaps even more dire - given that the analytic continuation of the linear transport equation is the Cauchy-Riemann equations; implying that the appropriately rescaled static quark propagator in Euclidean time is analytic as a function of the complex variable $x + it_E$. To be precise, the analytic continuation of Eq. (2.106) satisfies the Cauchy-Riemann equations:

$$i\frac{\mathrm{d}S(x',t_E)}{\mathrm{d}t_E} + \frac{\mathrm{d}S(x',t_E)}{dx'} = 0 \quad \text{where} \quad x' := \frac{\sqrt{1+v_x^2}}{v_x}x \tag{2.108}$$

and hence, $S(x',t_E)$ is complex analytic away from the origin, and should be matched onto a Dirac delta $\delta(x)$ at $t = 0$. Morally, the solution should be an analytic continuation of $\delta(x)$ away from $t = 0$, however it is not clear that there is a meaningful solution. This is related to Aglietti's comment [58] that even the *free* heavy quark effective theory with nonzero spatial velocity in Euclidean time *requires* a UV-regulator to even be defined. Given this issue, it is not immediately clear how such a theory can be nonperturbatively renormalized.

- A final example of 'bent' Wilson lines are investigations of the Euclidean cusp divergences. By this, we mean studying operators of the form:

  $$W_E((x,0,0,0),(0,0,0,0))W_E((0,0,0,0),(a,b,0,0)) \tag{2.109}$$

  where a, b are positive real numbers, the E subscript denotes that the Wilson lines are in Euclidean space, and the Euclidean angle between the two lines is given by $\arctan\left(\frac{b}{a}\right)$. In the continuum $\overline{\text{MS}}$ scheme, this operator has power divergences (poles at $d = 3$) corresponding to the static propagators, as well as a logarithmic divergence that depends on the Euclidean angle formed. This logarithmic divergence can be associated with the so-called 'cusp anomalous dimension' of the pointlike operator at the vertex in the auxiliary field formalism. For example, as the Euclidean angle is taken close to π, the resulting anomalous dimension becomes related to the static quark-antiquark potential up to breaking from conformal anomaly [62]. Furthermore, given the analogy to the cusps required for Isgur-Wise function calculations, TMD Soft functions, as well as heavy quark fragmentation (see Eq. (2.35) of Ref. [63]), one

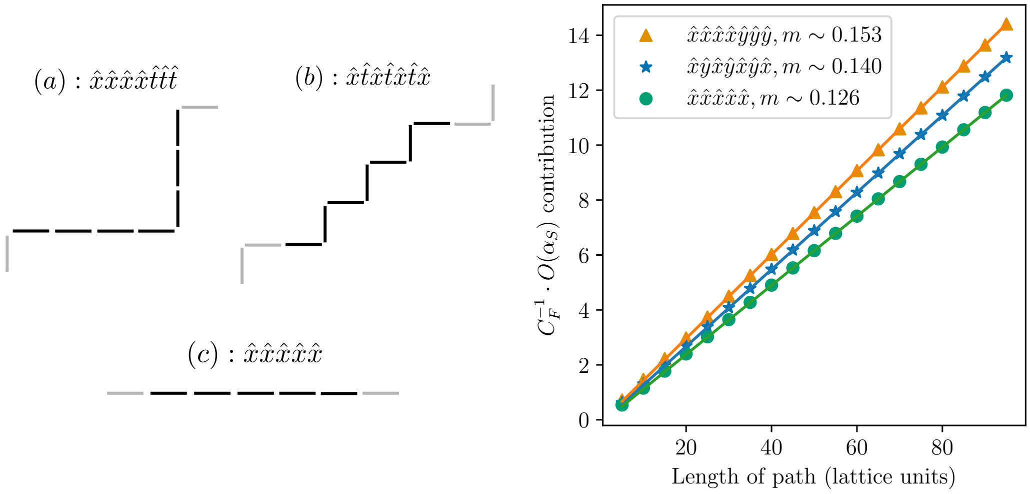

Figure 2.13: Subfigures (a) and (b) show two different ways of discretising a Wilson line that travels in an $\text{ArcTan}\left(\frac{3}{4}\right)$-Euclidean angle with respect to the x-axis. Each of the black segments is repeated many times, to get a macroscopic-length Wilson line pointing in the correct direction. In the continuum limit, both (a) and (b) should limit to the same operator, just with different matching coefficients. On the right is the negative of the $O(\alpha_S)$ coefficient of the linear divergence, also compared against $-\left(G_0' - \frac{G_0}{2}\right)$ which is the coefficient corresponding to the linear divergence in the straight line case (c) (derivation in Eq. (2.98)).

might wonder whether it is possible to extract such real-time physics from Euclidean cusp-like matrix elements.

One issue that arises in possible Lattice-QCD calculations of operators containing Euclidean cusps is the linear power-divergences arising from bent Wilson lines. For example (as shown in Fig. 2.13), it is possible to discretise a Wilson line that is at a Euclidean angle of $\text{ArcTan}(\frac{3}{4})$ with the x-axis as one that travels along the path given by iterating the steps $\hat{x}-\hat{t}-\hat{x}-\hat{t}-\hat{x}-\hat{t}-\hat{x}$, *or* the path given by iterating the steps $\hat{x} - \hat{x} - \hat{x} - \hat{x} - \hat{t} - \hat{t} - \hat{t}$, for a total of 4 steps in the $\hat{x}$ direction, and three steps in the $\hat{t}$ direction in either case. Both discretisations match onto the same operator in the continuum limit, however the right figure of Fig. 2.13 demonstrates that they have *different* linear power divergences - both of the linear divergences being more severe than what is computed for the straight line path of the same length.

BIBLIOGRAPHY

[1] Joshua Lin. Dirac Traces and the Tutte Polynomial. *JHEP*, 10 2024. doi: 10.1007/JHEP05(2025)235.

[2] F. J. Dyson. Divergence of perturbation theory in quantum electrodynamics. *Phys. Rev.*, 85:631–632, 1952. doi: 10.1103/PhysRev.85.631.

[3] M. Beneke. Renormalons. *Phys. Rept.*, 317:1–142, 1999. doi: 10.1016/S0370-1573(98)00130-6.

[4] Gerald V. Dunne and Mithat Ünsal. Resurgence and Trans-series in Quantum Field Theory: The CP(N-1) Model. *JHEP*, 11:170, 2012. doi: 10.1007/JHEP11(2012)170.

[5] John C. Collins. *Renormalization*, volume 26 of *Cambridge Monographs on Mathematical Physics*. Cambridge University Press, Cambridge, 7 2023. ISBN 978-0-521-31177-9, 978-0-511-86739-2, 978-1-00-940180-7, 978-1-00-940176-0, 978-1-00-940179-1. doi: 10.1017/9781009401807.

[6] Howard Georgi. Heavy quark effective field theory. In *Theoretical Advanced Study Institute in Elementary Particle Physics (TASI 91): Perspectives in the Standard Model*, 8 1991.

[7] Andrey G. Grozin. Lectures on multiloop calculations. *Int. J. Mod. Phys. A*, 19:473–520, 2004. doi: 10.1142/S0217751X04016775.

[8] Joshua Lin, William Detmold, and Stefan Meinel. Position-space renormalization schemes for four-quark operators in HQET. *JHEP*, 07:188, 2024. doi: 10.1007/JHEP07(2024)188.

[9] Dominik Stöckinger. Regularization by dimensional reduction: consistency, quantum action principle, and supersymmetry. *JHEP*, 03:076, 2005. doi: 10.1088/1126-6708/2005/03/076.

[10] Gerard 't Hooft and M. J. G. Veltman. Regularization and Renormalization of Gauge Fields. *Nucl. Phys. B*, 44: 189–213, 1972. doi: 10.1016/0550-3213(72)90279-9.

[11] C. Gnendiger et al. To d, or not to d: recent developments and comparisons of regularization schemes. *Eur. Phys. J. C*, 77(7):471, 2017. doi: 10.1140/epjc/s10052-017-5023-2.

[12] Marco Ciuchini, E. Franco, G. Martinelli, and L. Reina. The Delta S = 1 effective Hamiltonian including next-to-leading order QCD and QED corrections. *Nucl. Phys. B*, 415:403–462, 1994. doi: 10.1016/0550-3213(94)90118-X.

[13] K. Symanzik. Continuum Limit and Improved Action in Lattice Theories. 1. Principles and φ^4 Theory. *Nucl. Phys. B*, 226:187–204, 1983. doi: 10.1016/0550-3213(83)90468-6.

[14] Stefan Herrlich and Ulrich Nierste. Evanescent operators, scheme dependences and double insertions. *Nucl. Phys. B*, 455:39–58, 1995. doi: 10.1016/0550-3213(95)00474-7.

[15] Hassler Whitney. The coloring of graphs. *Annals of Mathematics*, 33(4):688–718, 1932. ISSN 0003486X, 19398980. doi: 10.2307/1968214.

[16] R. L. Brooks, C. A. B. Smith, A. H. Stone, and W. T. Tutte. The dissection of rectangles into squares. *Duke Mathematical Journal*, 7(1):312 – 340, 1940. doi: 10.1215/S0012-7094-40-00718-9.

[17] W. T. Tutte. A contribution to the theory of chromatic polynomials. *Canadian Journal of Mathematics*, 6: 80–91, 1954. doi: 10.4153/CJM-1954-010-9.

[18] Manoj K. Chari and Charles J. Colbourn. Reliability polynomials: A survey. *Combinatorica*, 1998. URL https://api.semanticscholar.org/CorpusID:1931075.

[19] Morwen B. Thistlethwaite. A spanning tree expansion of the jones polynomial. *Topology*, 26(3):297–309, 1987. ISSN 0040-9383. doi: https://doi.org/10.1016/0040-9383(87)90003-6.

[20] C. M. Fortuin and P. W. Kasteleyn. On the Random cluster model. 1. Introduction and relation to other models. *Physica*, 57:536–564, 1972. doi: 10.1016/0031-8914(72)90045-6.

[21] P. Rosenstiehl and R.C. Read. On the principal edge tripartition of a graph. In B. Bollobás, editor, *Advances in Graph Theory*, volume 3 of *Annals of Discrete Mathematics*, pages 195–226. Elsevier, 1978. doi: https://doi.org/10.1016/S0167-5060(08)70508-9.

[22] Matthias Jamin and Markus E. Lautenbacher. TRACER: Version 1.1: A Mathematica package for gamma algebra in arbitrary dimensions. *Comput. Phys. Commun.*, 74:265–288, 1993. doi: 10.1016/0010-4655(93)90097-V.

[23] Vladyslav Shtabovenko, Rolf Mertig, and Frederik Orellana. FeynCalc 10: Do multiloop integrals dream of computer codes? *Comput. Phys. Commun.*, 306:109357, 2025. doi: 10.1016/j.cpc.2024.109357.

[24] J. Kublbeck, M. Bohm, and Ansgar Denner. Feyn Arts: Computer Algebraic Generation of Feynman Graphs and Amplitudes. *Comput. Phys. Commun.*, 60:165–180, 1990. doi: 10.1016/0010-4655(90)90001-H.

[25] Anton K. Cyrol, Mario Mitter, and Nils Strodthoff. FormTracer - A Mathematica Tracing Package Using FORM. *Comput. Phys. Commun.*, 219:346–352, 2017. doi: 10.1016/j.cpc.2017.05.024.

[26] J. Kuipers, T. Ueda, J. A. M. Vermaseren, and J. Vollinga. FORM version 4.0. *Comput. Phys. Commun.*, 184: 1453–1467, 2013. doi: 10.1016/j.cpc.2012.12.028.

[27] Wolfram Research, Inc. Mathematica, Version 14.0. URL `https://www.wolfram.com/mathematica`. Champaign, IL, 2024.

[28] F. Jaeger, D. L. Vertigan, and D. J. A. Welsh. On the computational complexity of the jones and Tutte polynomials. *Mathematical Proceedings of the Cambridge Philosophical Society*, 108(1):35–53, 1990. doi: 10.1017/S0305004100068936.

[29] Walter Unger. On the k-colouring of circle-graphs. In Robert Cori and Martin Wirsing, editors, *STACS 88*, pages 61–72, Berlin, Heidelberg, 1988. Springer Berlin Heidelberg. ISBN 978-3-540-48190-4.

[30] Kenneth G. Wilson. The Renormalization Group: Critical Phenomena and the Kondo Problem. *Rev. Mod. Phys.*, 47:773, 1975. doi: 10.1103/RevModPhys.47.773.

[31] P. Weisz. Continuum Limit Improved Lattice Action for Pure Yang-Mills Theory. 1. *Nucl. Phys. B*, 212:1–17, 1983. doi: 10.1016/0550-3213(83)90595-3.

[32] Gerard 't Hooft. Naturalness, chiral symmetry, and spontaneous chiral symmetry breaking. *NATO Sci. Ser. B*, 59:135–157, 1980. doi: 10.1007/978-1-4684-7571-5_9.

[33] Kenneth G. Wilson. Confinement of Quarks. *Phys. Rev. D*, 10:2445–2459, 1974. doi: 10.1103/PhysRevD.10.2445.

[34] Holger Bech Nielsen and M. Ninomiya. Absence of Neutrinos on a Lattice. 1. Proof by Homotopy Theory. *Nucl. Phys. B*, 185:20, 1981. doi: 10.1016/0550-3213(82)90011-6. [Erratum: Nucl.Phys.B 195, 541 (1982)].

[35] Paul H. Ginsparg and Kenneth G. Wilson. A Remnant of Chiral Symmetry on the Lattice. *Phys. Rev. D*, 25: 2649, 1982. doi: 10.1103/PhysRevD.25.2649.

[36] Christof Gattringer and Christian B. Lang. *Quantum chromodynamics on the lattice*, volume 788. Springer, Berlin, 2010. ISBN 978-3-642-01849-7, 978-3-642-01850-3. doi: 10.1007/978-3-642-01850-3.

[37] Martin Lüscher. Exact chiral symmetry on the lattice and the Ginsparg-Wilson relation. *Phys. Lett. B*, 428: 342–345, 1998. doi: 10.1016/S0370-2693(98)00423-7.

[38] Kazuo Fujikawa. Path Integral Measure for Gauge Invariant Fermion Theories. *Phys. Rev. Lett.*, 42:1195–1198, 1979. doi: 10.1103/PhysRevLett.42.1195.

[39] David B. Kaplan. A Method for simulating chiral fermions on the lattice. *Phys. Lett. B*, 288:342–347, 1992. doi: 10.1016/0370-2693(92)91112-M.

[40] R. C. Brower, H. Neff, and K. Orginos. Mobius fermions. *Nucl. Phys. B Proc. Suppl.*, 153:191–198, 2006. doi: 10.1016/j.nuclphysbps.2006.01.047.

[41] Michael L. Wagman. Fifty ways to build a deuteron: a variational calculation of two-nucleon systems. *PoS*, LATTICE2021:419, 2022. doi: 10.22323/1.396.0419.

[42] S. Güsken. A Study of smearing techniques for hadron correlation functions. *Nucl. Phys. B Proc. Suppl.*, 17: 361–364, 1990. doi: 10.1016/0920-5632(90)90273-W.

[43] M. Albanese et al. Glueball Masses and String Tension in Lattice QCD. *Phys. Lett. B*, 192:163–169, 1987. doi: 10.1016/0370-2693(87)91160-9.

[44] Anna Hasenfratz and Francesco Knechtli. Flavor symmetry and the static potential with hypercubic blocking. *Phys. Rev. D*, 64:034504, 2001. doi: 10.1103/PhysRevD.64.034504.

[45] Martin Lüscher. Properties and uses of the Wilson flow in lattice QCD. *JHEP*, 08:071, 2010. doi: 10.1007/JHEP08(2010)071. [Erratum: JHEP 03, 092 (2014)].

[46] Colin Morningstar and Mike J. Peardon. Analytic smearing of SU(3) link variables in lattice QCD. *Phys. Rev. D*, 69:054501, 2004. doi: 10.1103/PhysRevD.69.054501.

[47] John B. Kogut and Leonard Susskind. Hamiltonian Formulation of Wilson's Lattice Gauge Theories. *Phys. Rev. D*, 11:395–408, 1975. doi: 10.1103/PhysRevD.11.395.

[48] Fritz Peter and Hermann Weyl. Die vollständigkeit der primitiven darstellungen einer geschlossenen kontinuierlichen gruppe. *Math. Ann.*, 97:737–755, 1927. doi: 10.1007/BF01447892.

[49] Erez Zohar and Michele Burrello. Formulation of lattice gauge theories for quantum simulations. *Phys. Rev. D*, 91(5):054506, 2015. doi: 10.1103/PhysRevD.91.054506.

[50] Stefano Capitani. Lattice perturbation theory. *Phys. Rept.*, 382:113–302, 2003. doi: 10.1016/S0370-1573(03)00211-4.

[51] Martin Lüscher and Peter Weisz. Coordinate space methods for the evaluation of Feynman diagrams in lattice field theories. *Nucl. Phys. B*, 445:429–450, 1995. doi: 10.1016/0550-3213(95)00185-U.

[52] Harald Dorn. Renormalization of Path Ordered Phase Factors and Related Hadron Operators in Gauge Field Theories. *Fortsch. Phys.*, 34:11–56, 1986. doi: 10.1002/prop.19860340104.

[53] Rainer Sommer. Non-perturbative Heavy Quark Effective Theory: Introduction and Status. *Nucl. Part. Phys. Proc.*, 261-262:338–367, 2015. doi: 10.1016/j.nuclphysbps.2015.03.022.

[54] G. Peter Lepage. Simulating heavy quarks. *Nucl. Phys. B Proc. Suppl.*, 26:45–56, 1992. doi: 10.1016/0920-5632(92)90228-K.

[55] Mari Carmen Bañuls, Krzysztof Cichy, C. J. David Lin, and Manuel Schneider. Parton Distribution Functions in the Schwinger model from Tensor Network States. 4 2025.

[56] Nathan Isgur and Mark B. Wise. Weak Decays of Heavy Mesons in the Static Quark Approximation. *Phys. Lett. B*, 232:113–117, 1989. doi: 10.1016/0370-2693(89)90566-2.

[57] Estia Eichten and Brian Russell Hill. An Effective Field Theory for the Calculation of Matrix Elements Involving Heavy Quarks. *Phys. Lett. B*, 234:511–516, 1990. doi: 10.1016/0370-2693(90)92049-O.

[58] U. Aglietti. Consistency and lattice renormalization of the effective theory for heavy quarks. *Nucl. Phys. B*, 421: 191–216, 1994. doi: 10.1016/0550-3213(94)90231-3.

[59] Jeffrey E. Mandula and Michael C. Ogilvie. A Lattice calculation of the heavy quark universal form-factor. *Nucl. Phys. B Proc. Suppl.*, 34:480–482, 1994. doi: 10.1016/0920-5632(94)90423-5.

[60] Anthony Francis, Issaku Kanamori, C. J. David Lin, Wayne Morris, and Yong Zhao. The lattice extraction of the TMD soft function using the auxiliary field representation of the Wilson line. In *40th International Symposium on Lattice Field Theory*, 12 2023.

[61] Peter Lax and Burton Wendroff. Systems of conservation laws. *Communications on Pure and Applied Mathematics*, 13(2):217–237, 1960. doi: https://doi.org/10.1002/cpa.3160130205. URL `https://onlinelibrary.wiley.com/doi/abs/10.1002/cpa.3160130205`.

[62] Andrey Grozin. QCD cusp anomalous dimension: current status. *Int. J. Mod. Phys.*, 38(04n05), 2023. doi: 10.1142/S0217751X23300041.

[63] Rebecca von Kuk, Johannes K. L. Michel, and Zhiquan Sun. Transverse momentum distributions of heavy hadrons and polarized heavy quarks. *JHEP*, 09:205, 2023. doi: 10.1007/JHEP09(2023)205.

Chapter 3

X-space Renormalization of HQET operators

Some content in this section reproduced with permission from the following reference: **Joshua Lin**, William Detmold, and Stefan Meinel. Position-space renormalization schemes for four-quark opera- tors in HQET. JHEP, 07:188, 2024. doi: 10.1007/JHEP07(2024)188.

Contents

The general pipeline for flavour physics calculations with Lattice-QCD is first an Operator Product Expansion, where physical results of interest are written as a sum over Wilson Coefficients multiplied by Matrix Elements. Due to the relative simplicity of Dimensional Regularisation and the $\overline{\text{MS}}$ scheme as compared to other renormalization schemes, $\overline{\text{MS}}$ is almost universally used in high-order perturbative calculations of Wilson Coefficients. Thus, a central difficulty for Lattice-QCD calculations is to determine matrix elements similarly renormalised in the $\overline{\text{MS}}$ scheme - which is difficult primarily because Dimensional Regularisation is naively not compatible with the Lattice regulator[1]. For simplicity, consider a set of operators $\{O_i\}$ of the same mass dimension that mix

---

[1] To my knowledge, there has never been a demonstration of 'nonperturbative dimensional regularisation'.

under renormalization. Borrowing notation from Ref [1], perturbative evaluations of the operator in some external state denoted by $|p\rangle$ behaves as follows in the two regulators:

$$\langle p|\mathcal{O}_i^{(\mathrm{Lat.})}|p\rangle = \sum_j \left(\delta_{ij} + \frac{g_0^2}{16\pi^2}(-\gamma_{ij}^{(0)} \log a^2p^2 + R_{ij}^{\mathrm{Lat.}}) + O(g_0^4) \right) \langle p|O_j^{\mathrm{tree}}|p\rangle, \tag{3.1}$$

$$\langle p|\mathcal{O}_i^{(\overline{\mathrm{MS}})}|p\rangle = \sum_j \left(\delta_{ij} + \frac{g_{\overline{\mathrm{MS}}}^2}{16\pi^2}(-\gamma_{ij}^{(0)} \log \frac{p^2}{\mu^2} + R_{ij}^{\overline{\mathrm{MS}}}) + O(g_{\overline{\mathrm{MS}}}^4) \right) \langle p|O_j^{\mathrm{tree}}|p\rangle, \tag{3.2}$$

where $R_{ij}^{\mathrm{Lat.}}, R_{ij}^{\overline{\mathrm{MS}}}$ are constants. This allows for the conversion between the two schemes:

$$\langle p|\mathcal{O}_i^{\overline{\mathrm{MS}}}|p\rangle = \sum_j \left(\delta_{ij} - \frac{g_0^2}{16\pi^2}(-\gamma_{ij}^{(0)} \log a^2\mu^2 + R_{ij}^{\mathrm{Lat.}} - R_{ij}^{\overline{\mathrm{MS}}}) + O(g_0^4) \right) \langle q|\mathcal{O}_j^{\mathrm{Lat.}}|q\rangle. \tag{3.3}$$

Such lattice perturbation theory was extensively used in early Lattice-QCD flavour-physics calculations. An improvement is possible however by instead of using the perturbative result for $\langle p|\mathcal{O}_i^{(\mathrm{Lat.})}|p\rangle$, to use the *nonperturbative* measurement of the Green's function in the ensemble. This is equivalent to introducing an intermediate, regulator-independent scheme in which the chosen Green's function is set equal to its tree level value. For momentum-space Green's functions, such schemes go under the name of RI-MOM [2],(or, RI-sMOM [3]) schemes.

An undesirable aspect of schemes like RI-MOM is that they involve gauge non-invariant correlation functions. For example, the renormalization of a fermion bilinear operator $\overline{\psi}\Gamma\psi$ involves calculating $\langle\psi(p)|(\overline{\psi}\Gamma\psi)(q)|\psi(r)\rangle$ for some choice of momenta p, q, r. These matrix elements *must* be calculated after fixing the gauge redundancies, or else the matrix elements are exactly zero[2]. In practice, different gauge fixing conditions can be used, for example Landau gauge whose continuum form is $\partial_\mu A_\mu = 0$ can be discretised on the lattice in various ways. The original proposal from Ref [2] proposed to minimize the functional:

$$\mathrm{Tr}\left[\sum_{\mu=1}^{4}(U_\mu(x) + U_\mu^\dagger(x))\right] \tag{3.4}$$

over gauge transformations of the original gauge configuration. Minimizing this functional (or solving for $\partial_\mu A_\mu = 0$ in the continuum) does not lead to a unique solution - instead there are multiple solutions known as Gribov copies [5]. These Gribov copies introduce an unavoidable systematic on the extracted renormalization constants. There have been some studies of the practical effect of Gribov copies [6, 7], with varying conclusions on their relative size compared to typically achievable statistical errors. In any case, it is slightly unnerving to include an uncontrollable systematic error into any calculation.

An alternative strategy is to choose intermediate renormalization schemes that use only gauge-invariant quantities. For example, one can instead impose renormalization conditions based on

---

[2] This statement seems trivially true as the matrix element has no singlet contribution under gauge transformations, though in principle one might worry that it is possible for gauge symmetries to be spontaneously broken. Elitzur's theorem demonstrates that this is impossible[4].

position-space correlation functions of gauge-invariant operators. In the literature this has been called the X-space scheme [8], or the gauge-invariant-renormalization-scheme (GIRS) [9]. For multiplicatively renormalizable operators, the X-space renormalized operator $\mathcal{O}^{(X)}$ can be related to the bare operator $O^{(0)}$ by $O^{(X)} = Z_{\mathcal{O}}^{(X)} \mathcal{O}^{(0)}$, where $Z_{\mathcal{O}}^{(X)}$ is an (often divergent) renormalization constant. One possible X-space renormalization scheme can be defined by the requirement that the renormalized two-point correlation function built from $\mathcal{O}^{(X)}$ is equal to its non-interacting (NI) value when the operators are separated by a fixed spacetime distance x:

$$\left\langle \mathcal{O}^{\dagger(X)}(0)\, \mathcal{O}^{(X)}(x) \right\rangle = \left\langle \mathcal{O}^{\dagger(0)}(0)\, \mathcal{O}^{(0)}(x) \right\rangle \Big|_{\mathrm{NI}} , \tag{3.5}$$

where $\sqrt{x^2}$ is the scale at which the operator is renormalized, and the non-interacting correlation function is defined as the $\alpha_S \to 0$ value of the correlation function[3]. Although the scheme is gauge invariant by definition, it requires more-complicated perturbative calculations in order to match to other schemes in the continuum. Matching calculations from X-space schemes to $\overline{\mathrm{MS}}$ have been performed for light-quark bilinears [10], heavy-light quark bilinears [11], dimension-5 operators appearing in the energy-momentum tensor [9], and supercurrent operators in supersymmetric theories [12].

When implementing RI-(s)MOM renormalization conditions at momentum p with a lattice discretisation, there is a 'window problem' where $\Lambda_{\mathrm{QCD}} \ll p \ll a^{-1}$ is required to keep all systematic uncertainties under control. Indeed, the RI-SMOM scheme [3] was introduced to remove infrared convergence issues in applications of the original RI-MOM scheme where some momenta were not in the desired range. Here, a is the lattice discretisation-scale that regulates the ultraviolet (UV) behaviour of the theory and Λ_{QCD} is the typical QCD scale that emerges through dimensional transmutation. The same window problem affects any position-space scheme, where $\sqrt{x^2} \ll \Lambda_{\mathrm{QCD}}^{-1}$ is required to control perturbation-theory errors appearing in the perturbative matching to $\overline{\mathrm{MS}}$, and $a \ll \sqrt{x^2}$ is required to control discretisation artifacts. In practice, this window problem must be investigated on a case-by-case basis, and various investigations have been performed in X-space schemes for the local light-quark bilinear operators using Wilson fermions [8, 13], twisted-mass fermions [14], as well as domain-wall fermions [15]. Furthermore, numerical studies of the feasibility of X-space renormalization conditions for renormalizing the QCD energy-momentum tensor [16], heavy-light quark bilinear operators [17], and operators in supersymmetric field theories [18] have been undertaken. There have also been numerical investigations of the possibility of using position-space schemes to match between three and four-flavor QCD [19, 20].

The X-space scheme is particularly suited to renormalizing Heavy Quark Effective Theory (HQET) operators. Choosing a reference frame in which the heavy-quark velocity has spatial components that vanish, $v = (1,0,0,0)^T$, the bare Euclidean propagator for a heavy quark Q in the

---

[3] The non-interacting correlation function in X-space schemes is sometimes referred to as 'tree-level', though this is a misnomer due to the fact that the noninteracting calculation of position-space correlation functions of composite operators involves loops. Note that the superscript labels '(0)' on the operators in the RHS of Eq. (3.5) are redundant as the non-interacting values for the bare and renormalised operators are the same.

static limit is naturally written in position space [21] as

$$\langle Q^{(0)}(0)\overline{Q}^{(0)}(x_E)\rangle_F = \delta_{\vec{x}_E,\vec{0}}\ \theta(-t_E)W^{(0)}(0,x_E)\frac{1+\gamma_0}{2}, \tag{3.6}$$

where $\langle\cdot\rangle_F$ indicates the path integral is performed over all the fermionic degrees of freedom but not the gauge degrees of freedom, and $W^{(0)}(a,b)$ is the bare straight Wilson line from a to b. A complication in lattice regularizations of the static theory is that the static-quark self-energy has a power divergence [22], which is caused by mixing between the kinetic term $\overline{Q}D_0Q$ and a mass-like term $m_{\text{stat}}\overline{Q}Q$, where $m_{\text{stat}} \sim O(\alpha_S)/a$ is radiatively generated. The X-space scheme proposed in this chapter utilizes ratios of three-point to two-point position-space correlation functions to nonperturbatively cancel this power divergence. Nonperturbatively-renormalized matrix-elements of HQET operators can thus be extracted without needing to determine m_{stat} explicitly, which would otherwise constitute another source of uncertainty.

In this chapter, a set of X-space schemes for renormalizing four-quark HQET operators is proposed, and the $O(\alpha_S)$ matching to $\overline{\text{MS}}$ is calculated in the static limit, extending the X-space approach used in Refs. [8, 9, 12]. The first set of operators that are considered are isospin-nonsinglet, four-quark operators $\tau_{ff'}(\overline{Q}\Gamma q_f)(\overline{q}_{f'}\Gamma' Q)$ where Γ,Γ' are spin-colour tensors, $q_f \in \{q_u, q_d\}$ are light-quark fields, and $\tau_{ff'}$ is a Pauli matrix in the light-quark flavor space. In the Heavy Quark Expansion (HQE) formalism, matrix elements of these $\Delta Q = 0$ (heavy-quark flavor preserving) operators are known as 'spectator contributions', and are the dominant $O(1/m_Q^3)$-corrections to the inclusive lifetimes of heavy (charm or bottom) hadrons [23, 24]. The second set of operators that are considered are $\Delta B = 2$ four-quark operators, relevant for determinations of $B-\overline{B}$-mixing [25]. Precise determinations of hadronic matrix-elements of these quantities will allow for better constraints on fundamental parameters of the Standard Model such as the CKM matrix-elements, and will also further constrain extensions of the Standard Model. Existing LQCD studies of these four-quark operators have utilized lattice perturbation-theory to perform matching to $\overline{\text{MS}}$ [26–29], and the nonperturbative renormalization-scheme proposed in this work will allow for more precise LQCD determinations of the renormalized matrix-elements [30].

The four-quark operators studied in this work do not renormalize multiplicatively but rather mix within multiplets of operators with the same quantum numbers, and therefore Eq. (3.5) must be generalized to define a scheme that determines the entire mixing-matrix. In order to provide a sufficient number of renormalization conditions to determine the full mixing-matrix, the X-space scheme proposed here utilize three-point correlation functions involving the four-quark operator with multiple choices of source and sink operators. There are many possibilities but to be concrete the source and sink operators used are heavy-light mesonic operators $\overline{Q}\Gamma q$ and heavy-light-light baryonic operators $\epsilon^{abc}[q^{aT}\Gamma_1 q^b]\Gamma_2 Q^c$ for various choices of the Dirac matrices Γ,Γ_1,Γ_2. Perturbative calculations of two-point correlation functions constructed from these operators have been performed in the literature, and these can be used to determine matching coefficients between X-space schemes and the $\overline{\text{MS}}$ scheme, which are presented to $O(\alpha_S)$ in Sec. 3.1.1. The four-quark operators also mix into evanescent operators (operators that explicitly vanish in $d=4$) in dimensional regularization.

To be able to utilize the X-space scheme as a regulator-independent scheme for conversion of lattice matrix-elements, the scheme is defined in terms of evanescent-subtracted operators. The X-space schemes, and $O(\alpha_S)$-matching to the $\overline{\text{MS}}$ scheme for the isospin non-singlet $\Delta Q = 0$ operators and the $\Delta B = 2$ operators are presented in Sec. 3.2. An overview of the conventions and integration techniques used in this section is given in Appendix B.

3.1 MULTIPLICATIVELY RENORMALIZABLE OPERATORS

Some text in this section reproduced with coauthors' permission from Ref. [31].

3.1.1 X-SPACE SCHEMES FOR HEAVY-LIGHT BILINEAR AND HEAVY-LIGHT-LIGHT TRILINEAR OPERATORS

In this section, the $O(\alpha_S)$ matching-factors between X-space-renormalized operators and $\overline{\text{MS}}$-renormalized operators for heavy-light mesonic, and heavy-light-light baryonic operators in HQET are presented. Choosing the frame in which the static heavy quark propagates purely in the Euclidean time direction, the Euclidean HQET Lagrangian used in the following calculations is given by

$$\mathcal{L} = \frac{1}{4} F_{\mu\nu} F_{\mu\nu} + \sum_{f=\{u,d\}} \overline{q}_f \gamma_\mu D_\mu q_f + \overline{Q} D_0 Q, \tag{3.7}$$

with two massless light-quarks q_u and q_d, and one static heavy-quark Q that satisfies $\frac{1+\gamma_0}{2} Q = Q$. To regulate the continuum theory, dimensional regularization (DR) is used, where $\gamma_5 = \gamma_0\gamma_1\gamma_2\gamma_3$ is treated in the 't Hooft-Veltman (HV) scheme [32]. Due to the heavy-quark term in the action not containing any Dirac matrices, in $d = 4$ there is an $SU(2)_h$ heavy-quark spin symmetry

$$Q \mapsto e^{-i\theta_j \gamma_5 \gamma_j} Q, \quad \overline{Q} \mapsto \overline{Q} e^{i\theta_j \gamma_5 \gamma_j} \tag{3.8}$$

that leaves the action invariant, where $\gamma_j \in \{\gamma_1, \gamma_2, \gamma_3\}$. The resulting effect of this symmetry is that local heavy-light mesonic operators are related by heavy-quark symmetry in the following $SU(2)_h$ doublets:

$$SU(2)_h \begin{cases} H_f^+(0^+) : \overline{q}_f Q \\ H_{f,i}^{*+}(1^+) : \overline{q}_f \gamma_5 \gamma_i Q \end{cases}, \quad SU(2)_h \begin{cases} H_f^-(0^-) : \overline{q}_f \gamma_5 Q \\ H_{f,i}^{*-}(1^-) : \overline{q}_f \gamma_i Q \end{cases}, \tag{3.9}$$

where the J^P quantum numbers of the state are listed along with the corresponding local heavy-light operator. Note that the ± superscripts refer to the parity of the operator, rather than the electromagnetic charge of the state. In Eq. (3.9) and what follows, γ_i indexes the $(d-1)$-dimensional spatial Dirac matrices, such that $\gamma_i \gamma_i = (d-1)\mathbb{1}$.[4] Since the antiparticle is integrated out in HQET,

---

[4] In $d = 4$, where spatial Dirac matrices γ_i take values in $\gamma_i \in \{\gamma_1, \gamma_2, \gamma_3\}$, the heavy-quark spin symmetry is indeed $SU(2)_h$. In dimensional regularization the spatial index i now varies over the $(d-1)$-dimensions that are not timelike, and formally the symmetry group is no longer $SU(2)_h$. This distinction, however, does not have any implications for the calculations presented in this section.

the operators shown in Eq. (3.9) form a basis for the heavy-light bilinear operators with no derivatives in $d = 4$.

The heavy-light-light baryonic operators of the form $\epsilon^{abc}[q^{aT}\tau\Gamma_1 q^b]\Gamma_2 Q^c$ for varying Dirac matrices Γ_1, Γ_2 and isospin matrices τ are also multiplicatively renormalizable. In the following, C is the charge-conjugation matrix satisfying $C\gamma_\mu C^{-1} = -\gamma_\mu^T$, with an explicit construction in dimensional regularization given in Sec. 2.1.3. The isospin matrices are written in terms of the antisymmetric τ^A or symmetric τ^S_α matrices

$$\tau^A := \begin{pmatrix} 0 & 1 \\ -1 & 0 \end{pmatrix}, \quad \tau^S_1 := \begin{pmatrix} 1 & 0 \\ 0 & 0 \end{pmatrix}, \quad \tau^S_0 := \frac{1}{\sqrt{2}}\begin{pmatrix} 0 & 1 \\ 1 & 0 \end{pmatrix}, \quad \tau^S_{-1} := \begin{pmatrix} 0 & 0 \\ 0 & 1 \end{pmatrix}. \tag{3.10}$$

Operators coupling to Λ_Q baryons (isospin singlets) are given by

$$\begin{aligned}
&\Lambda_1\left(\tfrac{1}{2}^+\right) : \epsilon^{abc}[q^{aT}\tau^A C\gamma_5 q^b]Q^c, \\
&\Lambda_2\left(\tfrac{1}{2}^+\right) : \epsilon^{abc}[q^{aT}\tau^A C\gamma_5\gamma_0 q^b]Q^c, \\
&\Lambda_1^-\left(\tfrac{1}{2}^-\right) : \epsilon^{abc}[q^{aT}\tau^A C q^b]Q^c, \\
SU(2)_h &\left\{\begin{array}{l} \Lambda_2^-\left(\tfrac{1}{2}^-\right) : \epsilon^{abc}[q^{aT}\tau^A C\gamma_5\gamma_i q^b]\gamma_i\gamma_5 Q^c, \\ \Lambda_i^{*-}\left(\tfrac{3}{2}^-\right) : \epsilon^{abc}[q^{aT}\tau^A C\gamma_5\gamma_i q^b]Q^c - \tfrac{1}{3}\epsilon^{abc}[q^{aT}\tau^A C\gamma_5\gamma_j q^b]\gamma_i\gamma_j Q^c. \end{array}\right.
\end{aligned} \tag{3.11}$$

The operators are labelled by their angular momentum representation and parity, J^P. The $SU(2)_h$-doublet $\{\Lambda_2^-, \Lambda_i^{*-}\}$ arises from decomposing the tensor product of a spin-1 light-quark doublet with the spin-$\frac{1}{2}$ heavy quark into irreducible spin representations. In particular, spin-$\frac{3}{2}$ operators such as Λ_i^{*-} satisfy the condition $\gamma_i\Lambda_i^{*-} = 0$ in $d = 4$. Operators coupling to Σ_Q-baryons which transforms in the isospin-triplet representation, are given by

$$\begin{aligned}
SU(2)_h &\left\{\begin{array}{l} \Sigma_{1,\alpha}\left(\tfrac{1}{2}^+\right) : \epsilon^{abc}[q^{aT}\tau^S_\alpha C\gamma_i q^b]\gamma_i\gamma_5 Q^c, \\ \Sigma^*_{1,\alpha,i}\left(\tfrac{3}{2}^+\right) : \epsilon^{abc}[q^{aT}\tau^S_\alpha C\gamma_i q^b]Q^c - \tfrac{1}{3}\epsilon^{abc}[q^{aT}\tau_A C\gamma_j q^b]\gamma_i\gamma_j Q^c, \end{array}\right. \\
SU(2)_h &\left\{\begin{array}{l} \Sigma_{2,\alpha}\left(\tfrac{1}{2}^+\right) : \epsilon^{abc}[q^{aT}\tau^S_\alpha C\gamma_0\gamma_i q^b]\gamma_i\gamma_5 Q^c, \\ \Sigma^*_{2,\alpha,i}\left(\tfrac{3}{2}^+\right) : \epsilon^{abc}[q^{aT}\tau^S_\alpha C\gamma_0\gamma_i q^b]Q^c - \tfrac{1}{3}\epsilon^{abc}[q^{aT}\tau^S_\alpha C\gamma_0\gamma_j q^b]\gamma_i\gamma_j Q^c, \end{array}\right. \\
SU(2)_h &\left\{\begin{array}{l} \Sigma^-_{1,\alpha}\left(\tfrac{1}{2}^-\right) : \epsilon^{abc}[q^{aT}\tau^S_\alpha C\gamma_5\gamma_0\gamma_i q^b]\gamma_i\gamma_5 Q^c, \\ \Sigma^{*-}_{1,\alpha,i}\left(\tfrac{3}{2}^-\right) : \epsilon^{abc}[q^{aT}\tau^S_\alpha C\gamma_5\gamma_0\gamma_i q^b]Q^c - \tfrac{1}{3}\epsilon^{abc}[q^{aT}\tau^S_\alpha C\gamma_5\gamma_0\gamma_j q^b]\gamma_i\gamma_j Q^c, \end{array}\right. \\
&\Sigma^-_{2,\alpha}\left(\tfrac{1}{2}^-\right) : \epsilon^{abc}[q^{aT}\tau^S_\alpha C\gamma_0 q^b]Q^c,
\end{aligned} \tag{3.12}$$

where α is the isospin index and i is the vector index of the spin-$\frac{3}{2}$ field. The operators in Eqs. (3.11) and (3.12) form a complete basis in $d = 4$ for local HQET heavy-light-light currents with no derivatives, of which the positive-parity local operators were previously classified in Refs [33, 34].

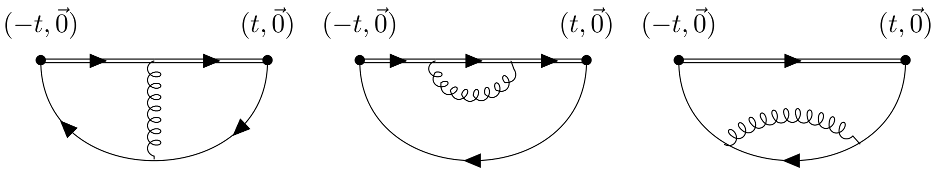

Figure 3.1: Diagrams for the $O(\alpha_S)$ contributions to the two-point position space correlator shown in Eq. (3.13), when $\mathcal{O}$ is one of the heavy-light currents listed in Eq. (3.9). The operator insertions are represented by the filled in dots in the diagrams above. Feynman rules are derived from Eq. (3.7), double lines refer to the static-quark propagator, single lines are light-quark propagators, and curly lines are gluons. The unlabelled positions of the interaction vertices are integrated over. The diagrams in order are referred to as $D_1^{HL}, D_1^{HH}, D_1^{LL}$.

The X-space scheme for multiplicatively-renormalizable currents is specified at a renormalization scale t^{-1} by the following condition:

$$\left\langle \mathcal{O}^{\dagger(R,X)}\left(-t,\vec{0}\right)\mathcal{O}^{(R,X)}\left(t,\vec{0}\right)\right\rangle = \left\langle \mathcal{O}^{\dagger(0)}\left(-t,\vec{0}\right)\mathcal{O}^{(0)}\left(t,\vec{0}\right)\right\rangle\Big|_{\mathrm{NI}}, \tag{3.13}$$

where R is a regulator (either DR or the lattice regulator), and X specifies the operators are renormalized in the X-space scheme. The subscript NI on the right-hand side of Eq. (3.13) refers to the non-interacting value of the correlator. If the operator has additional indices (such as isospin triplet indices α in the case of the Σ-interpolating operators in Eq. (3.12), or spatial gamma-matrix indices i) these additional indices are summed over on both sides of the renormalization condition. For example, in the 1^- mesonic channel (the B^* mesons if Q is a bottom quark), the renormalization condition is

$$\sum_i \left\langle (\overline{q}\gamma_i Q)^{\dagger(R,X)}\left(-t,\vec{0}\right)(\overline{q}\gamma_i Q)^{(R,X)}\left(t,\vec{0}\right)\right\rangle = \sum_i \left\langle (\overline{q}\gamma_i Q)^{(0)\dagger}\left(-t,\vec{0}\right)(\overline{q}\gamma_i Q)^{(0)}\left(t,\vec{0}\right)\right\rangle\Big|_{\mathrm{NI}}. \tag{3.14}$$

Furthermore, the open Dirac indices of the static heavy-quark and heavy anti-quark in the baryonic operators are traced over.

The position-space diagrams that contribute to the $O(\alpha_S)$ determination of the two-point correlation function for the heavy-light currents are shown in Fig. 3.1. Although chiral symmetry is broken by the HV-prescription for γ_5, the massless nature of the light quark still has consequences for the symmetries present in the renormalization factors. In particular, the specific Γ-matrix appearing in the interpolating operator $\mathcal{O} = \overline{q}\Gamma Q$ only affects the two-point correlation function by a constant factor, as the correlation function (to any order in α_S) has the form

$$\begin{aligned}\left\langle\left(\overline{Q}^{(\mathrm{DR},0)}\overline{\Gamma}q^{(\mathrm{DR},0)}\right)(-t,\vec{0})\ \left(\overline{q}^{(\mathrm{DR},0)}\Gamma Q^{(\mathrm{DR},0)}\right)(t,\vec{0})\right\rangle &= A\ \mathrm{Tr}\left(\frac{1+\gamma_0}{2}\overline{\Gamma}\gamma_0\Gamma\right)\\ &= AP\ \mathrm{Tr}\left(\frac{1+\gamma_0}{2}\overline{\Gamma}\Gamma\right),\end{aligned} \tag{3.15}$$

where A is a constant that does not depend on Γ, $P \in \{-1, +1\}$ is the parity of the state ($\gamma_0\Gamma = P\Gamma\gamma_0$), and $\overline{\Gamma} = \gamma_0\Gamma^\dagger\gamma_0$. This is because of the fact that regardless of the number of gluons attached to the light-quark line in the two-point correlation function, there are always an odd number of γ-matrices inserted (one for each massless propagator and one for each vertex). For example, shown below is the case with three gluons attached to the light quark:

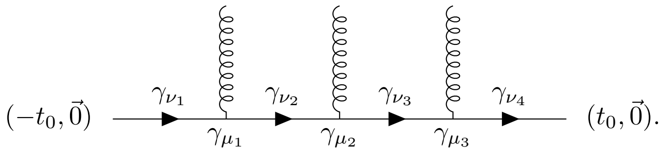

The only four-vector available for contraction is the purely timelike heavy-quark velocity v; thus, after performing integration over loop momenta and Fourier transforming to position space, the light-quark line is proportional to $\not{v} = \gamma_0$. The result of Eq. (3.15) is that all heavy-light operators $\bar{q}\Gamma Q$ renormalize multiplicatively with the same factor to all orders of α_S in the X-space scheme, regardless of the choice of Γ.

The diagrams in Fig. 3.1 can be computed by first calculating the corresponding two-loop momentum-space diagrams (also known as p-type integrals [35]) and taking a Fourier transform; further details of this computation are given in Sec. 3.1.2. In this section, the main results for the heavy-light and heavy-light-light operators are discussed. Writing $(\bar{q}\Gamma Q)^{(\mathrm{DR},S)} = Z^{(\mathrm{DR},S)}_{(\bar{q}\Gamma Q)}(\bar{q}^{(0)}\Gamma Q^{(0)})$ for the heavy-light currents (where S is a choice of renormalization scheme), the X-space renormalization factors are given by[5]

$$Z^{(\mathrm{DR},X)}_{(\bar{q}\Gamma Q)}(t,\mu) = 1 - \frac{\alpha_S(\mu)}{\pi\epsilon} - \frac{\alpha_S(\mu)}{\pi}\left(\frac{4}{3} + \frac{2\pi^2}{9} + \frac{1}{2}\log\left(4\pi e^{\gamma_E}\mu^2 t^2\right)\right) \tag{3.16}$$

in $d = 4 - \epsilon$ dimensions. Here, μ is the scale obtained after writing the renormalized coupling-constant as a dimensionless object $g^{(\mathrm{DR},\overline{\mathrm{MS}})} = \frac{1}{Z_g}\mu^{-\frac{\epsilon}{2}}g^{(0)}$, where $\alpha_S := \frac{(g^{(\mathrm{DR},\overline{\mathrm{MS}})})^2}{4\pi}$, and γ_E is the Euler-Mascheroni constant. It is possible to define an X-space scheme strong coupling $\alpha_S^{(\mathrm{DR},X)}$ (for example by fixing the two-point correlation function for the gluon correlator), but this work focuses on the matching of composite operators between X-space schemes and $\overline{\mathrm{MS}}$, and hence the α_S that is used is always renormalized in $\overline{\mathrm{MS}}$ at scale μ. The $\overline{\mathrm{MS}}$ renormalization factor

$$Z^{(\mathrm{DR},\overline{\mathrm{MS}})}_{(\bar{q}\Gamma Q)}(\mu) = 1 - \frac{\alpha_S(\mu)}{\pi\epsilon} - \frac{\alpha_S(\mu)}{2\pi}\log(4\pi e^{-\gamma_E}), \tag{3.17}$$

can be read off from Eq. (3.16) as the $\frac{1}{\epsilon}$ piece and the corresponding $\overline{\mathrm{MS}}$ logarithms. Comparing this to Eq. (3.16), note that the $\overline{\mathrm{MS}}$-counterterm contains factors of $+\frac{\alpha_S\gamma_E}{\pi}$, whereas the X-space counterterm contains corresponding factors of $-\frac{\alpha_S\gamma_E}{\pi}$. The difference in sign arises from the d-dimensional Fourier transform of the logarithmic structure [10]. This causes the conversion factor

---

[5] $O(\alpha_S^2)$ calculations of the two-point position-space correlation function of heavy-light currents can be found in Ref [11].

$\mathcal{O}$	$C_{1,\mathcal{O}}$	$C_{2,\mathcal{O}}$
Λ_1	$\frac{17}{6}$	2
Λ_2	$\frac{9}{4}$	1
$\Sigma_{1,\alpha}, \Sigma^*_{1,\alpha,i}$	$\frac{19}{12}$	1
$\Sigma_{2,\alpha}, \Sigma^*_{2,\alpha,i}$	$\frac{11}{6}$	$\frac{2}{3}$

$\mathcal{O}$	$C_{1,\mathcal{O}}$	$C_{2,\mathcal{O}}$
Λ_1^-	$\frac{3}{2}$	2
$\Lambda_2^-, \Lambda_1^{*-}$	$\frac{9}{4}$	1
$\Sigma^-_{2,\alpha}$	$\frac{19}{12}$	1
$\Sigma^-_{1,\alpha}, \Sigma^{*-}_{1,\alpha,i}$	$\frac{11}{6}$	$\frac{2}{3}$

Table 3.1: $O(\alpha_S)$ conversion factors from X-space renormalized operators to $\overline{\text{MS}}$-renormalized operators, for the different heavy-light-light baryonic operators. Refer to Eq. (3.19) for definitions of $C_{1,\mathcal{O}}, C_{2,\mathcal{O}}$. The two-point functions of the positive-parity heavy-light-light currents have previously been computed in the context of QCD sum rules [34].

$\mathcal{O}^{(\text{DR},\overline{\text{MS}})} = C^{(\text{DR},\overline{\text{MS}};\text{DR},X)}(t,\mu)\mathcal{O}^{(\text{DR},X)}(t)$ between X-space and $\overline{\text{MS}}$ to contain γ_E factors:

$$C^{(\text{DR},\overline{\text{MS}};\text{DR},X)}_{(\overline{q}\Gamma Q)}(t,\mu) = \frac{Z^{(\text{DR},\overline{\text{MS}})}_{(\overline{q}\Gamma Q)}(\mu)}{Z^{(\text{DR},X)}_{(\overline{q}\Gamma Q)}(t,\mu)} = 1 + \frac{\alpha_S(\mu)}{\pi}\left(\frac{4}{3} + \frac{2\pi^2}{9} + \frac{1}{2}\log\left(e^{2\gamma_E}\mu^2 t^2\right)\right). \tag{3.18}$$

In numerical studies utilizing X-space schemes, μ should be varied to provide an indication of the size of the error caused by truncating the perturbative series. A natural candidate for a central value of μ is given by the condition $\mu^2 = e^{-2\gamma_E}t^{-2}$ which would cancel the logarithm that appears in the matching factor.

For the heavy-light-light baryons, the $O(\alpha_S)$ conversion factors can be parametrized similarly as

$$C^{(\text{DR},\overline{\text{MS}};\text{DR},X)}_{\mathcal{O}}(t,\mu) = \frac{Z^{(\text{DR},\overline{\text{MS}})}_{\mathcal{O}}(\mu)}{Z^{(\text{DR},X)}_{\mathcal{O}}(t,\mu)} = 1 + \frac{\alpha_S}{\pi}\left(C_{1,\mathcal{O}} + \frac{2\pi^2}{9} + \frac{C_{2,\mathcal{O}}}{2}\log(e^{2\gamma_E}\mu^2 t^2)\right), \tag{3.19}$$

where the coefficients $C_{1,\mathcal{O}}, C_{2,\mathcal{O}}$ are given in Table 3.1 for $\mathcal{O}$ taken from Eqs. (3.11) and (3.12).[6] The calculations of the conversion factors proceed similarly to those for the heavy-light mesonic operators, by evaluating the baryonic analogues to the diagrams appearing in Fig. 3.1.

3.1.2 CALCULATION PROCEDURE FOR $O(\alpha_S)$ TWO-POINT MATCHING CALCULATION

In this subsection, a detailed calculation is presented for the heavy-light two point correlation function $\langle(\overline{Q}\Gamma_L q)(t)(\overline{q}\Gamma_R Q)(0)\rangle$, corresponding to the diagrams shown in Fig. 3.1. The calculations needed for the two-point baryonic correlation function are similar, only requiring different contractions at the source and the sink, which were implemented in Mathematica[36]. A computational

---

[6] Note that $Z^{(\text{DR},\text{MS})}_{\mathcal{O}}$ (which contains only the $\frac{1}{\epsilon}$ piece) can be read off as $Z^{(\text{DR},\text{MS})}_{\mathcal{O}} = \frac{-\alpha_S}{\pi\epsilon}C_{2,\mathcal{O}}$ as the γ_E factors are directly proportional to the $\frac{1}{\epsilon}$ pole.

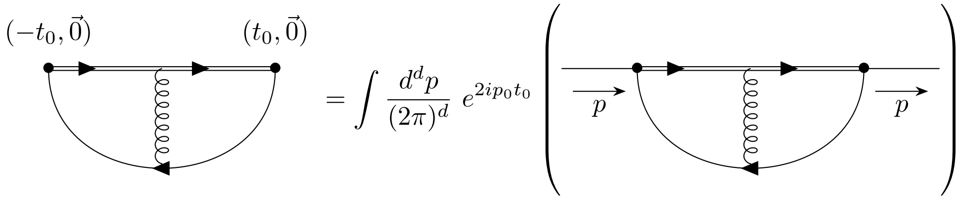

Figure 3.2: Example showing how the Fourier-transform relates a position-space diagram appearing in the $\langle \overline{Q}\Gamma q(t_0, \vec{0})(\overline{q}\Gamma Q)(-t_0, \vec{0})\rangle$ two-point correlation function to the corresponding momentum-space diagram.

difficulty with using position-space schemes is that even at tree-level, position-space correlation functions involve loop calculations. In the case of the two-point mesonic correlation function, the answer can be derived by utilising the position-space propagators Eqs. (2.10) and (2.13) (where the loop integral has been relegated to the Fourier transform used to derive the position-space propagators):

$$\begin{aligned} D_0(\Gamma_L, \Gamma_R) &= -N_C \mathrm{Tr}\left[[D_H^{-1}(-x_0)]\Gamma_L[D_L^{-1}(x_0)]\Gamma_R\right] \\ &= N_C \mathrm{Tr}\left[\frac{1+\not{v}}{2}\Gamma_L \not{v} \Gamma_R\right] \frac{i\Gamma(\frac{d}{2})x}{2\pi^{\frac{d}{2}}(-x^2)^{\frac{d}{2}}} \end{aligned} \tag{3.20}$$

Note that in dimensional regularisation, since the mass dimensions $[\psi] = [Q] = \frac{d-1}{2}$, even at tree level the position-space correlator will have d-dependence. For the two-loop $O(\alpha_S)$ diagrams listed in Fig. 3.1, a key observation is that the position-space calculation can be related to a momentum-space calculation via a fourier-transform, as shown for D_1^{HL} in Fig. 3.2. In momentum space, a new type of integral is required:

$$\begin{aligned} &(-v\cdot p)^{d-n_1-n_2-2n_3-2n_4-2n_5}\overline{I}(n_1, n_2, n_3, n_4, n_5) := \\ &\int \frac{d^dk_L d^dk_R}{(2\pi)^{2d}} \frac{1}{(v\cdot(p+k_L))^{n_1}(v\cdot(p+k_R))^{n_2}(-k_L^2)^{n_3}(-k_R^2)^{n_4}(-(k_L-k_R)^2)^{n_5}} \end{aligned} \tag{3.21}$$

corresponding to the schematic drawing showing the relation of the different n_i indices as momentum flows, static quarks as double lines and massless quarks as single lines:

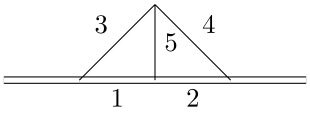

(3.22)

This integral is symmetric under swapping n_1 with n_2 and n_3 with n_4 at the same time. It satisfies the base conditions:

$$\overline{I}(n_1, n_2, n_3, n_4, 0) = \overline{I}_{HL}(n_1, n_3)\overline{I}_{HL}(n_2, n_4) \tag{3.23}$$

$$\overline{I}(0, n_2, n_3, n_4, n_5) = \overline{I}_{LL}(n_3, n_5)\overline{I}_{HL}\left(n_2, n_4+n_3+n_5-\frac{d}{2}\right) \tag{3.24}$$

$$\overline{I}(n_1, n_2, 0, n_4, n_5) = \overline{I}_{HL}(n_1, n_5)\overline{I}_{HL}(n_2+n_1+2n_5-d, n_4) \tag{3.25}$$

in terms of the integrals I_{LL}, I_{HL} introduced in Sec. 2.1.2 and tabulated in Appendix B. These base conditions are derived by noticing that setting one of the n_i values to zero effectively contracts the diagram in such a way that there is always an independent sub-diagram that can be computed. To simplify the integral in the case that all the $n_i > 0$, one can utilise Integration-by-Parts (IBP) relations, where the trick is to notice that the dimensionally regulated integral of a total derivative is zero. In the case of this two-loop integral, one particular relation for example is given by:

$$\int \frac{d^d k_L d^d k_R}{(2\pi)^{2d}} \partial^{\mu}_{k_L} \left[\frac{k^{\mu}_L}{(v\cdot(p+k_L))^{n_1}(v\cdot(p+k_R))^{n_2}(-k_L^2)^{n_3}(-k_R^2)^{n_4}(-(k_L-k_R)^2)^{n_5}} \right] = 0 \tag{3.26}$$

By expanding out the action of the ∂_{k_L} on the inserted numerator and each denominator factor, one finds:

$$\begin{aligned} &\int \frac{d^d k_L d^d k_R}{(2\pi)^{2d}} \frac{d - n_1\left(1 - \frac{v\cdot p}{v\cdot(p+k_L)}\right) - 2n_3 - n_5\left(1 + \frac{-k^2}{-(k_L-k_R)^2} - \frac{-k_R^2}{-(k_L-k_R)^2}\right)}{(v\cdot(p+k_L))^{n_1}(v\cdot(p+k_R))^{n_2}(-k_L^2)^{n_3}(-k_R^2)^{n_4}(-(k_L-k_R)^2)^{n_5}} \\ &= \left(d - n_1(1+\mathbf{1}^+) - 2n_3 - n_5\left(1 + \mathbf{3}^+\mathbf{5}^- - \mathbf{4}^+\mathbf{5}^-\right)\right)\overline{I}(n_1,n_2,n_3,n_4,n_5) = 0 \end{aligned} \tag{3.27}$$

where the bolded number operators act by increasing/decreasing the arguments to the $\overline{I}$ function whilst maintaining its dimensionlessness, for example:

$$\mathbf{3}^{\pm}\overline{I}(n_1,n_2,n_3,n_4,n_5) = (-v\cdot p)^{\pm 2}\overline{I}(n_1,n_2,n_3\pm 1,n_4,n_5) \tag{3.28}$$

the ±2 in this case because n_3 corresponds to a light propagator that has mass dimension $[-2]$. Note that the leading d in Eq. (3.27) comes from the $\partial^{\mu}_{k_L} k^{\mu}_L = d$. In general, a whole suite of IBP-formulas can be derived by taking derivatives with respect to either of the loop-integrals multiplied by some internal momentum scale. For example, applying the $\partial_{k_L}\cdot k_R$ to the integrand gives the IBP relation:

$$\left(-n_1\mathbf{1}^+(1+\mathbf{2}^-) - n_3\mathbf{3}^+(\mathbf{5}^- - \mathbf{3}^- - \mathbf{4}^-) + n_5\left(1 + \mathbf{4}^+\mathbf{5}^- - \mathbf{3}^+\mathbf{5}^-\right)\right)\overline{I}(n_1,n_2,n_3,n_4,n_5) = 0 \tag{3.29}$$

These different IBP relations become important cross-checks in the computational implementation of these multiloop integrals. The particular linear combination $\partial_{k_3}(k_3 - k_4)$ gives a particularly simple relation:

$$(d - n_1 - n_3 - 2n_5 + n_1\mathbf{1}^+\mathbf{2}^- + n_3\mathbf{3}^+(\mathbf{5}^- - \mathbf{4}^-))\overline{I}(n_1,n_2,n_3,n_4,n_5) = 0 \tag{3.30}$$

which can be rearranged to give:

$$\overline{I}(n_1,n_2,n_3,n_4,n_5) = \frac{-n_1\mathbf{1}^+\mathbf{2}^- - n_3\mathbf{3}^-(\mathbf{5}^- - \mathbf{4}^-)}{d - n_1 - n_3 - 2n_5}\overline{I}(n_1,n_2,n_3,n_4,n_5) \tag{3.31}$$

Applying this equation will lower one of the arguments n_2, n_4 or n_5, allowing one to reduce the case with general arguments to a base case. This general strategy of applying IBP relations, and reducing the tensors that appear in the numerator into structures that look like the propagators in the denominator, is known as Laporta's algorithm [37].

To calculate the diagrams D_1^{HL}, D_1^{HH} and D_1^{LL}, firstly each diagram must be decomposed into evaluations of the master integral $\overline{I}(n_1, \ldots, n_5)$. In general, each of the diagrams will have a tensor-decomposition of the form $I^{\alpha_1\alpha_2\cdots}G^{\alpha_1\alpha_2\cdots}$, where the I-tensor is the loop integration over only the propagators and momentum factors, and the G-tensor indicates some external Dirac structures that the result is contracted against. The loop-integral tensor will have a decomposition into:

$$I^{\alpha_1\alpha_2\cdots} = (g_{\alpha_1\alpha_2}\cdots)I_0 + (v_{\alpha_1}v_{\alpha_2}\cdots)I_1 + \cdots =: \sum_i T_i^{\alpha_1\alpha_2\cdots}I_i, \tag{3.32}$$

where in the case of these HQET diagrams the only tensors available are $g^{\mu\nu}$ and v^{μ}. The sum over index i in Eq. (3.32) decomposes the integral into all possible combinations of $g^{\mu\nu}$ and v^{μ} that match the number of indices that the I-tensor has. To solve for the I_i, note that $T_i^{\alpha_1\alpha_2\cdots}I^{\alpha_1\alpha_2\cdots}$ can be computed as a scalar integral, as the numerator will then become some combination of scalars and raising/lowering operators of the form $\mathbf{1}^-, \mathbf{2}^-, \cdots$. Then:

$$I_i = (T^{\alpha_1\alpha_2\cdots}T^{\alpha_1\alpha_2\cdots})^{-1}_{ij}\left(T_j^{\alpha_1\alpha_2\cdots}I^{\alpha_1\alpha_2\cdots}\right) \tag{3.33}$$

To see this in action, consider the D_1^{HL} diagram:

$$\begin{aligned}
D_1^{\mathrm{HL}}(\Gamma_L, \Gamma_R) =& - \mu^{4-d}\int \frac{d^dp}{(2\pi)^d}e^{-ix_0p}\int \frac{d^dk_1 d^dk_2}{(2\pi)^{2d}}\mathrm{Tr}\Bigg(\frac{1+\not{v}}{2}\frac{i}{v\cdot(k_2+p)}(igv^{\mu}T^A) \\
& \frac{i}{v\cdot(k_1+p)}\Gamma_L\frac{i}{\not{k}_1}(ig\gamma^{\mu}T^A)\frac{i}{\not{k}_2}\Gamma_R\Bigg)\frac{-i}{(k_1-k_2)^2} \\
=& - iC_FN_c\mu^{4-d}\int\frac{d^dp}{(2\pi)^d}e^{-ix_0p}\mathrm{Tr}\left(\frac{1+\not{v}}{2}\Gamma_L\gamma^{\nu}\not{v}\gamma^{\rho}\Gamma_R\right) \\
& \left[\int\frac{d^dk_1d^dk_2}{(2\pi)^{2d}}\frac{k_1^{\nu}k_2^{\rho}}{(k_1-k_2)^2k_1^2k_2^2(v\cdot(k_2+p))(v\cdot(k_1+p))}\right]
\end{aligned} \tag{3.34}$$

Labelling the integral surrounded by square braces as $I^{\nu\rho}$, note that:

$$\begin{aligned}
I^{\nu\rho} &= g^{\nu\rho}I_0 + v^{\nu}v^{\rho}I_1 = g^{\nu\rho}\left(\frac{1}{d-1}I^{\alpha\alpha} - \frac{1}{d-1}v_{\alpha}v_{\beta}I^{\alpha\beta}\right) + v^{\nu}v^{\rho}\left(-\frac{1}{d-1}I^{\alpha}_{\alpha} + \frac{d}{d-1}v_{\alpha}v_{\beta}I^{\alpha\beta}\right) \\
I^{\alpha\alpha} &= \frac{1}{2}\left(\mathbf{3}^- + \mathbf{4}^- - \mathbf{5}^-\right), \quad v_{\alpha}v_{\beta}I^{\alpha\beta} = \mathbf{1}^-\mathbf{2}^- + \mathbf{1}^- + \mathbf{2}^- + 1
\end{aligned} \tag{3.35}$$

Note that also:

$$g^{\nu\rho}(\gamma^{\nu}\not{v}\gamma^{\rho}) = (2-d)\not{v}, \quad v^{\nu}v^{\rho}(\gamma^{\nu}\not{v}\gamma^{\rho}) = \not{v} \tag{3.36}$$

so that:

$$\begin{aligned}
D_1^{\mathrm{HL}} =& - iC_FN_c\mu^{4-d}D_H^{-1}(-x_0, -2d+6)e^{-i\pi(2d-6)}\mathrm{Tr}\left(\frac{1+\not{v}}{2}\Gamma_L\not{v}\Gamma_R\right) \\
& \left(2 + 2\cdot\mathbf{1}^- + 2\cdot\mathbf{2}^- + 2\cdot\mathbf{1}^-\mathbf{2}^- - \frac{1}{2}\mathbf{3}^- - \frac{1}{2}\mathbf{4}^- + \frac{1}{2}\mathbf{5}^-\right)\overline{I}(1,1,1,1,1)
\end{aligned} \tag{3.37}$$

Completing the integral, we have:

$$D_1^{\mathrm{HL}} = \frac{D_0C_F\alpha_S}{\pi\epsilon} + \frac{D_0C_F\alpha_S}{6\pi}\left(6 + 3\gamma_E + 2\pi^2 + 3\log\pi + 3\log(-x^2\mu^2)\right). \tag{3.38}$$

The diagram in Fig. 3.1 with a gluon attached to the heavy line is slightly simpler, since the momentum integral has a single tensor index which must be contracted against v^μ. The diagram yields:

$$\begin{aligned}
D_1^{\mathrm{HH}} =& - \int \frac{d^d p}{(2\pi)^d} e^{-ix_0 p} \int \frac{d^d k_1 d^d k_2}{(2\pi)^d} \mathrm{Tr}\Bigg(\frac{1+\not{v}}{2} \frac{i}{v\cdot(k_1+p)} (igv^\mu T^a) \frac{i}{v\cdot(k_2+p)} \\
& (igv^\mu T^a) \frac{i}{v\cdot(k_1+p)} \Gamma_L \frac{i}{\not{k}_1} \Gamma_R \Bigg) \frac{-i}{(k_2-k_1)^2} \\
=& - iC_F N_c \int \frac{d^d p}{(2\pi)^d} e^{-ix_0 p} \int \frac{d^d k_1 d^d k_2}{(2\pi)^{2d}} \frac{k_1^\nu}{(v\cdot(k_1+p))^2 (v\cdot(k_2+p)) k_1^2 (k_2-k_1)^2} \mathrm{Tr}\left(\frac{1+\not{v}}{2} \Gamma_L \gamma^\nu \Gamma_R \right) \\
=& - iC_F N_c D_H^{-1}(-x_0, -2d+6) e^{-i\pi(2d-6)} \left(\mathbf{1}^- + 1\right) \tilde{I}(2,1,1,0,1) \mathrm{Tr}\left(\frac{1+\not{v}}{2} \Gamma_L \not{v} \Gamma_R \right) \\
=& \frac{D_0 C_F \alpha_S}{\pi\epsilon} + \frac{D_0 C_F \alpha_S}{2\pi} \left(2 + \gamma_E + \log\pi + \log(-\mu^2 x^2)\right).
\end{aligned} \tag{3.39}$$

And finally, the diagram in Fig. 3.1 with a gluon attached to the light-quark line gives:

$$\begin{aligned}
D_1^{LL} =& - \int \frac{d^d p}{(2\pi)^d} e^{-ix_0 p} \int \frac{d^d k_1 d^d k_2}{(2\pi)^d} \mathrm{Tr}\left(\frac{1+\not{v}}{2} \frac{i}{v\cdot(k_1+p)} \Gamma^\mu \frac{i}{\not{k}_1} (ig\gamma^\mu T^a) \frac{i}{\not{k}_2} (ig\gamma^\mu T^a) \frac{i}{\not{k}_1} \Gamma^\mu \right) \frac{-i}{(k_2-k_1)^2} \\
=& - iC_F N_c \int \frac{d^d p}{(2\pi)^d} e^{-ix_0 p} \int \frac{d^d k_1 d^d k_2}{(2\pi)^{2d}} \frac{k_1^\alpha k_2^\beta k_1^\rho}{v\cdot(k_1+p) k_1^4 k_2^2 (k_2-k_1)^2} \mathrm{Tr}\left(\frac{1+\not{v}}{2} \Gamma_L \gamma^\alpha \gamma^\nu \gamma^\beta \gamma^\nu \gamma^\rho \Gamma_R \right).
\end{aligned} \tag{3.40}$$

Note that the same strategy of decomposing the momentum integral would still work in this case, however the integral is now a five-index tensor which is slightly more complicated. In this particular situation however, the γ-matrices simplify:

$$\begin{aligned}
\gamma_\alpha \gamma_\nu \gamma_\beta \gamma_\nu \gamma_\rho &= (2-d)(g_{\alpha\beta}\gamma_\rho + g_{\beta\rho}\gamma_\alpha - g_{\alpha\rho}\gamma_\beta) \\
&\to (2-d)\left[(-\mathbf{5}^- + \mathbf{3}^- + \mathbf{4}^-)(\mathbf{1}^- + 1) - \mathbf{3}^-(\mathbf{2}^- + 1)\right],
\end{aligned} \tag{3.41}$$

where the $\epsilon_{\alpha\beta\gamma\rho}$ term is dropped because it vanishes after contraction, and expressed the rest in terms of raising/lowering operators gives the answer:

$$D_1^{LL} = -\frac{D_0 C_F \alpha_S}{2\pi\epsilon} - \frac{D_0 C_F \alpha_S}{4\pi}(\gamma_E + \log\pi + \log(-\mu^2 x^2)). \tag{3.42}$$

Summing these three contributions recovers the result presented in Eq. (3.16).

3.1.3 Decay constants

The renormalization conditions presented in this section are not directly applicable to two-point correlation functions computed with the static heavy-quark action in Lattice-HQET as $\mathcal{O}^{(\mathrm{DR},X)}(t) \neq \mathcal{O}^{(\mathrm{lat},X)}(t)$. The reason for this disagreement is that the lattice regulator introduces a power-divergent mixing between the static kinetic operator $\overline{Q}D_0Q$ and a radiatively generated mass-term

$m_{\text{stat}}\overline{Q}Q$ where $m_{\text{stat}} \sim O(\alpha_S)/a$. The relationship between matrix elements of the operators renormalized in the two different regulators is

$$\langle\cdots|\mathcal{O}^{(\text{lat},X)}(t)|\cdots\rangle = e^{m_{\text{stat}}t}\langle\cdots|\mathcal{O}^{(\text{DR},X)}(t)|\cdots\rangle, \tag{3.43}$$

where $|\cdots\rangle$ represents arbitrary states. Without an additional renormalization condition that can be used to extract m_{stat}, it is not possible to match matrix elements of $\mathcal{O}^{(\text{lat},X)}$ to matrix elements in continuum renormalization schemes.

Since the self-energy power divergence affects all the two-point correlation functions discussed in this section in the same fashion, it is, however, possible to take ratios to cancel this self-energy divergence rather than computing it. As an example application, consider the following QCD matrix elements:

$$\langle 0|(\overline{q}_f\gamma_\mu\gamma_5 b)^{(\text{DR},\overline{\text{MS}})}|\overline{B}_f(p)\rangle = ip_\mu f_{B_f}^{\overline{\text{MS}}}, \tag{3.44}$$

$$\langle 0|\left(\epsilon^{abc}[q^{aT}\tau_A C\gamma_5 q^b]\tfrac{1+\gamma_0}{2}b^c_\alpha\right)^{(\text{DR},\overline{\text{MS}})}|\Lambda_b(p,s)\rangle = im_{\Lambda_b}N_\alpha(p,s)f^{\overline{\text{MS}}}_{\Lambda_{b,1}}, \tag{3.45}$$

where b is a (relativistic) bottom quark field, p_μ is a Euclidean four-momentum, s is the spin of the Λ_b-baryon, and N_α is the baryon Dirac spinor satisfying $\overline{N}(p,s)N(p,s') = 2m_{\Lambda_b}\delta_{ss'}$. Here, f_{B_f} is the mesonic decay-constant, and $f_{\Lambda_{b,1}}$ is the normalization constant for one of the distribution amplitudes of the Λ_b baryon [38]. The states in Eqs. (3.44) and (3.45) have standard relativistic normalization

$$\langle\overline{B}_f(p')|\overline{B}_f(p)\rangle = 2E_{\overline{B}_f(p)}(2\pi)^3\delta^3(\vec{p}-\vec{p}'), \tag{3.46}$$

$$\langle\Lambda_b(p',s')|\Lambda_b(p,s)\rangle = 2\delta_{ss'}E_{\Lambda_b(p,s)}(2\pi)^3\delta^3(\vec{p}-\vec{p}'). \tag{3.47}$$

Note that, given the conventions of Eqs. (3.44) and (3.45), the mass dimension of f_{B_f} is 1, while the mass dimension of $f_{\Lambda_{b,1}}$ is 2 (using the normalization for distribution amplitudes from Ref [39]). The decay constants $f_{B_f}, f_{\Lambda_{b,1}}$ as defined above do not have well-defined limits as $m_b \to \infty$, as the relativistic normalization of states does not behave well in this limit. The $m_b \to \infty$ limit can be studied by switching to a non-relativistic normalization for the HQET states:

$$_{\text{NR}}\langle\overline{B}_f(v,k')|\overline{B}_f(v,k)\rangle_{\text{NR}} = (2\pi)^3\delta^3(\vec{k}-\vec{k}'), \tag{3.48}$$

$$_{\text{NR}}\langle\Lambda_b(v,k',s')|\Lambda_b(v,k,s)\rangle_{\text{NR}} = \delta_{ss'}(2\pi)^3\delta^3(\vec{k}-\vec{k}'), \tag{3.49}$$

where $p_\mu = m_X v_\mu + k_\mu$. The relativistically normalised and non-relativistically normalised states additionally differ by $O(\frac{1}{m_b})$ effects, which are irrelevant in a static limit analysis. Furthermore, matching the QCD operators to HQET operators with $\overline{\text{MS}}$ matching factors $D(\mu)$, and dropping the $O(\frac{1}{m_b})$ contributions gives [40]

$$H_f^{(\text{DR},\overline{\text{MS}})} = (\overline{q}_f\gamma_5 Q)^{(\text{DR},\overline{\text{MS}})} = D_{H_f}(\mu)(\overline{q}_f\gamma_0\gamma_5 b)^{(\text{DR},\overline{\text{MS}})}, \tag{3.50}$$

$$\Lambda_{1,\alpha}^{(\text{DR},\overline{\text{MS}})} = \left([q^{aT}\tau_A C\gamma_5 q^b]Q^c_\alpha\epsilon_{abc}\right)^{(\text{DR},\overline{\text{MS}})} = D_{\Lambda_1}(\mu)\left([q^{aT}\tau_A C\gamma_5 q^b]\tfrac{1+\gamma_0}{2}b^c_\alpha\epsilon_{abc}\right)^{(\text{DR},\overline{\text{MS}})}. \tag{3.51}$$

Combining the matching of the operators and states from QCD to HQET with Eqs. (3.44) and (3.45) gives the relationships

$$im_{B_f} f^{\text{stat},\overline{\text{MS}}}_{B_f} = D_{H_f}(\mu)^{-1}\sqrt{2m_{B_f}}\langle 0|H_f^{(\text{DR},\overline{\text{MS}})}|\overline{H}_f(v,k)\rangle_{\text{NR}}, \tag{3.52}$$

$$im_{\Lambda_b} N_\alpha(p,s) f^{\text{stat},\overline{\text{MS}}}_{\Lambda_{b,1}} = D_{\Lambda_1}(\mu)^{-1}\sqrt{2m_{\Lambda_{b,1}}}\langle 0|\Lambda^{(\text{DR},\overline{\text{MS}})}_{1,\alpha}|\Lambda_b(v,k,s)\rangle_{\text{NR}}, \tag{3.53}$$

where the superscript 'stat' has been prepended to the label of the decay constants to emphasize that $O(\frac{1}{m_b})$ corrections have been dropped in the derivation. The matrix elements on the right-hand sides of Eqs. (3.52) and (3.53) are defined completely in the static HQET limit, and hence have no heavy-quark mass dependence. Therefore, up to logarithmic corrections due to the matching factors, the combinations $f^{\text{stat},\overline{\text{MS}}}_{B_f}\sqrt{m_{B_f}}$ and $f^{\text{stat},\overline{\text{MS}}}_{\Lambda_{b,1}} m_{\Lambda_b}$ are constant in the $m_b \to \infty$ limit.

To extract the ratio of the static decay constants using the X-space scheme as an intermediate nonperturbative renormalization scheme, the bare two-point correlation functions are first calculated in Lattice HQET:

$$T_{H_f}(t) := \langle H_f^{(\text{lat},0)}(t,\vec{0}) H_f^{(\text{lat},0)\dagger}(0,\vec{0})\rangle = |Z_{H_f}|^2 e^{-E_{H_f} t} + \text{excited states}, \tag{3.54}$$

$$T_{\Lambda_1}(t) := \sum_\alpha \left\langle \Lambda^{(\text{lat},0)}_{1,\alpha}(t,\vec{0})\Lambda^{(\text{lat},0)\dagger}_{1,\alpha}(0,\vec{0})\right\rangle = |Z_{\Lambda_1}|^2 e^{-E_{\Lambda_{Q,1}} t} + \text{excited states}, \tag{3.55}$$

and fitted at large Euclidean time-separations, t, to extract Z_{H_f} and Z_{Λ_1}. Note that the energies E_{H_f}, E_{Λ_1} are the binding energies of the respective hadrons shifted by the static quark mass m_{stat}. By renormalizing the operators in the X-space scheme at reference scale t_0^{-1} and then matching to the $\overline{\text{MS}}$ scheme, an expression for the ratio of the decay constants in the $\overline{\text{MS}}$ scheme can be derived as

$$\frac{f^{\text{stat},\overline{\text{MS}}}_{B_f}}{f^{\text{stat},\overline{\text{MS}}}_{\Lambda_{b,1}}}(\mu) = \left(\frac{T_{H_f}(t_0)}{T^{\text{NI}}_{H_f}(t_0)}\frac{T^{\text{NI}}_{\Lambda_1}(t_0)}{T_{\Lambda_1}(t_0)}\right)^{\frac{1}{2}} \times \left(\frac{C^{\text{DR},\overline{\text{MS}};\text{DR},X}_{\overline{Q}\Gamma q}(t_0,\mu)}{C^{\text{DR},\overline{\text{MS}};\text{DR},X}_{\Lambda_1}(t_0,\mu)}\right) \times \left(\frac{D_{\Lambda_1}(\mu)}{D_{H_f}(\mu)}\right) \times \frac{Z_{H_f}\sqrt{2}m_{\Lambda_b}}{Z_{\Lambda_1}\sqrt{m_{B_f}}}, \tag{3.56}$$

where the first factor renormalizes the bare operators in the X-space scheme, the second factor converts to the $\overline{\text{MS}}$ scheme in the dimensionally-regulated continuum, and the third factor matches the renormalized HQET operators to QCD operators in the $\overline{\text{MS}}$ scheme. All the renormalization and matching in this expression is performed at the scale t_0^{-1} for simplicity, but hybrid schemes where the renormalized operators are run before performing matching are also possible. For instance, running the operators in $\overline{\text{MS}}$ from the scale t_0^{-1} to the scale m_b before matching the HQET operators to QCD is usually desirable, as this cancels the large logarithms appearing if the t_0^{-1} scale is very different from m_b.

Alternatively, it is possible to renormalize these operators using a ratio of the form:

$$\frac{|\langle \mathcal{O}^{(X)}(t)\mathcal{O}^{(X),\dagger}(0)\rangle|^2}{|\langle \mathcal{O}^{(X)}(2t)\mathcal{O}^{(X),\dagger}(0)\rangle|} = Z^2_{\mathcal{O}}\frac{|\langle \mathcal{O}^{(0)}(t)\mathcal{O}^{(0),\dagger}(0)\rangle|^2}{|\langle \mathcal{O}^{(0)}(2t)\mathcal{O}^{(0),\dagger}(0)\rangle|} = \left.\frac{|\langle \mathcal{O}(t)\mathcal{O}^{\dagger}(0)\rangle|^2}{|\langle \mathcal{O}(2t)\mathcal{O}^{\dagger}(0)\rangle|}\right|_{\text{noninteracting}} \tag{3.57}$$

by noticing that the static quark power divergence cancels between the numerator and denominator, leaving a factor of $Z^2_{\mathcal{O}}$, allowing for the renormalization of the endpoint operators. This approach is discussed further and utilised in Sec. 4.2.8.

3.2 FOUR-QUARK OPERATORS

Some text in this section reproduced with coauthors' permission from Ref. [31].

3.2.1 $\overline{\text{MS}}$ RENORMALIZATION OF FOUR-QUARK OPERATORS

The X-space renormalization of the four-quark operators is made complicated by the fact that they mix. Before discussing position-space renormalization schemes, this section presents a review of the $\overline{\text{MS}}$ renormalization of the set of $\Delta B = 0$ four-quark operators relevant for spectator effects, as well as the set of $\Delta B = 2$ operators relevant for $B - \overline{B}$ mixing. Using the solution of $\overline{I}_{HL}$ given in Eq. (2.20), the $O(\alpha_S)$-divergences in the Green's functions displayed in Fig. 2.1 can be calculated as:

$$\begin{aligned}
(i\mathcal{M}^{abcd}_{\alpha\beta\gamma\delta})^{(b)} &= -\frac{\alpha_S}{\pi\epsilon}\mu^{4-d}\left(\frac{1+\not{v}}{2}T^A\Gamma_L\right)^{bd}_{\beta\delta}\left(\Gamma_R\frac{1+\not{v}}{2}T^A\right)^{ca}_{\gamma\alpha},\\
(i\mathcal{M}^{abcd}_{\alpha\beta\gamma\delta})^{(c)} &= \frac{\alpha_S}{2\pi\epsilon}\mu^{4-d}\left(\frac{1+\not{v}}{2}\Gamma_L\right)^{bd}_{\beta\delta}\left(T^A\Gamma_R T^A\frac{1+\not{v}}{2}\right)^{ca}_{\gamma\alpha},\\
(i\mathcal{M}^{abcd}_{\alpha\beta\gamma\delta})^{(d)} &= -\frac{\alpha_S}{2\pi\epsilon}\mu^{4-d}\left(\frac{1+\not{v}}{2}\Gamma_L T^A\right)^{bd}_{\beta\delta}\left(\Gamma_R T^A\frac{1+\not{v}}{2}\right)^{ca}_{\gamma\alpha},\\
(i\mathcal{M}^{abcd}_{\alpha\beta\gamma\delta})^{(e)} &= -\frac{\alpha_S}{2\pi\epsilon}\mu^{4-d}\left(\frac{1+\not{v}}{2}T^A\Gamma_L\right)^{bd}_{\beta\delta}\left(T^A\Gamma_R\frac{1+\not{v}}{2}\right)^{ca}_{\gamma\alpha},\\
(i\mathcal{M}^{abcd}_{\alpha\beta\gamma\delta})^{(f)} &= \frac{\alpha_S}{2\pi\epsilon}\mu^{4-d}\left(\frac{1+\not{v}}{2}T^A\Gamma_L T^A\right)^{bd}_{\beta\delta}\left(\Gamma_R\frac{1+\not{v}}{2}\right)^{ca}_{\gamma\alpha},\\
(i\mathcal{M}^{abcd}_{\alpha\beta\gamma\delta})^{(g)} &= \frac{\alpha_S}{8\pi\epsilon}\mu^{4-d}\left(\frac{1+\not{v}}{2}\Gamma_L\gamma^\mu\gamma^\nu T^A\right)^{bd}_{\beta\delta}\left(T^A\gamma^\nu\gamma^\mu\Gamma_R\frac{1+\not{v}}{2}\right)^{ca}_{\gamma\alpha},
\end{aligned}\tag{3.58}$$

where the superscripts $(b)-(g)$ refer to the different diagrams appearing in Fig. 2.1, and the operator is assumed to take the form $(\overline{Q}\Gamma_L q)(\overline{q}\Gamma_R Q)$. It is useful to keep these formulas in this form, because it is clear that the evanescent operators are completely determined by diagram (g) (Dirac structures appearing in all other diagrams simplifies to be a multiplicative factor). Furthermore, it then takes minimal effort to translate these results to the $\Delta B = 2$ operators, which have a different contraction form $(\overline{Q}\Gamma_L q)(\overline{Q}\Gamma_R q)$. The basis of $\Delta B = 0$ operators of interest for spectator effects (discussed further in Chapter 4) are conventionally written in the basis

$$\begin{aligned}
\mathcal{O}^f_1 &\coloneqq (\overline{Q}\gamma_\mu P_L q_f)(\overline{q}_f\gamma_\mu P_L Q), & \mathcal{O}^f_2 &\coloneqq (\overline{Q}P_L q_f)(\overline{q}_f P_R Q),\\
\mathcal{O}^f_3 &\coloneqq (\overline{Q}\gamma_\mu P_L T^A q_f)(\overline{q}_f\gamma_\mu P_L T^A Q), & \mathcal{O}^f_4 &\coloneqq (\overline{Q}P_L T^A q_f)(\overline{q}_f P_R T^A Q),
\end{aligned}\tag{3.59}$$

where $f \in \{u, d\}$ index the flavours of quarks that are taken to be massless in this section. Note that the flavor-singlet combinations of the operators such as $\mathcal{O}^u + \mathcal{O}^d$ will mix with the lower-dimensional $\overline{Q}Q$ operator in a power-divergent way. When acting on B-hadrons, $\overline{Q}Q$ is the identity operator, leading to an a^{-3} additive mixing to the operators in lattice-HQET computations. This section focuses on the renormalization of the isospin-nonsinglet contributions such as $\mathcal{O}^u - \mathcal{O}^d$ where the mixing with the $\overline{Q}Q$ operators cancel, and the four-quark operators are protected from power-divergent mixing. The f-label on the four-quark operators is omitted in what follows, as it should be understood that all operators refer to the isospin-nonsinglet versions.

In dimensional regularization, four-quark operators such as those listed in Eq. (3.59) mix with evanescent operators, which are operators that formally vanish in $d = 4$ due to their Dirac structure. Different choices of basis for the evanescent operators lead to finite shifts in the $\overline{\text{MS}}$ renormalized matrix elements [41, 42]. Working in the HV scheme, the basis of evanescent operators appearing at $O(\alpha_S)$ chosen here is written as

$$\begin{aligned}
E_1 &\coloneqq (\overline{Q}\gamma_\mu P_L \gamma_\alpha \gamma_\beta q)(\overline{q}\gamma_\beta \gamma_\alpha \gamma_\mu P_L Q) - 4\mathcal{O}_1, \\
E_2 &\coloneqq (\overline{Q}P_L \gamma_\alpha \gamma_\beta q)(\overline{q}\gamma_\beta \gamma_\alpha P_R Q) - 4\mathcal{O}_2, \\
E_3 &\coloneqq (\overline{Q}\gamma_\mu P_L \gamma_\alpha \gamma_\beta T^A q)(\overline{q}\gamma_\beta \gamma_\alpha \gamma_\mu P_L T^A Q) - 4\mathcal{O}_3, \\
E_4 &\coloneqq (\overline{Q}P_L \gamma_\alpha \gamma_\beta T^A q)(\overline{q}\gamma_\beta \gamma_\alpha P_R T^A Q) - 4\mathcal{O}_4.
\end{aligned} \tag{3.60}$$

The Dirac structures present in these evanescent operators occur in the one-loop diagram with a gluon attached to the two light quarks, as shown in Fig. 2.4. In order for the proposed X-space scheme to be regulator-independent, evanescent contributions to operators must be subtracted for all regulators, and the renormalization conditions must be formulated for the subtracted operators [43, 44]. In general, all operators in $\{\mathcal{O}_1, \mathcal{O}_2, \mathcal{O}_3, \mathcal{O}_4\}$ will mix with each other, but to $O(\alpha_S)$ in $\overline{\text{MS}}$ the operators mix in sub-bases, with $\{\mathcal{O}_1, \mathcal{O}_3, E_1, E_3\}$ having the same mixing pattern as $\{\mathcal{O}_2, \mathcal{O}_4, E_2, E_4\}$. The MS-renormalization conditions for $i \in \{1, 2\}$ are given by

$$\begin{pmatrix} \mathcal{O}_i^{(0)} \\ \mathcal{O}_{i+2}^{(0)} \end{pmatrix} = \begin{pmatrix} 1 + \frac{2\alpha_S}{\pi\epsilon} & -\frac{3\alpha_S}{2\pi\epsilon} & 0 & \frac{\alpha_S}{8\pi\epsilon} \\ -\frac{\alpha_S}{3\pi\epsilon} & 1 + \frac{\alpha_S}{4\pi\epsilon} & \frac{\alpha_S}{36\pi\epsilon} & \frac{7\alpha_S}{48\pi\epsilon} \end{pmatrix} \begin{pmatrix} \mathcal{O}_i^{(\text{MS})} \\ \mathcal{O}_{i+2}^{(\text{MS})} \\ E_i^{(\text{MS})} \\ E_{i+2}^{(\text{MS})} \end{pmatrix}. \tag{3.61}$$

The first generation of bare evanescent operators $\{E_1, \cdots, E_4\}$ themselves mix at $O(\alpha_S)$ with a second generation of bare evanescent operators containing even more complicated Dirac structures (such as $(\overline{Q}P_L \gamma_{\alpha_1}\gamma_{\alpha_2}\gamma_{\alpha_3}\gamma_{\alpha_4} q)(\overline{q}\gamma_{\alpha_4}\gamma_{\alpha_3}\gamma_{\alpha_2}\gamma_{\alpha_1} P_R Q)$) [41]. Such higher-order evanescent operators are omitted in Eq. (3.61) as the matching conditions presented later between $\overline{\text{MS}}$ and X-space schemes are not sensitive to them at $O(\alpha_S)$.

Subtracting the $\frac{1}{\epsilon}$ evanescent contributions to the physical operators gives evanescent-subtracted operators $\tilde{\mathcal{O}}_i$ that can be used in regulator-independent schemes. By reading off the coefficients from Eq. (3.61) they are defined to be, for $i \in \{1, 2\}$,

$$\tilde{\mathcal{O}}_i^{(0)} = \mathcal{O}_i^{(0)} - \frac{\alpha_S}{8\pi\epsilon} E_{i+2}^{(0)}, \quad \tilde{\mathcal{O}}_{i+2}^{(0)} = \mathcal{O}_{i+2}^{(0)} - \frac{\alpha_S}{36\pi\epsilon} E_i^{(0)} - \frac{7\alpha_S}{48\pi\epsilon} E_{i+2}^{(0)}. \tag{3.62}$$

In later sections of this thesis, the focus will be on the $\Delta Q = 0$ operators relevant to Spectator Effect calculations. The renormalization calculations of this thesis are however applicable to other

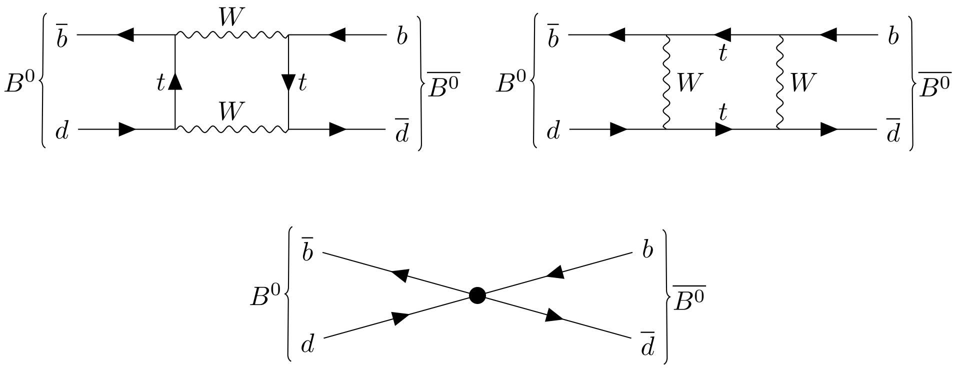

Figure 3.3: The top two diagrams show the dominant box-diagrams contributing to the $B - \overline{B}$ mixing rate. The bottom diagram displays the 4-quark effective field theory treatment after integrating out the electroweak scale physics.

classes of four-quark operators, such as the collection of $\Delta Q = 2$ operators. In the Standard Model, neutral B-mesons (B^0, B_s^0) mix with their own antiparticles. The lowest-order diagrams contributing to this in the Standard Model are box diagrams with the exchange of two weak bosons and top quarks shown in Fig. 3.3. After integrating out physics at and above the weak scale leads to $\Delta B = 2$ four-quark operators. When matching these operators to HQET, the Lagrangian is expanded to include a static antiquark Q_- that travels in the opposite direction to the static quark Q_+ (compare to the Q_+-propagator Eq. (3.6)):

$$\langle Q_-^{(0)}(0)\overline{Q}_-^{(0)}(x_E)\rangle_F = \delta_{\vec{x}_E,\vec{0}}\ \theta(t_E)W^{(0)}(0,x_E)\frac{1-\gamma_0}{2}, \tag{3.63}$$

where $\frac{1\pm\gamma_0}{2}Q_\pm = Q_\pm$. A basis of the relevant $\Delta Q = 2$ operators in HQET is

$$\begin{aligned} \mathcal{Q}_1 &:= (\overline{Q}_+P_Lq)(\overline{Q}_-P_Lq), \quad & \mathcal{Q}_2 &:= (\overline{Q}_+P_LT^Aq)(\overline{Q}_-P_LT^Aq), \\ \mathcal{Q}_3 &:= (\overline{Q}_+P_Lq)(\overline{Q}_-P_Rq), \quad & \mathcal{Q}_4 &:= (\overline{Q}_+P_LT^Aq)(\overline{Q}_-P_RT^Aq). \end{aligned} \tag{3.64}$$

The operators $\mathcal{Q}_1, \mathcal{Q}_2$ contribute to neutral B-meson mixing in the Standard Model, and $\mathcal{Q}_3, \mathcal{Q}_4$ are contributions that could arise from possible new physics [25]. The full basis of $\Delta Q = 2$ operators also contains $\{\mathcal{Q}_1, \mathcal{Q}_2\}$ with left-handed projectors swapped with right-handed projectors ($P_L \leftrightarrow P_R$), but these are related by parity and so renormalize with the same factors as $\{\mathcal{Q}_1, \mathcal{Q}_2\}$. There are also additional $\Delta Q = 2$ operators when Q is relativistic, but these are related to the operators in Eq. (3.64) in the static quark limit [45]:

$$(\overline{Q}_+\gamma_\mu P_Lq)(\overline{Q}_-\gamma_\mu P_Lq) = \frac{8}{3}\mathcal{Q}_1 + 4\mathcal{Q}_2 \qquad \text{in} \quad d = 4. \tag{3.65}$$

The evanescent operators are defined as

$$\begin{aligned}
F_1 &\coloneqq (\overline{Q}_+ P_L \gamma_\alpha \gamma_\beta q)(\overline{Q}_- P_L \gamma_\alpha \gamma_\beta q) - \frac{32}{3}\mathcal{Q}_1 - 16\mathcal{Q}_2, \\
F_2 &\coloneqq (\overline{Q}_+ P_L T^A \gamma_\alpha \gamma_\beta)(\overline{Q}_- P_L T^A \gamma_\alpha \gamma_\beta q) - \frac{32}{9}\mathcal{Q}_1 - \frac{16}{3}\mathcal{Q}_2 \\
F_3 &\coloneqq (\overline{Q}_+ P_L \gamma_\alpha \gamma_\beta q)(\overline{Q}_- P_R \gamma_\alpha \gamma_\beta q) - 4\mathcal{Q}_3, \\
F_4 &\coloneqq (\overline{Q}_+ P_L T^A \gamma_\alpha \gamma_\beta)(\overline{Q}_- P_R T^A \gamma_\alpha \gamma_\beta q) - 4\mathcal{Q}_4,
\end{aligned} \tag{3.66}$$

where the γ-matrix structure is governed by the $O(\alpha_S)$ diagram with a single gluon attached to the two light quarks. The mixing pattern is given by the following MS renormalization:

$$\begin{pmatrix} \mathcal{Q}_1^{(0)} \\ \mathcal{Q}_2^{(0)} \end{pmatrix} = \begin{pmatrix} 1 + \frac{14\alpha_S}{9\pi\epsilon} & \frac{4\alpha_S}{3\pi\epsilon} & 0 & -\frac{\alpha_S}{8\pi\epsilon} \\ \frac{8\alpha_S}{27\pi\epsilon} & 1 + \frac{10\alpha_S}{9\pi\epsilon} & \frac{-\alpha_S}{36\pi\epsilon} & \frac{\alpha_S}{24\pi\epsilon} \end{pmatrix} \begin{pmatrix} \mathcal{Q}_1^{\mathrm{MS}} \\ \mathcal{Q}_2^{\mathrm{MS}} \\ F_1^{\mathrm{MS}} \\ F_2^{\mathrm{MS}} \end{pmatrix}, \tag{3.67}$$

$$\begin{pmatrix} \mathcal{Q}_3^{(0)} \\ \mathcal{Q}_4^{(0)} \end{pmatrix} = \begin{pmatrix} 1 + \frac{2\alpha_S}{\pi\epsilon} & \frac{3\alpha_S}{2\pi\epsilon} & 0 & -\frac{\alpha_S}{8\pi\epsilon} \\ \frac{\alpha_S}{3\pi\epsilon} & 1 + \frac{3\alpha_S}{2\pi\epsilon} & \frac{-\alpha_S}{36\pi\epsilon} & \frac{\alpha_S}{24\pi\epsilon} \end{pmatrix} \begin{pmatrix} \mathcal{Q}_3^{\mathrm{MS}} \\ \mathcal{Q}_4^{\mathrm{MS}} \\ F_3^{\mathrm{MS}} \\ F_4^{\mathrm{MS}} \end{pmatrix}. \tag{3.68}$$

Correspondingly, the evanescent-subtracted operators are defined for $i \in \{1,3\}$ as

$$\tilde{\mathcal{Q}}_i^{(0)} = \mathcal{Q}_i^{(0)} + \frac{\alpha_S}{8\pi\epsilon} F_{i+1}^{(0)}, \quad \tilde{\mathcal{Q}}_{i+1}^{(0)} = \tilde{\mathcal{Q}}_{i+1}^{(0)} + \frac{\alpha_S}{36\pi\epsilon} F_i^{(0)} - \frac{\alpha_S}{24\pi\epsilon} F_{i+1}^{(0)} \tag{3.69}$$

3.2.2 POSITION-SPACE SCHEMES

As the four-quark operators that are the focus of this section are $\Delta Q = 0$, and the static quark can only travel in the timelike direction, an X-space scheme utilising two-point correlation functions of $\tilde{\mathcal{O}}_i$ (similar to that proposed in Sec. 3.1.1 for the bilinear and trilinear operators) is not possible to define. The reason is that the corresponding two-point correlation functions are zero (due to the $\theta(-t_E)$ portion of the static heavy quark propagator shown in Eq. (3.6)). A possible way to rectify this is to compactify the time direction (for instance, in a thermal calculation), but this would likely be significantly more complicated due to the Matsubara sums required in the computation [46].

Instead, three-point correlation functions combining $\tilde{\mathcal{O}}_i$ with different choices of source and sink operators can be used to define an X-space renormalization scheme. Such an approach was also considered, for example, in the X-space renormalization of the QCD stress-energy tensor [9]. Taking ratios of three-point correlation functions to appropriate two-point correlation functions cancels the renormalization factors of the source and sink operators, provided they are multiplicatively renormalizable. In HQET, this has the added benefit of cancelling the static-quark self-energy divergence. Writing the renormalized $\Delta Q = 0$ operators as $\tilde{\mathcal{O}}_i^{(R,X)}(t) = Z_{ij}^{(R,X)}(t)\tilde{\mathcal{O}}_j^{(0)}$, the renormalization condition is defined here by a choice of four source-operator/sink-operator combinations (labelled as

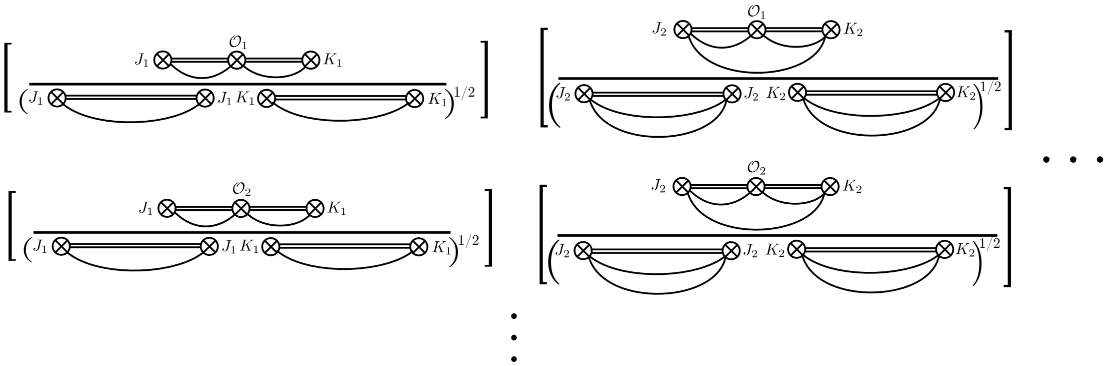

Figure 3.4: Schematic drawing showing the matrix of correlation functions used to define the position-space renormalization scheme defined in Eq. (3.70). Each row corresponds to a different operator, and only two rows have been drawn in this figure (though there are four total for the $\Delta B = 0$ operators considered for spectator-effects). Also, only two source/sink combinations $(J_1, K_1), (J_2, K_2)$ are shown - though in practice there need to be at least as many as the number of operators, to completely define the mixing matrix. In this figure, it is assumed that (J_1, K_1) are heavy-light operators, and (J_2, K_2) are heavy-light-light operators.

J_n, K_n respectively, $n \in \{1, 2, 3, 4\}$) and is given by (shown schematically in Fig. 3.4):

$$\frac{\langle J_n^\dagger(-t,\vec{0})\tilde{\mathcal{O}}_i^{(R,X)}(0,\vec{0})K_n(t,\vec{0})\rangle}{\sqrt{|\langle J_n^\dagger(-t,\vec{0})J_n(t,\vec{0})\rangle\langle K_n^\dagger(-t,\vec{0})K_n(t,\vec{0})\rangle|}} = \frac{\langle J_n^\dagger(-t,\vec{0})\tilde{\mathcal{O}}_i^{(0)}(0,\vec{0})K_n(t,\vec{0})\rangle}{\sqrt{|\langle J_n^\dagger(-t,\vec{0})J_n(t,\vec{0})\rangle\langle K_n^\dagger(-t,\vec{0})K_n(t,\vec{0})\rangle|}}\Bigg|_{\mathrm{NI}} \tag{3.70}$$

(for all n; no sum over n implied) at a fixed t. In the same way as for the two-point X-space condition presented in Sec. 3.1.1, additional indices on the source and sink operators should be summed over on both sides of the condition, and the open spinor indices are traced over if the source and sink are baryonic. Since the source and sink operators are multiplicatively renormalizable, this causes the Z-factors of the source and sink to cancel in these ratios, so they are not labelled as bare or renormalized. Furthermore, the static-quark self-energy cancels in these ratios of correlation functions with the same physical length of the Wilson line, allowing for nonperturbative renormalization of the operators without determination of m_{stat}. Defining

$$T_{i,n}(t) := \frac{\langle J_n^\dagger(-t,\vec{0})\tilde{\mathcal{O}}_i^{(0)}(0,\vec{0})K_n(t,\vec{0})\rangle}{\sqrt{|\langle J_n^\dagger(-t,\vec{0})J_n(t,\vec{0})\rangle\langle K_n^\dagger(-t,\vec{0})K_n(t,\vec{0})\rangle|}} = T_{i,n}^{(0)}(t) + \alpha_S T_{i,n}^{(1)}(t) + O(\alpha_S^2), \tag{3.71}$$

where $T_{i,n}^{(0)}(t)$ is the noninteracting value, the X-space renormalization conditions can then be solved as

$$Z_{ij}^{(X)} = \sum_n T_{i,n}^{(0)}(t)T_{n,j}^{-1}(t) = \mathbb{1}_{i,j} - \alpha_S \sum_n T_{i,n}^{(1)}(t)(T^{(0)}(t))_{n,j}^{-1} + O(\alpha_S^2), \tag{3.72}$$

which is well-defined as long as the four source/sink pairs, $n \in \{1,2,3,4\}$, are chosen so that the noninteracting matrix $T^{(0)}_{i,n}(t)$ is invertible in $d = 4$.

The natural candidates for the source and sink operators are the mesonic and baryonic currents discussed in Sec. 3.1.1. The requirement that $T^{(0)}_{i,n}(t)$ is invertible restricts which sets of source/sink pairs can be chosen. For instance,

- It is not possible to use four mesonic source/sink pairs, as, for any mesonic source/sink pair (J_M, K_M), the matrix element $\langle J^\dagger_M(-t,\vec{0})\tilde{\mathcal{O}}^{(0)}_i K_M(t,\vec{0})\rangle|_{\mathrm{NI}}$ vanishes for $i \in \{3,4\}$ due to the color trace.

- The three-point correlation function with Λ_Q-baryons as both source and sink vanishes due to isospin symmetry (the four-quark operator is an isospin nonsinglet and Λ is an isospin-singlet, so overall matrix element is nonsinglet and hence zero)

- The three-point correlation function with Λ_Q-baryon as a source and a Σ_Q-baryon as a sink vanishes as neither the Λ_Q nor the four-quark operator has right-handed light quark fields, but the Σ_Q has one left handed and one right handed (this is a consequence of chiral symmetry).

- The three-point correlation function with Σ_Q as both source and sink, using the $I_z = 0$ component of each Σ_Q will cause the correlator to vanish, as the corresponding Clebsch-Gordon coefficient vanishes.

For the remaining nonzero ratios of correlation functions, the noninteracting ratios are parametrized as

$$T^{(0)}_{i,n}(t) = T^{(0,0)}_{i,n}\frac{1}{\pi^2 t^{3-\epsilon}}\left(\frac{\pi}{4}e^{\gamma_E}\right)^{\frac{\epsilon}{2}} + T^{(0,1)}_{i,n}\frac{\epsilon}{\pi^2 t^{3-\epsilon}} + O(\epsilon^2). \tag{3.73}$$

In dimensional regularization, after removing factors of δ^{d-1} corresponding to the δ-function in position space from the static quark propagators, $T_{i,n}(t)$ has dimension $3-\epsilon$, accounted for by the factor of $t^{-(3-\epsilon)}$ in Eq. (3.73). The specific source/sink pairs that are studied in this section are the negative-parity heavy-light mesonic operators and the positive-parity heavy-light-light baryonic operators discussed in Sec. 3.1.1. The values of the decomposition for the noninteracting ratio for these source/sink operators (J,K) are tabulated in Table 3.2. Every choice of four linearly independent source/sink operators from this list (there are 28 different choices in total) defines a different X-space scheme. In a similar way to the parametrization of the noninteracting contribution to the ratio of correlation functions in Eq. (3.73), the $O(\alpha_S)$-contribution to the ratios are parametrized by

$$T^{(1)}_{i,n} = T^{(1,0)}_{i,n}\frac{1}{\epsilon\pi^3 t^{3-2\epsilon}}\left(\frac{\pi}{4}e^{\gamma_E}\mu\right)^{\epsilon} + T^{(1,1)}_{i,n}\frac{1}{\pi^3 t^{3-2\epsilon}} + T^{(1,2)}_{i,n}\frac{1}{\pi t^{3-2\epsilon}} + O(\epsilon). \tag{3.74}$$

For the various source/sink pairs, the $O(\alpha_S)$ matrix elements for the ratio have been calculated and are tabulated in Table 3.3.

n	J_n	K_n	$T^{(0,0)}_{1,n}$	$T^{(0,0)}_{2,n}$	$T^{(0,0)}_{3,n}$	$T^{(0,0)}_{4,n}$	$T^{(0,1)}_{1,n}$	$T^{(0,1)}_{2,n}$	$T^{(0,1)}_{3,n}$	$T^{(0,1)}_{4,n}$
1	H^-_f	H^-_f	-6	-6	0	0	3	3	0	0
2	$H^{*-}_{f,i}$	$H^{*-}_{f,i}$	-6	0	0	0	3	0	0	0
3	Λ_1	$\Sigma_{2,0}$	$-2\sqrt{3}$	$-\sqrt{3}$	$\frac{4}{\sqrt{3}}$	$\frac{2}{\sqrt{3}}$	$\frac{4}{\sqrt{3}}$	$\frac{1}{\sqrt{3}}$	$\frac{-8}{3\sqrt{3}}$	$\frac{-2}{3\sqrt{3}}$
3^*	Λ_2	$\Sigma_{1,0}$	$2\sqrt{3}$	$\sqrt{3}$	$\frac{-4}{\sqrt{3}}$	$\frac{-2}{\sqrt{3}}$	$-2\sqrt{3}$	$\frac{-2}{\sqrt{3}}$	$\frac{4}{\sqrt{3}}$	$\frac{4}{3\sqrt{3}}$
4	$\Sigma_{1,\alpha}$	$\Sigma_{1,\alpha}$	6	1	-4	$\frac{-2}{3}$	$\frac{-11}{3}$	$\frac{-3}{2}$	$\frac{22}{9}$	1
4^*	$\Sigma_{2,\alpha}$	$\Sigma_{2,\alpha}$	-6	-1	4	$\frac{2}{3}$	$\frac{-5}{3}$	$\frac{-1}{2}$	$\frac{10}{9}$	$\frac{1}{3}$
5	$\Sigma^*_{1,\alpha,i}$	$\Sigma^*_{1,\alpha,i}$	0	-2	0	$\frac{4}{3}$	$\frac{2}{3}$	0	$\frac{-4}{9}$	0
5^*	$\Sigma^*_{2,\alpha,i}$	$\Sigma^*_{2,\alpha,i}$	0	-2	0	$\frac{4}{3}$	$\frac{2}{3}$	0	$\frac{-4}{9}$	0

Table 3.2: Decomposition for the noninteracting ratio of correlation functions according to Eq. (3.73), for varying source-sink pairs (J_n, K_n). The source/sink pairs $n = 3$ and $n = 3^*$ give the same noninteracting matrix elements $(T^{(0,0)}_{i,n})$ in $d = 4$ up to a sign, and hence may not both be chosen as part of the set of four source/sink operators used in the renormalization condition due to the requirement that $T^{(0)}_{i,n}$ is invertible. The same is true for $n = 4, 4^*$ and $n = 5, 5^*$.

Choosing the specific source/sink pairs $n \in \{1,2,3,4\}$ from the list of source/sink pairs presented in Tables 3.2 and 3.3, the X-space renormalization matrix can be calculated using Eq. (3.72) as

$$Z^{(X)}_{ij,n\in\{1,2,3,4\}} = \mathbb{1} - \alpha_S(\mu)\left(\frac{\pi}{4}e^{\gamma_E}t^2\mu^2\right)^{\frac{\epsilon}{2}} \begin{pmatrix} \frac{2}{\pi\epsilon} + \frac{24+4\pi^2}{9\pi} & 0 & \frac{-3}{2\pi\epsilon} + \frac{-9+24\pi^2}{24\pi} & \frac{-5}{4\pi} \\ 0 & \frac{2}{\pi\epsilon} + \frac{24+4\pi^2}{9\pi} & \frac{-1}{16\pi} & \frac{-3}{2\pi\epsilon} + \frac{-63+72\pi^2}{72\pi} \\ \frac{-1}{3\pi\epsilon} + \frac{-15+4\pi^2}{54\pi} & \frac{-1}{9\pi} & \frac{1}{4\pi\epsilon} + \frac{90+56\pi^2}{144\pi} & \frac{-1}{12\pi} \\ \frac{-1}{36\pi} & \frac{-1}{3\pi\epsilon} + \frac{-15+4\pi^2}{54\pi} & \frac{-3}{16\pi} & \frac{1}{4\pi\epsilon} + \frac{414+168\pi^2}{432\pi} \end{pmatrix}, \quad (3.75)$$

where $\mathbb{1}$ is the 4×4 identity matrix. As a check, it can be verified that the $\frac{1}{\epsilon}$ divergent pieces match up with the MS counterterms presented in Eq. (3.61). The corresponding conversion factor from the

n	$T^{(1,0)}_{1,n}$	$T^{(1,0)}_{2,n}$	$T^{(1,0)}_{3,n}$	$T^{(1,0)}_{4,n}$	$T^{(1,1)}_{1,n}$	$T^{(1,1)}_{2,n}$	$T^{(1,1)}_{3,n}$	$T^{(1,1)}_{4,n}$	$T^{(1,2)}_{1,n}$	$T^{(1,2)}_{2,n}$	$T^{(1,2)}_{3,n}$	$T^{(1,2)}_{4,n}$
1	-12	-12	2	2	-10	-10	$\frac{4}{3}$	$\frac{5}{6}$	$-\frac{8}{3}$	$-\frac{8}{3}$	$-\frac{4}{9}$	$-\frac{4}{9}$
2	-12	0	2	0	-10	0	$\frac{2}{3}$	$\frac{1}{6}$	$-\frac{8}{3}$	0	$-\frac{4}{9}$	0
3	$-6\sqrt{3}$	$-3\sqrt{3}$	$\sqrt{3}$	$\frac{\sqrt{3}}{2}$	$-\frac{8}{\sqrt{3}}$	$-\frac{7}{\sqrt{3}}$	$\frac{7}{3\sqrt{3}}$	$\frac{5}{3\sqrt{3}}$	$\frac{4}{3\sqrt{3}}$	$\frac{2}{3\sqrt{3}}$	$\frac{10}{9\sqrt{3}}$	$\frac{5}{9\sqrt{3}}$
3^*	$6\sqrt{3}$	$3\sqrt{3}$	$-\sqrt{3}$	$-\frac{\sqrt{3}}{2}$	$\sqrt{3}$	$\frac{3\sqrt{3}}{2}$	$-\frac{2}{\sqrt{3}}$	$-\frac{\sqrt{3}}{2}$	$-\frac{4}{3\sqrt{3}}$	$-\frac{2}{3\sqrt{3}}$	$-\frac{10}{9\sqrt{3}}$	$-\frac{5}{9\sqrt{3}}$
4	18	3	-3	$-\frac{1}{2}$	$\frac{22}{3}$	-1	$-\frac{43}{18}$	$\frac{5}{12}$	$-\frac{4}{3}$	$-\frac{2}{9}$	$-\frac{10}{9}$	$-\frac{5}{27}$
4^*	-18	-3	3	$\frac{1}{2}$	$-\frac{73}{3}$	$-\frac{31}{6}$	$\frac{103}{18}$	$\frac{25}{36}$	$\frac{4}{3}$	$\frac{2}{9}$	$\frac{10}{9}$	$\frac{5}{27}$
5	0	-6	0	1	$\frac{4}{3}$	-6	$-\frac{8}{9}$	$\frac{3}{2}$	0	$\frac{4}{9}$	0	$\frac{10}{27}$
5^*	0	-6	0	1	$\frac{4}{3}$	$-\frac{19}{3}$	$-\frac{8}{9}$	$\frac{31}{18}$	0	$\frac{4}{9}$	0	$\frac{10}{27}$

Table 3.3: Decomposition for the $O(\alpha_S)$ contribution to the ratios of correlation functions defined in Eq. (3.74). The source/sink pair index n is the same as used in Table 3.2.

X-space scheme to $\overline{\mathrm{MS}}$ is given by

$$C^{(\overline{\mathrm{MS}};X)}_{ij,n\in\{1,2,3,4\}} := \sum_k Z^{(\overline{\mathrm{MS}})}_{ik} (Z^{(X)})^{-1}_{kj,n\in\{1,2,3,4\}} = \mathbb{1}+$$
$$\alpha_S(\mu)\begin{pmatrix} \frac{\log(\beta)}{\pi}+\frac{4\pi}{9}+\frac{8}{3\pi} & 0 & -\frac{3\log(\beta)}{4\pi}+\pi-\frac{3}{8\pi} & -\frac{5}{4\pi} \\ 0 & \frac{\log(\beta)}{\pi}+\frac{4\pi}{9}+\frac{8}{3\pi} & -\frac{1}{16\pi} & -\frac{3\log(\beta)}{4\pi}+\pi-\frac{7}{8\pi} \\ -\frac{\log(\beta)}{6\pi}+\frac{2\pi}{27}-\frac{5}{18\pi} & -\frac{1}{9\pi} & \frac{\log(\beta)}{8\pi}+\frac{7\pi}{18}+\frac{5}{8\pi} & -\frac{1}{12\pi} \\ -\frac{1}{36\pi} & -\frac{\log(\beta)}{6\pi}+\frac{2\pi}{27}-\frac{5}{18\pi} & -\frac{3}{16\pi} & \frac{\log(\beta)}{8\pi}+\frac{7\pi}{18}+\frac{23}{24\pi} \end{pmatrix}, \tag{3.76}$$

where $\beta := e^{2\gamma_E}\frac{\mu^2 t^2}{16}$. A natural choice for μ is $\mu^2 = 16e^{-2\gamma_E}/t^2$ which would cancel the factors of $\log(\beta)$ appearing in the matching coefficient. In principle, when converting matrix elements computed with lattice HQET to $\overline{\mathrm{MS}}$-renormalized matrix elements, varying over the different choices of source/sink pairs, as well as varying over the scale t that the X-space scheme is defined at before perturbatively running to a common scale, will give an indication on the error due to $O(\alpha_S^2)$ terms that have been neglected in this study.

Single baryonic heavy-light-light currents cannot be used as source/sink pairs for the $\Delta B = 2$ four-quark operators, as the corresponding three-point functions all vanish. Fortunately, enough constraints can be derived with the mesonic heavy-light currents as source/sink pairs to constitute a valid X-space scheme. Although chiral symmetry is formally broken by the HV γ_5 scheme, the massless nature of the light quarks causes the operators to mix in the 2×2 subblocks presented in Eqs. (3.67) and (3.68). Thus, only two source/sink pairs are needed in the X-space scheme. Using the choice $(\overline{Q}\gamma_5 q, \overline{q}\gamma_5 Q)$ and $(\overline{Q}\gamma_i\gamma_5 q, \overline{q}\gamma_i\gamma_5 Q)$, the $O(\alpha_S)$ matching matrices are found to be

$$C^{(\overline{\mathrm{MS}},X)}_{\{O_1,O_2\}} = \mathbb{1} + \frac{\alpha_S}{\pi}\begin{pmatrix} \frac{7\log(\beta)}{9} + \frac{4\pi^2}{9} + \frac{23}{9} & \frac{2\log(\beta)}{3} - \frac{\pi^2}{3} + \frac{4}{3} \\ \frac{4\log(\beta)}{27} - \frac{2\pi^2}{27} + \frac{8}{27} & \frac{5\log(\beta)}{9} + \frac{5\pi^2}{9} + \frac{19}{9} \end{pmatrix}, \tag{3.77}$$

$$C^{(\overline{\mathrm{MS}},X)}_{\{O_3,O_4\}} = \mathbb{1} + \frac{\alpha_S}{\pi}\begin{pmatrix} \log(\beta) + \frac{4\pi^2}{9} + \frac{25}{9} & \frac{3\log(\beta)}{4} - \frac{\pi^2}{3} + \frac{7}{6} \\ \frac{\log(\beta)}{6} - \frac{2\pi^2}{27} + \frac{7}{27} & \frac{3\log(\beta)}{4} + \frac{5\pi^2}{9} + \frac{43}{18} \end{pmatrix}, \tag{3.78}$$

where $\beta := e^{2\gamma_E}\frac{\mu^2 t^2}{16}$.

3.2.3 CALCULATION STRATEGY

Unlike the two-point functions, which could be Fourier-transformed into momentum-space diagrams with a single external scale p as in Sec. 3.1.2, there is no analogous transformation for the three-point functions, which effectively have *two* external scales corresponding to the distance between the operator and source, and the distance between the operator and sink. Instead, at $O(\alpha_S)$ the position-space diagrams can all be split up into a number of component pieces. For example, one diagram topology that appears in the $O(\alpha_S)$ contribution to the three-point mesonic function $\langle \overline{Q}\Gamma^\dagger q(-t_0,\vec{0})\cdot(\overline{Q}\Gamma_L q)(\overline{q}\Gamma_R Q)(0,\vec{0})\cdot\overline{q}\Gamma Q(t_0,\vec{0})\rangle$ can be written as

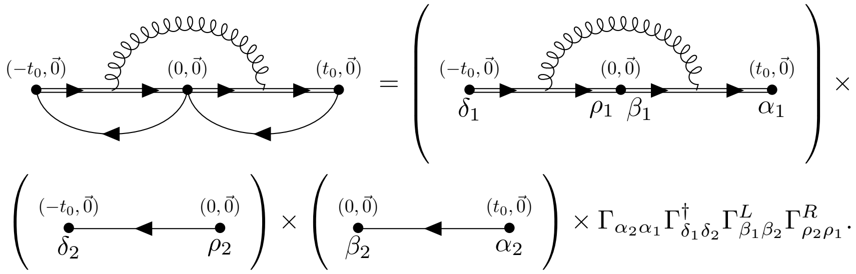

Here, $\alpha_i, \beta_i, \rho_i, \delta_i$ are Dirac-color indices. As well as the position-space propagators and self-energy diagrams, there are three $O(\alpha_S)$ diagrams to compute, corresponding to a gluon attaching to two heavy-quark propagators, a gluon attaching on one end to a heavy-quark propagator and on the other end to a light-quark propagator, and a gluon attaching to two light-quark propagators. In the case of the $\Delta Q = 0$ four-quark operators, the diagram with a gluon attaching to two heavy-quark propagators can be directly calculated in Minkowski space as follows:

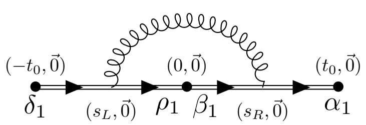

$$\begin{aligned}&= \left[\frac{1+\not{v}}{2}(igv_\mu T_A)\right]_{\alpha_1\beta_1}\left[\frac{1+\not{v}}{2}(igv_\mu T_A)\right]_{\rho_1\delta_1}\cdot\int_{-t_0}^{0} ds_L\int_0^{t_0} ds_R\int\frac{d^dk}{(2\pi)^d}\frac{-ie^{is_Lk-is_Rk}}{k^2}\\ &= [\not{v}T_A]_{\alpha_1\beta_1}[\not{v}T_A]_{\rho_1\delta_1}\left(-\frac{\alpha_S}{\pi\epsilon}-\frac{\alpha_S}{2\pi}\left(2+\log\left(-\frac{1}{4}e^{\gamma_E}\pi\mu^2t_0^2\right)\right)\right),\end{aligned} \tag{3.79}$$

where the static nature of the heavy quark has been utilized to integrate the vertex insertions at s_L and s_R along the line connecting the three operators. For the two diagrams involviong gluons attaching to light-quarks, additional master integrals are required. Relabelled from the basis from Appendix A of [9], and in Minkowski space, there is a Tripod diagram T_{LL} and a Wedge diagram W_{LL}:

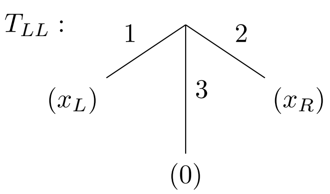

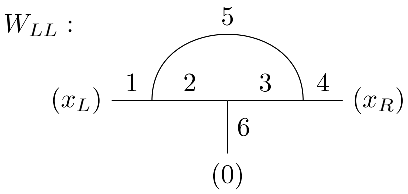

whose form are

$$T_{LL}(x_L,x_R;n_1,n_2,n_3) := \int\frac{d^dp_Ld^dp_R}{(2\pi)^{2d}}\frac{e^{ip_Lx_L}e^{-ip_Rx_R}}{(-p_L^2)^{n_1}(-(p_L-p_R)^2)^{n_2}(-p_R^2)^{n_3}}, \tag{3.80}$$

and

$$\begin{aligned}&W_{LL}(x_L,x_R;n_1,n_2,n_3,n_4,n_5,n_6) :=\\ &\int\frac{d^dp_Ld^dp_Rd^dk}{(2\pi)^{3d}}\frac{e^{ip_Lx_L}e^{-ip_Rx_R}}{(-p_L^2)^{n_1}(-(p_L-k)^2)^{n_2}(-(p_R-k)^2)^{n_3}(-p_R^2)^{n_4}(-k^2)^{n_5}(-(p_L-p_R)^2)^{n_6}}.\end{aligned} \tag{3.81}$$

The W_{LL} master integral has base cases whenever an internal line vanishes, or when two external lines vanish:

$$\begin{aligned}W_{LL}(n_2=0) &= I_{LL}(n_3,n_5)T_{LL}(x_L,x_R;n_1,-\frac{d}{2}+n_3+n_5+n_4,n_6)\\ W_{LL}(n_5=0) &= I_{LL}(n_2,n_3)T_{LL}(x_L,x_R;n_1,n_4,-\frac{d}{2}+n_2+n_3+n_6)\\ W_{LL}(n_3=0) &= I_{LL}(n_2,n_5)T_{LL}(x_L,x_R;-\frac{d}{2}+n_1+n_2+n_5,n_4,n_6)\\ W_{LL}(n_1=n_4=0) &= D_S^{-1}(x_L-x_R;n_5)T_{LL}(x_L,x_R;n_2,n_3,n_6)\\ W_{LL}(n_1=n_6=0) &= D_S^{-1}(x_L;n_2)T_{LL}(x_L,x_R;n_5,n_4,n_3)\\ W_{LL}(n_4=n_6=0) &= D_S^{-1}(-x_R;n_3)T_{LL}(n_1,n_5,n_2)\end{aligned} \tag{3.82}$$

In general, W_{LL} can be reduced to these base cases by use of integration-by-parts relations (derived from inserting $\partial_k \cdot k$ in front of the integrand of Eq. (3.81)):

$$W_{LL}(x_L, x_R; \vec{n}) = \frac{n_2 \mathbf{2}^+(\mathbf{5}^- - \mathbf{1}^-) + n_3 \mathbf{3}^+(\mathbf{5}^- - \mathbf{4}^-)}{d - n_2 - n_3 - 2n_5} W_{LL}(x_L, x_R; \vec{n}), \tag{3.83}$$

where $\vec{n} = (n_1, \cdots, n_6)$, and $m^{\pm} W(x_L, x_R, \vec{n}) = W(x_L, x_R, \vec{n}')$ with $\vec{n}' = \vec{n}$ for all components except the m-th component, $n'_m = n_m \pm 1$ (this is the notation used in Ref [35]). Eq. (3.83) reduces the W master integral to base cases where either n_2, n_3 or n_5 equals zero in the argument of W. In these cases, the integral reduces to a p-type integral and the T master integral, which can be performed explicitly using Schwinger parameters:

$$\frac{1}{A^n} = \frac{e^{-\frac{in\pi}{2}}}{\Gamma(n)} \int_0^\infty s^{n-1} e^{isA} \quad \text{where} \quad \mathrm{Im}(A) > 0, n > 0 \tag{3.84}$$

Before presenting the solution to T_{LL}, we first note that the solution should satisfy the following symmetry relations:

$$\begin{aligned} T_{LL}(x_L, x_R; n_1, n_2, n_3) &= T_{LL}(-x_R, -x_L; n_2, n_1, n_3) \\ &= T_{LL}(-x_L, x_R - x_L; n_3, n_2, n_1) \\ &= T_{LL}(x_L - x_R, -x_R; n_1, n_3, n_2) \\ &= T_{LL}(-x_L, -x_R; n_1, n_2, n_3) \end{aligned} \tag{3.85}$$

If any of the $n_i \leq 0$, then there are base cases for the T_{LL}

$$\begin{aligned} T_{LL}(x_L, x_R; x_1 = 0) &= D_S^{-1}(x_L; n_3) D_S^{-1}(x_L - x_R; n_2) \\ T_{LL}(x_L, x_R; x_2 = 0) &= D_S^{-1}(x_L - x_R; n_2) D_S^{-1}(-x_R; n_3) \\ T_{LL}(x_L, x_R; x_3 = 0) &= D_S^{-1}(x_L; n_1) D_S^{-1}(x_R; n_2) \end{aligned} \tag{3.86}$$

when one of the n_i are zero, and by differentiating against x one can attain the result for negative integer values of n_i:

$$\begin{aligned} T_{LL}(x_L, x_R; -|n_1|, |n_2|, |n_3|) &= (\partial^2_{(x_L)})^{|n_1|} T_{LL}(x_L, x_R; 0, |n_2|, |n_3|) \\ T_{LL}(x_L, x_R; |n_1|, -|n_2|, |n_3|) &= (\partial^2_{(x_R)})^{|n_2|} T_{LL}(x_L, x_R; |n_1|, 0, |n_3|) \\ T_{LL}(x_L, x_R; |n_1|, |n_2|, -|n_3|) &= \left((\partial_{(x_L)} + \partial_{(x_R)})^2\right)^{|n_3|} T_{LL}(x_L, x_R; |n_1|, |n_2|, 0) \end{aligned} \tag{3.87}$$

After completing the square, p_L, p_R can be integrated over using the following integral:

$$S(s; n) := \int \frac{d^d p}{(2\pi)^d} (-p^2)^n e^{is(p^2 + i\epsilon)} = \frac{i^{-\frac{d}{2} - n + 1} \Gamma(\frac{d}{2} + n)}{(4\pi)^{\frac{d}{2}} \Gamma(\frac{d}{2})} s^{-\frac{d}{2} - n} \quad \forall n \in \mathbb{Z}, n \geq 0 \tag{3.88}$$

To simplify the integral:

$$\begin{aligned} T_{LL}(x_1, x_2; n_1, n_2, n_3) = &\frac{i^{n_1 + n_2 + n_3}}{\Gamma(n_1)\Gamma(n_2)\Gamma(n_3)} \int_0^\infty ds_1 ds_2 ds_3 \; S(s_1 + s_3; 0) S\left(s_2 + \frac{s_1 s_3}{s_1 + s_3}; 0\right) \\ &s_1^{n_1 - 1} s_2^{n_2 - 1} s_3^{n_3 - 1} \exp\left(-i \frac{s_2 x_L^2 + s_3 (x_L - x_R)^2 + s_1 x_R^2}{4 s_1 s_2 + 4 s_2 s_3 + 4 s_1 s_3}\right) \exp\left(-\epsilon(s_1 + s_2 + s_3)\right) \end{aligned} \tag{3.89}$$

one can change variables to x_i where x_1, x_2 integrated from 0 to 1, and x_3 is integrated from 0 to ∞:

$$\begin{gathered} x_1 = \frac{s_3}{s_2 + s_3}, \quad x_2 = 1 - \frac{s_2 s_3}{s_1 s_2 + s_1 s_3 + s_2 s_3}, \quad x_3 = \frac{s_1 s_2 s_3}{s_1 s_2 + s_1 s_3 + s_2 s_3} \\ s_1 = \frac{x_3}{1 - x_2}, \quad s_2 = \frac{x_3}{x_1 x_2}, \quad s_3 = \frac{x_3}{(1 - x_1) x_2} \end{gathered} \tag{3.90}$$

for which x_2 and x_3 can be integrated over analytically to find:

$$\begin{gathered} T_{\mathrm{LL}}(x_1, x_2; n_1, n_2, n_3) = \frac{-\Gamma(\frac{d}{2} - n_1)\Gamma(d - n_1 - n_2 - n_3)}{\Gamma(n_2)\Gamma(n_3)\Gamma(\frac{d}{2}) 4^{n_1+n_2+n_3} \pi^d} (-x_R^2)^{-d+n_1+n_2+n_3} \\ \int_0^1 \mathrm{d}x (1 - x_1)^{-\frac{d}{2}+n_1+n_2-1} x_1^{-\frac{d}{2}+n_1+n_3-1} {}_2F_1\left(\frac{d}{2} - n_1, d - n_1 - n_2 - n_3, \frac{d}{2}, \frac{-(x_L - x_1 x_R)^2}{x_1(1 - x_1) x_R^2}\right) \end{gathered} \tag{3.91}$$

This matches the result given in [9], up to a minus sign due to the fact this calculation was performed in Minkowski space. Interestingly, the symmetries shown in Eq. (3.85) are not manifestly obvious in this answer, for example the $R \leftrightarrow L$ symmetry is broken by the choice of which momenta to integrate out first. An important case will be needed later is $T_{LL}(x_L, x_R; 1, 1, 1)$, in which case one can perform a series expansion in ϵ and swap the order with the integral over x, which does not lead to any additional divergences.

Using the results for T_{LL} and W_{LL}, diagrams with a gluon attaching to a heavy-quark propagator on one end and to a light-quark propagator on the other end can be calculated in Minkowski space, for instance:

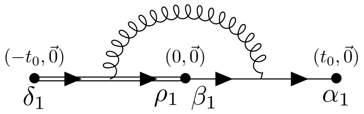

$$\begin{aligned} &= \int \frac{d^d p_L d^d p_R}{(2\pi)^{2d}} \int_{-t_0}^{0} ds_L \left[\frac{i}{\not{p}_R}(ig\gamma_\mu T_A)\frac{i}{\not{p}_R - \not{p}_L}\right]_{\alpha_1\beta_1} \left[\frac{1 + \not{v}}{2}(igv_\mu T^A)\right]_{\rho_1\delta_1} \frac{-ie^{ip_L^0 s_L - ip_R^0 t_0}}{p_L^2} \\ &= -ig^2 \int_{-t_0}^{0} ds_L \left[\gamma_\alpha \not{v} \gamma_\beta T^A\right]_{\alpha_1\beta_1} \left[\frac{1 + \not{v}}{2} T^A\right]_{\rho_1\delta_1} \frac{\partial}{\partial x_R^\alpha}\left(\frac{\partial}{\partial x_R^\beta} + \frac{\partial}{\partial x_L^\beta}\right) T(x_L, x_R; 1, 1, 1)\Big|_{\substack{x_L \to (s_L, \vec{0}) \\ x_R \to (t_0, \vec{0})}} \end{aligned} \tag{3.92}$$

Finally, the diagram with a gluon attaching to two light lines can be reduced to the W_{LL} master integral

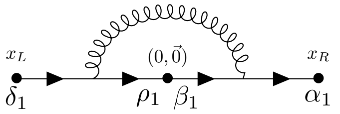

$$\begin{aligned} &= -ig^2 \mu^{4-d} (\gamma^\alpha \gamma^\mu \gamma^\beta T^a)_{\alpha\beta} (\gamma^\rho \gamma^\mu \gamma^\delta T^a)_{\rho\delta} \\ &\times \int \frac{d^d p_L d^d p_R d^d k}{(2\pi)^{3d}} \frac{e^{ip_L x_L - ip_R x_R} \, p_R^\alpha (p_R - k)^\beta (p_L - k)^\rho p_L^\delta}{(-p_L^2)(-(p_L - k)^2)(-(p_R - k)^2)(-p_R^2)(-k^2)}, \end{aligned} \tag{3.93}$$

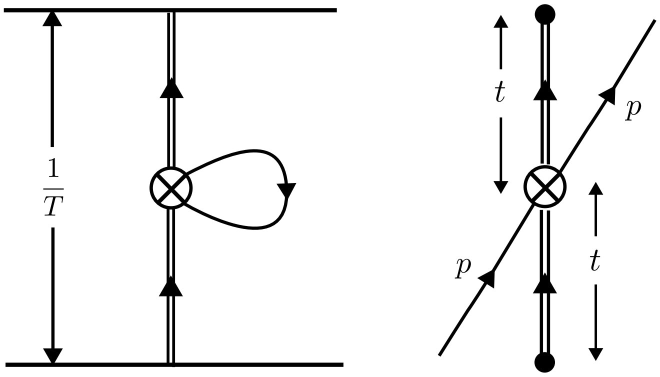

Figure 3.5: For isospin-singlet version of the operator, it's possible to evaluate the expectation values of the operator at finite temperature T to obtain renormalization conditions, as shown on the left. It is also possible to consider an RI-xMOM scheme (mixed position-space/momentum-space scheme) where the heavy quark propagates for a fixed time t before and after the operator, and the incoming/outgoing light quark is set to a fixed four-momenta p.

where the factors of p_L, p_R in the numerator can be handled by differentiating with respect to x_L, x_R. Calculating Eqs. (3.79), (3.92) and (3.93) at the relevant values of x_L and x_R is the main computation involved in calculating the $O(\alpha_S)$ contribution to the ratios of three-point correlation functions to two-point correlation functions presented in Table 3.3.

3.2.4 Alternate renormalization schemes for 4-quark HQET operators

There are many variations in position-space renormalization prescriptions, the simplest of which being changing the source/sink operators, or the time-separations used in the schemes defined in Sec. 3.2.2. For the isospin-singlet versions of the operators, it is also possible to consider expectation values of the operator at finite temperature T and obtain nonzero results for renormalization purposes, as shown on the left of Fig. 3.5. This is a simpler calculation compared to the three-point correlation functions required for the scheme proposed in Sec. 3.2.2, however it comes with a number of theoretical complexities. For this to be useful, one requires $T \gg \Lambda_{\mathrm{QCD}}$, and also to perform the perturbative calculations of this expectation value at finite temperature (requiring sums over Matsubara modes [46]), and furthermore requires subtraction of the linear power divergence of the static quark propagator, possibly simply by dividing by the Polyakov loop.

Alternatively, it is possible to use a modification of the RI-MOM scheme known as the RI-xMOM scheme [47] that utilises mixed position-space/momentum-space Green's functions to renormalize the four-quark operators. These types of schemes have been utilised have been utilised for similar operators utilised in hadronic structure measurements, where spacelike Wilson lines are renormalized via matching to an auxiliary field formalism. For HQET four-quark operators, a scheme such as shown on the right of Fig. 3.5 can be utilised, where the static quark is propagated for some fixed Euclidean time t before and after the operator insertion, and a light quark enters and exits with a given momentum p. The downside to such a construction is that it both requires gauge-fixing, and also requires additional renormalization conditions to renormalize the static self-energy divergence. For example, the scheme proposed in Ref [47] requires recovering the bare mass m_{stat} associated with the static quark action by:

$$m_{\text{stat}} = \frac{\mathrm{d}}{\mathrm{d}t} \log \mathrm{Tr} \left(\langle Q(t) \overline{Q}(0) \rangle \right) \tag{3.94}$$

where Q is the static field operator, and the propagator is just the Wilson line of length t. Using such a scheme would require calculations of the momentum-space Green's function of the four-quark operators in a fixed gauge, for example the Coulomb gauge, at fixed kinematics.

These schemes can also be extended to renormalize the isospin-singlet versions of the $\Delta B = 0$ four-quark operators. This requires introducing the additional operator $\overline{Q}Q$, due to the power-divergent mixings.Due to this additional operator, an additional source/sink pair will need to be introduced to fully constrain the new mixing matrix.

Bibliography

[1] Stefano Capitani. Lattice perturbation theory. *Phys. Rept.*, 382:113–302, 2003. doi: 10.1016/S0370-1573(03)00211-4.

[2] G. Martinelli, C. Pittori, Christopher T. Sachrajda, M. Testa, and A. Vladikas. A General method for nonperturbative renormalization of lattice operators. *Nucl. Phys. B*, 445:81–108, 1995. doi: 10.1016/0550-3213(95)00126-D.

[3] C. Sturm, Y. Aoki, N. H. Christ, T. Izubuchi, C. T. C. Sachrajda, and A. Soni. Renormalization of quark bilinear operators in a momentum-subtraction scheme with a nonexceptional subtraction point. *Phys. Rev. D*, 80:014501, 2009. doi: 10.1103/PhysRevD.80.014501.

[4] S. Elitzur. Impossibility of Spontaneously Breaking Local Symmetries. *Phys. Rev. D*, 12:3978–3982, 1975. doi: 10.1103/PhysRevD.12.3978.

[5] V. N. Gribov. Quantization of Nonabelian Gauge Theories. *Nucl. Phys. B*, 139:1, 1978. doi: 10.1016/0550-3213(78)90175-X.

[6] Leonardo Giusti, S. Petrarca, B. Taglienti, and N. Tantalo. Remarks on the gauge dependence of the RI / MOM renormalization procedure. *Phys. Lett. B*, 541:350–355, 2002. doi: 10.1016/S0370-2693(02)02243-8.

[7] Maria Luigia Paciello, Claudio Parrinello, Silvano Petrarca, Bruno Taglienti, and Anastassios Vladikas. Gribov copies and smeared correlation functions in lattice QCD. *Phys. Lett. B*, 289:405–410, 1992. doi: 10.1016/0370-2693(92)91240-A.

[8] V. Gimenez, Leonardo Giusti, S. Guerriero, V. Lubicz, G. Martinelli, S. Petrarca, J. Reyes, B. Taglienti, and E. Trevigne. Non-perturbative renormalization of lattice operators in coordinate space. *Phys. Lett. B*, 598:227–236, 2004. doi: 10.1016/j.physletb.2004.07.053.

[9] M. Costa, I. Karpasitis, T. Pafitis, G. Panagopoulos, H. Panagopoulos, A. Skouroupathis, and G. Spanoudes. Gauge-invariant renormalization scheme in QCD: Application to fermion bilinears and the energy-momentum tensor. *Phys. Rev. D*, 103(9):094509, 2021. doi: 10.1103/PhysRevD.103.094509.

[10] K. G. Chetyrkin and A. Maier. Massless correlators of vector, scalar and tensor currents in position space at orders α_s^3 and α_s^4: Explicit analytical results. *Nucl. Phys. B*, 844:266–288, 2011. doi: 10.1016/j.nuclphysb.2010.11.007.

[11] K. G. Chetyrkin and A. G. Grozin. Correlators of heavy–light quark currents in HQET: OPE at three loops. *Nucl. Phys. B*, 976:115702, 2022. doi: 10.1016/j.nuclphysb.2022.115702.

[12] Georg Bergner, Marios Costa, Haralambos Panagopoulos, Stefano Piemonte, I. Soler Calero, and Gregoris Spanoudes. Nonperturbative renormalization of the supercurrent in N=1 supersymmetric Yang-Mills theory. *Phys. Rev. D*, 107(3):034502, 2023. doi: 10.1103/PhysRevD.107.034502.

[13] Salvatore Cali, Krzysztof Cichy, Piotr Korcyl, and Jakob Simeth. Running coupling constant from position-space current-current correlation functions in three-flavor lattice QCD. *Phys. Rev. Lett.*, 125:242002, 2020. doi: 10.1103/PhysRevLett.125.242002.

[14] Krzysztof Cichy, Karl Jansen, and Piotr Korcyl. Non-perturbative renormalization in coordinate space for $N_f = 2$ maximally twisted mass fermions with tree-level Symanzik improved gauge action. *Nucl. Phys. B*, 865:268–290, 2012. doi: 10.1016/j.nuclphysb.2012.08.006.

[15] M. Tomii, G. Cossu, B. Fahy, H. Fukaya, S. Hashimoto, T. Kaneko, and J. Noaki. Renormalization of domain-wall bilinear operators with short-distance current correlators. *Phys. Rev. D*, 94(5):054504, 2016. doi: 10.1103/PhysRevD.94.054504.

[16] Gregoris Spanoudes, Constantia Alexandrou, Jacob Finkenrath, Kyriakos Hadjiyiannakou, Haralambos Panagopoulos, and Shuhei Yamamoto. Non-perturbative renormalization of quark and gluon operators using a gauge-invariant scheme. *PoS*, LATTICE2022:125, 2023. doi: 10.22323/1.430.0125.

[17] Piotr Korcyl, Christoph Lehner, and Tomomi Ishikawa. Non-perturbative renormalization of the static quark theory in a large volume. *PoS*, LATTICE2015:254, 2016. doi: 10.22323/1.251.0254.

[18] Ivan Soler, Georg Bergner, Marios Costa, Haralambos Panagopoulos, Gregoris Spanoudes, and Stefano Piemonte. Supercurrent renormalization of $\mathcal{N} =$ supersymmetric Yang-Mills theory on the lattice. *PoS*, LATTICE2022: 222, 2023. doi: 10.22323/1.430.0222.

[19] Masaaki Tomii. Towards non-perturbative matching of three/four-flavor Wilson coefficients with aposition-space procedure. *PoS*, LATTICE2018:216, 2019. doi: 10.22323/1.334.0216.

[20] Masaaki Tomii. Non-perturbative matching of three/four-flavor Wilson coefficients with a position-space procedure. *PoS*, LATTICE2019:174, 2020. doi: 10.22323/1.363.0174.

[21] Estia Eichten and Brian Russell Hill. An Effective Field Theory for the Calculation of Matrix Elements Involving Heavy Quarks. *Phys. Lett. B*, 234:511–516, 1990. doi: 10.1016/0370-2693(90)92049-O.

[22] Rainer Sommer. Non-perturbative Heavy Quark Effective Theory: Introduction and Status. *Nucl. Part. Phys. Proc.*, 261-262:338–367, 2015. doi: 10.1016/j.nuclphysbps.2015.03.022.

[23] M. Neubert and Christopher T. Sachrajda. Spectator effects in inclusive decays of beauty hadrons. *Nucl. Phys. B*, 483:339–370, 1997. doi: 10.1016/S0550-3213(96)00559-7.

[24] Alexander Lenz. Lifetimes and heavy quark expansion. *Int. J. Mod. Phys. A*, 30(10):1543005, 2015. doi: 10.1142/S0217751X15430058.

[25] F. Gabbiani, E. Gabrielli, A. Masiero, and L. Silvestrini. A Complete analysis of FCNC and CP constraints in general SUSY extensions of the standard model. *Nucl. Phys. B*, 477:321–352, 1996. doi: 10.1016/0550-3213(96)00390-2.

[26] Tomomi Ishikawa, Yasumichi Aoki, Jonathan M. Flynn, Taku Izubuchi, and Oleg Loktik. One-loop operator matching in the static heavy and domain-wall light quark system with O(a) improvement. *JHEP*, 05:040, 2011. doi: 10.1007/JHEP05(2011)040.

[27] Massimo Di Pierro and Christopher T. Sachrajda. A Lattice study of spectator effects in inclusive decays of B mesons. *Nucl. Phys. B*, 534:373–391, 1998. doi: 10.1016/S0550-3213(98)00580-X.

[28] Massimo Di Pierro, Christopher T Sachrajda, and Christopher Michael. An Exploratory lattice study of spectator effects in inclusive decays of the Λ_b baryon. *Phys. Lett. B*, 468:143, 1999. doi: 10.1016/S0370-2693(99)01166-1. [Erratum: Phys.Lett.B 525, 360–360 (2002)].

[29] V. Gimenez and J. Reyes. Calculation of the continuum lattice HQET matching for the complete basis of four fermion operators: Reanalysis of the B0 - anti-B0 mixing. *Nucl. Phys. B*, 545:576–606, 1999. doi: 10.1016/S0550-3213(98)00867-0.

[30] Joshua Lin, William Detmold, and Stefan Meinel. Lattice Study of Spectator Effects in b-hadron Decays. *PoS*, LATTICE2022:417, 2023. doi: 10.22323/1.430.0417.

[31] Joshua Lin, William Detmold, and Stefan Meinel. Position-space renormalization schemes for four-quark operators in HQET. *JHEP*, 07:188, 2024. doi: 10.1007/JHEP07(2024)188.

[32] Gerard 't Hooft and M. J. G. Veltman. Regularization and Renormalization of Gauge Fields. *Nucl. Phys. B*, 44: 189–213, 1972. doi: 10.1016/0550-3213(72)90279-9.

[33] S. Groote, J. G. Korner, and Oleg I. Yakovlev. Two loop anomalous dimensions of heavy baryon currents in heavy quark effective theory. *Phys. Rev. D*, 54:3447–3456, 1996. doi: 10.1103/PhysRevD.54.3447.

[34] A. G. Grozin and Oleg I. Yakovlev. Baryonic currents and their correlators in the heavy quark effective theory. *Phys. Lett. B*, 285:254–262, 1992. doi: 10.1016/0370-2693(92)91462-I.

[35] Andrey G. Grozin. Lectures on multiloop calculations. *Int. J. Mod. Phys. A*, 19:473–520, 2004. doi: 10.1142/S0217751X04016775.

[36] Wolfram Research, Inc. Mathematica, Version 14.0. URL `https://www.wolfram.com/mathematica`. Champaign, IL, 2024.

[37] S. Laporta. High-precision calculation of multiloop Feynman integrals by difference equations. *Int. J. Mod. Phys. A*, 15:5087–5159, 2000. doi: 10.1142/S0217751X00002159.

[38] Patricia Ball, Vladimir M. Braun, and Einan Gardi. Distribution Amplitudes of the Lambda(b) Baryon in QCD. *Phys. Lett. B*, 665:197–204, 2008. doi: 10.1016/j.physletb.2008.06.004.

[39] Vladimir M. Braun et al. Nucleon distribution amplitudes and proton decay matrix elements on the lattice. *Phys. Rev. D*, 79:034504, 2009. doi: 10.1103/PhysRevD.79.034504.

[40] R. M. Baxter et al. Quenched heavy light decay constants. *Phys. Rev. D*, 49:1594–1605, 1994. doi: 10.1103/PhysRevD.49.1594.

[41] Stefan Herrlich and Ulrich Nierste. Evanescent operators, scheme dependences and double insertions. *Nucl. Phys. B*, 455:39–58, 1995. doi: 10.1016/0550-3213(95)00474-7.

[42] Marco Ciuchini, E. Franco, V. Lubicz, G. Martinelli, I. Scimemi, and L. Silvestrini. Next-to-leading order QCD corrections to Delta F = 2 effective Hamiltonians. *Nucl. Phys. B*, 523:501–525, 1998. doi: 10.1016/S0550-3213(98)00161-8.

[43] Christoph Lehner and Christian Sturm. Matching factors for Delta S=1 four-quark operators in RI/SMOM schemes. *Phys. Rev. D*, 84:014001, 2011. doi: 10.1103/PhysRevD.84.014001.

[44] Marco Ciuchini, E. Franco, G. Martinelli, L. Reina, and L. Silvestrini. An Upgraded analysis of epsilon-prime epsilon at the next-to-leading order. *Z. Phys. C*, 68:239–256, 1995. doi: 10.1007/BF01566672.

[45] D. Becirevic, V. Gimenez, G. Martinelli, M. Papinutto, and J. Reyes. B parameters of the complete set of matrix elements of delta B = 2 operators from the lattice. *JHEP*, 04:025, 2002. doi: 10.1088/1126-6708/2002/04/025.

[46] Claude W. Bernard. Feynman Rules for Gauge Theories at Finite Temperature. *Phys. Rev. D*, 9:3312, 1974. doi: 10.1103/PhysRevD.9.3312.

[47] Jeremy Green, Karl Jansen, and Fernanda Steffens. Nonperturbative Renormalization of Nonlocal Quark Bilinears for Parton Quasidistribution Functions on the Lattice Using an Auxiliary Field. *Phys. Rev. Lett.*, 121(2): 022004, 2018. doi: 10.1103/PhysRevLett.121.022004.

Chapter 4

Spectator Effects

Some content in this section adapted with permission from the following references:

Joshua Lin, William Detmold, and Stefan Meinel. Lattice Study of Spectator Effects in b-hadron Decays. PoS, LATTICE2022:417, 2023. doi: 10.22323/1.430.0417.

Joshua Lin, William Detmold, and Stefan Meinel. Position-space renormalization schemes for four-quark opera- tors in HQET. JHEP, 07:188, 2024. doi: 10.1007/JHEP07(2024)188.

Contents

A large part of what makes Lattice-QCD interesting is that there is not always a straightforward connection between quantities that can be efficiently calculated in Euclidean time, and quantities of phenomenological interest. There are theoretical guarentees that reconstructing all the information of the Minkowski theory is possible in-principle, sketched in Fig. 4.1. In the top-left corner, the

$$\begin{tikzcd}
\text{Wightman Axioms} & \begin{array}{c}\text{Lattice Correlation Functions}\\ \langle 0|\phi(x_1)\cdots\phi(x_n)|0\rangle_{\mathrm{E}}\end{array} \arrow[d, "\text{Continuum Limit}"] \\
\begin{array}{c}\text{Wightman Functions}\\ \langle 0|\phi(x_1)\cdots\phi(x_n)|0\rangle\end{array} \arrow[u, "\text{Wightman Reconstruction Theorem}"] & \begin{array}{c}\text{Schwinger Functions}\\ \langle 0|\phi(x_1)\cdots\phi(x_n)|0\rangle_{\mathrm{E}}\end{array} \arrow[l, "\text{OS Reconstruction Theorem}"']
\end{tikzcd}$$

Figure 4.1: Sketch of how (in principle) a Minkowski-time theory is reconstructed from lattice-discretised Euclidean-time correlation functions. The correlation functions here are written in terms of some representative scalar field $\phi(x)$, but there is no obstruction to using gauge, or fermion, degrees of freedom.

Wightman Axioms [1] are a particular formalisation of what a Quantum Field Theory in Minkowski space-time *is*, and state that fields should be operator-valued tempered distributions satisfying certain axioms (e.g. Poincare covariance, causality). By the Wightman reconstruction theorem, the data of a collection of fields satisfying the Wightman axioms is *equivalent* to the data of 'Wightman functions' (correlation functions of fields in Minkowski time) satisfying certain axioms. By the Osterwalder-Schrader reconstruction theorem [2], it is possible to formally Wick rotate the information contained in 'Schwinger functions' (correlation functions of fields in Euclidean space-time) to reconstruct the corresponding Minkowski-time functions. Lattice-QCD provides noisy measurements of lattice-discretised Euclidean correlation functions, and hence by taking the appropriate infinite statistics and continuum limits, *in principle* the full data of the Minkowski-time theory should be able to be recovered.[1]

Though real-time information is recoverable *in principle*, the actual task of finding an algorithm to recover a given physical quantity from Euclidean data varies in difficulty. Certain observables can

---

[1] This is, of course, with the caveat that in $3+1$d, there have been no proofs that the continuum limit of *any* interacting Lattice-QFT exists. Simple examples one might consider, such as the lattice scalar ϕ^4 theory or Lattice-QED, turn out to not have any continuum limits. In the case of ϕ^4 theory, there were early numerical studies providing strong evidence for this fact [3], much later confirmed by formal proofs of the quantum triviality of the $3+1$d theory [4]. For Lattice-QED, there is a perturbative Landau pole that suggests that the theory may not be UV-complete. In fact, studies [5] of Lattice-QED suggest that the theory appears trivial, and that the approximate location of the Landau pole is inaccessible to Lattice-QED for *any* choice of bare parameters due to spontaneous chiral symmetry breaking. The interacting Lattice-QFTs that have the most numerical evidence of having well-behaved continuum limits are asymptotically free, vector-like gauge theories such as QCD. Proving that the continuum limit exists for QCD essentially amounts to a solution of the associated Clay Millenium Problem.

be straightforwardly computed from lattice discretised correlation functions. For example, by fitting two-point functions to spectral decompositions, one can extract masses and overlap factor matrix elements:

$$\langle \mathcal{O}(t)\mathcal{O}^{\dagger}(0)\rangle = \sum_{n=1}^{\infty}\langle 0|\mathcal{O}|n\rangle\ e^{-E_n t}\ \langle n|\mathcal{O}^{\dagger}|0\rangle. \tag{4.1}$$

Both the energies and overlap factors differ from their bare continuum values by $O(a^m)$ errors, where a is the lattice-spacing and m is the order to which the action and operators used are improved. Certain flavour physics matrix elements where both in and out states consist of (at most) a single stable hadron can be extracted from three-point-correlation functions, and are therefore sometimes referred to as 'gold-plated' [6, 7]. In contrast vacuum condensates such as $\langle 0|F^A_{\mu\nu}F^A_{\mu\nu}|0\rangle$ that look simple to evaluate as they only require inserting a single operator into the spacetime volume; are actually plagued with power-divergent mixings in the continuum limit, as well as renormalon issues in their definition [8][2].

Inclusive decay rates of hadrons are one of the more theoretically difficult observables to extract. As it is unrealistic to try and sum over all decay modes of a given state, it is common to focus instead on utilising the optical theorem to write the inclusive decay rate $\Gamma(H)$ of a hadron H as:

$$\Gamma(H) = \frac{1}{2m_H}\langle H|\mathcal{T}|H\rangle, \quad \mathcal{T} = \mathrm{Im}\left(i\int \mathrm{d}^4x T[\mathcal{H}_{\text{eff}}(x)\mathcal{H}_{\text{eff}}(0)]\right), \tag{4.2}$$

where m_H is the mass of the hadron H, and $\mathcal{H}_{\text{eff}}$ denotes the effective hamiltonian that mediates the decay. Note that the optical theorem, as expressed in Eq. (4.2), is the leading order contribution under the assumption that $\mathcal{H}_{\text{eff}}$ is suppressed, and $\mathcal{T}$ contains corrections of the order of $\sim \mathcal{H}^4_{\text{eff}}$. There are various methods being explored to facilitate calculations of Eq. (4.2) when H is a b-hadron. The Heavy-Quark Expansion starts by Taylor-expanding the two currents in Eq. (4.2) as a sum over local operators (the Operator-Product-Expansion (OPE) as covered in Sec. 4.1.2), to write the inclusive rate as a product of perturbatively computible coefficients (which are functions of m_b), with nonperturbative matrix elements. One immediate problem with this approach is that because all the operators appearing in the OPE have the same quantum numbers, they mix under renormalization. This is exacerbated in Lattice-QCD studies, because the operators appear with lower mass dimensions, leading to power-divergent mixings in $\frac{1}{a}$ as the continuum limit is taken. To deal with these issues, various interesting proposals to provide theoretical calculations are being considered:

- A class of recently proposed methods involves measuring the corresponding 4-point Euclidean correlation functions and recovering the inclusive decay rates by analytic continuation/spectral reconstruction [9–12]. Ref. [12] numerically demonstrates the viability of one such method at unphysical parameters and includes a suite of comparisons to OPE predictions.

---

[2] Note that unlike the gluon condensate, the chiral condensate $\langle\overline{\psi}\psi\rangle$ is physical, due to its appearance in the Gell-mann-Oakes-Renner relation (see Footnote 13 of Ref. [8])

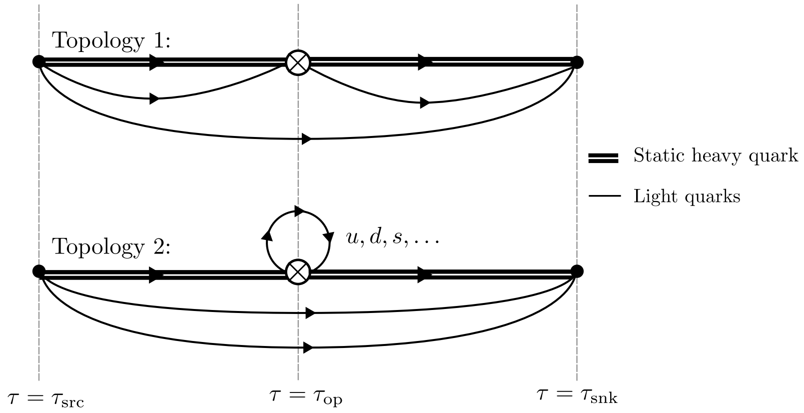

Figure 4.2: The two types of contractions that are relevant for Spectator Effect calculations, in the case that the source and sink are given by heavy-light-light baryonic operators. Topology 1 contractions appear in both flavour non-singlet and flavour singlet contributions. Topology 2 is the so-called 'eye-contraction' appearing in flavour singlet calculations that cause the operator to mix with lower dimensional operators.

- A Heavy-Quark Expansion exists for the masses of the heavy mesons, where the perturbative coefficients are different from those appearing in the expansion for inclusive rates, but the matrix elements are universal. In Ref. [13], the b-hadron masses were calculated with lattice-QCD for multiple different values of the b-quark mass, which allows for the matrix elements to be extracted by fits, providing predictions for the inclusive lifetimes.

- By studying the Lattice-regularised theory at a fixed physical Wilson-flow time (see Sec. 2.2.3), the lattice-spacing scale a^{-1} is effectively removed from the system and replaced by the flow-time scale $t^{-\frac{1}{2}}$. Operators of different mass dimensions that previously mixed with inverse powers of the lattice spacing now mix with powers of the flow-time scale, which does not diverge in the continuum limit. To match these operators to perturbatively defined schemes such as $\overline{\mathrm{MS}}$ requires computing a short flow-time expansion of the operators [14, 15]. A similar 'window problem' to nonperturbative renormalization arises, where $\sqrt{t} \gg a$ is required to remove lattice discretisation artifacts, but $\sqrt{t} \ll \Lambda_{\mathrm{QCD}}^{-1}$ is required for perturbatively-computed short-flow-time results to be trustworthy. This scheme has recently been explored as an idea to regulate the OPE appearing for heavy hadron inclusive lifetimes in Ref. [16].

- The standard Heavy-Quark Expansion matches the QCD operators appearing in the OPE to HQET operators. This has the effect of suppressing many of the power divergences, as the HQET action provides additional symmetries preventing certain mixings. Not all power-divergences are suppressed though. Consider for example four-quark operators of the form

$\tau_{ij}(\overline{Q}\Gamma_L q_i)(\overline{q}_j\Gamma_R Q)$, where i, j are flavour indices, and τ is a light-quark flavour-matrix. If τ is in the non-singlet channel (the adjoint representation of $\mathrm{SU}(N_f)$), these operators are protected from power-divergent mixings, and constitute the non-singlet contribution to the Spectator Effects wherein light quarks participate in the decay of the heavy hadron. If τ however is in the singlet channel (identity matrix), the light quarks can contract in an 'eye-diagram' as shown in Fig. 4.2, causing power-divergent mixing with operators such as $\overline{Q}Q$.

- After a Heavy-Quark Expansion has been performed, it is possible to determine the matrix elements via Sum Rules calculations [17]. The general idea is to link matrix elements of the form $\langle H|\mathcal{O}|H\rangle$ that are required for the Heavy-Quark Expansion to three-point correlation functions of the form $\langle 0|\mathcal{J}(t)\mathcal{O}(0)\mathcal{J}^\dagger(-t)|0\rangle$, where $\mathcal{J}$ excites the hadronic state of interest H. Then, these three-point correlation functions can be expanded in an OPE, expressing them in terms of vacuum condensates such as the chiral $\langle 0|\overline{\psi}\psi|0\rangle$ and gluon $\langle 0|F_A^{\mu\nu}F_A^{\mu\nu}|0\rangle$ condensates, which can be either fitted from other sum-rules expressions, or nonperturbatively calculated using Lattice-QCD.

In light of the list of new approaches being investigated, a rigorous study of the OPE expansion provides a much needed cross-check between the different methods. This section focuses on a numerical study of the matrix elements appearing in the Heavy-Quark Expansion. The OPE matrix elements are also interesting in light of the tension between inclusive extractions (which performs fits of experimental data to OPE predictions) and exclusive extractions of the CKM matrix elements, as discussed in Sec. 1.2. Sec. 4.1 provides a review of the theory of heavy-hadron decays, and how they can be calculated with the Heavy-Quark Expansion. Lattice-QCD computations were performed at three separate lattice spacings of the RBC-UKQCD (2+1)-flavor Domain Wall Fermion ensembles, and in Sec. 4.2.8, a calculation of the heavy-light decay constant f_B^{HQET} which describes purely leptonic decays of heavy-light mesons is presented. In Sec. 4.2.9, a calculation of the Spectator Effect matrix elements for the heavy-light meson are presented.

4.1 Theory of Spectator Effects

4.1.1 b-hadron decays

After the discovery of CP violation in kaon decays [18], it was proposed that a third generation of quarks (now known as the bottom and top quarks) could explain the origin of CP violation in the Standard Model [19]. Four years later in 1977 the bottom quark was discovered at Fermilab [20]. Starting in the 1990s, accelerators and detectors known as B-factories were designed with the purpose of providing precision measurements of b-hadron properties. For example, both the Belle at KEKB and Babar at SLAC experiments used electron-positron collisions with center of mass energies tuned to the $\Upsilon(4S)$ resonance, which decays to $\overline{B}B$ with a branching reatio greater than 96%. In more recent years, LHCb [21] has further pushed our understanding of b-physics.

Thanks to these experimental efforts, many of the masses and lifetimes of many b-hadrons are

J^P	Name and quark content	Mass (GeV)	Lifetime (picoseconds)
0^-	$B^+(\bar{b}u)$	5279.41(7)	1.638(4)
0^-	$B^0(\bar{b}d)$	5279.63(20)	1.517(4)
0^-	$B_s^0(\bar{b}s)$	5366.91(11)	1.516(6)
$\frac{1}{2}^+$	$\Lambda_b^0(udb)$	5619.57(16)	1.468(9)
$\frac{1}{2}^+$	$\Xi_b^-(dsb)$	5797.0(4)	1.570(23)
$\frac{1}{2}^+$	$\Xi_b^0(usb)$	5791.7(4)	1.477(32)
$\frac{1}{2}^+$	$\Omega_b^-(ssb)$	6045.8(8)	1.64(16)

Table 4.1: Table of selected b-mesons and b-baryons, and their associated J^P quantum numbers (J = angular momentum, P = parity), mass and lifetimes. Note that both parity and quark content are *not* actual quantum numbers of the Standard Model due to parity and flavour violating processes. They are however quantum numbers of QCD, and are approximately conserved up to processes occuring at the electroweak scale, thus hadrons can often be associated with parity and quark contents.

known to percent or sub-percent precision, as shown in Table 4.1. The fact that all the masses of the different hadrons are approximately the same is not so surprising, given that the masses are all of the form $m_b + O(\Lambda_{\text{QCD}})$ given the heavy mass of the b-quark. What perhaps is surprising is their lifetimes are approximately the same as well. As explained in Sec. 4.1.2, the Heavy-Quark Expansion provides the reason: the dominant decay modes of b-hadrons correspond to decays of the b-quark within the b-hadron that do not involve the light quark degrees of freedom. For example, some primary decay channels of the B-mesons are shown schematically in the following diagrams:

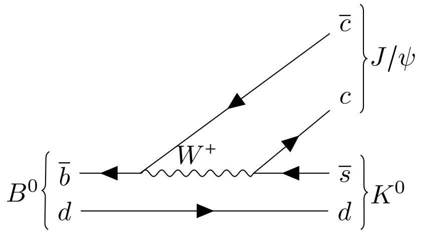

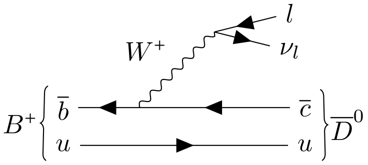

Note that these decays do not involve the light quark, hence they are ‘spectator independent’. In contrast, a decay mode of a B-meson which involves the light quark is a ‘weak annihilation’ process, as shown in the following figure:

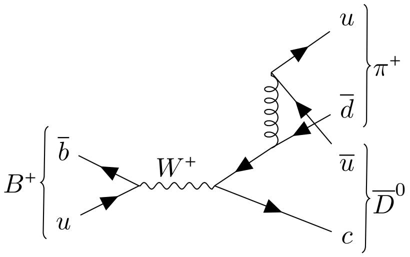

These processes are suppressed relative to decays of the b-quark in isolation, however they currently are much less well determined theoretically. The rest of this section focuses on the phenomenology of these Spectator Effects, and Sec. 4.2 presents a lattice-QCD calculation of the corresponding matrix elements.

4.1.2 Heavy Quark Expansion

The large scale separations between the QCD degrees of freedom and the electroweak scale makes practically including electroweak bosons in Lattice-QCD calculations difficult - not to mention the fact that there have been no convincing demonstrations of lattice discretisations of 3 + 1d non-Abelian chiral gauge theories (see Sec. 2.2.2). Instead, flavour-physicists utilise this scale separation to define effective field theories describing the low-energy degrees of freedom. A general method for constructing effective quantum field theories is to split the degrees of freedom of an original Lagrangian into light, X, and heavy, Y, degrees of freedom, and integrate out the heavy degrees of freedom order-by-order. Schematically, the procedure can be described by:

$$\mathcal{L}(X,Y) = \mathcal{L}_{\text{light}}(X) + \mathcal{L}_{\text{heavy}}(X,Y) = \mathcal{L}_{\text{light}}(X) + \sum_{n=1}^{\infty} \frac{1}{\Lambda_Y^n} \mathcal{L}^{(n)}(X) \tag{4.3}$$

where Λ_Y is a mass parameter associated with the heavy degrees of freedom, $\mathcal{L}^{(n)}(X)$ is a space of n-dimensional operators involving the X fields, and the matching is perfomed in such a way as to preserve correlation functions of the light degrees of freedom. In the case of defining an effective theory of weak decays, the heavy degrees of freedom that are to be integrated out are the $W^\pm, Z$ bosons, the Higgs boson, as well as the top quark. To approach this procedure formally in the case of integrating out the W-bosons (which is the dominant effect to be considered in most electroweak decays of heavy hadrons), one considers the part of the Standard Model Lagrangian involving the weak bosons after electroweak-symmetry breaking:

$$\begin{aligned} \mathcal{L}_W = &-\frac{1}{2}(\partial_\mu W^+_\nu - \partial_\nu W^+_\mu)(\partial^\mu W^{-\nu} - \partial^\nu W^{-\mu}) + M_W^2 W^+_\mu W^{-\mu} \\ &+ \frac{g_L}{2\sqrt{2}}(J^+_\mu W^{+\mu} + J^-_\mu W^{-\mu}) \quad \text{where} \quad J^+_\mu = \bar{\mathbf{u}}^i_L \gamma^\mu V^{ij} \mathbf{d}^j_L, \quad J^-_\mu = (J^+_\mu)^\dagger \end{aligned} \tag{4.4}$$

In the equation above, the currents $J^\pm_\mu$ encode only the coupling to quarks: leptonic decays can also be included by modifying the $J^\pm_\mu$ currents to include the leptonic couplings. The explicit solution of the contribution of this part of the Lagrangian to the partition function is given by:

$$\begin{aligned}
Z_W &= \int \mathcal{D}W^{\pm}\exp(i\int \mathrm{d}^4x\mathcal{L}_W) \\
&= \int \mathcal{D}W^{\pm}\exp\left(i\int \mathrm{d}^4x\ \mathrm{d}^4y\ W^+_\mu(x)K^{\mu\nu}(x,y)W^-_\nu(y) + i\frac{g_L}{2\sqrt{2}}\int \mathrm{d}^4x\ \left(J^+_\mu W^{+\mu}(x) + J^-_\mu W^{-\mu}(x)\right)\right) \\
&\propto \exp\left(-i\int \mathrm{d}^4x\ \mathrm{d}^4y\ \frac{g_L^2}{8}J^-_\mu(x)(K^{-1})^{\mu\nu}(x,y)J^+_\nu(y)\right),
\end{aligned} \tag{4.5}$$

where K^{-1} denotes the propagator:

$$K_{\mu\nu}(x,y) = \delta^{(4)}(x-y)[g_{\mu\nu}(\partial^2 + M_W^2) - \partial_\mu\partial_\nu], \quad K^{-1}_{\mu\nu}(k) = \frac{-1}{k^2 - M_W^2}\left(g_{\mu\nu} - \frac{k_\mu k_\nu}{M_W^2}\right). \tag{4.6}$$

Thus, the W bosons have been integrated out and replaced by a nonlocal Lagrangian. The idea now is to use an OPE to expand K^{-1} in terms of local operators as a series in $1/M_W^2$, when the interaction energy is small. To lowest order in M_W^{-1}, the propagator is $K^{-1}_{\mu\nu} = \delta^{(4)}(x-y)g_{\mu\nu}/M_W^2$, in which case the charged current interaction Lagrangian becomes:

$$\mathcal{L}_{\text{eff}} = -\frac{G_F}{\sqrt{2}}J^-_\mu(x)J^{+\mu}(x), \qquad G_F := \frac{\sqrt{2}g_L^2}{8M_W^2}, \tag{4.7}$$

where G_F is known as Fermi's constant. For the quark-only couplings, the effective Lagrangian is spanned by the following two operators:

$$O_1 = (\bar{c}^i_L\gamma^\mu b^i_L)(\bar{d}^j_L\gamma_\mu u^j_L), \quad O_2 = (\bar{c}^i_L\gamma^\mu b^j_L)(\bar{d}^j_L\gamma_\mu u^i_L), \tag{4.8}$$

which mix under renormalization, where the i,j are indexing the color indices. Note that both O_1, O_2 are the only Lorentz, and colour singlets in the tensor representation $\bar{c}_L \otimes b_L \otimes \bar{d}_L \otimes u_L$. The operators are protected from mixing with operators containing right-handed fields by approximate chiral symmetry.

Supposing that the decay of a hadron H is governed by an effective hamiltonian $\mathcal{H}_{\text{eff}}$, its decay into arbitrary final states can be written as:

$$\Gamma(H) = \frac{1}{2m_H}\sum_X \int_{\text{PhaseSpace}}(2\pi)^4\delta^{(4)}(p_H - p_X)|\langle X|\mathcal{H}_{\text{eff}}|B\rangle|^2, \tag{4.9}$$

where X indexes the set of allowed final states. Note that the integral over phase space depends on the particular choice of X, for instance different numbers of particles in the final states requires different phase space integrals. The optical theorem transforms the total decay rate to:

$$\Gamma(H) = \frac{1}{2m_H}\langle H|\mathcal{T}|H\rangle, \quad \mathcal{T} = \text{Im}\left[i\int \mathrm{d}^4x\ T[\mathcal{H}_{\text{eff}}(x)\mathcal{H}_{\text{eff}}(0)]\right]. \tag{4.10}$$

Note that the energy released in the decay of a b-quark is a large scale compared to Λ_{QCD}, due in part to the gap between the charm and bottom quark masses. This large decay energy causes the integration over current insertions in Eq. (4.10) to be dominated by the region where $x^2 \ll \Lambda_{\text{QCD}}$, and *another* OPE can be performed by expanding the product of currents as a local sum of QCD operators with the same quantum numbers. Because the flavour symmetry is enforced in pure QCD, all these operators will be $\Delta B = 0$ operators meaning that the net bottom quark number is unchanged by the operator, and it takes the form of $\bar{b}_{i,\alpha} b_{j,\beta}$ possibly contracted with additional fields (where i, j are colour indices, and α, β are spin indices). To be precise, the lowest three operators in the OPE take the form [22]:

$$\begin{aligned}\Gamma(H_b) = \frac{G_F^2 m_b^5}{192\pi^3}|V_{cb}|^2 \Bigg\{ c_3 \frac{\langle H_b|\bar{b}b|H_b\rangle}{2M_{H_b}} + \frac{c_5}{m_b^2}\frac{\langle H_b|\bar{b}g_s\sigma_{\mu\nu}F^{\mu\nu}b|H_b\rangle}{2M_{H_b}} \\ + \frac{c_6}{m_b^3}\frac{\langle H_b|(\bar{b}\Gamma_L q)(\bar{q}\Gamma_R b)|H_b\rangle}{M_{H_b}} + O\left(\frac{1}{m_b^4}\right)\Bigg\},\end{aligned} \tag{4.11}$$

where c_3, c_5, c_6 are perturbatively calculable Wilson coefficients, and $\sigma_{\mu\nu} = i[\gamma_\mu, \gamma_\nu]/2$. Γ_L, Γ_R are spin-colour structures that will be specified later. The QCD operators appearing in this OPE all mix with each other as they have the same quantum numbers by definition, leading to power divergences as the continuum limit is approached for a lattice regularisation.

To suppress this mixing, the QCD operators can be matched to HQET:

$$\begin{aligned}\Gamma(H_b) = \frac{G_F^2 m_b^5}{192\pi^3}|V_{cb}|^2 \Bigg\{ c_3 \left[1 - \frac{\mu_\pi^2(H_Q) - \mu_G^2(H_Q)}{2m_b^2} + O\left(\frac{1}{m_b^3}\right)\right] + 2c_5\left[\frac{\mu_G^2(H_Q)}{m_b^2} + O\left(\frac{1}{m_b^3}\right)\right] \\ + \frac{c_6}{m_b^3}\frac{\langle H_Q|(\bar{Q}\Gamma_L q)(\bar{q}\Gamma_R Q)|H_Q\rangle}{M_{H_b}} + O\left(\frac{1}{m_b^4}\right)\Bigg\},\end{aligned} \tag{4.12}$$

where the relativistic b field has been matched to the static HQET Q field, the b-hadron state has been matched to a nonrelativistic state H_Q (but the relativistic normalisation has been kept), and the kinetic and chromomagnetic energies of the B-meson are given by:

$$\mu_\pi^2 = \frac{\langle H_Q|\bar{Q}(i\vec{D})^2 Q|H_Q\rangle}{2M_{H_b}}, \qquad \mu_G^2 = \frac{\langle H_Q|\bar{Q}\frac{g}{2}\sigma_{\mu\nu}F^{\mu\nu}Q|H_Q\rangle}{2M_{H_b}} \tag{4.13}$$

These matrix elements are well known from fits to the heavy quark expansions of the B-meson spectrum [23]. Instead, for the rest of the section, the focus will be on the 4-quark matrix elements known as the Spectator Effects.

4.1.3 SPECTATOR EFFECTS

In the Heavy-Quark Expansion of the inclusive lifetime presented in Eq. (4.12), there are various terms that contribute at the order $\frac{1}{m_b^3}$. However, as shown in Fig. 4.3 the 'Spectator Effects' where a light quark participates in the decay is phase space enhanced relative to the other contributions as it appears from a one-loop diagram rather than a two-loop diagram [24]. The four operators that contribute to the Spectator Effects are:

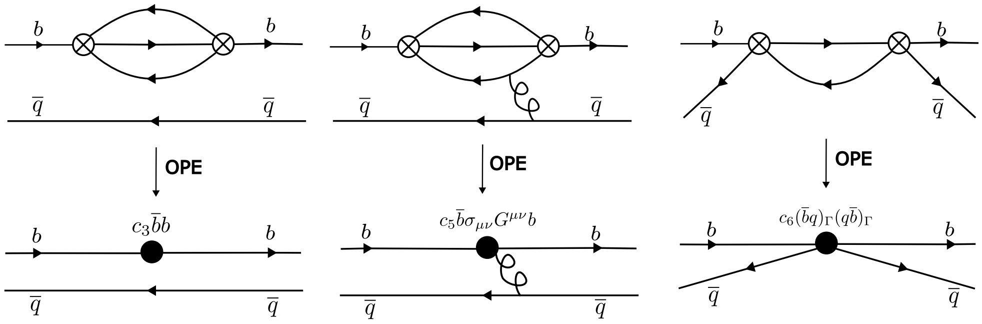

Figure 4.3: Schematic of the Operator Product Expansion. Note that the third diagram (representing the Spectator Effects where light quarks participate in the decay) is a one-loop diagram, which contributes to a $16\pi^2$ phase-space enhancement over the other two diagrams.

$$\begin{aligned} O^f_{V-A} &= (\overline{Q}\gamma_\mu P_L q_f)(\overline{q}_f\gamma^\mu P_L Q), \quad & O^f_{S-P} &= (\overline{Q}P_L q_f)(\overline{q}_f P_R Q), \\ T^f_{V-A} &= (\overline{Q}\gamma_\mu P_L T^A q_f)(\overline{q}_f\gamma^\mu P_L T^A Q), \quad & T^f_{S-P} &= (\overline{Q}P_L T^A q_f)(\overline{q}_f P_R T^A Q), \end{aligned} \tag{4.14}$$

where f labels the flavour of the light quark. As depicted in Fig. 4.2, the matrix elements of these operators in a b-hadron state contain two different types of contractions, the ‘eye’ contraction where the light quark is contracted in a loop and effectively does not participate in the decay, and the connected contraction that actually parametrises the Spectator Effects. Both contributions are important for the full determination of the inclusive lifetimes, however the connected contractions are simpler because they do not give rise to power-divergent mixings with the $\overline{Q}Q$ operator. Also, note that in ratios of the inclusive decay rates of the charged B meson to the neutral B meson:

$$\frac{\Gamma_{B^+}}{\Gamma_{B^0}} = 1 + \frac{\mu_\pi^2(B^0) - \mu_\pi^2(B^+)}{2m_b^2} + \frac{c_G}{c_3}\frac{\mu_G^2(B^+) - \mu_G^2(B^0)}{2m_b^2} \tag{4.15}$$

$$+ \frac{c_6(B^+)}{c_3}\frac{\langle B^+|O|B^+\rangle}{m_b^3 M_B} - \frac{c_6(B^0)}{c_3}\frac{\langle B^0|O|B^0\rangle}{m_b^3 M_B} + O\left(\frac{\Lambda^4}{m_b^4}\right), \tag{4.16}$$

the prefactors completely cancel out, and the leading order matrix elements largely cancel due to isospin symmetry, leaving an enhanced contribution from the Spectator Effects. In the isospin symmetric limit, defining the operators:

$$\mathcal{O}_1 := O^d_{V-A} - O^u_{V-A}, \quad \mathcal{O}_2 := O^d_{S-P} - O^u_{S-P} \tag{4.17}$$

$$\mathcal{O}_3 := T^d_{V-A} - T^u_{V-A}, \quad \mathcal{O}_4 := T^d_{S-P} - T^u_{S-P} \tag{4.18}$$

$$\tag{4.19}$$

then $\langle B_0|\mathcal{O}_i|B_0\rangle$ exactly capture the Spectator Effect contributions, by cancelling out the eye contraction diagram exactly. This is also equivalent in a sense to normal ordering the operators [24].

The vacuum-saturation-approximation offers an order-of-magnitude estimation of the sizes of the Spectator Effect matrix elements by inserting a complete set of states and restricting to the vacuum state:

$$\langle B_0|\mathcal{O}_i|B_0\rangle \approx \sum_n \langle B_0|(\overline{Q}\Gamma_{L,i}q)|n\rangle\langle n|(\overline{q}\Gamma_{R,i}Q)|B_0\rangle \approx \langle B_0|(\overline{Q}\Gamma_{L,i}q)|\Omega\rangle\langle\Omega|(\overline{q}\Gamma_{R,i}Q)|B_0\rangle \tag{4.20}$$

where Ω is the interacting vacuum state. Note that there is no particularly good motivation for the vacuum saturation hypothesis, and historically it was used only when Lattice-QCD results were not available for these types of quantities. It is conventional to parameterise the Spectator Effects in terms of so-called 'bag parameters' $B_{1,2}, \epsilon_{1,2}$ as [24]:

$$\begin{aligned} \langle B_0|\mathcal{O}_1|B_0\rangle_{\text{nr}} &= \frac{f_B^2 M_B}{8} B_1, \quad \langle B_0|\mathcal{O}_2|B\rangle_{\text{nr}} = \frac{f_B^2 M_B}{8} B_2, \\ \langle B_0|\mathcal{O}_3|B_0\rangle_{\text{nr}} &= \frac{f_B^2 M_B}{8} \epsilon_1, \quad \langle B_0|\mathcal{O}_4|B\rangle_{\text{nr}} = \frac{f_B^2 M_B}{8} \epsilon_2, \end{aligned} \tag{4.21}$$

where f_B is the heavy-light decay constant defined by:

$$-if_B \frac{m_B}{2} v_\mu = \langle\Omega|\overline{q}\gamma_\mu\gamma_5 Q|B_d\rangle_{\text{nr}}, \tag{4.22}$$

and the 'nr' subscript refers to the nonrelativistic normalisation of states (for full details of the normalization, see Sec. 4.2.3). With this definition, the vacuum saturation hypothesis is that $B_1 = B_2 = 1$ and $\epsilon_0 = \epsilon_1 = 0$. It is also possible to define analogous quantities for b-baryons such as the Λ_b baryon:

$$\langle\Lambda_b|\mathcal{O}_1|\Lambda_b\rangle_{\text{nr}} = \frac{f_B^2 M_B}{8} L_1, \quad \langle\Lambda_b|\mathcal{O}_3|\Lambda_b\rangle_{\text{nr}} = \frac{f_B^2 M_B}{8} L_2, \tag{4.23}$$

as suggested in Ref. [25], where there are only two relevant matrix elements due to heavy quark spin symmetry. Note that in the baryonic case, there is no vacuum saturation argument that is possible, as the quantum numbers of the baryon do not match 'half' of the $\mathcal{O}_i$ operators, hence the decomposition into L_1, L_2 bag parameters in Eq. (4.23) is only schematic. These baryonic matrix elements are not investigated in this section, and are left to future work.

Besides the tensions in inclusive/exclusive measurements of V_{ub}, V_{cb} as discussed in Sec. 1.2, another motivation to measure the Spectator Effects are the recent reorderings of measured lifetimes in the charm-baryon sector [26, 27]. Due to the lighter mass of the charm quark, higher dimensional operators appearing in the OPE are much more significant contribution to the inclusive lifetimes. Earlier analyses with heavy quark expansions suggested the originally measured hierarchy (induced by operators up to dimension 6) [28–31], however including dimension 7 operators can provide an explanation of the updated hierarchy [28, 32, 33].

There are very few Lattice-QCD calculations of the Spectator Effect matrix elements. The earliest studies were performed in quenched HQET [34, 35], which means that the light quark fermion determinant was set to one in the path integral, and the matrix elements were matched to the static theory. Quenched QCD was utilised in early lattice studies due to its lower computational cost,

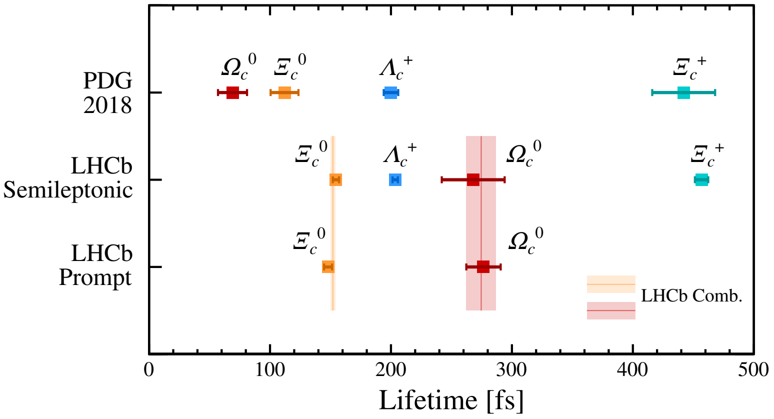

Figure 4.4: Figure from Ref. [27] showing the recent inversion in charm-baryon lifetime hierarchies, where the new measurement of the Ω_c^0 lifetimes are in 7σ tension with the world average reported by PDG in 2018.

however comes with systematic uncertainties that are difficult to estimate. A study of the matrix elements in full QCD was presented in a conference proceedings in Ref. [36] by extrapolation in the heavy quark mass using a number of different ensembles, however the details of the calculation were never published. Recently, an effort has been made to measure the QCD Spectator Effect matrix elements by using gradient flow to suppress the power-divergent mixings between the operators [16]. The measurements are still preliminary as the short-flow time expansion and matching to $\overline{\text{MS}}$ has not been completed in its entirety, and small flow-time mixing with lower-dimensional operators has been ignored.

Because the matrix elements in this section are computed in the static limit of HQET, using them in the Heavy-Quark Expansion as predictions of the inclusive lifetimes of b-hadrons comes with associated perturbative uncertainties due to the matching between QCD operators and HQET operators. In contrast, calculations of the matrix elements directly in QCD are usually performed at unphysically light values of the b-quark mass, as it is difficult to create ensembles with a lattice spacing fine enough to suppress $O(am_b)$-discretisation errors. Matrix elements at the physical point can be recovered through an extrapolation in m_b. The static limit matrix elements are also useful as an anchor point in this strategy as they provide the value at $m_b = \infty$, turning the extrapolation into an interpolation which is much better constrained [37].

4.2 Determination of Spectator Effect matrix elements in Lattice QCD

4.2.1 Domain Wall Fermion Ensembles

In choosing a lattice action to calculate quantities relevant for weak phenomenology, it is common to use Ginsparg-Wilson fermions as they suppress mixings with operators in different chiral representations. For this study, we used configurations generated by the RBC-UKQCD[3] collaboration listed in Table 4.2. The ensembles were generated with 3 flavours of quarks in the 'sea', meaning that the up down and strange quarks were included in the path-integral action, and the charm, bottom, and top quarks were not. This is a good approximation of most hadronic physics because the heavy quarks effectively decouple at low energy scales. The masses of the up and down quark were chosen to be degenerate, whereas the strange quark mass was heavier.The action used for the fermions in the 24I, 32I and 32Ifine ensembles was a Shamir domain wall fermion action [38, 39], which is a particular case of the Mobius action discussed in Sec. 2.2.2 where $b = 1, c = 0$ on all steps in the fifth-dimension. These Shamir ensembles were used to measure correlation functions, perform fits and extract bare matrix elements. The fourth-ensemble labelled 48 is a finer-discretisation ensemble, that was added later in the analysis for the purposes of step-scaling (as described in Sec. 4.2.5) to reduce the size of the error arising from the perturbative mathching between X-space and $\overline{\mathrm{MS}}$ schemes. This finer ensemble uses a Möbius domain-wall fermion action with $b = 1.5, c = 0.5$ on all steps in the fifth-dimension. It also differs from the other ensembles in that the temporal direction has open boundary conditions - this is often done for practical reasons to allow for faster thermalisation of the Monte-Carlo-Markov-Chains used to sample from the path integral, because instantons can flow in and out of the open boundary, essentially solving the topological freezing problem [40]. This comes at the expense of only being able to compute reliably correlation functions in the 'bulk' far away from the open boundary edges. The gauge action used for all the ensembles is an Iwasaki gauge action [41] which includes traces of Wilson loops larger than the simple plaquette used in the Wilson action (Eq. (2.54)) and coefficients tuned to improve the continuum limit behaviour of the gauge theory.

Because the masses of the up and down quark are set to be equal, these ensembles all have perfect isospin symmetry, causing the charged and neutral pions to have the same mass. Note that the physical pion masses are actually given by $m_{\pi^\pm} = 139.57\text{MeV}, m_{\pi^0} = 134.98\text{MeV}$. Ignoring the slight isospin-asymmetry evident in the physical pion masses, it is clear from Table 4.2 that the dominant difference is that the ensembles used have much larger masses for the up and down quarks than in the physical case. This is primarily done because the computational cost of computing propagators for heavier quark masses is cheaper, and thus it is easier to achieve low statistical errors with larger quark masses. This is especially true for Ginsparg-Wilson fermions such as the Möbius action, where the computational cost is an order of magnitude more than fermion actions that don't satisfy the Ginsparg-Wilson relation. In principle it is possible to utilise ensembles with various different pion

---

[3] A collaboration between RIKEN-BNL, Brookhaven National Laboratory, Columbia University, and Lattice-QCD physicists at UK institutions.

[4] C.Lehner, private communication

Ensemble	Lattice Volume	a^{-1} (GeV)	m_π (MeV)	N_{cfgs}	N_p	N_s
24I	$24^3 \times 64(\times 16)$	1.785(5)	339.7(1.3)	247	444	2133
32I	$32^3 \times 64(\times 16)$	2.383(9)	302.4(1.2)	142	373	303
32Ifine	$32^3 \times 64(\times 12)$	3.148(17)	371(5)	113	1062	2230
48	$48^3 \times 192\text{o}(\times 12)$	3.5(1)	280	13	30	0

Table 4.2: Values taken from Table IX in Ref. [42]. The lattice volume is denoted by $\text{LX}^3 \times \text{LT}(\times N_5)$ where LX is the number of points in each spatial direction, LT is the number of points in the temporal direction and N_5 is the number of points in the fifth-dimension. N_{cfgs} is the number of configurations used on each ensemble, and N_p/N_s are respectively the number of point/smeared source propagators computed on each ensemble. For ensemble 48, the ‘o’ indicates that open boundary conditions are imposed in the temporal direction. The scale-setting for the ensemble labelled 48 is unpublished, and received by private communication[4].

masses to perform a coupled chiral-continuum extrapolation to the continuum, physical theory (with the correct pion mass), but given that the ensembles available in this study have large pion masses this is not attempted. Instead, the point of view is taken that the extracted matrix elements will correspond approximately to the matrix-elements in a theory with $m_\pi \sim 350\text{MeV}$, which can be used as an estimate for the physical-point matrix element, or compared against HQET sum-rules predictions in a theory with a similarly heavy pion mass.

There are also systematic errors associated with simulating QCD in a finite volume and at finite temperature. Heuristically, $e^{-m_\pi L}$ controls the size of the dominant finite volume effects due to the lightest mode wrapping around the box (where L is the physical length of the box), and should be as small as possible if calculations are used to extract infinite volume quantities. Similarly, the temperature T should ideally be much smaller than Λ_{QCD} to suppress finite temperature effects. Calculating both of these quantities for the ensembles listed in Table 4.2, both effects are most severe for the 32IF ensemble for which $e^{-m_\pi L} \approx 0.02$, and $T \approx 50\text{MeV}$, leading to percent-level errors. In this section, both of these effects are ignored as subleading sources of error.

Light quark fermion propagators are computed on each of the ensembles using either point sources (no smearing), or gaussian smearing as described in Sec. 2.2.3. It is technically possible to compute propagators with different bare quark masses than what was used in the path integral action, for the purposes of taking a chiral limit of the extracted matrix elements. However, this can lead to observables which have infinite variance[43], as there are field configurations on which the fermion determinant in the path integral is nonzero, but the Dirac matrix used for the propagator calculation has zero modes. This problem is avoided in this study, as the bare quark masses used in the propagator generation are the same as what was used in generating the configurations, which is sometimes described as the ‘unitary limit’. The gaussian smearing kernel is fixed on every ensemble, and corresponds to a smearing width of $4.35a$ in 30 iterations on the 24 and 32I ensemble, and a width of $5.75a$ in 60 iterations on the 32IF ensemble. There are no smeared propagators computed in the 48 ensemble, as it is only used for renormalization purposes, and hence the operators are all point-like.

4.2.2 LATTICE ARTIFACTS IN POSITION-SPACE

Following Ref. [44], the free Domain-Wall (Shamir-action) fermion propagator in momentum space, and in the infinite N_5 and infinite volume limit, is given by:

$$W(p) = 1 - M - 2r\sum_{\mu}\sin^2\frac{p_\mu}{2}, \tag{4.24}$$

$$\cosh(\alpha) = \frac{1 + W^2 + \sum_\mu \sin^2 p_\mu}{2|W|}, \tag{4.25}$$

$$S_q(p) = \langle q(-p)\overline{q}(p)\rangle = \frac{-i\gamma_\mu \sin p_\mu + (1 - We^{-\alpha})m}{-(1 - e^{\alpha}W) + m^2(1 - We^{-\alpha})}, \tag{4.26}$$

where r is the Wilson parameter, conventionally set to $r = -1$, and $1 < M \leq 2$ is the mass parameter of the five-dimensional modes (set equal to 1.8 for the ensembles shown in Table 4.2). As shown in Ref. [45], the infinite N_5 propagator is a function of $b-c$ and does *not* depend on $b+c$, thus Eq. (4.24) is also the expression for the tree-level propagator for the Mobius action $b = 1.5, c = 0.5$ used for the finest ensemble. Note that at tree-level, the propagator $S_q(p)$ shown in Eq. (4.24) is suppressed compared to the usual continuum propagator value by a factor of $(1 - w_0)^2$, where $w_0 = 1 - \rho$.

By numerically performing a Fourier transform of the momentum-space propagator, it is possible to compare the position-space results against the numerically-computed position-space propagators on each ensemble, as well as the continuum result, as shown in Fig. 4.5. The bare light quark masses used (corresponding to the bare masses utilised in the ensemble generation) are light enough that the propagators are all approximately in the massless (chiral) limit.

This comparison is of critical importance to consider when deciding how to implement a X-space renormalization scheme. The point is that in any X-space scheme, the renormalization condition is of the form:

$$\langle \mathcal{O}^{(X)}(x_1)\dots\mathcal{O}^{(X)}(x_n)\rangle_{\text{interacting}} = \langle \mathcal{O}(x_1)\dots\mathcal{O}(x_n)\rangle_{\text{free}} \tag{4.27}$$

Suppose that the typical separation between the x_i coordinates is given by x. When implementing Eq. (4.27) in a lattice discretisation, one ideally wants to work in a regime where x is large enough such that discretisation artifacts are suppressed, and it does not matter whether the right-hand-side free correlation function is computed with the free continuum propagators or using free lattice propagators. In Fig. 4.5, this corresponds to choosing x such that the black crosses approach the dashed line (corresponding to the overall normalisation), which requires $x \gtrsim 20$. In practice, this is quite difficult to achieve whilst still maintaining that the chosen x is perturbative ($x \ll \Lambda_{\text{QCD}}$). In Ref. [46], it was proposed to simply use the lattice tree-level propagator when implementing Eq. (4.27), which will cancel the leading lattice artifacts. Although it is not clear whether this procedure is completely systematically under control, this is the procedure used in this section.

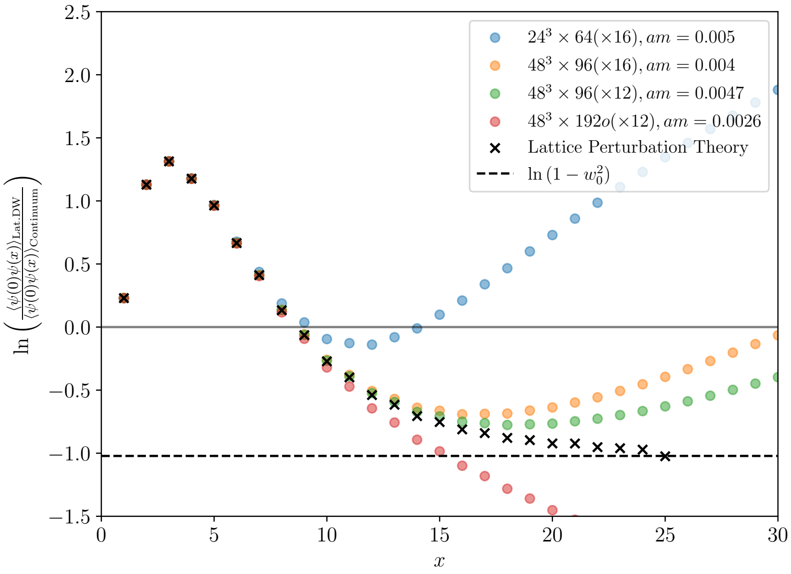

Figure 4.5: The filled in circles shows the logarithm of the ratio between the position-space free propagators computed numerically using the different bare parameters on each ensemble listed in Table 4.2, divided by the free massless continuum propagator $\|\langle\overline{\psi}(0)\psi(x)\rangle\| = \frac{1}{2\pi^2x^3}$ where the spin-structure has been removed. In crosses, this is also compared against the result utilising the free massless lattice domain-wall-fermion propagator (in the infinite N_5 and infinite volume limits) given by Eq. (4.24). Note that the domain-wall fermion propagators are suppressed by a factor of $(1-w_0^2)$ compared to the continuum result in the $x\to\infty$ limit. The x-axis is presented in lattice units.

4.2.3 CORRELATION FUNCTIONS AND MATRIX ELEMENTS

In this section, strict isospin symmetry is imposed ($m_u = m_d$), and hence there is no distinction made between the positive B^+-meson and the neutral B^0-meson, they are both labelled as simply the B-meson. The B-meson decay constant f_B in the static limit is defined by

$$\left\langle\Omega\middle|\left(\overline{q}\gamma_\mu\gamma_5 Q_v\right)^R(\mu)\middle|B\left(v,\vec{k}\right)\right\rangle_{\mathrm{nr}} = -if_B^{\mathrm{HQET},R}(\mu)\sqrt{\frac{m_B}{2}}v_\mu, \tag{4.28}$$

where R denotes a choice of renormalization-scheme defined at scale μ, Ω refers to the unit-normalised interacting vacuum, and the phase of the $|B(v,\vec{k})\rangle$ state is chosen such that f_B is real and positive. The subscript ‘nr’ denotes continuum states with nonrelativistic HQET normalization defined by:

$$\left\langle B\left(v',\vec{k}'\right)\middle|B\left(v,\vec{k}\right)\right\rangle_{\mathrm{nr}} = v_0\delta_{vv'}(2\pi)^3\delta^3\left(\vec{k}-\vec{k}'\right) \tag{4.29}$$

where $\delta_{vv'}$ is a Kroneker-delta over different discrete v-sectors, and $\delta^3\left(\vec{k}-\vec{k}'\right)$ is a Dirac delta. In the rest of this work $v = (1,0,0,0)$ is always set to be purely timelike, such that the static-quark states in the lattice are indexed by their spatial quantum number $\vec{x}$:

$$\langle B(\vec{y})|B(\vec{x})\rangle_{\text{lat.}} = \delta^3_{\vec{x},\vec{y}} \tag{4.30}$$

where the subscript 'lat.' refers to states in a lattice with N_s sites in each of three spatial dimensions, and lattice spacing a. The lattice nonrelativistic momentum states are related to the position eigenstates by a Fourier transform:

$$\left|B(\vec{k})\right\rangle_{\text{lat}} = \sqrt{a^3}\sum_{\vec{x}} e^{-i\vec{k}\cdot\vec{x}}\,|B(\vec{x})\rangle_{\text{lat}}\,, \qquad {}_{\text{lat}}\left\langle B(\vec{k})\middle|B(\vec{k}')\right\rangle_{\text{lat}} = a^3 N_s^3 \delta^3_{\vec{k},\vec{k}'}. \tag{4.31}$$

where lattice momenta are restricted to discrete values:

$$\vec{k} = \frac{2\pi}{N_s a}\cdot(n_1, n_2, n_3), \qquad 0 \le n_1, n_2, n_3 < N_s. \tag{4.32}$$

This normalisation is chosen such that the lattice state approaches the continuum state $|B(\vec{k})\rangle_{\text{lat}} \to |B(\vec{k})\rangle_{\text{nr}}$ as the continuum and infinite volume limits are taken. f_B can be extracted from the spectral decomposition of lattice two-point correlation functions:

$$C^{(2)}_{s_1,s_2}(t) := \langle\Omega|\,(\bar{q}\gamma_5 Q)^{(0),s_1}_{\text{lat.}}(t,\vec{x})(\overline{Q}\gamma_5 q)^{(0),s_2}_{\text{lat.}}(0,\vec{x})|\Omega\rangle = Z^*_{s_1} Z_{s_2} e^{-Et} + \text{excited states}, \tag{4.33}$$

where s_1, s_2 refer to potentially different smearings, (0) refers to the bare lattice operators, Z_{s_1}, Z_{s_2} are the associated (possibly complex) overlap operators:

$$Z_{s_i} := \langle\Omega|(\bar{q}\gamma_5 Q)^{(0),s_i}_{\text{lat.}}(0,\vec{x})|B(\vec{x})\rangle_{\text{lat}}. \tag{4.34}$$

Note that the parameter E in Eq. (4.33) does not correspond to the energy of the B-meson in HQET, due to the linear power divergence of the static quark that requires renormalization. In this chapter, operators are always renormalized in intermediate position-space schemes (studied in Chapter 3) before being matched to perturbatively defined schemes such as $\overline{\text{MS}}$. Such a procedure leads to renormalization factors (unfortunately also labelled by Z):

$$Z^R_{\bar{q}\gamma_5 Q}(\mu)(\bar{q}\gamma_5 Q)^{(0)}_{\text{lat.}} = (\bar{q}\gamma_5 Q)^R(\mu). \tag{4.35}$$

The static decay constant can then be extracted in the continuum and infinite volume limit as:

$$f_B^{\text{HQET}}(\mu) = \lim_{a\to 0}\lim_{L\to\infty} |Z_P| Z^R_{\bar{q}\gamma_5 Q}(\mu)\sqrt{\frac{2a^3}{m_B}}, \tag{4.36}$$

where P corresponds to pointlike-smearing (in other words, no smearing at all). Note that quark propagators are conventionally computed in units of the lattice-spacing, meaning that quantities such as Z_P extracted from correlation functions must have their units restored before usage, $Z_P = a^{-3} Z_P^{\text{raw}}$.

The Spectator-Effect matrix elements for B-mesons are expressed as:

$$\langle B(v,\vec{k}'=\vec{0})|\mathcal{O}_i^R(\mu)|B(v,\vec{k}=\vec{0})\rangle_{\text{nr}} = \frac{\left(f_B^{\text{HQET},R}(\mu)\right)^2 m_B}{8}\tilde{B}_i^R(\mu) \tag{4.37}$$

for $i \in \{1,2,3,4\}$. Note that the bag parameters B_i, ϵ_i have been combined into a single vector of length 4, $\tilde{B}_i$. This will simplify discussion of their mixing under renormalization. To extract the four-quark matrix elements requires fitting the spectral decomposition of three-point correlation functions:

$$\begin{aligned} C^{(3)}_{s_1,s_2,i}(t_1,t_2) &:= \langle\Omega|\,(\overline{q}\gamma_5 Q)^{(0),s_1}_{\text{lat.}}(t_2,\vec{x})\;\mathcal{O}^{(0)}_{i,\text{lat.}}(0,\vec{x})\;(\overline{Q}\gamma_5 q)^{(0),s_2}_{\text{lat.}}(-t_1,\vec{x})|\Omega\rangle \qquad (4.38)\\ &= Z^*_{s_1} Z_{s_2} e^{-E(t_1+t_2)}\langle B(\vec{x})|\mathcal{O}^{(0)}_{i,\text{lat.}}(0,\vec{x})|B(\vec{x})\rangle_{\text{lat.}} + \text{excited states}, \qquad (4.39)\end{aligned}$$

where the four-quark-operator insertion is always unsmeared. The bare operators are related to renormalized operators in some scheme R and scale μ by the invertible matrix $Z^R_{ij}(\mu)$:

$$Z^R_{ij}(\mu)\mathcal{O}^{(0)}_{j,\text{lat}} = \mathcal{O}^R_i(\mu). \qquad (4.40)$$

The bag parameters can be related to the matrix elements calculated in Lattice-HQET by:

$$\tilde{B}^R_i(\mu) = \lim_{a\to 0}\lim_{L\to\infty}\frac{8a^3}{\left(f_B^{\text{HQET},R}(\mu)\right)^2 m_B} Z^R(\mu)_{ij}\langle B(\vec{x})|\mathcal{O}^{(0)}_{j,\text{lat}}(0,\vec{x})|B(\vec{x})\rangle_{\text{lat.}} \qquad (4.41)$$

Once again, one must be careful to restore factors of the lattice-spacing into the matrix element extracted from correlation functions computed in units of the lattice-spacing.

4.2.4 Running of α_S

To use renormalization-group running equations to express matrix elements at some physical scale, such as the mass of the bottom quark m_b, one needs to know the values of α_S for all intermediate scales to solve the RG differential equations. From the most recent Particle Data Group review [47], the values of α_S and m_Z used are given by:

$$\alpha_S^{(5)}(m_Z) = 0.1180 \pm 0.0009, \qquad m_Z = 91.1880 \pm 0.0020\ \text{GeV} \qquad (4.42)$$

where $\alpha_S^{(N_f)}$ indicates that the running coupling has been renormalized in a theory containing N_f quarks. The running of $\alpha_S(\mu)$ as a function of μ is given by the β-function:

$$-\frac{\mu}{2\alpha_S^{\overline{\text{MS}}}}\frac{\mathrm{d}\alpha_S^{\overline{\text{MS}}}}{\mathrm{d}\mu} = \beta(\alpha_S) = \frac{\epsilon}{2} + \beta_0\left(\frac{\alpha_S^{\overline{\text{MS}}}}{4\pi}\right) + \beta_1\left(\frac{\alpha_S^{\overline{\text{MS}}}}{4\pi}\right)^2 + \ldots \qquad (4.43)$$

where in this thesis, α_S will always refer to the $\overline{\text{MS}}$ renormalized values. The $\frac{\epsilon}{2}$ term vanishes as $d \to 4$ and is dropped in future expressions, but its presence is important for the consistency of renormalization in dimensional regularisation. The β function has been calculated for QCD as a function of N_f flavours of fermions in the theory as [48]:

$$\begin{aligned}\beta(\alpha_S, N_f = 3) &= \beta_0\left(\frac{\alpha_S}{4\pi}\right)(1 + 0.565884\alpha_S + 0.453014\alpha_S^2 + 0.676967\alpha_S^3 + 0.580928\alpha_S^4),\\ \beta(\alpha_S, N_f = 4) &= \beta_0\left(\frac{\alpha_S}{4\pi}\right)(1 + 0.490197\alpha_S + 0.308790\alpha_S^2 + 0.485901\alpha_S^3 + 0.280601\alpha_S^4),\\ \beta(\alpha_S, N_f = 5) &= \beta_0\left(\frac{\alpha_S}{4\pi}\right)(1 + 0.401347\alpha_S + 0.149427\alpha_S^2 + 0.317223\alpha_S^3 + 0.080921\alpha_S^4), \qquad (4.44)\end{aligned}$$

where $\beta_0 = 11 - \frac{2N_f}{3}$ is the one-loop result. The result for multiples of N_f is needed because the $\overline{\text{MS}}$ scheme does not decouple heavy modes automatically, and all operators and coupling constants should in principle be matched between an $(N_f - 1)$-flavour theory and an N_f-flavour theory when running μ past the mass of a fermion. An explicit artifact of this observation is that a pure $\overline{\text{MS}}$ calculation would predict that all flavours of quarks q should influence the β function, even when $\mu \ll m_q$, which is clearly unphysical. It is for this reason that $\overline{\text{MS}}$ is sometimes referred to as an unphysical renormalization scheme.

The ensembles used in this section (and listed in Table 4.2) all have three flavours of quarks in the sea, hence the renormalization of the operators should be performed in the $N_f = 3$ theory. To determine $\alpha_S^{(3)}$ using the known value of $\alpha_S^{(5)}(m_Z)$ requires first matching between a 5 flavour theory and a 4 flavour theory at the mass of the bottom quark, and then matching between 4 flavour theory and 3 flavour theory at the mass of the charm quark. Assuming that the decoupling equation is $\zeta_g^2 \alpha_S^{(N_f+1)}(m_h) = \alpha_S^{(N_f)}(m_h)$, and is performed at the scale corresponding to the heavy quark m_h being integrated out, then this decoupling ratio is given by [49, 50] [5]:

$$\begin{aligned}\zeta_g^2 =& 1 + 0.1528\left(\frac{\alpha_S^{(N_f+1)}(m_h)}{\pi}\right)^2 + (0.9721 - 0.0847N_f)\left(\frac{\alpha_S^{(N_f+1)}(m_h)}{\pi}\right)^3 && (4.45)\\ &+ (5.1703 - 1.0099N_f - 0.0220N_f^2)\left(\frac{\alpha_S^{(N_f+1)}(m_h)}{\pi}\right)^4 + O(\alpha_S^5), && (4.46)\end{aligned}$$

where m_h is renormalized in the $\overline{\text{MS}}$ scheme. The masses m_b, m_c are given by:

$$m_b(\mu = m_b) = 4.183 \pm 0.007 \text{ GeV}, \tag{4.47}$$

$$m_c(\mu = m_c) = 1.2730 \pm 0.0028 \text{ GeV}. \tag{4.48}$$

Now, equations Eqs. (4.44) and (4.45) can be used to find the $\alpha_S^{(3)}$ at various scales:

$$\begin{aligned}\alpha_S^{(3)}(1.785 \text{ GeV}) &= 0.317 \pm 0.007,\\ \alpha_S^{(3)}(2.383 \text{ GeV}) &= 0.273 \pm 0.005,\\ \alpha_S^{(3)}(3.148 \text{ GeV}) &= 0.242 \pm 0.004,\\ \alpha_S^{(3)}(3.500 \text{ GeV}) &= 0.232 \pm 0.004,\\ \alpha_S^{(3)}(4.183 \text{ GeV}) &= 0.217 \pm 0.003. && (4.49)\end{aligned}$$

The significance of the first four scales used in Eq. (4.49) is that they are the values of a^{-1} for the four ensembles listed in Table 4.2. The last scale is approximately the mass of the b-quark. Errors from α_S^5 contributions have been ignored, errors from $\alpha_S(m_Z), m_Z, m_b, m_c$ are assumed to be

---

[5] Note that there appears to be a minor typo in Ref. [49], Eq (2.1) should read $\mathcal{L}^{\text{QCD}}(g^0, m^0, \dots) = \mathcal{L}'(g^{0\prime}, m^{0\prime}, \dots)$ where the unprimed quantities refer to the full theory, and the primed quantities to the effective theory with some heavy modes integrated out.

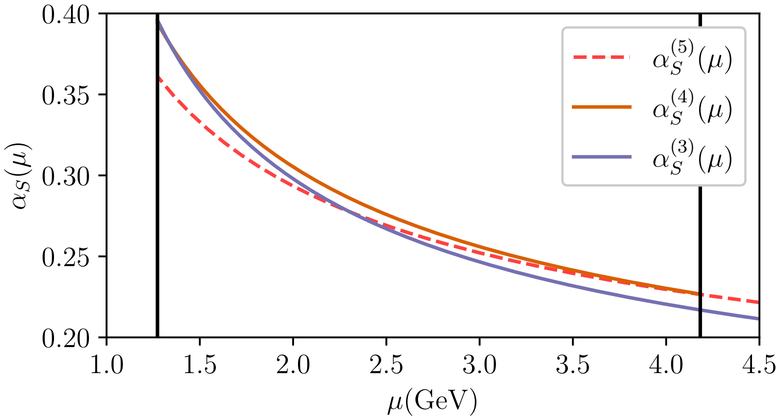

Figure 4.6: $\alpha_S^{(N_f)}(\mu)$ plotted as a function of μ by numerically integrating Eq. (4.44) and Eq. (4.45) for $N_f = 3, 4, 5$ in the range between m_c and m_b (the two vertical black lines).

independent in the determination of the errors shown in Eq. (4.49), and errors from lattice-spacing determination are *not* included: the purpose of Eq. (4.49) is simply to give an indication of the size of perturbation theory errors one should expect at these different scales. α_S is known precisely over the whole range of interest (percent level errors), and will be a small contribution to the final error budget.

Fig. 4.6 shows the difference between using the 3, 4, or 5-flavour α_S for $m_c \leq \mu \leq m_b$. Note that for $\alpha_S^{(3)}$, the value of $\alpha_S^{(4)}$ first has to be run down to the m_c scale, before matching to the 3-flavour theory and running back to larger values of μ.

4.2.5 Step-Scaling and Renormalization Group Running

When implementing nonperturbative renormalization schemes such as the schemes proposed in Chapter 3, there is a window problem where $t \gg a$ is required to suppress discretisation errors, but $t^{-\frac{1}{2}} \gg \Lambda_{\text{QCD}}$ is required for the perturbative matching coefficient to be well defined. Given that $\alpha_S(a^{-1})$ on the three lattices 24, 32I and 32IF is relatively large, this window may not exist at all for a given operator depending on the order to which the renormalization group equations are known. To avoid this, step-scaling to the finer lattice labelled 48 is utilised, where bare operators in a coarse lattice are first matched to their bare counterparts on the fine lattice, before matching to X-space at a higher scale. To see how this works, suppose that $T(t)$ represents the correlation matrix that is matched to the noninteracting (NI) value in order to define the X-space scheme. Choosing coarse and fine scales t_c, t_f on coarse and fine lattices with lattice spacings a_c, a_f respectively, the total renormalization factor is given by:

$$Z_{ij}^{(X)}(\mu = ct_f^{-1}) = \left(T^{(0,\text{fine lat.})}(t_f)\left(T^{(\text{fine lat.})}(t_f)\Big|_{\text{NI}}\right)^{-1}\right) \times \\ \left(T^{(0,\text{fine lat.})}(t_c)\left(T^{(\text{fine lat.})}(t_c)\Big|_{\text{NI}}\right)^{-1}\right)^{-1} \times \left(T^{(0,\text{coarse lat.})}(t_c)\left(T^{(\text{coarse lat.})}(t_c)\Big|_{\text{NI}}\right)^{-1}\right) \quad (4.50)$$

where all matrix indices have been suppressed. In Eq. (4.50), the constant c should be varied in the analysis to provide an estimate of the uncertainty due to perturbation theory. This procedure renormalises operators defined on a coarse lattice in terms of a fine scale t_f, so that errors due to matching to $\overline{\text{MS}}$ are suppressed. Due to the small Euclidean separations used, this procedure requires only a few additional propagators to be generated on a fine lattice as the statistical uncertainties are not very large. A technicality that arises is that if t_c is chosen to be an integer multiple of a_c, it will not be an integer multiple of a_f (unless the lattice parameters are tuned such that a_c is a multiple of a_f). Measurements of $T^{(0,\text{fine lat.})}(t)$ can however be fit to splines of fixed order to interpolate a value for $T^{(0,\text{fine lat.})}(t_c)$, the simplest scheme being a first-order spline (linear fit) to the neighboring points

$$T^{(0,\text{fine lat.})}(t_c) := \\ T^{(0,\text{fine lat.})}\left(a_f\left\lfloor\frac{t_c}{a_f}\right\rfloor\right) + \left(\frac{t_c}{a_c} - \left\lfloor\frac{t_c}{a_c}\right\rfloor\right)\left(T^{(0,\text{fine lat.})}\left(a_f\left\lceil\frac{t_c}{a_f}\right\rceil\right) - T^{(0,\text{fine lat.})}\left(\left\lfloor\frac{t_c}{a_f}\right\rfloor\right)\right), \quad (4.51)$$

where $\lfloor\cdot\rfloor, \lceil\cdot\rceil$ are the integer floor and ceiling functions respectively.

After renormalizing into X-space scheme, the rest of the matching procedure can be schematically visualised in the following diagram:

$$\begin{tikzcd}
\mathcal{O}^{(0,\text{Lattice})}_{\text{HQET}} \arrow[d, swap, "\text{nonperturbative}"] & & \\
\mathcal{O}^{(\text{X})}_{\text{HQET}}(t_f, \mu = ct_f^{-1}) \arrow[r] \arrow[d] & \mathcal{O}^{(\text{X})}_{\text{HQET}}(cm_b^{-1}, \mu = m_b) \arrow[d] & \\
\mathcal{O}^{(\overline{\text{MS}})}_{\text{HQET}}(\mu = ct_f^{-1}) \arrow[r] & \mathcal{O}^{(\overline{\text{MS}})}_{\text{HQET}}(\mu = m_b) \arrow[d] & \\
 & \mathcal{O}^{(\overline{\text{MS}})}_{\text{QCD}}(\mu = m_b) \arrow[r] & \mathcal{O}^{(\overline{\text{MS}})}_{\text{QCD}}(\mu^2 = m_W^2)
\end{tikzcd}$$

The ambiguity of defining a dimensional regularisation scale μ corresponding to a given fine scale t_f^{-1} used in an X-space scheme is parametrised by a real positive constant c in the above diagram. Due to only one-loop anomalous dimensions being available for the running of the four-quark $\Delta B = 0$ HQET operators, the running between the lattice scale ct_f^{-1} and m_b is only available to leading-logarithmic (LL) accuracy, which is the same in both X-space and $\overline{\text{MS}}$ when operators in X-space are run along the trajectory defined by a constant $c = \mu t_X$. Combining this leading-logarithmic running with the $O(\alpha_S)$ matching derived in Chapter 3 causes the square connecting $\mathcal{O}^{(\mathrm{X})}_{\mathrm{HQET}}(\mu^2 = c^2 t_f^{-2})$ to $\mathcal{O}^{\overline{\mathrm{MS}}}_{\mathrm{HQET}}(\mu^2 = m_b^2)$ to not commute: the two different paths (running and then matching, or matching and then running) result in *different* results. This is because the matching performed at either $\mu = ct_f^{-1}$ or $\mu = m_b$ gives different results, even though the logarithmic running in either scheme is the same. In other words, the calculation is not consistent to NLO order - leading logarithmic running should be combined with a leading order matching in order to give a consistent renormalization of the operators. In Sec. 4.2.9 the operators are NLO matched before they are LL run to a higher scale, with the understanding that when the NLO anomalous dimensions for the four quark $\Delta B = 0$ operators become available, they can easily included into the analysis to give a consistent NLO renormalization of the matrix elements.

4.2.6 The role of Wilson flow

As mentioned in the introduction of this section, Wilson flow can be used to regulate power divergences appearing in an OPE. This requires Wilson flowing of the fermion fields along with the gauge fields whose evolution equations are described in Eq. (2.79). One prescription for flowing the fermion fields in the continuum can be written as [51]:

$$\frac{\mathrm{d}}{\mathrm{d}t}\psi_t = D_\mu D_\mu \psi_t, \tag{4.52}$$

where ψ_t is a flowed fermion field at time t, and D_μ is the continuum Dirac operator. In fact, at finite Wilson flow time all composite operator divergences vanish, and composite operators renormalize multiplicatively according to their field content. For this reason, Wilson flow can be used as a (partial) regulator of QCD itself, and matrix elements computed at fixed physical Wilson flow time have well-defined continuum limits.

In the calculations presented in this section, Wilson flow is *not* used as a regulator of UV-divergences, instead it is simply used as a smearing procedure to improve the signal-to-noise ratio of correlation functions including a static quark propagator. The quark fields are never flowed in this section, and all light quark propagators refer to their values computed on unflowed gauge configurations. The static quark propagator is computed on flowed configurations, fixed to $a^{-2}t = 2.0$ where a is the lattice spacing of the ensemble being used. This has the effect of causing the physical flow time t to vanish as the continuum limit $a \to 0$ is taken. The flowed configurations were computed by iterating the Runge-Kutta scheme described in Appendix C of Ref. [52] 200 times, corresponding to a Wilson flow time-step of $\mathrm{d}t = 0.01a^2$ on each ensemble.

4.2.7 Fitting Procedure

The Lattice-QCD observables considered in this section are all derived from correlation functions, which as observables have the form:

$$\langle f \rangle = \frac{\int \mathcal{D}U e^{-S[U]} f(U)}{\int \mathcal{D}U \; e^{-S[U]}}, \tag{4.53}$$

where for simplicity the action here is simply written as a function of the gauge fields U. Ideally, one would have a collection of uncorrelated samples drawn from the probability distribution $U_1, U_2, \ldots, U_n \sim \frac{1}{Z}e^{-S[U]}$, with correlation functions $f_i(U_t)$ evaluated on each of the samples, where i indexes over a different number of measurements. Because the samples used in Lattice-QCD are nearly always generated using a Monte-Carlo-Markov-Chain (including those in Table 4.2), the samples are never completely decorrelated. Furthermore, for the propagators computed on these ensembles, the matrix $f_i(U_t)$ has missing entries due to some measurements not being available on certain configurations. The final complication is the fact that there are multiple f_i functions which correspond to a single correlation function observable: for instance the two-point correlation function $\langle \mathcal{O}(t,\vec{x})\mathcal{O}^\dagger(0,\vec{x})\rangle$ is $\vec{x}$-independent, however different choices of $\vec{x}$ correspond to formally different functions f_i.

The first simplification made in our analysis is that all f_i that correspond to the same physical observable (up to symmetries) are averaged over per configuration. After averaging, each f_i corresponds to measurements of either the two-point or three-point functions at fixed time-separations and smearing choices:

$$C^{(2)}_{s_1,s_2,t_f}(t) = \langle (\overline{q}_{s_2}\gamma_5 Q_{t_f})(t)(\overline{Q}_{t_f}\gamma_5 q_{s_1})(0)\rangle \tag{4.54}$$

$$C^{(3)}_{s_1,s_2,t_f,i}(t_1,t_2) = \langle (\overline{q}_{s_2}\gamma_5 Q)(t_2)\mathcal{O}_i(0)(\overline{Q}\gamma_5 q_{s_1})(-t_1)\rangle \tag{4.55}$$

Note that this notation is slightly more detailed than the notation used earlier in Eqs. (4.33) and (4.38), as the generic smearing of composite operators has now been specified to a choice of smearing s_1, s_2 for the light quark field, and a choice of Wilson flow-time t_f for the static quark propagator. The spatial indices on all operators have been dropped due to spatial invariance of the correlation functions. The sample mean and covariance are then calculated taking into account that certain entries may be missing:

$$\overline{f_i} := \frac{1}{N_i}\sum_t f_i(U_t), \qquad \overline{\sigma}^2_{ij} = \frac{1}{N_{ij}-1}\sum_t (f_i - \overline{f_i})(f_j - \overline{f_j}) \tag{4.56}$$

where each of the sums are only performed over configurations where the corresponding measurements exist, N_i denotes the number of configurations on which the correlation function f_i was measured, and N_{ij} denotes the number of configurations on which both f_i and f_j were measured. The autocorrelations remaining due to memory effects in the gauge field generation can be measured by calculating the normalised autocorrelation function:

$$\rho_i(\tau) = \frac{1}{\sigma^2_{f_i}}\mathbb{E}_t[(f_i(U_t) - \overline{f_i})(f_i(U_{t+\tau}) - \overline{f_i})] \tag{4.57}$$

which measures how correlated a measurement of f_i is at Monte-Carlo time t with the measurement of f_i at Monte-Carlo time $t+\tau$. $\rho_i(\tau) \to e^{-\tau/\Delta}$ is expected to decay exponentially at long times, where Δ is the autocorrelation time. For a further discussion of the spectral decomposition of autocorrelation times in the Langevin limit see Appendix C.0.2. For now it suffices to note that for the configurations in the 24, 32I and 32IF ensembles, autocorrelations of 2 and 3-point correlation functions were measured to be negligible, and the samples are treated as independent.

When the smearing used at the source and sink are equal ($s_1 = s_2 = s$), the two-point and three-point correlation functions defined in Eq. (4.54) have spectral decompositions given by:

$$C^{(2)}_{s,s,t_f}(t) = \sum_{n=1}^{\infty} |Z_n|^2 e^{-E_n t} \approx_{t\to\infty} |Z_1|^2 e^{-E_1 t}, \tag{4.58}$$

$$C^{(3)}_{s,s,t_f,i}(t_1,t_2) = \sum_{m,n=1}^{\infty} Z_m Z_n^* e^{-E_m t_1} e^{-E_n t_2} \langle m|\mathcal{O}_i|n\rangle \approx_{t_1,t_2\to\infty} |Z_1|^2 e^{-E_1(t_1+t_2)} \langle 1|\mathcal{O}_i|1\rangle, \tag{4.59}$$

where the sum is over all states with the same quantum numbers as the $(\overline{Q}\gamma_5 q)$ operator, and as before the overlap factors have been defined as $Z_n := \langle\Omega|(\overline{q}_s\gamma_5 Q_{t_f})|n\rangle$ with $|\Omega\rangle$ being the interacting vacuum state. There are certain combinations of these correlation functions that approximately extract physical observables of interest. For example the effective energy approximates the lowest lying state's energy in the large separation limit:

$$E_{\mathrm{eff},s,t_f}(t) := -\frac{1}{a}\log\left(\frac{C^{(2)}_{s,s,t_f}(t+a)}{C^{(2)}_{s,s,t_f}(t)}\right) \approx_{t\to\infty} E_1 \tag{4.60}$$

and a ratio of a three-point function to a two-point function approximates the corresponding matrix element:

$$\frac{C^{(3)}_{s,s,t_f,i}(t_1,t_2)}{C^{(2)}_{s,s,t_f}(t_1+t_2)} \approx_{t_1,t_2\to\infty} \langle 1|\mathcal{O}_i|1\rangle \tag{4.61}$$

Whilst these derivative quantities can be fitted to extract the energies and matrix elements, it is more common to directly perform fits of the spectral decompositions of the 2 and 3-point functions shown in Eq. (4.58).

Fits in this section were implemented with the gvar and corrfitter packages [53], and the analysis procedure is similar to the one performed in Ref. [54]. When fitting correlation functions, often the correlation functions are truncated to large Euclidean time regions where it is believable that the excited state contamination has been sufficiently suppressed, and only the states of interest remain. Making such a choice in a principled manner is difficult however, as the fits can be made to have a low χ^2 by restricting the fitting range to a tiny region. In this section, fits are performed on a range of different fitting regions before being model averaged to account for this factor. For a given fitting range, there is also the choice of how many excited states to fit the data to. As the number of excited states used increases, the number of parameters in the fits increase, and the corresponding χ^2 of the fit decreases. To determine how many excited states to include for a given fit range, the Akaike Information Criteria [55] is used. Explicitly, the number of excited states included in the fit is increased until the $\chi^2/N_{\mathrm{d.o.f}}$ improves by less than a fixed constant $\mathcal{A}$, where $N_{\mathrm{d.o.f}}$ is the number of degrees of freedom in the fit. For all the fits f that have $\chi^2/N_{\mathrm{d.o.f}} < 2$, associated to extracted

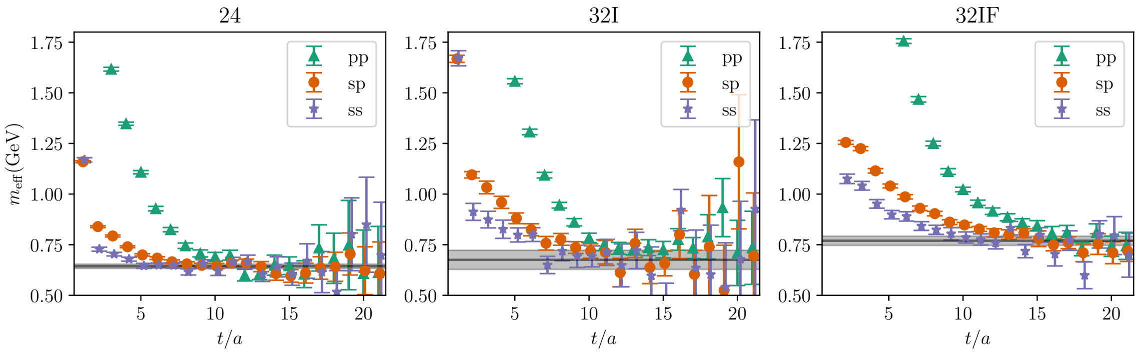

Figure 4.7: Plots showing the static-light two-point effective mass $m_{\mathrm{eff}} = -\frac{1}{a}\log\left(\frac{\langle \mathcal{O}_{s_1}(t+a)\mathcal{O}^\dagger_{s_2}(0)\rangle}{\langle \mathcal{O}_{s_1}(t)\mathcal{O}^\dagger_{s_2}(0)\rangle}\right)$ where a is the lattice spacing, and $\mathcal{O} = \overline{Q}\gamma_5 q$, on each of the three ensembles. The subscripts s_1, s_2 denote that the source and sink can be smeared differently, the data labelled *pp* corresponds to both being point-like, *sp* meaning one is pointlike and the other is smeared, and *ss* means both source and sink are smeared. The data shown is at a fixed flow-time of $t = 2.0$ in lattice units. The shaded bands correspond to the fitted energies.

quantities M_f with statistical uncertainty δM_f, they are then weighted according to:

$$\begin{gathered} w_f = \frac{p_f(\delta M_f)^{-2}}{\sum_{f'} p_{f'}(\delta M_{f'})^{-2}}, \quad \overline{M} = \sum_f w_f M_f, \\ \delta_{\mathrm{stat}}\overline{M}^2 = \sum_f w_f \delta M_f^2, \quad \delta_{\mathrm{sys}}\overline{M}^2 = \sum_f w_f (M_f - \overline{M}_f)^2, \quad \delta\overline{M}^2 = \delta_{\mathrm{stat}}\overline{M_f}^2 + \delta_{\mathrm{sys}}\overline{M_f}^2, \end{gathered} \tag{4.62}$$

where $p_f = \Gamma(N_{\mathrm{d.o.f}}/2, \chi^2/2)/\Gamma(N_{\mathrm{d.o.f}}/2)$ is the p-value of each respective fit, and $\overline{M} \pm \delta\overline{M}$ is the final model-averaged fit.

4.2.8 f_B^{HQET} RESULTS

In order to compute the static-light decay constant f_B^{HQET}, combined fits to $C^{(2)}_{p,p,2.0a^2}, C^{(2)}_{s,p,2.0a^2}$ and $C^{(2)}_{s,s,2.0a^2}$ are performed. The fitting ranges were parametrised by four integers $t_s^{\min}, t_p^{\min}, t_s^{\max}, t_p^{\max}$ where the point-point correlation functions were only fit in the range $[t_p^{\min}, t_p^{\max}]$, and the strange-point and strange-strange correlation functions were only fit in the range $[t_s^{\min}, t_s^{\max}]$. The fitting ranges were varied such that $t_s^{\min} \in [3, 25]$, $t_p^{\min} \in [t_s^{\min}, 25]$, $t_s^{\max} \in [t_s^{\min} + 3, 35]$, $t_p^{\max} \in [t_p^{\min} + 3, 35]$. There were also corresponding fitting ranges included where the point-point correlation functions were *not* fit, and only the smear-point and smear-smear correlation functions were fit in the same ranges. The AIC used in these fits was $\mathcal{A} = 0.5$. The model-averaged ground-state energies are compared against effective mass plots in Fig. 4.7.

To compute the perturbative renormalization and running of the heavy-light current required for extraction of f_B, firstly a calculation of the two-point correlation function in $\overline{\text{MS}}$ is required:

$$C^{\overline{\text{MS}}}(t) := \langle (\bar{q}\,\Gamma Q)^{(\overline{\text{MS}})}(0)(\overline{Q}\Gamma q)^{(\overline{\text{MS}})}(t)\rangle = \sum_{n=0}^{\infty} C_n(t)\frac{N_c}{2\pi^2 t^3}\left(\frac{\alpha_S}{4\pi}\right)^n, \tag{4.63}$$

where the $C_n(t)$ depends on t only logarithmically, and are given by:

$$\begin{aligned} &C_0(t) = 1, \qquad C_1(t) = 28.213 + 8L_t,\\ &C_2(t) = 154.647 + 817.580L_t + 104L_t^2,\\ &C_3(t) = 10907.039 + 13815.600L_t + 18834.968L_t^2 + 1525.333L_t^3, \end{aligned} \tag{4.64}$$

as calculated in Ref. [56], where $L_t := \log \frac{\mu t e^{\gamma_E}}{2}$. In Eq. (4.64), $N_c = 3$ and $N_f = 3$ have been utilised. To run the renormalized matrix element using the renormalization group, a calculation of the running of the heavy-light operator renormalization constant $Z_{\overline{\text{MS}}}(\overline{Q}\Gamma q)^{(0)} = (\overline{Q}\Gamma q)^{\overline{\text{MS}}}$ is needed, where:

$$\frac{\mathrm{d}\log Z_{\overline{\text{MS}}}}{\mathrm{d}\log\mu} = \sum_{n=1}^{\infty}\gamma_n\left(\frac{\alpha_S}{4\pi}\right)^n. \tag{4.65}$$

A completely consistent renormalization and running requires an $O(\alpha_S^{n+1})$-calculation of the perturbative running coefficients if a $O(\alpha_S^n)$ calculation of the matching is used (as the order is promoted after running). Corresponding to the $O(\alpha_S^3)$ matching coefficients listed in Eq. (4.64), there are $O(\alpha_S^4)$ running coefficients computed in Ref. [57]:

$$\gamma_1 = +4, \quad \gamma_2 = +42.0258, \quad \gamma_3 = +514.291, \quad \gamma_4 = +6308.65. \tag{4.66}$$

Note that the anomalous dimensions quoted in Eq. (4.66) are the negative of those computed in Ref. [57], due to the fact that the convention used in Ref. [57] was the opposite $(\overline{Q}\Gamma q)^{(0)} = Z^{\overline{\text{MS}}}(\overline{Q}\Gamma q)^{\overline{\text{MS}}}$ of what is used in this thesis, as can be confirmed by comparing γ_1 to the expected value from Eq. (2.28).

To cancel the linear divergences, the X-space scheme used is:

$$\left(\frac{C(t)^2}{C(2t)}\right)^{(X)} = \left(\frac{C(t)^2}{C(2t)}\right)^{(\text{tree})}, \tag{4.67}$$

so that if $\mathcal{O}^{(\overline{\text{MS}})} = C^{(\overline{\text{MS}},X)}\mathcal{O}^{(X)}$, the conversion factor can be calculated as:

$$\begin{aligned} C^{(\overline{\text{MS}},X)}(t) =& 1 + \frac{\alpha_S}{4\pi}\left(14.106 + 2L_{t/2}\right)\\ &+\left(\frac{\alpha_S}{4\pi}\right)^2\Big[-33.763 + 415.457L_t - 207.728L_{2t} + 30L_t^2 - 8L_tL_{2t} - 9L_{2t}^2\\ &+ n_f\left(3.864 - 21.041L_t - 1.333L_t^2 + 10.515L_{2t} + 0.667L_{2t}^2\right)\Big]. \end{aligned} \tag{4.68}$$

Before attempting to step-scale renormalize the static-light current, first the window problem is investigated in Fig. 4.8. In the left plot, the X-space renormalization factors $Z^{(X)}$ are plotted as

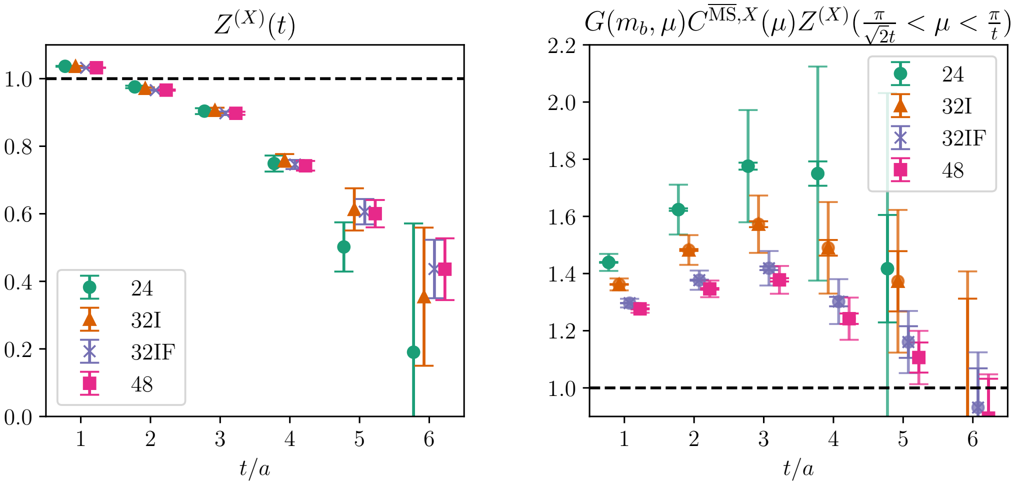

Figure 4.8: The left figure shows the X-space renormalization factor of the static-light current as a function of t/a for each of the four ensembles. The right figure shows the total factor required to renormalize the bare operator into the $\overline{\mathrm{MS}}$ scheme at $\mu = m_b$. The inner error-bars are due to statistical error, and the outer error-bars are due to errors from perturbation theory errors obtained by varying the scale μ used after matching to X-space by a factor of $\sqrt{2}$.

a function of $\frac{t}{a}$, and are *not* expected to exhibit any plateaus, because the scale is varying at each time-step. The right plot combines $Z^{(X)}$ with the matching to $\overline{\mathrm{MS}}$ coefficient $C^{(\overline{\mathrm{MS}},X)}$ calculated in Eq. (4.68), as well as the evolution kernel $G(m_b,\mu)$ that numerically integrates Eq. (4.65) in order to run to the scale $\mu = m_b$. Because these conversion rates are now all from the bare lattice operators to $\overline{\mathrm{MS}}$ at a fixed scale, there should be a plateau in the data corresponding to the usable window of timescales. The perturbative error was estimated by uniformly drawing the initially used μ from the range $(\frac{\pi}{\sqrt{2}t}, \frac{\pi}{t})$. The maximum value of this range was chosen because in the Wilsonian picture of renormalization, by integrating out momentum modes with $p > \frac{\pi}{t}$, correlation functions where the operators are separated by a distance t should be approximately given by their non-interacting values.

The figure seems to suggest that for each of the ensembles there is an approximate window for $2 \le \frac{t}{a} \le 4$. For the coarser lattices 24 and 32I and to some extent 32IF, the perturbative errors grow significantly for larger values of t/a, and would prohibit precision extraction of the corresponding matrix element regardless of the statistical precision achieved. In order to combat these effects, step-scaling to the 48 ensemble is investigated in Fig. 4.9. In the limit of infinite statistics, the t_c scale only needs to satisfy $t_c \gg a_c$ in order to suppress discretisation artifacts in the coarse lattice, which automatically implies that the discretisation artifacts are suppressed in the fine lattice as well. t_f should satisfy a genuine window problem, with both $t_f \gg a_f$ to suppress discretisation artifacts,

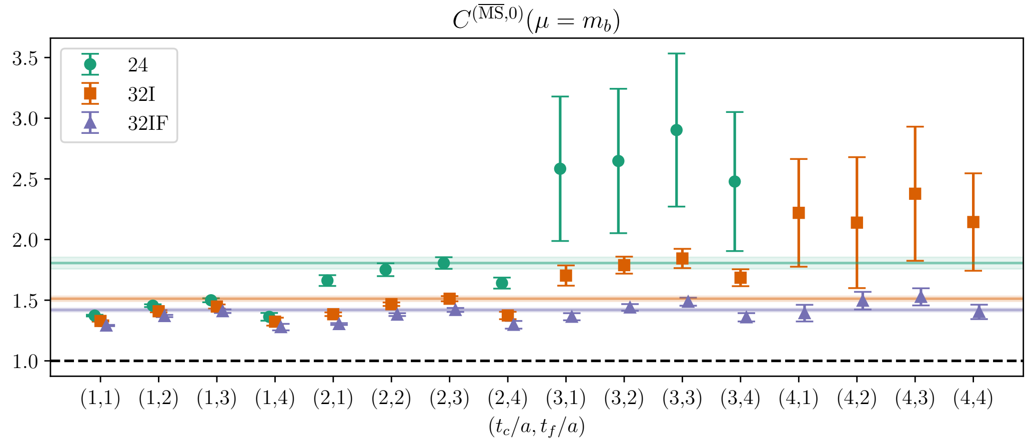

Figure 4.9: The conversion factor from bare operator to $\overline{\mathrm{MS}}$ renormalized at $\mu = m_b$ for the static-light operator, using the step-scaling procedure described in Sec. 4.2.5. Along the x-axis are different choices for the coarse and fine timescales $(t_c/a, t_f/a)$. The error bars include errors due to perturbation theory by varying the μ used in the matching to $\overline{\mathrm{MS}}$ in the range $(\frac{\pi}{\sqrt{2}t_f}, \frac{\pi}{t_f})$. The horizontal bands correspond to the values specified at $(t_c/a, t_f/a) = (2,3)$, which are ultimately used to renormalize the matrix elements.

as well as $t_f^{-1} \gg \Lambda_{\mathrm{QCD}}$ to suppress perturbative errors. The two coarser ensembles shown in Fig. 4.9 do not show very clear plateaus, but the plateau is reasonable for the 32IF ensemble. For this study, $(t_c/a, t_f/3) = (2,3)$ was used for all three ensembles and the corresponding matching coefficient is plotted in Fig. 4.9 as a horizontal band. Note that the values derived from this choice also are consistent with the plateaus shown in Fig. 4.8, but with smaller uncertainties as one would expect from step-scaling.

By combining these matching coefficients with the fitted bare matrix elements, $f_B^{\mathrm{HQET}}(\mu = m_B)$ can be plotted as a function of the lattice spacing, as shown in Fig. 4.10. As there has not been any $O(a)$ improvement of the operators used, the continuum limit fit takes a linear form $f_B^{\mathrm{HQET}}(a) = f_0 + a f_1$ for some fitted constants f_0, f_1, and quadratic and higher order errors have been dropped. As f_B^{HQET} has been computed in a theory with light quark masses corresponding to $m_\pi \approx 350\mathrm{MeV}$ it is not directly comparable to results at the physical point, however it is consistent with chiral-continuum limits taken in Ref. [58]. More propagators on the finer ensembles, with a possible inclusion of a fourth lattice spacing may drastically improve the precision of the result extracted in this section. $O(a)$ improvement of the operators would require new X-space schemes with expanded bases of source and sink operators to handle the new operator mixings, which have not yet been derived.

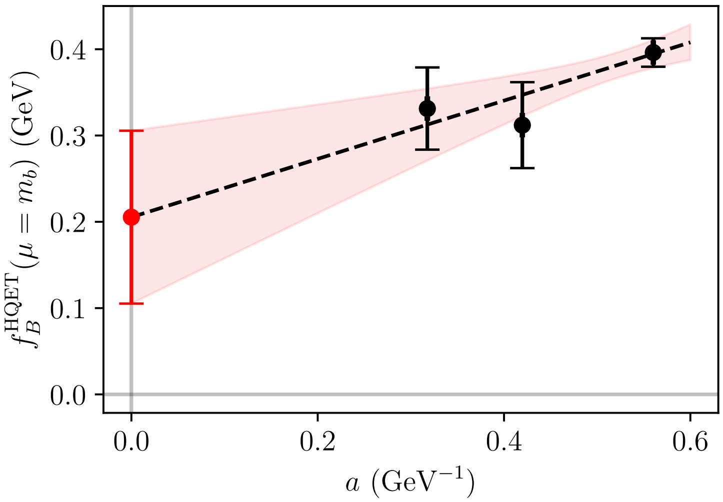

Figure 4.10: A linear continuum limit fit of f_B renormalized in $\overline{\mathrm{MS}}$ at $\mu = m_b$. The value fitted in the continuum limit is given by 0.2 ± 0.1GeV.

4.2.9 SPECTATOR EFFECT RESULTS

Instead of directly implementing the Spectator Effect operators:

$$\begin{aligned} \mathcal{O}_1 &= (\bar{b}\gamma_\mu P_L q)(\bar{q}\gamma^\mu P_L b), \quad & \mathcal{O}_2 &= (\bar{b}P_L q)(\bar{q}P_R b), \\ \mathcal{O}_3 &= (\bar{b}\gamma_\mu P_L T^A q)(\bar{q}\gamma^\mu P_L T^A b), \quad & \mathcal{O}_4 &= (\bar{b}P_L T^A q)(\bar{q}P_R T^A b), \end{aligned} \tag{4.69}$$

it is more convenient in practice to implement a different basis of operators:

$$\begin{aligned} \tilde{\mathcal{O}}_1 &= (\bar{b}_i\gamma_\mu P_L q_i)(\bar{q}_j\gamma^\mu P_L b_j), \quad & \tilde{\mathcal{O}}_2 &= (\bar{b}_i P_L q_i)(\bar{q}_j P_R b_j), \\ \tilde{\mathcal{O}}_3 &= (\bar{b}_i\gamma_\mu P_L q_j)(\bar{q}_j\gamma^\mu P_L b_i), \quad & \tilde{\mathcal{O}}_4 &= (\bar{b}_i P_L q_j)(\bar{q}_j P_R b_i), \end{aligned} \tag{4.70}$$

where the i, j indices are colour indices. This is because the adjoint index of the T^A operator no longer needs to be summed over. Note that because there are two quarks and two antiquarks, there are actually two different colour singlets contractions corresponding to the two singlets in $3\otimes3\otimes\overline{3}\otimes\overline{3}$, where 3 refers to the fundamental SU(3) representation. The relation:

$$T^A_{ab}T^A_{cd} = \frac{1}{2}\delta_{ad}\delta_{cb} - \frac{1}{6}\delta_{ab}\delta_{cd} \tag{4.71}$$

for $N_c = 3$ [6] allows the two sets of operators to be related by a change of basis:

$$\begin{pmatrix} \mathcal{O}_1 \\ \mathcal{O}_2 \\ \mathcal{O}_3 \\ \mathcal{O}_4 \end{pmatrix} = \begin{pmatrix} 1 & 0 & 0 & 0 \\ 0 & 1 & 0 & 0 \\ -\frac{1}{6} & 0 & \frac{1}{2} & 0 \\ 0 & -\frac{1}{6} & 0 & \frac{1}{2} \end{pmatrix} \begin{pmatrix} \tilde{\mathcal{O}}_1 \\ \tilde{\mathcal{O}}_2 \\ \tilde{\mathcal{O}}_3 \\ \tilde{\mathcal{O}}_4 \end{pmatrix} \tag{4.72}$$

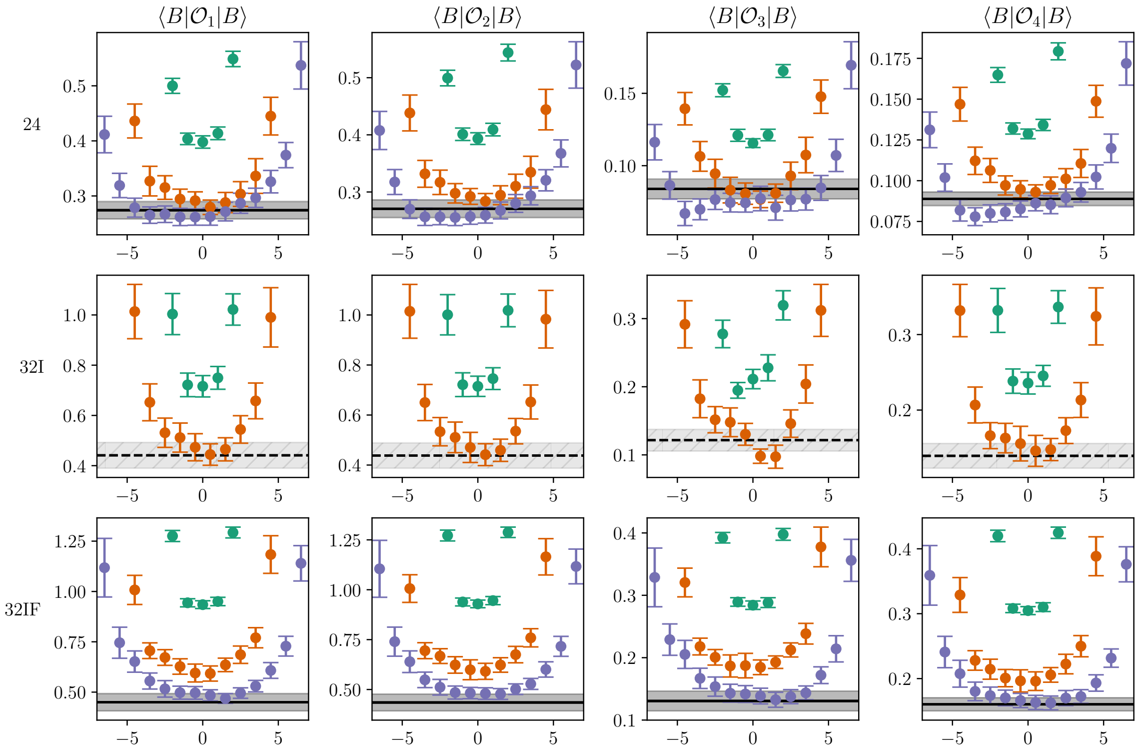

Figure 4.11: Plots showing the 3-point to 2-point correlation function ratios defined in Eq. (4.61), normalised to show the matrix element with normalisation defined in Eq. (4.37). Each row corresponds to a different ensemble, and each column corresponds to the four Spectator Effect operators. Model-averaged fitted values for the matrix elements are also plotted as shaded bands in each subfigure. 32I fitted values are hatched due to lack of 3-point correlation functions with source sink separations larger than 11, leading to unreliable fits.

The bare matrix elements were extracted from a coupled fit to $C^{(2)}_{s,s,2.0a^2}$ and $C^{(3)}_{s,s,2.0a^2,i}$, following a similar procedure as described in Sec. 4.2.8. The fitting ranges were defined by four positive integers, $t_2^{\min}, t_2^{\max}, t_3^{\min}, t_3^{\max}$, where $C^{(2)}_{s,s,2.0a^2}$ was fit in the range $[t_2^{\min}, t_2^{\max}]$. $C^{(3)}_{s,s,2.0a^2,i}$ was fit for all 3-point functions where both the source-operator and the operator-sink separation was at least $t_3^{\min}$, and the source-sink separation was no greater than $t_3^{\max}$. For all three ensembles, $t_2^{\min}$ was varied in the range $[10, 15]$, and $t_3^{\min}$ was varied in the range $[15, 20]$, and $t_3^{\min}$ was varied in the range $[2, 9]$. For the 24 and 32IF ensembles, source-sink spearations up to 20 were available, however the 32I ensemble only has source-sink separations up to 11, causing difficulty in proper isolation of the ground state in the three-point functions. Due to this limitation, $t_3^{\max}$ was varied in the range $[15, 20]$ for the 24 and 32IF ensembles, and was set equal to 11 for 32I. This lead to fairly unreliable

---

[6] See Appendix B for a list of colour matrix identities written for all N_c.

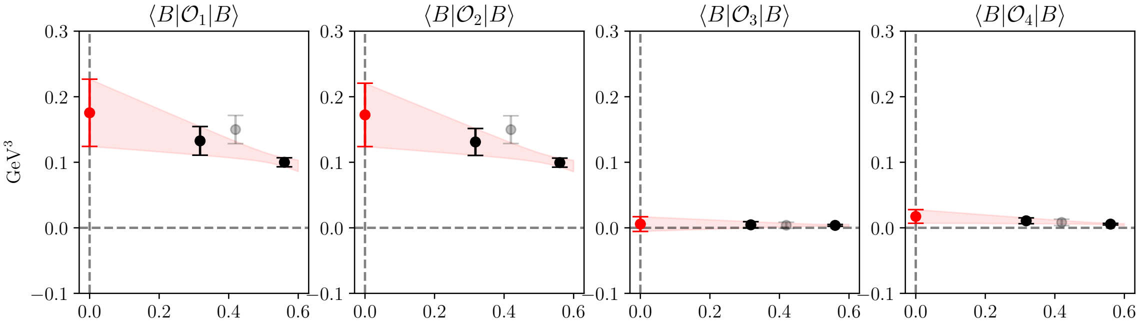

Figure 4.12: Continuum limit of the four matrix elements relevant to Spectator Effects for B-meson decay, renormalised at $\mu = m_b$ in the $\overline{\text{MS}}$-scheme. The fitted matrix elements from the 32I ensemble have been included as gray points in this plot, but have not been included in the linear continuum limit fit due to the correlation function fits for that ensemble not being reliable.

fits for the $32I$ ensemble, thus the extracted matrix element has been hatched in Fig. 4.11, and has not been included in the continuum limit fit. The AIC penalty used for all three ensembles was $\mathcal{A} = 1.0$.

The operators were renormalised with the X-space scheme proposed in Sec. 3.2.2, with the choice source-sink operators given by $\{(H_f^{-1}, H_f^{-1}), (H_{f,i}^{*-}, H_{f,i}^{(*i)}), (\Lambda_1, \Sigma_{2,0}), (\Lambda_2, \Sigma_{1,0})\}$, corresponding to the matching matrix in Eq. (3.76). The renormalization was step-scaled with the 48 ensemble as described in Sec. 4.2.8, with step-scaling times $(t_c, t_f) = (2, 3)$. Perturbative errors from renormalization have been similarly estimated as in Sec. 4.2.8 by varying the $\mu \in (\frac{\pi}{\sqrt{2}t_f}, \frac{\pi}{t})$ independently of any of the other sources of error. After renormalization and matching, the leading-logarithmic running of the $\overline{\text{MS}}$-renormalized operators can be read off from the $O(\alpha_S)$ counterterms derived in Sec. 3.2.1 as:

$$\mu \frac{\mathrm{d}\mathcal{O}^{\overline{\text{MS}}}}{\mathrm{d}\mu} = \frac{\alpha_S}{\pi} \begin{pmatrix} 2 & -\frac{3}{2} \\ -\frac{1}{3} & \frac{1}{4} \end{pmatrix} \mathcal{O}^{\overline{\text{MS}}}, \tag{4.73}$$

where the operators mix in the $(V-P)$ and $(S-P)$ two-by-two subblocks, with an explicit solution given by:

$$\mathcal{O}^{\overline{\text{MS}}}(\mu) = \exp\left(\int_{\mu_0}^{\mu} \mathrm{d}\mu \, \frac{\alpha_S}{\pi\mu} \begin{pmatrix} 2 & -\frac{3}{2} \\ -\frac{1}{3} & \frac{1}{4} \end{pmatrix} \right) \mathcal{O}^{\overline{\text{MS}}}(\mu_0), \tag{4.74}$$

where the exponential is a matrix exponential.

The linear continuum limit fit for the $\overline{\text{MS}}$-renormalized matrix elements at $\mu = m_b$ is shown in Fig. 4.12. This represents the first unquenched determination of the Spectator Effect matrix elements with nonperturbative renormalization. Interestingly, the extracted matrix elements are approximately consistent with the vacuum saturation hypothesis, which predicts that the $\mathcal{O}_3$ and $\mathcal{O}_4$ matrix elements should be zero. For comparison against matrix elements extracted from experiment;

a proper chiral limit will need to be taken to extrapolate the matrix elements to the physical point. This is left to a future work.

BIBLIOGRAPHY

[1] R. F. Streater and A. S. Wightman. *PCT, spin and statistics, and all that.* 1989. ISBN 978-0-691-07062-9.

[2] Konrad Osterwalder and Robert Schrader. AXIOMS FOR EUCLIDEAN GREEN'S FUNCTIONS. *Commun. Math. Phys.*, 31:83–112, 1973. doi: 10.1007/BF01645738.

[3] M. Lüscher and P. Weisz. Scaling Laws and Triviality Bounds in the Lattice phi**4 Theory. 1. One Component Model in the Symmetric Phase. *Nucl. Phys. B*, 290:25–60, 1987. doi: 10.1016/0550-3213(87)90177-5.

[4] Michael Aizenman and Hugo Duminil-Copin. Marginal triviality of the scaling limits of critical 4D Ising and ϕ_4^4 models. *Annals Math.*, 194(1):163, 2021. doi: 10.4007/annals.2021.194.1.3.

[5] M. Gockeler, R. Horsley, V. Linke, Paul E. L. Rakow, G. Schierholz, and H. Stuben. Is there a Landau pole problem in QED? *Phys. Rev. Lett.*, 80:4119–4122, 1998. doi: 10.1103/PhysRevLett.80.4119.

[6] C. T. H. Davies et al. High Precision Lattice QCD Confronts Experiment. *Phys. Rev. Lett.*, 92:022001, 2004. doi: 10.1103/PhysRevLett.92.022001.

[7] Takashi Kaneko. Status and progress of lattice QCD. In *12th International Workshop on the CKM Unitarity Triangle*, 4 2024.

[8] M. Beneke. Renormalons. *Phys. Rept.*, 317:1–142, 1999. doi: 10.1016/S0370-1573(98)00130-6.

[9] Maxwell T. Hansen, Harvey B. Meyer, and Daniel Robaina. From deep inelastic scattering to heavy-flavor semileptonic decays: Total rates into multihadron final states from lattice QCD. *Phys. Rev. D*, 96(9):094513, 2017. doi: 10.1103/PhysRevD.96.094513.

[10] Shoji Hashimoto. Inclusive semi-leptonic B meson decay structure functions from lattice QCD. *PTEP*, 2017(5): 053B03, 2017. doi: 10.1093/ptep/ptx052.

[11] Paolo Gambino and Shoji Hashimoto. Inclusive Semileptonic Decays from Lattice QCD. *Phys. Rev. Lett.*, 125 (3):032001, 2020. doi: 10.1103/PhysRevLett.125.032001.

[12] Paolo Gambino, Shoji Hashimoto, Sandro Mächler, Marco Panero, Francesco Sanfilippo, Silvano Simula, Antonio Smecca, and Nazario Tantalo. Lattice QCD study of inclusive semileptonic decays of heavy mesons. *JHEP*, 07: 083, 2022. doi: 10.1007/JHEP07(2022)083.

[13] P. Gambino, A. Melis, and S. Simula. Extraction of heavy-quark-expansion parameters from unquenched lattice data on pseudoscalar and vector heavy-light meson masses. *Phys. Rev. D*, 96(1):014511, 2017. doi: 10.1103/PhysRevD.96.014511.

[14] Christopher Monahan and Kostas Orginos. Locally smeared operator product expansions in scalar field theory. *Phys. Rev. D*, 91(7):074513, 2015. doi: 10.1103/PhysRevD.91.074513.

[15] Martin Lüscher and Peter Weisz. Perturbative analysis of the gradient flow in non-abelian gauge theories. *JHEP*, 02:051, 2011. doi: 10.1007/JHEP02(2011)051.

[16] Matthew Black, Robert Harlander, Fabian Lange, Antonio Rago, Andrea Shindler, and Oliver Witzel. Using Gradient Flow to Renormalise Matrix Elements for Meson Mixing and Lifetimes. *PoS*, LATTICE2023:263, 2024. doi: 10.22323/1.453.0263.

[17] Matthew Black, Martin Lang, Alexander Lenz, and Zachary Wüthrich. HQET sum rules for matrix elements of dimension-six four-quark operators for meson lifetimes within and beyond the Standard Model. *JHEP*, 04:081, 2025. doi: 10.1007/JHEP04(2025)081.

[18] J. H. Christenson, J. W. Cronin, V. L. Fitch, and R. Turlay. Evidence for the 2π Decay of the K_2^0 Meson. *Phys. Rev. Lett.*, 13:138–140, 1964. doi: 10.1103/PhysRevLett.13.138.

[19] Makoto Kobayashi and Toshihide Maskawa. CP Violation in the Renormalizable Theory of Weak Interaction. *Prog. Theor. Phys.*, 49:652–657, 1973. doi: 10.1143/PTP.49.652.

[20] S. W. Herb et al. Observation of a Dimuon Resonance at 9.5 GeV in 400 GeV Proton-Nucleus Collisions. *Phys. Rev. Lett.*, 39:252–255, 1977. doi: 10.1103/PhysRevLett.39.252.

[21] I. Belyaev, G. Carboni, N. Harnew, C. Matteuzzi, and F. Teubert. The history of LHCb. *Eur. Phys. J. H*, 46 (1):3, 2021. doi: 10.1140/epjh/s13129-021-00002-z.

[22] Alexander Lenz. Lifetimes and heavy quark expansion. *Int. J. Mod. Phys. A*, 30(10):1543005, 2015. doi: 10.1142/S0217751X15430058.

[23] I. I. Bigi, Th. Mannel, and N. Uraltsev. Semileptonic width ratios among beauty hadrons. *JHEP*, 09:012, 2011. doi: 10.1007/JHEP09(2011)012.

[24] M. Neubert and Christopher T. Sachrajda. Spectator effects in inclusive decays of beauty hadrons. *Nucl. Phys. B*, 483:339–370, 1997. doi: 10.1016/S0550-3213(96)00559-7.

[25] Massimo Di Pierro, Chris T. Sachrajda, and Chris Michael. An exploratory lattice study of spectator effects in inclusive decays of the λ_b baryon. *Physics Letters B*, 468(1-2):143–149, nov 1999. doi: 10.1016/s0370-2693(99) 01166-1. URL `https://doi.org/10.1016%2Fs0370-2693%2899%2901166-1`.

[26] Roel Aaij et al. Measurement of the Ω_c^0 baryon lifetime. *Phys. Rev. Lett.*, 121(9):092003, 2018. doi: 10.1103/PhysRevLett.121.092003.

[27] Roel Aaij et al. Measurement of the lifetimes of promptly produced Ω_c^0 and Ξ_c^0 baryons. *Sci. Bull.*, 67(5):479–487, 2022. doi: 10.1016/j.scib.2021.11.022.

[28] Boris Blok and Mikhail A. Shifman. Lifetimes of charmed hadrons revisited. Facts and fancy. In *3rd Workshop on the Tau-Charm Factory*, 11 1991.

[29] Alexander Lenz and Thomas Rauh. D-meson lifetimes within the heavy quark expansion. *Phys. Rev. D*, 88: 034004, 2013. doi: 10.1103/PhysRevD.88.034004.

[30] Hai-Yang Cheng. A Phenomenological analysis of heavy hadron lifetimes. *Phys. Rev. D*, 56:2783–2798, 1997. doi: 10.1103/PhysRevD.56.2783.

[31] G. Bellini, Ikaros I. Y. Bigi, and P. J. Dornan. Lifetimes of charm and beauty hadrons. *Phys. Rept.*, 289:1–155, 1997. doi: 10.1016/S0370-1573(97)00005-7.

[32] Hai-Yang Cheng. Phenomenological Study of Heavy Hadron Lifetimes. *JHEP*, 11:014, 2018. doi: 10.1007/JHEP11(2018)014.

[33] Hai-Yang Cheng. Charmed baryon physics circa 2021. *Chin. J. Phys.*, 78:324–362, 2022. doi: 10.1016/j.cjph.2022.06.021.

[34] Massimo Di Pierro and Christopher T. Sachrajda. A Lattice study of spectator effects in inclusive decays of B mesons. *Nucl. Phys. B*, 534:373–391, 1998. doi: 10.1016/S0550-3213(98)00580-X.

[35] Massimo Di Pierro, Christopher T Sachrajda, and Christopher Michael. An Exploratory lattice study of spectator effects in inclusive decays of the Λ_b baryon. *Phys. Lett. B*, 468:143, 1999. doi: 10.1016/S0370-2693(99)01166-1. [Erratum: Phys.Lett.B 525, 360–360 (2002)].

[36] Damir Becirevic. Theoretical progress in describing the B meson lifetimes. *PoS*, HEP2001:098, 2001. doi: 10.22323/1.007.0098.

[37] Rainer Sommer, Alessandro Conigli, Julien Frison, Patrick Fritzsch, Antoine Gérardin, Jochen Heitger, Gregorio Herdoiza, Simon Kuberski, Carlos Pena, and Hubert Simma. A strategy for B-physics observables in the continuum limit. *PoS*, LATTICE2023:268, 2024. doi: 10.22323/1.453.0268.

[38] Yigal Shamir. Chiral fermions from lattice boundaries. *Nucl. Phys. B*, 406:90–106, 1993. doi: 10.1016/0550-3213(93)90162-I.

[39] Vadim Furman and Yigal Shamir. Axial symmetries in lattice QCD with Kaplan fermions. *Nucl. Phys. B*, 439: 54–78, 1995. doi: 10.1016/0550-3213(95)00031-M.

[40] Martin Lüscher and Stefan Schaefer. Lattice QCD without topology barriers. *JHEP*, 07:036, 2011. doi: 10.1007/JHEP07(2011)036.

[41] Y. Iwasaki. Renormalization Group Analysis of Lattice Theories and Improved Lattice Action. II. Four-dimensional non-Abelian SU(N) gauge model. 12 1983.

[42] T. Blum et al. Domain wall QCD with physical quark masses. *Phys. Rev. D*, 93(7):074505, 2016. doi: 10.1103/PhysRevD.93.074505.

[43] Cagin Yunus and William Detmold. Infinite variance in Monte Carlo sampling of lattice field theories. *Phys. Rev. D*, 106(9):094506, 2022. doi: 10.1103/PhysRevD.106.094506.

[44] Stefano Capitani. Lattice perturbation theory. *Phys. Rept.*, 382:113–302, 2003. doi: 10.1016/S0370-1573(03)00211-4.

[45] Masaaki Tomii. Unphysical poles and dispersion relations for Möbius domain-wall fermions in free field theory at finite L_s. *Phys. Rev. D*, 96(7):074504, 2017. doi: 10.1103/PhysRevD.96.074504.

[46] Piotr Korcyl, Christoph Lehner, and Tomomi Ishikawa. Non-perturbative renormalization of the static quark theory in a large volume. *PoS*, LATTICE2015:254, 2016. doi: 10.22323/1.251.0254.

[47] S. Navas et al. Review of particle physics. *Phys. Rev. D*, 110(3):030001, 2024. doi: 10.1103/PhysRevD.110.030001.

[48] F. Herzog, B. Ruijl, T. Ueda, J. A. M. Vermaseren, and A. Vogt. The five-loop beta function of Yang-Mills theory with fermions. *JHEP*, 02:090, 2017. doi: 10.1007/JHEP02(2017)090.

[49] Y. Schröder and M. Steinhauser. Four-loop decoupling relations for the strong coupling. *JHEP*, 01:051, 2006. doi: 10.1088/1126-6708/2006/01/051.

[50] K. G. Chetyrkin, Johann H. Kuhn, and Christian Sturm. QCD decoupling at four loops. *Nucl. Phys. B*, 744:121–135, 2006. doi: 10.1016/j.nuclphysb.2006.03.020.

[51] Martin Lüscher. Chiral symmetry and the Yang–Mills gradient flow. *JHEP*, 04:123, 2013. doi: 10.1007/JHEP04(2013)123.

[52] Martin Lüscher. Properties and uses of the Wilson flow in lattice QCD. *JHEP*, 08:071, 2010. doi: 10.1007/JHEP08(2010)071. [Erratum: JHEP 03, 092 (2014)].

[53] G.P. Lepage, B. Clark, C.T.H. Davies, K. Hornbostel, P.B. Mackenzie, C. Morningstar, and H. Trottier. Constrained curve fitting. *Nuclear Physics B - Proceedings Supplements*, 106-107:12–20, mar 2002. doi: 10.1016/s0920-5632(01)01638-3. URL `https://doi.org/10.1016%2Fs0920-5632%2801%2901638-3`.

[54] S. R. Beane, W. Detmold, R. Horsley, M. Illa, M. Jafry, D. J. Murphy, Y. Nakamura, H. Perlt, P. E. L. Rakow, G. Schierholz, P. E. Shanahan, H. Stüben, M. L. Wagman, F. Winter, R. D. Young, and J. M. Zanotti and. Charged multihadron systems in lattice qcd+qed. *Physical Review D*, 103(5), mar 2021. doi: 10.1103/physrevd.103.054504. URL `https://doi.org/10.1103%2Fphysrevd.103.054504`.

[55] H. Akaike. A new look at the statistical model identification. *IEEE Transactions on Automatic Control*, 19(6):716–723, 1974. doi: 10.1109/TAC.1974.1100705.

[56] Andrey G. Grozin. Correlators of heavy-light quark currents in HQET: Perturbative contribution at 4 loops. 11 2024.

[57] Andrey Grozin. Anomalous dimension of the heavy-light quark current in HQET up to four loops. *JHEP*, 02:198, 2024. doi: 10.1007/JHEP02(2024)198.

[58] Yasumichi Aoki, Tomomi Ishikawa, Taku Izubuchi, Christoph Lehner, and Amarjit Soni. Neutral B meson mixings and B meson decay constants with static heavy and domain-wall light quarks. *Phys. Rev. D*, 91(11):114505, 2015. doi: 10.1103/PhysRevD.91.114505.

CHAPTER 5

HEAVY QUARKS PROPAGATING IN QUARK GLUON PLASMA

Some content in this section reproduced with permission from the following reference:

Joshua Lin, Di Luo, Xiaojun Yao, and Phiala E. Shanahan. Real-time dynamics of the Schwinger model as an open quantum system with Neural Density Operators. JHEP, 06:211, 2024. doi: 10.1007/JHEP06(2024)211.

Contents

An interesting use of bottom quarks is as probes of the thermal QCD medium, for example as produced at heavy ion collider experiments. The generic situation that will be considered is when $m_Q \gg T \gg \Lambda_{\text{QCD}}$ where T is the temperature of the medium, such that the light degrees of freedom are all thermalised in the quark-gluon-plasma phase of QCD, but the heavy quarks with mass m_Q are much heavier and act as nonrelativistic probes of the media. One observable of interest is the nuclear-modification-factor

$$R_{AA} = \frac{N_{AA}}{\langle T_{AA}\rangle \sigma^{pp}}, \tag{5.1}$$

where A is the number of nucleons in each of the colliding ions, N_{AA} is the observed number of bottomonium states (of given quantum numbers) produced per event in heavy-ion collisions, σ^{pp} is

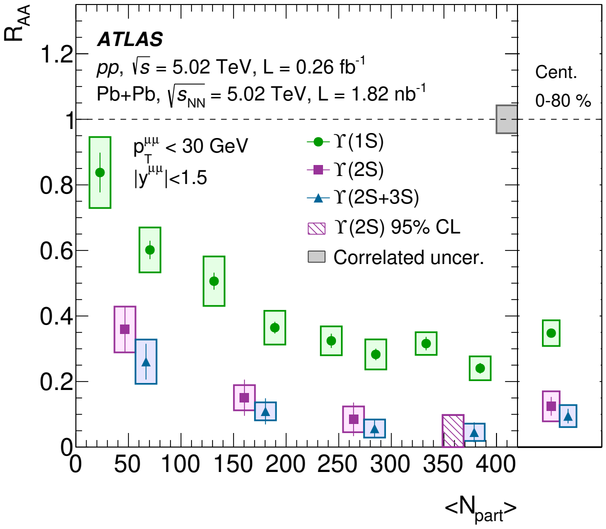

Figure 5.1: Figure from Ref. [1] showing the experimentally measured R_{AA} values from the ATLAS experiment for Pb+Pb collisions with a center of mass energy per nucleon pair of 5.02 TeV. The x-axis shows the fitted mean number of participant nucleons in the collision $\langle N_{\mathrm{part}} \rangle$, and the different colours refer to the radial excitations of the S-wave bottomonium state.

the cross-section for producing bottomonium in *pp* collisions at the same kinematics, and $\langle T_{AA} \rangle$ is the mean nuclear overlap function (how many nucleons collide in the interaction) [1]. R_{AA} is normalised such that any deviation from 1 indicates the presence of nuclear effects not present in *pp* collisions: chiefly the production of Quark-Gluon-Plasma medium for the heavy quarks to propagate through. Due to the deconfining nature of the QGP, $\overline{Q}Q$-pairs produced during the initial hard collision $(Q = c, b)$ are allowed to stream through the QGP unimpeded, before forming hadrons which contain a single heavy quark or antiquark, such as the $\overline{Q}u, \overline{u}Q$ mesons, leading to a suppression of heavy quarkonia production [2]. The experimental data in Fig. 5.1 can be interpreted as showing that as the number of participants in a heavy-ion collision increases (equivalently, as the collision becomes more central), the produced fireball of Quark-Gluon-Plasma grows larger in size, and hence there is more suppression of the bottomonium states (leading to a smaller value of R_{AA}).

A quantitative understanding of such heavy-quark observables measured at heavy-ion colliders requires first-principles simulations of the nonrelativistic dynamics and subsequent hadronisation of heavy quarks in the thermal medium. A general difficulty in simulating quantum dynamics of relativistic quantum field theories is the exponential scaling of the dimension of the Hilbert space as either the IR or UV cutoffs are removed[1]. State of the art calculations are still very far away from calculating meaningful QCD real-time dynamics, and have mostly been constrained to simpler

---

[1] Alternatively, for nonrelativistic systems, the exponential scaling in the number of particles included.

theories (simpler gauge groups, or less space-time dimensions). The corner of quantum dynamics given by heavy quarks in a thermal medium actually corresponds to a simple corner of quantum dynamics, as the bottom quarks can be treated in the nonrelativistic limit, and the quark-gluon-plasma degrees of freedom can be traced out leaving an Open Quantum System formulation [3]. In the high-temperature limit, the time evolution of the density matrix $\rho(t)$ describing the heavy-quark degrees of freedom can be written as a Lindblad equation:

$$\frac{\mathrm{d}\rho(t)}{\mathrm{d}t} = -i[H,\rho(t)] + \int \mathrm{d}^{d-1}\vec{x}\mathrm{d}^{d-1}\vec{y}D(\vec{x},\vec{y})_{ij}\left(O(\vec{x})_i\rho(t)O(\vec{y})_j^\dagger - \frac{1}{2}\left\{O(\vec{y})_j^\dagger O(\vec{x})_i,\rho(t)\right\}\right), \tag{5.2}$$

where $D(\vec{x},\vec{y})_{ij}$ is a coupling matrix that is required to be positive-semidefinite to ensure that the density matrix $\rho(t)$ remains positive, and trace normalised. H is a Hamiltonian describing the heavy-quark degrees of freedom (usually matched to some EFT such as HQET, NRQCD, or pNRQCD depending on the system of interest). The operators $O(\vec{x})_i$ mediate the interaction between the heavy quarks and the thermal medium that has been integrated out, and may depend on an additional internal index i.

Numerical studies of these Lindbladians have focused on in-medium dynamics of a single heavy quark Q, or a single quarkonia pair $\overline{Q}Q$ [4]. This is sufficient to study bottomonium production in current heavy-ion collision experiments, since the average number of bottom-antibottom pairs produced in one collision event is close to one. However, in order to study charmonium (charm-anticharm bound state) production in heavy ion collisions, many more $Q\bar{Q}$ pairs must be tracked. For example Pb-Pb collisions at the LHC reach a center of mass energy of 5.02 TeV per nucleon-nucleon pair, causing $O(100)$ $\bar{c}c$-pairs to be produced per collision [5]. A full quantitative treatment of the in-medium dynamics of multiple $\overline{Q}Q$-pairs would require simulation of all the pairs, as any two (QQ, $\bar{Q}\bar{Q}$ or $Q\bar{Q}$) can interact via a two-body potential that approaches zero at large distances. This motivates exploring algorithms which can simulate the quantum dynamics at lower cost.

An approach that offers a quadratic scaling improvement (but still stuffers exponential scaling in the volume) is Master Equation Unraveling (also known as Quantum Trajectories), where the Lindblad equation is converted into a stochastic Schrödinger equation [6, 7]. In this approach, the Lindbladian is first put into canonical form:

$$\frac{\mathrm{d}\rho(t)}{\mathrm{d}t} = -i[H,\rho] - \frac{1}{2}\sum_m\left[\{c_m^\dagger c_m,\rho\} - 2c_m\rho c_m^\dagger\right] \tag{5.3}$$

where the coupling matrix ($D(\vec{x},\vec{y})_{ij}$ in Eq. (5.2)) has been diagonalised after UV and IR regulators have been introduced, and the eigenvalues of the coupling matrix have been absorbed into the 'jump-operators' c_m. To solve this equation over a small time δt given an initial pure state $|\phi(t)\rangle$, the following steps are performed [8]:

- A proposed update $|\phi^{(1)}(t+\delta t)\rangle$ is prepared by evolving the initial pure state under an effective, non-hermitian evolution kernel:

$$|\phi^{(1)}(t+\delta t)\rangle = \left(1 - i\delta t\left(H - \frac{i}{2}\sum_m c_m^\dagger c_m\right)\right)|\phi(t)\rangle. \tag{5.4}$$

This new state is not normalised, and the deviation of its norm from one is related to each of the c_m operators characterising the different dissipative channels:

$$\langle \phi^{(1)}(t+\delta t)|\phi^{(1)}(t+\delta t)\rangle = 1 - \delta t \sum_m \langle \phi(t)|c_m^\dagger c_m|\phi(t)\rangle = 1 - \sum_m \delta p_m, \tag{5.5}$$

where $\delta_p = \sum_m \delta p_m$ is the total loss in probability.

- With probability $1 - \delta_p$, accept the proposal by defining the time evolved state to be the properly normalised $\phi^{(1)}$ state:

  $$|\phi(t+\delta t)\rangle = \frac{|\phi^{(1)}(t+\delta t)\rangle}{\sqrt{1-\delta p}}. \tag{5.6}$$

  Otherwise, with probability δp_m, define the time evolved state to be:

  $$|\phi(t+\delta t)\rangle = \frac{c_m|\phi(t)\rangle}{\sqrt{\delta p_m/\delta t}}. \tag{5.7}$$

After iterating this procedure, one obtains a single pure state trajectory $|\phi_1(t)\rangle$. In practice, one generates many such trajectories, $|\phi_1(t)\rangle, |\phi_2(t)\rangle, \ldots |\phi_N(t)\rangle$ following the same procedure. As $\delta t \to 0$, the true density matrix $\rho(t)$ is given by an ensemble average $\rho(t) \approx \frac{1}{N}\sum_{i=1}^{N} |\phi_i(t)\rangle\langle\phi_i(t)|$. Note that the procedure described here is a first-order discretisation of a stochastic differential equation, and it may be possible to utilise higher order integrators. The utility of this approach is that instead of storing and evolving the full density matrix, which has size $\dim(\mathcal{H})^2$ where $\mathcal{H}$ is the Hilbert space, one only has to store and evolve wavefunctions, which have size $\dim(\mathcal{H})$. If the initial state is a pure-state, and one is interested in the short-time Lindbladian evolution, then the number of trajectories N_{traj} needed is relatively small and Master Equation Unraveling offers a quadratic improvement in cost. As time progresses however, the state becomes more entangled (eventually limiting towards the thermal distribution) causing the number of trajectories needed to increase rapidly.

Alternatively, variational approaches have also become popular methods to approximate real-time quantum dynamics. The key idea is to parametrise complicated wavefunctions or density matrices in terms of a few variational parameters that encode physical properties of the state in question. This chapter discusses my work in utilising Neural Network parametrisations of density matrices to simulate the dynamics of quarks in an Open Quantum System framework. Before applying these methods to the full $3+1$d situation, they are tested for the Schwinger Model, which is a $1+1$d $U(1)$-gauge theory which shares many features with QCD such as confinement and chiral symmetry breaking. We utilise the Neural Density Operator (NDO) ansatz [9], which parametrises density matrices over a finite collection of spin-$\frac{1}{2}$ degrees of freedom and is reviewed in Sec. 5.1. The open quantum system framework applied to the Schwinger model is reviewed in Sec. 5.2.1, and its associated symmetries are investigated in Sec. 5.2.2. Subsequently, Neural-Network parametrisations of density matrices are investigated for the open Schwinger Model, and shown to be able to reproduce both the short-time quantum dynamics, as well as the long-time thermal properties of the steady state.

- To investigate the Lindbladian dynamics of strings in Sec. 5.2.3, product states containing string configurations are prepared and Lindbladian evolution is performed using the Time Dependent Variational Principle (TDVP) introduced in Sec. 5.1.1. Comparisons to exact results are shown on small lattice sizes, and the scaling of the method as lattice size is increased is studied. Finally, Lindbladian evolution of string states on an $L = 20$ lattice are computed with tVMC, for which exact diagonalization methods are infeasible.
- The thermal behaviour of the system is studied in Sec. 5.2.4 by extracting the steady state of the Lindblad equation. The learned state is compared to exact diagonalization results on an $L = 4$ lattice, before being bootstrapped up to an $L = 32$ volume lattice (see Fig. 5.5). The key observable that is studied is the chiral condensate, which measures the chiral symmetry breaking and is the prototypical order parameter for the confinement/deconfinement phase transition. By performing a scan in the physical parameters, it is confirmed that the learned NDO state is sensitive to this phase transition.

5.1 VARIATIONAL PARAMETERISATIONS OF QUANTUM STATES

Some text in this section reproduced with coauthors' permission from Ref. [10].

When exact solutions become difficult to compute, variational approximations of quantum states become useful. For pure quantum states, the central idea is to define a variational map $\psi : \mathbb{R}^N \to \mathcal{H}$ from a space of N (real) parameters to a Hilbert space $\mathcal{H}$, ideally in the limit that $N \ll \dim(\mathcal{H})$. The variational map is most useful when the image of the map ψ in some sense well-approximates the states of interest. Historically, this was first used in the context of finding ground states of Hamiltonians, because given a Hamiltonian $H \in \mathcal{H}^* \otimes \mathcal{H}$ the bound:

$$\frac{\langle\psi(\alpha)|H|\psi(\alpha)\rangle}{\langle\psi(\alpha)|\psi(\alpha)\rangle} = \sum_{n\geq 0} E_n \frac{\langle\psi(\alpha)|n\rangle\langle n|\psi(\alpha)\rangle}{\langle\psi(\alpha)|\psi(\alpha)\rangle} \geq E_0 \tag{5.8}$$

means that variational energies always form upper bounds on the true ground state energy E_0 (where E_n are the exact energies of the Hamiltonian H and $\psi(\alpha)$ is a variational parametrisation in terms of parameters α), *regardless* of the variational map ψ chosen. Choosing a better variational map (in the sense that the image more closely approximates the true ground state) gives *better* bounds on the ground state energy.

As shown in Fig. 5.2, variational ansatze span from more interpretable options to less interpretable options. One diagnostic to determine the representation power of an ansatz is the amount of entanglement it is able to capture. Specifically, supposing that a physical system is split into two subregions A and B, and letting ρ_A be the reduced density matrix defined on subregion A (tracing out degrees of freedom in B), the entanglement entropy is defined by:

$$S_A = -\mathrm{Tr}(\rho_A \log \rho_A) \tag{5.9}$$

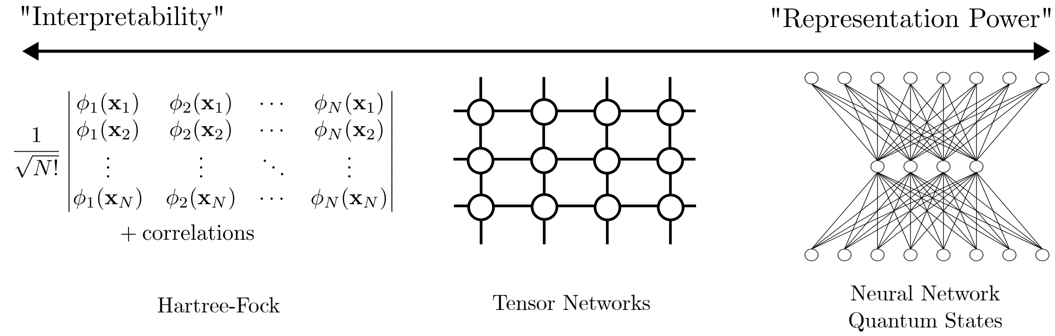

Figure 5.2: Variational parametrisations of quantum states live on a spectrum from more interpretable parametrisations (such as Hartree-Fock, where at it's core, a multiparticle wavefunction is built from symmetrising appropriately over single-particle wavefunctions) to more complicated parametrisations. Neural Networks tend to be regarded as the canonical black-box, where individual weights in the network do not have much physical significance. Tensor-networks are (perhaps somewhat provocatively) placed in the middle, due to fact there exists some physical interpretation of the bonds as encoding entanglement in the theory.

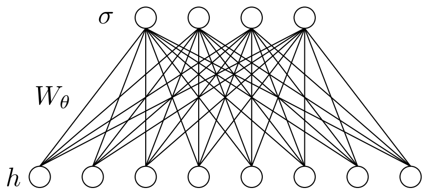

Figure 5.3: Schematic drawing of the Restricted-Boltmann-Machine network.

The growth of S_A as the size of the region A is smoothly increased is one diagnostic for how complicated a quantum state is. In particular, if the entanglement entropy depends linearly on the area of the boundary of A, it is known as an area-law state. Instead, if it scales linearly with the volume of the region A it is known as a volume-law state. Ground states of gapped-Hamiltonians are expected to be area-law entangled, whereas generic quantum states (including thermal states) are expected to be volume-law entangled. For the purpose of real-time evolution under the Lindblad equation, one of the interesting physics questions is 'how does the initial state thermalise'. Studying this question requires ansatz to be able to capture volume-law entangled states. This is difficult with Tensor Networks as they can only parametrise Area-Law entanglement efficiently [11]. There are however some indications that Neural Network quantum states may be able to efficiently parametrise volume-law states [12–14].

The types of variational ansatz usable for a given problem depends on the structure of the

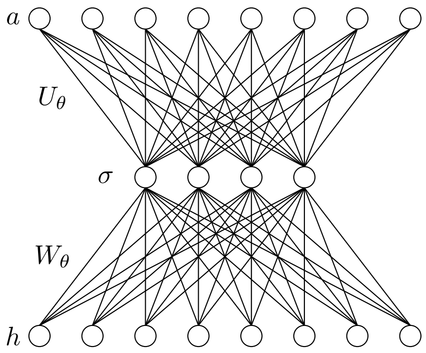

$$\begin{tikzcd}
p(\sigma, a, h) = \frac{1}{2}\exp(a^T U\sigma + h^T W\sigma + d^T a + b^T\sigma + c^T h) \arrow[d, "\text{Sum over hidden bits}"] \\
\langle \sigma, a|\psi\rangle = \sum_h p(h, \sigma, a) \arrow[d, "\text{Trace over ancillary bits}"] \\
\langle \sigma|\rho|\sigma'\rangle = \sum_a \langle \sigma, a|\psi\rangle\langle\psi|\sigma', a\rangle
\end{tikzcd}$$

Figure 5.4: Diagrammatic representation of the Neural Density Operator as presented in Refs. [9, 19]. In the center are the physical spins σ, which take values $\sigma_i \in \{-1, +1\}$ for $i = 0, \ldots, L-1$. Note that σ here denotes the basis states, not Pauli matrices. There are also hidden bits $h_j \in \{-1, 1\}$ and ancillary bits $a_k \in \{-1, 1\}$ for $j = 0, \ldots, M_h L - 1$, $k = 0, \ldots, M_a L - 1$.

Hilbert space in question. For example, oftentimes lattice discretisations of field theories have total Hilbert spaces that can be written as tensor products over local Hilbert spaces $\mathcal{H} = \otimes_i \mathcal{H}_i$ where i ranges over the lattice sites, and $\mathcal{H}_i$ encodes the local degrees of freedom at each site. This is not always true for gauge theories, as the natural Kogut-Susskind [15] (Sec. 2.2.4) discretisation of gauge theories require imposing local gauss-law constraints on the Hilbert space, which breaks the tensor product structure. However, for open-boundary condition $1+1$ dimensionsal gauge theories such as the Schwinger model, the gauge fields can be integrated out leaving a non-local theory of fermions that does have the necessary tensor product structure. For these kinds of Hilbert spaces, a simple Neural Network ansatz is a Restricted Boltzmann Machine (RBM). These are a specialised case of Boltzmann Machines [16, 17], which are Neural Networks defined by taking an Ising-model like energy on a fully connected graph, where each edge's coupling is a tunable parameter. The RBM (shown in Fig. 5.3) restricts this by computing Ising-like weights on a bipartite graph, with the interpretation that one set of nodes are 'inputs' and one set of nodes are 'outputs'. Such a structure was used in the seminal Ref. [14] to construct a variational ansatz:

$$\psi(\sigma; W) = \sum_h e^{\sum_j a_j \sigma_j^z + \sum_i b_i h_i + \sum_{i,j} W_{ij} h_i \sigma_j^z} \tag{5.10}$$

where the layer of nodes labelled $h_i \in \{-1, +1\}$ are 'hidden' nodes that are summed over to define a wavefunction over the physical spins σ. The set of complex parameters are given by biases a, b and a coupling matrix W_{ij}. Formal theorems show that as the number of hidden nodes in the RBM is taken to infinity (equivalently, the number of parameters is taken to infinity), any pure state wavefunction can be approximated by this ansatz [18].

A natural idea to extend variational parametrisations of pure states into mixed states is to introduce some auxiliary qubits a, which are then traced over. Performing this procedure for the

RBM ansatz Eq. (5.10) where the auxiliary qubits are simply appended to the real qubits, this would give a parametrisation that universally approximates the space of density matrices on the physical qubits, as long as the number of auxiliary qubits is at least the number of physical qubits and in the limit that the number of hidden bits is taken to infinity. This is due to the fact that every density matrix on N qubits has a purification on $2N$ qubits, and the RBM construction is universally approximating on the space of wavefunctions over $2N$ qubits. However, the issue with this parametrisation is that the procedure of tracing out the auxiliary qubits cannot be done analytically, and it would not be practical to manually have to trace out auxiliary qubits as this involves a sum over an exponentially large Hilbert space.

Instead one can use an analytically tractable parametrisation, such as the NDO shown in Fig. 5.4. To be concrete, this is a parametrisation of density matrices $\rho : \mathbb{C}^N \to \mathcal{H} \otimes \mathcal{H}^*$ where $\mathbb{C}^N$ is the parameter-space [9, 19]. The parametrisation can be explicitly written as:

$$\begin{aligned}
\log(\langle\sigma|\rho|\sigma'\rangle) &= \sum_{j=0}^{L-1} (b_j\sigma_j + b_j^*\sigma_j') + \sum_{k=0}^{M_h L-1} \mathcal{X}_k + \sum_{p=0}^{M_a L-1} \mathcal{Y}_p, \\
\mathcal{X}_k &= \log\cosh\left(c_k + \sum_{j=0}^{L-1} W_{kj}\sigma_j\right) + \log\cosh\left(c_k^* + \sum_{j=0}^{L-1} W_{kj}^*\sigma_j'\right), \\
\mathcal{Y}_p &= \log\cosh\left(d_p + d_p^* + \sum_{j=0}^{L-1} (U_{pj}\sigma_j + U_{pj}^*\sigma_j')\right).
\end{aligned} \tag{5.11}$$

There are two positive hyperparameters M_h, M_a (chosen such that $M_h L$ and $M_a L$ are integers) that control the size of the complex parameter space α:

$$\alpha = \{W \in \mathbb{C}^{M_h L \times L}, U \in \mathbb{C}^{M_a L \times L}, b \in \mathbb{C}^L, c \in \mathbb{C}^{M_h L}, d \in \mathbb{C}^{M_a L}\}. \tag{5.12}$$

For fixed M_h, M_a, the total number of complex parameters in α grows quadratically as L increases. By construction the density matrix represented by Eq. (5.11) is Hermitian and positive definite, as it is defined as a trace over ancillary qubits of a pure-state wavefunction.

Note that it is not clear whether or not this parametrisation is universally approximating (in fact, it might not be). A more recently introduced Autoregressive Gram-Hadamard Density Operator (AGHDO) ansatz [20] which generalised the NDO construction in Eq. (5.11) to be 'deep' was shown to be universally approximating. Implementing the AGHDO ansatz for realistic in-medium bottomonium simulations is underway, however the rest of this section will focus on the NDO construction and its application to the Schwinger Model.

In practice, it is conventional to represent the density matrix numerically as $\log\langle\sigma|\rho|\sigma'\rangle$, rather than $\langle\sigma|\rho|\sigma'\rangle$, as it increases numerical stability when parametrising matrices whose entries range over several orders of magnitude [21]. Another practical concern is that the definition of α as a set of complex parameters can lead to numerical instabilities as those parameters are varied (e.g., in optimization/training), due to the branch point singularities of the $\log\cosh$ function; a possible regulator is given by replacing the $\log\cosh$ functions appearing in the definition of Eq. (5.11) with a regulated log cosh function:

$$\mathrm{RLC}(z) \coloneqq \frac{\log\cosh\left(\frac{\tanh(|z|)}{|z|}z\right)}{\left(\frac{\tanh(|z|)}{|z|}\right)}, \tag{5.13}$$

which no longer has any branch-cuts, has the same behaviour near $z = 0$ as log cosh, but is no longer holomorphic. As a result, this modification causes certain values of the parameters α to no longer yield positive-definite density matrices, possibly introducing systematic uncertainties.

5.1.1 TIME DEPENDENT VARIATIONAL PRINCIPLE

A method to simulate the real-time dynamics of quantum states parametrised by some set of variational parameters α is the Time Dependent Variational Principle (TDVP) [22]. In the case of Lindbladian dynamics with $\frac{d}{dt}\rho(t) = \mathcal{L}\rho$, minimizing the L^2-norm (denoted $\|\cdot\|_2$) between the true time derivative $\mathcal{L}\rho$ and the difference induced by an infinitesimal variation in the neural network parameters α gives:

$$\min_{\dot\alpha}\left\|\sum_i \dot\alpha_i \frac{\partial\rho_a}{\partial\alpha_i} - \sum_b \mathcal{L}_{ab}\rho_b\right\|_2 \implies \dot\alpha = \mathcal{S}^{-1}f \tag{5.14}$$

where

$$(\mathcal{O}_i)_{ab} \coloneqq \delta_{ab}\frac{\partial\ln(\rho_a)}{\partial\alpha_i}, \quad \mathcal{S}_{ij} \coloneqq \rho^\dagger\mathcal{O}_i^\dagger\mathcal{O}_j\rho + \rho^\dagger\mathcal{O}_j^\dagger\mathcal{O}_i\rho, \quad f_i \coloneqq \rho^\dagger\mathcal{O}_i^\dagger\mathcal{L}\rho + \rho^\dagger\mathcal{L}^\dagger\mathcal{O}_i\rho, \tag{5.15}$$

where ρ denotes the vectorised density matrix (with a single index over the matrix entries), so that the Lindbladian super-operator $\mathcal{L}$ acts on it as a regular matrix $\rho \mapsto \mathcal{L}\rho$. $\mathcal{S}$ is the Quantum Geometric Tensor (QGT) [23], which is the pullback of the L^2 metric $\|\cdot\|_2$ on the vectorized space of density matrices, along the variational parametrisation map $\rho : \mathbb{C}^N \to \mathcal{H}\otimes\mathcal{H}^*$. The QGT parametrises the change of the physical density matrix under an infinitesimal change in the parameters of the neural network.

In any variational parametrisation of a large Hilbert space, the forces f_i and the QGT $\mathcal{S}_{ij}$ are expensive to compute exactly. Instead, it is possible to construct Markov Chain Monte Carlo (MCMC) to estimate these quantities. The combination of the TDVP algorithm with stochastic estimation is known as the time-dependent Variational Monte Carlo (tVMC). The forces f_i and QGT $\mathcal{S}_{ij}$ from Eq. (5.14) can be rewritten as:

$$\mathcal{S}_{ij} = Z\sum_a \frac{\|\rho_a\|^2}{Z} 2\mathrm{Re}\left((\mathcal{O}_i^\dagger)_{aa}(\mathcal{O}_j)_{aa}\right), \quad f_i = Z\sum_a \frac{\|\rho_a\|^2}{Z} 2\mathrm{Re}\left((\mathcal{O}_i^\dagger)_{aa}\sum_b \frac{\mathcal{L}_{ab}\rho_b}{\rho_a}\right), \tag{5.16}$$

where $Z = \sum_a \|\rho_a\|^2$ is a normalization constant. When evaluating the time derivative of the parameters $\dot\alpha = \mathcal{S}^{-1}f$, the factors of Z cancel, and Eq. (5.16) can be stochastically estimated using a MCMC that draws samples from the basis states of the doubled Hilbert space $\mathcal{H}\otimes\mathcal{H}^*$ according to the probability distribution $\|\rho_a^2\|/Z$. To regulate the possible divergences that may appear in inverting $\mathcal{S}$, a small diagonal offset is added ($\mathcal{S}_{ij} \mapsto \mathcal{S}_{ij} + \epsilon\delta_{ij}$) which ensures its invertability. Note that this offset should be taken to be as small as possible, as it introduces a systematic error into the simulated Lindbladian evolution. Physical observables of interest O (such as the chiral condensate or electric field for the Open Schwinger Model) can be stochastically estimated via the following identity (which is expressed in terms of basis elements of the original, un-doubled Hilbert space):

$$\langle O\rangle = \frac{\mathrm{Tr}(\rho O)}{\mathrm{Tr}(\rho)} = \sum_{\sigma}\left(\frac{\langle\sigma|\rho|\sigma\rangle}{\mathrm{Tr}(\rho)}\right)\left(\frac{\langle\sigma|\rho O|\sigma\rangle}{\langle\sigma|\rho|\sigma\rangle}\right), \tag{5.17}$$

which requires constructing a separate MCMC to sample from the diagonal of the density matrix according to the probability distribution $|\sigma\rangle \sim \langle\sigma|\rho|\sigma\rangle$.

Regardless of the initial state, in simulating the Lindbladian dynamics as $t \to \infty$ the system is driven towards its steady-state. This algorithm is also known as the Stochastic Reconfiguration algorithm, and can be recast as a preconditioned version of regular gradient descent [24, 25]. Adding larger diagonal shifts to $\mathcal{S}$ in the Stochastic Reconfiguration framework brings the updates closer to regular gradient descent, and does not bias the machine-learned steady state (in contrast to the systematic uncertainty that it introduces in the Lindbladian evolution itself). For finite values of M_h, M_a, the NDO parametrisation will not capture the full space of density matrices, which introduces systematic errors in both the estimated Lindbladian evolution, as well as the estimated steady states. Furthermore, the Monte-Carlo estimations of the QGT and forces come with inherent statistical uncertainty that only vanishes in the limit that the number of samples used is taken to infinity.

5.1.2 Initialization and bootstrapping

Real-time Lindbladian dynamics requires algorithms to prepare initial states of interest. In this section, we focus on the real-time evolution of product initial states. It is possible to set the weights of the NDO by hand to prepare given product states. Consider the case of preparing a product state $\rho_{\vec{a}} = |\vec{a}\rangle\langle\vec{a}| = |a_1 a_2 \cdots a_L\rangle\langle a_1 a_2 \cdots a_L|$ (where $\mathrm{Tr}(\sigma_z^{(i)}\rho_{\vec{a}}) = a_i$). A simple scheme is given by setting:

$$W_{kj} = \lambda a_j \delta_{k1} + O(\epsilon), \quad c_k = \lambda L \delta_{k1} + O(\epsilon) \tag{5.18}$$

with all other parameters initialized to $O(\epsilon)$ random numbers. The W_{kj} weights picks out the $\rho_{\vec{a}}$-state, and the c_k bias term breaks the symmetry between $\rho_{\vec{a}}$ and $\rho_{-\vec{a}}$, so that the overall NDO represents the state $\rho_{\mathrm{NDO}} = \rho_{\vec{a}} + O(e^{-\lambda}) + O(\epsilon)$. For the traditional TDVP algorithm used to evolve the state, using a finite but small ϵ is important to regulate the state otherwise the system can be 'frozen' in the initial state. These types of problems can be resolved by using alternative time-evolution strategies such as the p-tVMC algorithm [26].

An alternate method to initialize the state of interest is to construct a Lindbladian whose steady state is the state of interest. An example scheme for constructing product states in the Schwinger model is to set the Hamiltonian to zero, and choose a collection of jump-operators c_{ij} for the canonical form of the Lindbladian shown in Eq. (5.3):

$$\left\{\sigma_+^{(i)}\sigma_-^{(j)} \;\middle|\; 1 \le i, j \le L, \quad a_i = -1, \quad a_j = +1\right\} \tag{5.19}$$

which by construction gives $\mathcal{L}\rho_{\vec{a}} = 0$. A potential concern is that the Lindblad equation has other stable states other than the desired $\rho_{\vec{a}}$. Note however that stable states must satisfy:

$$0 = \dot{\rho}_{\text{stab}} = \sum_{p,m} \sigma_+^{(p)} \sigma_-^{(m)} \rho\, \sigma_-^{(p)} \sigma_p^{(m)} \qquad \Longrightarrow \qquad \forall p, m : \quad \langle \psi_2 | \sigma_+^{(p)} \sigma_-^{(m)} \rho\, \sigma_-^{(p)} \sigma_p^{(m)} | \psi_1 \rangle = 0 \tag{5.20}$$

for any basis states ψ_1, ψ_2. If ψ_1, ψ_2 are not $|\vec{a}\rangle$, then there is always some p, m that makes the above nonzero, and thus $\langle \psi_1 | \rho | \psi_2 \rangle = 0$. Thus ρ can only have nonzero entries in the row/column containing ψ. Now, suppose $\rho = |\psi\rangle\langle\psi| + \alpha|\psi\rangle\langle\varphi| + \overline{\alpha}|\varphi\rangle\langle\psi| + \cdots$ for some basis state $\varphi \neq \psi$. Restricting to the $|\psi\rangle, |\varphi\rangle$ basis we see that the determinant of ρ is negative, so there must be a eigenvector with negative eigenvalue, which also exists for the larger matrix - which is impossible as ρ is positive semi-definite. Thus, $\rho = \rho_{\vec{a}}$ is the only stable state of the Lindbladian.

When probing the steady-state properties of a system with the Stochastic Reconfiguration algorithm, initializing the NDO to an arbitrary state will lead to the correct steady state. However, initializing the model to a state close to the true solution can reduce simulation times drastically. One strategy is to exploit the approximate translational symmetry of the system, which is broken by $O(e^{-L\Delta E})$ effects due to the open boundary conditions, where ΔE is the gap between the ground state and the first excited state. The approximate translational symmetry implies that the steady state on a lattice of size $2L$ has approximately the same structure on the left and right halves of the lattice as the steady state on a lattice of size L with the same bare parameters. This motivates a transfer learning procedure where an NDO on a size L lattice is first optimized to the steady state, with the resulting weights then used to initialize an NDO on a size $2L$ lattice, as shown in Fig. 5.5. By stitching together two copies of the smaller NDO together, the structure of the steady state is preserved on both halves, and the Stochastic Reconfiguration algorithm need only learn the coupling between the halves.

5.2 Open Quantum Systems

Some text in this section reproduced with coauthors' permission from Ref. [10].

Modern computational resources (classical or quantum) are still far too limited to compute high fidelity real-time simulations of QCD - preventing direct simulation of heavy quarks embedded within a QGP medium. In certain parameter regimes however it is possible to simplify the underlying QFT to arrive at a tractable Effective Field Theory. As shown in Fig. 5.6, by first matching QCD onto a nonrelativistic EFT by making use of the $m_Q \gg \Lambda_{\text{QCD}}$, and then by integrating out the light QGP modes that are assumed to have thermalised at a temperature $T \gg \Lambda_{\text{QCD}}$, one arrives at a Lindblad equation that has far fewer degrees of freedom than the initial system. Before attempting the full $3 + 1$d (p)NRQCD Lindbladian evolution with variational parametrisations, it is useful to have a benchmark on a simpler open QFT in order to verify that the systematic errors introduced by variational parametrisations can be controlled. This section presents a study using Neural Density Operators to parametrise the real-time evolution of density matrices in the Schwinger Model, introduced in the following subsection.

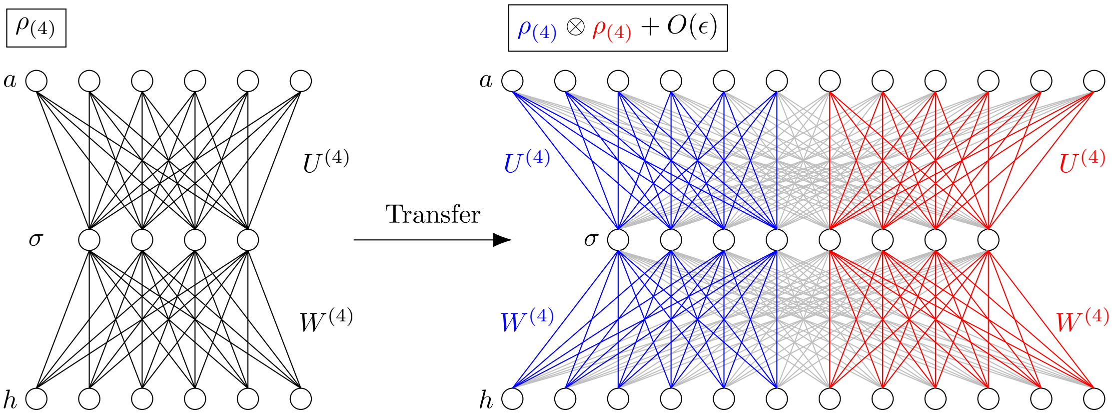

$$U^{(8)} = \begin{bmatrix} U^{(4)} & 0 \\ 0 & U^{(4)} \end{bmatrix} + O(\epsilon), \quad W^{(8)} = \begin{bmatrix} W^{(4)} & 0 \\ 0 & W^{(4)} \end{bmatrix} + O(\epsilon), \tag{5.21}$$

$$b^{(8)} = \begin{bmatrix} b^{(4)} & b^{(4)} \end{bmatrix} + O(\epsilon), \quad c^{(8)} = \begin{bmatrix} c^{(4)} & c^{(4)} \end{bmatrix} + O(\epsilon), \quad d^{(8)} = \begin{bmatrix} d^{(4)} & d^{(4)} \end{bmatrix} + O(\epsilon)$$

Figure 5.5: The procedure for transferring weights from a network optimized to represent a density matrix defined on L lattice sites to a network representing one on $2L$ sites (for any fixed values of M_a, M_h). Shown in the figure is a schematic for transferring weights $\alpha^{(4)} = \{U^{(4)}, W^{(4)}, b^{(4)}, c^{(4)}, d^{(4)}\}$ from an NDO with $M_a = M_h = 1.5$ on an $L = 4$ lattice to weights $\alpha^{(8)}$ for an $L = 8$ NDO, with the weight definitions from Eq. (5.11). The $\epsilon \ll 1$ are small random numbers.

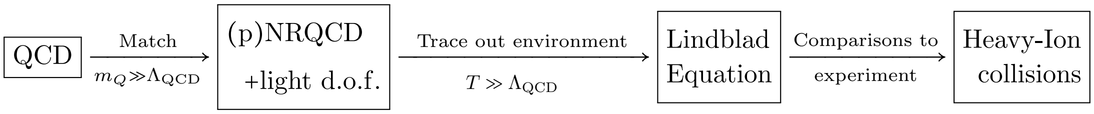

Figure 5.6: Schematic of first integrating out the heavy quark mass scale to match to Non-Relativistic QCD, before tracing out the environment to obtain an effective description of heavy quarks as a Lindblad Equation. This Lindblad equation can then be simulated and compared to experiment.

5.2.1 LATTICE-DISCRETISED SCHWINGER MODEL AS AN OPEN QUANTUM SYSTEM

Due to the difficulty of directly implementing new numerical techniques for QCD; it has become popular to focus attention on simpler gauge theories first to demonstrate the utility and scalability of new methods, before moving onto more physical situations. The Schwinger Model is a $U(1)$-gauge theory with a massive relativistic fermion (sometimes called an electron) in $1+1$d that shares many of the features of QCD, such as confinement and chiral symmetry breaking [27]. The Schwinger model as an open quantum system (coupled to a thermal environment) has been studied as a model of heavy quarkonia in the QGP [28, 29]. It is important to note however that the Schwinger action is *not* matched to a nonrelativistic action: this marks a fairly important difference between the strategy outlined in Fig. 5.6 and what is carried out in this section. Because the fermions are not matched to a nonrelativistic action, the Hilbert space actually exhibits exponential scaling with the volume, and there can be arbitrary particle-antiparticle fluctuations in the system.

A prototypical construction is to consider a Schwinger-model fermion ψ of mass m coupled to a scalar field ϕ:

$$\mathcal{L} = -\frac{1}{4}F_{\mu\nu}F^{\mu\nu} + \overline{\psi}(i\not{D} - m)\psi + g\phi\overline{\psi}\psi + \mathcal{L}_{\text{env}}(\phi). \tag{5.22}$$

where the scalars ϕ are environmental degrees of freedom with associated lagrangian $\mathcal{L}_{\text{env}}(\phi)$. In the analogy to heavy quarks embedded within the QGP, the ϕ degrees of freedom are the light quarks and gluons that make up the QGP. We consider the Open Quantum System formalism that traces out these environmental degrees of freedom in the Quantum Brownian Motion limit ($T \to \infty$) leaving a Lindblad equation describing the remaining Schwinger degrees of freedom [28]. Note that the gauge links are not traced out in this derivation of the Lindblad equation, although in $1+1$d the gauge links can be integrated out explicitly with open boundary conditions. So in one regard, this system is simpler than the eventual 3+1d NRQCD setup as it is in a lower dimension with a simpler gauge group, but in another regard it is more difficult given that matching to a nonrelativistic theory is not performed, and the Hilbert space scales explicitly with the volume of the system.

To numerically simulate the Schwinger Model, the theory is discretised onto a lattice with L points indexed by $0 \leq i, j, \cdots \leq (L-1)$ and lattice spacing a. In a staggered discretisation for the Schwinger fermion, the lattice has $\frac{L}{2}$ physical sites, with electrons occupying the even sites and positrons occupying the odd sites. A general Lindbladian evolution for such a system coupled to a thermal reservoir at temperature T is parametrised (up to $O(1/T^2)$ effects) by a spatial coupling matrix D_{ij} and operators O_i:

$$\mathcal{L}\rho(t) := \frac{\mathrm{d}\rho(t)}{\mathrm{d}t} = -i\big[H, \rho(t)\big] + a^2 \sum_{i,j} D_{ij}\left(\widetilde{O}_i \rho(t) \widetilde{O}_j^\dagger - \frac{1}{2}\big\{\widetilde{O}_j^\dagger \widetilde{O}_i, \rho(t)\big\}\right), \tag{5.23}$$

$$\widetilde{O}_i \equiv O_i - \frac{1}{4T}\big[H, O_i\big], \quad \widetilde{O}_i^\dagger \equiv O_i + \frac{1}{4T}\big[H, O_i\big]. \tag{5.24}$$

Note that Eqs. (5.23) and (5.24) are lattice discretised versions of Eq. (5.2), where the $O(1/T)$ correction performed in Eq. (5.24) enforces that the thermal density matrix $e^{-H/T}$ is a stable state of the Lindblad evolution up to $O(1/T^2)$ corrections. All super-operators such as the Lindbladian $\mathcal{L}$ that act on the space of operators are labelled in calligraphic font. The coupling matrix D_{ij} physically encodes the length-scale of correlations in the environment (the Debye screening length). To construct the Hamiltonian on a lattice with L total sites, notice that the Kogut-Susskind Hamiltonian

(Eq. (2.83), with lattice-spacing factors restored) takes the form:

$$H = \frac{a}{2}\sum_{j=0}^{L-2} E_{j,j+1}^2 - \frac{i}{2a}\sum_{j=0}^{L-2}\left(\psi_j^\dagger U_{j,j+1}\psi_{j+1} - \psi_{j+1}^\dagger U_{j+1,j}\psi_j\right) + \frac{m}{a}\sum_{j=0}^{L-1}(-1)^j\psi_j^\dagger\psi_j \tag{5.25}$$

for the Schwinger model, where there is no magnetic term due to the theory being constructed in 1+1d, and the coupling strength e has been absorbed into the definition of the electric field operator. The $U(1)$-gauge group has irreducible representations indexed by integers, where $E_{j,j+1}$ acting on a link counts the integer amount of flux passing through that link in units of e. One problem with digitizing the Hamiltonian in Eq. (5.25) is that it is not clear how to deal with fermionic operators, which have the anticommutation relations:

$$\{\psi_j, \psi_k^\dagger\} = \delta_{j,k}, \quad \{\psi_j, \psi_k\} = 0, \quad \{\psi_j^\dagger, \psi_k^\dagger\} = 0 \tag{5.26}$$

To handle this, the Jordan-Wigner transformation [30] maps fermionic operators to spin operators, where each site j is associated with a qubit degree of freedom, on which one can act Pauli matrices (hermitian generators of SU(2)):

$$\sigma^x = \begin{pmatrix} 0 & 1 \\ 1 & 0 \end{pmatrix}, \quad \sigma^y = \begin{pmatrix} 0 & -i \\ i & 0 \end{pmatrix}, \quad \sigma^z = \begin{pmatrix} 1 & 0 \\ 0 & -1 \end{pmatrix}, \quad \sigma^\pm = \frac{\sigma^x \pm i\sigma^y}{2}. \tag{5.27}$$

The fermionic operators are mapped as follows:

$$\psi_j^\dagger \equiv \left(\prod_{i<j} +i\sigma_i^z\right)\sigma_j^+, \quad \psi_j \equiv \left(\prod_{i<j} -i\sigma_i^z\right)\sigma_j^- \tag{5.28}$$

then, the Hamiltonian is the sum $H = H_{\text{kin.}} + H_{\text{mass}} + H_{\text{elec.}}$, where:

$$H_{\text{kin.}} \equiv \frac{1}{2a}\sum_{i=0}^{L-2}\left(\sigma_i^+\sigma_{i+1}^- + \sigma_{i+1}^+\sigma_i^-\right), \quad H_{\text{mass}} \equiv m\sum_{i=0}^{L-1} O_i, \quad H_{\text{elec.}} \equiv \frac{a}{2}\sum_{i=0}^{L} E_i^2, \tag{5.29}$$

$$O_i \equiv (-1)^i\frac{\sigma_i^z + 1}{2a}, \quad E_i \equiv e\left(\ell_0 + \frac{1}{2}\sum_{j=0}^{i-1}(\sigma_j^z + (-1)^j)\right), \tag{5.30}$$

and where m, e are the bare mass and electric charge respectively, and ℓ_0 denotes the boundary condition, labelling the incoming electric flux at the $i = 0$ lattice site. Note that the different sectors of ℓ_0 are not coupled by the Hamiltonian, and it is a boundary condition specifying the 'background' flux. In this study, $\ell_0 = 0$ is always used, and results are closer to the infinite volume result when computed in the 'bulk' far away from the boundaries.

Note that in this formulation, the $U(1)$ gauge field is completely determined by the boundary condition ℓ_0 and distribution of particles within the system by solving the local gauss law at every vertex, as shown in Fig. 5.7. For this reason, it is sometimes said that the gauge field has been integrated out after this mapping is performed.

The D_{ij} matrix appearing in Eq. (5.23) encodes the coupling between the Schwinger Model degrees of freedom and the environment degrees of freedom (in the example Lagrangian shown in

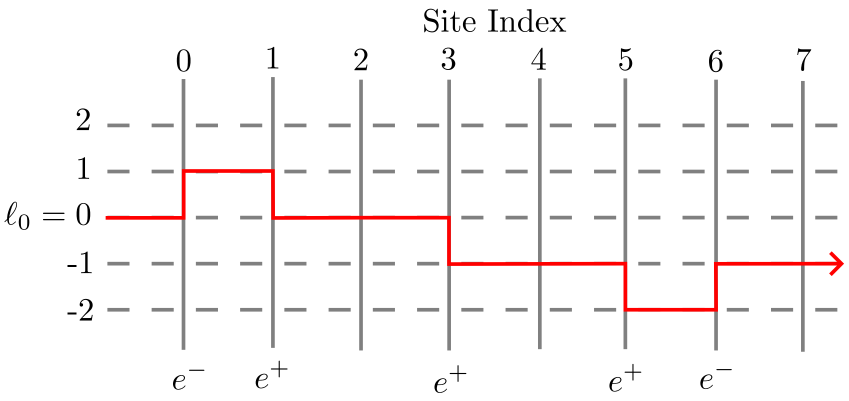

Figure 5.7: A drawing of an example basis state in the Hilbert space corresponding to $\ell_0 = 0$, and total charge $N = -1$. Electrons occupy the even sites and positrons occupy the odd sites, both having the effect of altering the flux $\frac{1}{e}E$ that passes through them by ±1.

Eq. (5.22), this is a Yukawa coupling to an environment scalar). Its specific value will depend on the strength of the Yukawa coupling as well as the Lagrangian describing the environment degrees of freedom $\mathcal{L}_\phi$, and can in principle be computed perturbatively. As discussed in further detail in Sec. 5.2.2 below, CP-conservation of the total Hamiltonian shown in Eq. (5.22) places constraints on the form of the D_{ij} matrix, in particular the Lindbladian $\mathcal{L}$ must be weakly CP-preserving ($[CP \otimes CP, \mathcal{L}] = 0$). Results presented in this section will focus on two special limits:

$$\text{Delta Coupling}: D_{ij} = D_0 \delta_{ij}, \quad \text{Constant Coupling}: D_{ij} = D_0 \mathbf{1}_{ij}, \tag{5.31}$$

where the Delta Coupling is point-like, and $\mathbf{1}_{ij}$ evaluates to 1 for any choice of $\{i, j\}$ in order that the Constant Coupling has effectively infinite range. The Delta Coupling is 'weakly CP-preserving' ($[CP \otimes CP, \mathcal{L}] = 0$) whereas the Constant Coupling is 'strongly CP-preserving' ($\mathcal{L}^\dagger(CP) = 0$) which leads to qualitatively different Lindbladian evolution behaviours.

5.2.2 SYMMETRIES OF THE OPEN SCHWINGER MODEL

There are two relevant discrete symmetries for the Schwinger-model Hamiltonian that split the Hilbert space into distinct sectors. Firstly there is the net particle number operator $N = \sum_{i=0}^{L-1} \sigma_i^z$ that is equal to the number of particles minus the number of antiparticles in the state (equivalently, this is also the net $U(1)$-charge of a state). Most results in this section focus on the neutral sector $N = 0$, which restricts the full Hilbert space of dimension 2^L to a subspace with dimension $\binom{L}{\frac{L}{2}}$. The second symmetry is the CP-symmetry (shown schematically in Fig. 5.8, whose operator is given by $\text{CP} = S \cdot (\prod_{i=0}^{L-1} \sigma_i^x)$ where S is the unitary operator that swaps all sites i with $L - i + 1$. Note that the Schwinger-model does *not* have separate charge (C) and parity (P) symmetries, and the naive guesses for such symmetries ($\prod_{i=0}^{L-1} \sigma_i^x$ and S respectively) do *not* commute with the Schwinger-model Hamiltonian. The CP operator swaps positive charge with negative charge $N \leftrightarrow -N$, but within each fixed $|N|$ subspace the CP operator can be diagonalized to give the following subspace dimensions:

	$\lvert N\rvert = 0$	$\lvert N\rvert = 2n > 0$
$CP = +1$	$\frac{1}{2}\binom{L}{\frac{L}{2}} + 2^{\frac{L}{2}-1}$	$\frac{1}{2}\binom{L}{\frac{L}{2}+n}$
$CP = -1$	$\frac{1}{2}\binom{L}{\frac{L}{2}} - 2^{\frac{L}{2}-1}$	$\frac{1}{2}\binom{L}{\frac{L}{2}+n}$

Note that the CP-even and CP-odd sectors in the $|N| = 0$ subspace do not have the same dimension, due to the existence of basis states that get mapped to themselves under the CP-operator. Under ordinary Hamiltonian evolution, N and CP quantum numbers are preserved by the evolution, which is encoded in the theorem $([Q, H] = 0) \iff (\frac{d}{dt}Q = 0)$. The situation is more involved under Lindbladian evolution as there are two different senses in which charge can be conserved: a charge operator Q is 'strongly-conserved' if $\frac{\mathrm{d}}{\mathrm{d}t}Q = 0$ (in the Heisenberg picture where operators evolve), or 'weakly-conserved' if $[Q \otimes Q, \mathcal{L}] = 0$ where $\mathcal{L}$ is the Lindbladian. As shown in Ref. [31], strong-conservation implies weak conservation, but weak-conservation does not imply strong conservation (a schematic is shown in Fig. 5.8a). Fig. 5.8b shows for the specific case of CP-conservation in the Open Schwinger Model the different behaviours under Lindbladian evolution in each case, when starting from a state of definite CP-properties. The entire space shown is the space of density matrices, i.e. positive-definite matrices that live in $\mathcal{H} \otimes \mathcal{H}^*$ where $\mathcal{H}$ is the Schwinger model Hilbert space. The innermost box is the space spanned by states of the form $|\psi_+\rangle\langle\psi_+|$, where $\mathrm{CP}|\psi_+\rangle = |\psi_+\rangle$. This includes for example the free vacuum state $|0\rangle\langle 0|$, or string product states such as $|e^+(x)e^-(\frac{L}{2} - x)\rangle\langle e^+(x)e^-(\frac{L}{2} - x)|$. The center box $\langle CP\rangle = +1$ represents density matrices ρ where $\mathrm{Tr}(CP \cdot \rho) = 1$, and the outer box $\mathcal{CP} = +1$ denotes density matrices that satisfy $\mathcal{CP}\rho \equiv CP \cdot \rho \cdot CP = \rho$.

The different conservation properties lead to different long-term behaviour under Lindbladian dynamics, in particular the steady state of the Lindbladian lives in different sectors, as shown in Fig. 5.8b. Strong CP conservation causes $\langle CP\rangle$ to be conserved during Lindbladian evolution. For such a Lindbladian there are two steady states, one with $\langle CP\rangle = +1$ and the other with $\langle CP\rangle = -1$ which can be thought of as restrictions of the thermal state into the two CP sectors. Weak CP conservation preserves the $\mathcal{CP}$-sector that the initial state lives in. So long as the initial state is in the $\mathcal{CP} = +1$ sector, Lindbladian evolution is guaranteed to approach the thermal state as the thermal state also lives in the $\mathcal{CP} = +1$ sector. Finally, in the case that there is no CP conservation, the unique steady state will still be approximately thermal.

For the choice of coupling operators $O_i = (\overline{\psi}\psi)_i$, the number operator N is always strongly-conserved, regardless of the choice of coupling matrix D_{ij}. In particular this means that the Lindbladian dynamics has no direct access to chemical potential effects, as the different fixed-N sectors are decoupled. It is still possible to indirectly probe chemical potential effects by simulating the different fixed-N sectors and appropriately reweighting. The CP super-operator $\mathcal{CP} = CP \otimes CP$ splits the space of density matrices into $\mathcal{CP}$-even and $\mathcal{CP}$-odd sectors. Note that regardless of the

CP-nature of a pure state, they are all $\mathcal{CP}$-even. As long as the CP-operator of the subsystem can be extended to a unitary CP_{tot} symmetry of the entire Hilbert space (assuming the medium is CP-symmetric), then there is weak CP-conservation up to corrections that vanish in the Quantum Brownian Motion limit:

$$\begin{aligned} [CP_{\text{tot}}, H_{\text{tot}}] = 0 &\implies CP_{\text{tot}} e^{iH_{\text{tot}}t}|\psi\rangle = e^{iH_{\text{tot}}t} CP_{\text{tot}}|\psi\rangle \\ &\implies \mathcal{CP} e^{\mathcal{L}t} \, \text{Tr}_{\text{env}}(|\psi\rangle\langle\psi|) \approx e^{\mathcal{L}t} \mathcal{CP} \, \text{Tr}_{\text{env}}(|\psi\rangle\langle\psi|) \implies [\mathcal{CP}, \mathcal{L}] \approx 0. \end{aligned} \tag{5.32}$$

This requirement rules out certain choices of coupling matrix D_{ij} that are not weakly-CP conserving. For example, a previously considered ansatz for the coupling matrix is an open boundary condition Gaussian $D_{ij} = D_0 \exp(-\frac{1}{2}\frac{|i-j|^2}{w^2})$ for some width $w > 0$ [29], however this D-matrix violates the weak CP-preservation condition. The physical implication is that the time-evolved electric fields no longer satisfy the symmetry $\langle E_i \rangle(t) = \langle E_{L-i} \rangle(t)$. A modified ansatz that satisfies weak CP-preservation is the periodic Gaussian coupling:

$$D^g_{ij}(w) := D_0 \sum_{n=-\infty}^{\infty} \frac{1}{w\sqrt{2\pi}} \, e^{-\frac{1}{2}\left(\frac{nL+i-j}{w}\right)^2} = \frac{D_0}{L} \vartheta_3 \left((i-j) \cdot \frac{\pi}{L}, \; e^{-\frac{2\pi^2 w^2}{L^2}} \right) \tag{5.33}$$

which can be expressed in terms of the Jacobi-theta function ϑ_3. The parameter D_0 controls the overall coupling strength, and w is the width of the Gaussian. In the general case with w a finite number, the D matrix can be diagonalized numerically on the open-boundary condition lattice to obtain a list of L jump-operators:

$$D = U^\dagger \cdot \text{diag}(\lambda_1, \cdots, \lambda_n) \cdot U, \quad F_i = \sqrt{\lambda_i} U_{ij} \tilde{O}_j, \tag{5.34}$$

$$\mathcal{L}\rho(t) = -i[H, \rho(t)] + a^2 \sum_i \left(F_i \rho(t) F_i^\dagger - \frac{1}{2}\{F_i^\dagger F_i, \rho(t)\} \right). \tag{5.35}$$

The couplings studied in Sec. 5.2.3 are limits of the periodic Gaussian coupling, with the delta coupling being the limit as $w \to 0$ and the constant coupling being the limit as $w \to \infty$:

$$\lim_{w\to 0} w\sqrt{2\pi} \cdot D^g_{ij}(w) = D_0 \delta_{ij}, \quad \lim_{w\to\infty} L \cdot D^g_{ij}(w) = D_0 \mathbf{1}_{ij}. \tag{5.36}$$

5.2.3 LINDBLADIAN DYNAMICS

The Lindbladian dynamics of the Open Schwinger Model as presented in Sec. 5.2.1 is numerically studied with the bare parameters shown in Table 5.1. Parameter set 1 is in a regime where Lindbladian evolution of string states leads to string breaking, and matches the parameters studied in an earlier work [29]. Parameter set 2 is chosen such that the Lindbladian dynamics starting with string product states of length 3, and with the two different types of couplings (see Eq. (5.31)), are approximately equal for small times but show deviations when simulated for long time intervals. The spectra of the associated Lindbladian operators are shown in Fig. 5.9. Note that for the δ-couplings,

$$\begin{tikzcd}
 & {[Q,H] = [Q,F_l] = 0 \quad \forall l} \arrow[dl, Leftrightarrow] \arrow[dr, Rightarrow] & \\
\frac{d}{dt}Q = \mathcal{L}^\dagger(Q) = 0 \arrow[rr, Rightarrow] & & {[\mathcal{Q},\mathcal{L}] = 0}
\end{tikzcd}$$

(a) Relationship between discrete conserved charges Q and dynamical symmetries [31]. F_l are the diagonalized jump operators corresponding to the Lindbladian $\mathcal{L}$, see Eq. (5.35). $\mathcal{Q} = Q \otimes Q$ is the charge super-operator, and $\mathcal{L}^\dagger(Q)$ notates the Heisenberg evolution of Q.

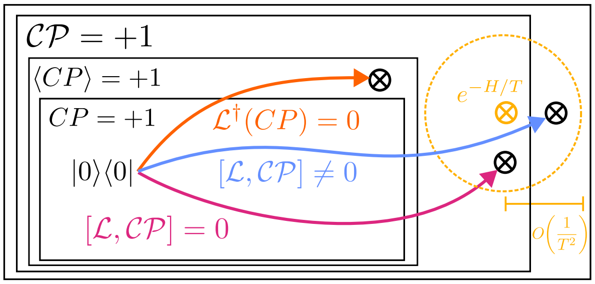

(b) Different evolutions and steady states depending on the CP-nature of the coupling matrix. The pictured initial state is the free ground state. Orange depicts strong CP conservation, maroon depicts weak CP conservation and blue depicts no CP conservation.

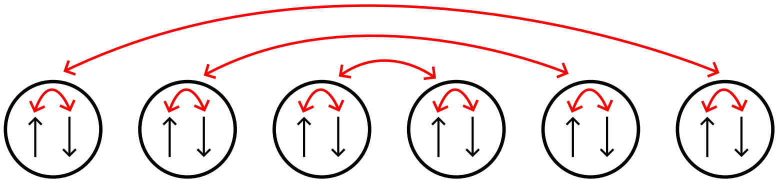

(c) Schematic of the CP operator, which is a combination of a bond-reflection S and swapping $\uparrow, \downarrow$ on each staggered site, where $\uparrow, \downarrow$ represent the spin-$\frac{1}{2}$ basis of σ^z. Note that there are no individual C, P symmetries - in particular $[H, S] \neq 0$, and $[H, \prod \sigma_x] \neq 0$.

Figure 5.8: Details of the CP operator for the discretised Schwinger Model.

	a	m	e	T	D_{ij}
Parameter set 1 (delta):	1	0	0.5	10	$0.15\ \delta_{ij}$
Parameter set 2 (delta):	0.6	0.5	2	1.5	$0.72\ \delta_{ij}$
Parameter set 2 (constant):	0.6	0.5	2	1.5	$0.216\ \mathbf{1}_{ij}$

Table 5.1: Bare parameter sets for the Lindblad operator described in Sec. 5.2.1, which are simulated at various lattice sizes with NDO+tVMC in Sec. 5.2.3.

there is a well-defined Lindbladian gap Δ between the largest real value of the nonzero eigenvalues, and the unique zero eigenvalue which corresponds to the steady state. This gap controls the long-time exponential decay towards the steady state, where the excited contributions die at least as fast as $e^{-\Delta}$. Because the constant coupling is strongly CP-preserving, the lindbladian must have multiple zeros (implying no Lindbladian gap) - interestingly the entire spectrum seems to collapse to the imaginary axis in this case.

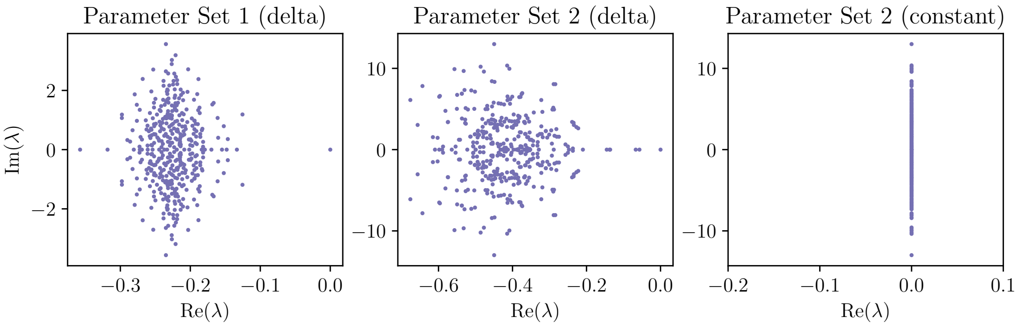

Figure 5.9: Eigenvalues of the Lindbladian operator for the three sets of parameters introduced in Table 5.1, for the 6-site lattice Schwinger model in the $N = 0$ sector.

The initial states studied are product states describing n electrons and n positrons:

$$|e^+(x_1)\cdots e^+(x_n)e^-(y_1)\cdots e^-(y_n)\rangle = \sigma^-_{2x_1+1}\cdots\sigma^-_{2x_n+1}\sigma^+_{2y_1}\cdots\sigma^+_{2y_n}|\downarrow\uparrow\cdots\downarrow\uparrow\rangle. \tag{5.37}$$

Here, x_i, y_i label physical sites rather than staggered sites, and the state $|\downarrow\uparrow\cdots\downarrow\uparrow\rangle$ is the free vacuum product state expressed in the Z-computational basis. Observables that are useful for visualising the real-time dynamics are the dimensionless chiral condensate and the electric field expressed in units of e:

$$\overline{\psi}\psi := \frac{1}{L}\sum_{i=0}^{L-1}(-1)^i\frac{\sigma^z_i + 1}{2}, \quad E_i = \frac{1}{2}\sum_{j=0}^{i-1}(\sigma^z_j + (-1)^j). \tag{5.38}$$

When initialising to product states containing string configurations, the time-evolved electric field $\langle E_i^{\text{string}}\rangle(t)$ contains large vacuum fluctuations, which can be removed by subtracting the electric field of the time-evolved free vacuum state $|\downarrow\uparrow\cdots\downarrow\uparrow\rangle$, giving $\langle E_i^{\text{vac.sub.}}\rangle(t) := \langle E_i^{\text{string}}\rangle(t) - \langle E_i^{\text{vacuum}}\rangle(t)$. For illustration purposes it is also useful to define a shifted electric field $\tilde{E}_i(t)$, which has been shifted by its value at $t = 0$, $\langle\tilde{E}_i\rangle(t) := \langle E_i\rangle(t) - \langle E_i\rangle(0)$.

Fig. 5.10 shows a comparison of $\langle\overline{\psi}\psi\rangle(t)$ between results computed with NDO-tVMC and results computed using exact representations, for parameter set 1 on an $L = 10$ lattice. Both NDO-tVMC and the exact results use the 4-th order Runge-Kutta integrator with $\mathrm{d}t = 0.05$ to integrate the Lindblad equation. The diagonal shift regulator for the Quantum Geometric Tensor inversion is set to $5\cdot 10^{-5}$. A total of 2^{17} samples were used in both MCMCs when estimating observables/forces, and the size of the NDO was varied as labelled in the figure. It was observed that vacuum fluctuations cause systematic errors in the computed Lindbladian evolutions of the chiral condensate that grow in time, which are relatively suppressed for string product states compared to vacuum product states. Fig. 5.10(a) demonstrates that the network size significantly affects the systematic uncertainty in the tVMC-NDO algorithm, with larger network sizes resulting in smaller errors due to the higher representation power.

Fig. 5.11 compares the vacuum subtracted electric fields $\langle E^{\text{string}}\rangle(t) - \langle E^{\text{vacuum}}\rangle(t)$ between the NDO-tVMC determination (using the largest network $(M_h, M_a) = (10, 10)$) and the exact result.

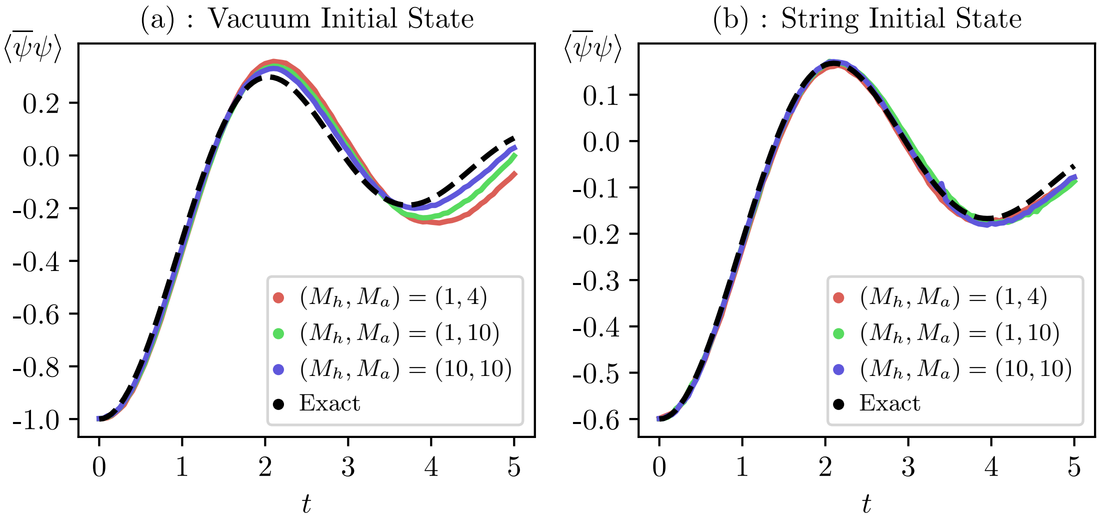

Figure 5.10: Studies of parameter set 1, on an $L = 10$ lattice. (a) The Lindbladian dynamics of the chiral condensate $\langle\overline{\psi}\psi\rangle$ computed with NDO's of various sizes, compared with the exact result. (b) The same, but with the string state $\sigma_3^- \sigma_6^+ |\downarrow\uparrow \cdots \downarrow\uparrow\rangle$ as the initial state.

Qualitative agreement is observed between the solutions; for a more quantitative comparison, the shifted electric fields $\langle\tilde{E}_i^{\text{string}}\rangle(t) - \langle\tilde{E}_i^{\text{vacuum}}\rangle(t)$ are compared between the NDO-tVMC calculation and exact results in Fig. 5.12. Due to the fact that the δ-coupling is weakly CP-conserving, the electric fields satisfy the symmetry $\langle E_i\rangle(t) = \langle E_{L-i}\rangle(t)$. Fig. 5.12 demonstrates that the NDO-tVMC algorithm has preserved this symmetry well in the simulated Lindbladian dynamics, as the results of measurements of the electric field on each half of the lattice are consistent.

The NDO-tVMC method is able to simulate different types of coupling matrices D_{ij}. Parameter set 2 is specifically tuned such that the vacuum-subtracted chiral condensate has similar Lindbladian dynamics for small times when comparing the delta coupling to the constant coupling with the initial string state $\sigma_3^- \sigma_6^+ |\downarrow\uparrow \cdots \downarrow\uparrow\rangle$—Fig. 5.13 shows that they share the same first oscillation, but diverge in behaviour afterwards. As the constant coupling is strongly-CP conserving, there are two distinct steady states and the long-time dynamics of the constant coupling dynamics does not match the long-time dynamics of the delta coupling dynamics. Fig. 5.13 demonstrates the ability of the NDO-tVMC to distinguish between the two types of coupling.

One of the advantages of the NDO approach is that it can be applied to lattice sizes L where exact calculations are computationally intractable. However, it is important that the uncertainties arising from the truncated parameterisation of the NDO can be controlled or estimated. In particular, for an NDO parameterisation with fixed (M_h, M_a), the number of complex parameters in the model

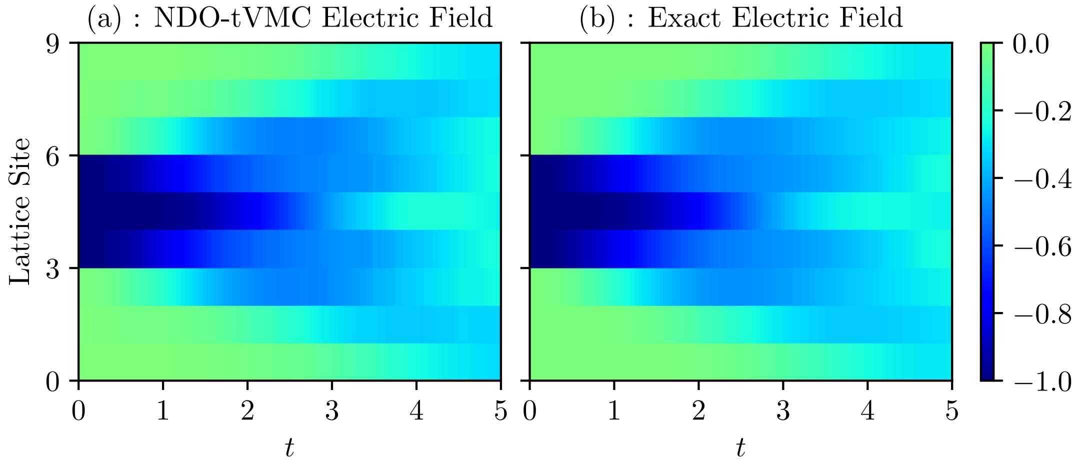

Figure 5.11: The vacuum-subtracted electric fields as a function of time, computed for parameter set 1 with string state $\sigma_3^- \sigma_6^+ | \downarrow\uparrow \cdots \downarrow\uparrow\rangle$. (a) The result computed with a $(M_h, M_a) = (10, 10)$ NDO which has been rolling-averaged over three timesteps to reduce statistical noise. (b) The exact result.

grows quadratically with the lattice size, whereas the dimension of the space of density matrices grows exponentially, as shown in Fig. 5.14(a). The effects of this (increasingly severe) truncation can be quantified in the regime of lattice sizes L where exact calculations are possible, in order to understand the scaling of systematic effects. Fig. 5.14(b) shows the scaling of the normalised error in the chiral condensate for the vacuum initial state evaluated at $t = 2$:

$$\mathrm{Err}[\langle\overline{\psi}\psi\rangle(t=2)] := \frac{1}{2}\left(\langle\overline{\psi}\psi\rangle_{\mathrm{NDO}}(t=2) - \langle\overline{\psi}\psi\rangle_{\mathrm{exact}}(t=2)\right) \tag{5.39}$$

as a function of the lattice size L holding all other hyperparameters constant (number of samples used in the MCMCs, regulator choice for the QGT inversion). The factor of $\frac{1}{2}$ accounts for the normalisation as $\langle\overline{\psi}\psi\rangle \in [-1, 1]$. The time $t = 2$ is chosen as the peak of the first oscillation in the time-evolved chiral condensate, as observed in Fig. 5.10(a). As shown in Fig. 5.14(b), at fixed time $t = 2$ and for fixed (M_h, M_a) the scaling of the error as a function of lattice size is fairly mild, suggesting that the accuracy of the NDO-tVMC algorithm can be controlled as the lattice size is increased to larger values where exact results are not available. Other sources of systematic error in the NDO-tVMC algorithm include the number of samples used in the MCMC chains [26], choice of regulator for the Quantum Geometric Tensor inversion [32], and the timestep used in ODE integrator.

The normalised error in the chiral condensate for the vacuum initial state is shown as a function of simulation time in Fig. 5.15, for a variety of lattice sizes with the largest tested NDOs, $(M_h, M_a) = (10, 10)$. The approximate curve collapse for times $t \leq 2$ once again suggests mild scaling of errors

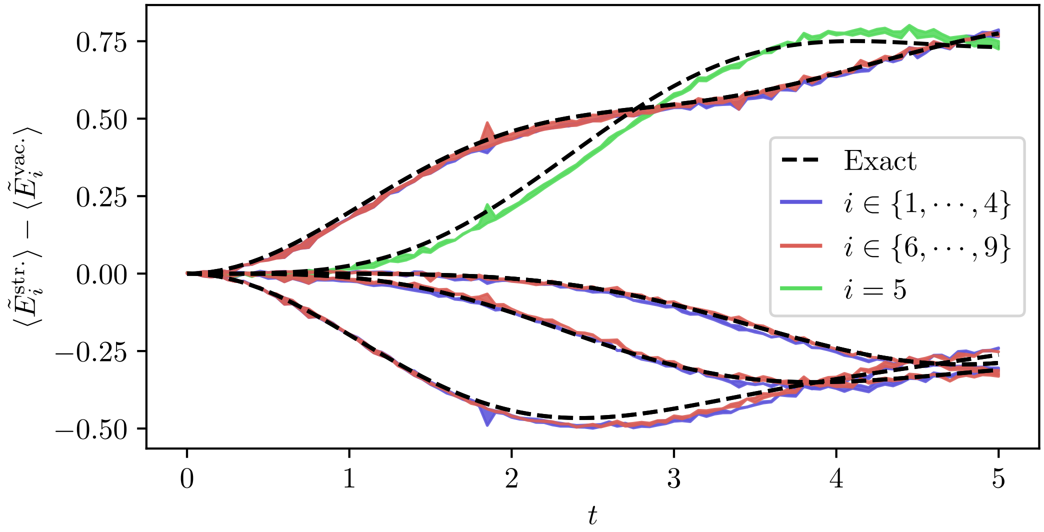

Figure 5.12: The same data as Fig. 5.11, with the shifted vacuum-subtracted electric field at each lattice site shown as a separate line. The NDO-tVMC electric fields measured on the left/right half of the lattice are denoted by blue/red bands. The green band corresponds to the electric field link exactly in the center of the lattice.

as the lattice-size is increased at early to intermediate times during the evolution of the system. At later simulation times, the scaling of errors as a function of lattice size is less controlled; note, however, that there is no simple relationship between the size of the error for different lattice sizes. Although the time $t = 2$ corresponds to a physically relevant timescale (the first peak of the chiral condensate evolution for the vacuum initial state), it does not correspond to a maximum/minimum in $\mathrm{Err}[\langle \overline{\psi}\psi \rangle]$.

To demonstrate the utility of the NDO-tVMC approach for larger lattice sizes where exact results are computationally intractable to achieve, the Lindbladian dynamics of various initial states are simulated on an $L = 20$ lattice, as shown in Fig. 5.16. The real dimension of the space of density matrices is approximately $3 \cdot 10^{10}$, which was parametrised by 9280 real parameters corresponding to $M_h = 1, M_a = 4$ in the NDO construction. In Fig. 5.16(a) an initial e^+e^- pair joined by a short string splits into two strings due to the pair creation of an e^+e^- pair in-between the two fermions, which is the same physical scenario simulated in Fig. 5.11, but on a larger lattice size where finite volume effects are suppressed. Fig. 5.16(b) illustrates that the dynamics of multi-string states can be investigated, at the same computational cost as simulating the dynamics of single-string states. Finally, Fig. 5.16(c) shows the dynamics of a long string, which can not be investigated on smaller lattice sizes.

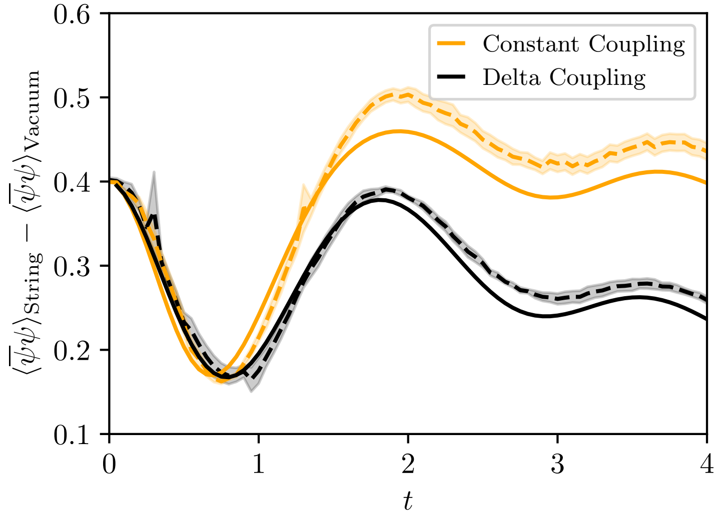

Figure 5.13: Vacuum-subtracted chiral condensates computed with NDO-tVMC (dashed lines) for the two types of couplings in parameter set 2, with initial string state $\sigma_3^- \sigma_6^+ | \downarrow\uparrow \cdots \downarrow\uparrow\rangle$. Shaded bands indicate statistical uncertainty estimated by MCMC, added in quadrature with the uncertainty computed as the spread over three separate runs of the simulation. Exact results (solid lines) are shown for comparison. Results are computed on an $L = 10$ lattice, with $(M_h, M_a) = (10, 10)$.

5.2.4 STEADY STATE PROPERTIES

Extracting the steady state solution $\rho_{\text{stab.}}$, which by definition satisfies:

$$\mathcal{L}\rho_{\text{stab.}} = 0 \quad \implies \quad \rho_{\text{stab.}} = \exp(-H/T) + O(T^{-2}), \tag{5.40}$$

allows thermal properties of the system to be probed. Note that the thermal properties of relativistic QFTs such as the Schwinger Model and QCD can be obtained by discretising the Euclidean path integral and performing Monte-Carlo over the resulting distribution, as in Lattice-QCD. It might then seem strange and roundabout to study the thermal density matrix by preparing it variationally as the long-time limit of the Lindblad evolution. Such a study however serves two purposes: firstly it serves as a check that neural network variational parametrisations can adequately capture the volume-law entanglement expected in thermal distributions. Secondly, this approach allows one to explore regions of phase-space that are impossible for path-integral Monte Carlo due to sign problems, for instance due to a chemical potential or a θ-term.

As discussed in Sec. 5.1, Stochastic Reconfiguration with a finite diagonal shift as a regulator for the Quantum Geometric Tensor inversion is used to drive the NDO towards the steady state. Transfer-learning allows weights on smaller lattice sizes to be used as initialization for training on

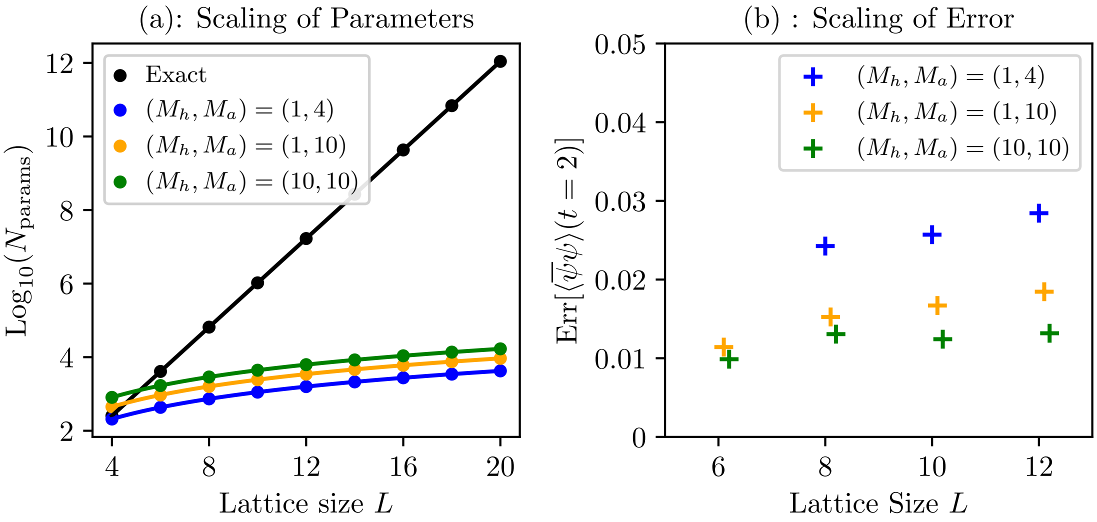

Figure 5.14: (a) Scaling of the number of parameters in the NDO construction at a fixed set of choices of (M_h, M_a) with the size of the lattice L, compared to the complex dimension of $\mathcal{H} \otimes \mathcal{H}^*$ (black line). The three trajectories shown are the same choices used in the comparison of Fig. 5.10. (b) Scaling of errors at $t = 2$ for parameter set 1 and the vacuum initial state as a function of the lattice size L.

larger lattice sizes, which both reduces training costs and increases the reliability of results, as described in Fig. 5.5. For a small $L = 4$ lattice size, exact results for the steady state are easily computable; comparisons of the chiral condensate as determined with Stochastic Reconfiguration to the exact results are shown in Fig. 5.17. Results shown are computed for a compact parameterisation with $(M_h, M_a) = (1, 1)$. A diagonal shift of 0.01 is used, with 16000 samples distributed over 16 independent chains for both the MCMC chains, and the system is trained for 6000 steps. The Lindbladian used is the delta-coupling Lindbladian $D_{ij} = \delta_{ij}$, which is chosen to ensure a unique steady state solution (as opposed to the constant coupling which has two separate steady states). The chiral symmetry breaking transition can be seen by the nonzero chiral condensate as the temperature is decreased, or as the bare mass is increased (explicit chiral symmetry breaking).

Instead of studying the system at a finite chemical potential μ, the system is studied at a finite net charge - which can be Legendre transformed to recover results at finite μ. The steady state of the $L = 4$ system is used to bootstrap to results on larger lattice sizes where exact results can not be achieved; the state is transferred to an $L = 8$ lattice size, and retrained. This process is repeated twice, yielding an approximation of the steady state on a $L = 32$ lattice size. In the transfer learning, 8000 samples are distributed over 128 independent chains, and gradients are clipped to have maximum L^2 norm 1 [33]. The Stochastic Reconfiguration regulator parameter is set to $\epsilon = 0.1$

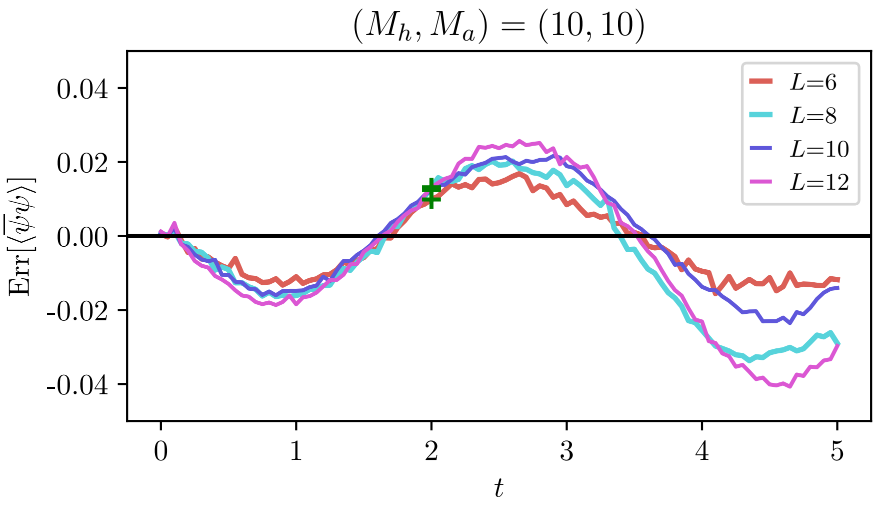

Figure 5.15: For the largest neural network shapes tested ($(M_h, M_a) = (10, 10)$), the normalised error in the chiral condensate for the vacuum initial state is shown as a function of time for various lattice sizes. The green markers denote the same points as those shown with the same symbol in Fig. 5.14(b).

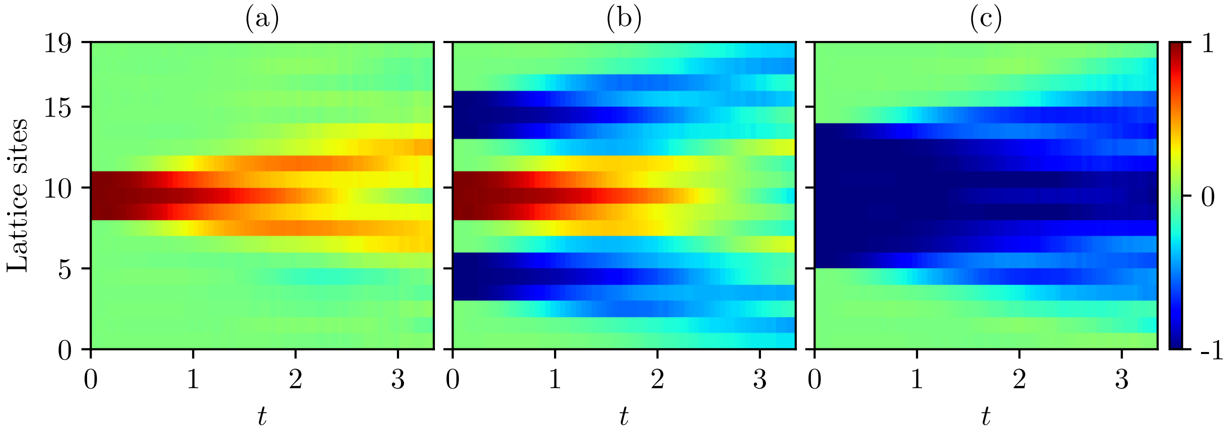

Figure 5.16: The vacuum-subtracted electric field as a function of time for various initial states, for parameter set 1 on an $L = 20$ lattice. (a) Initial state is a single short string $\sigma^+_8\sigma^-_{11}|\downarrow\uparrow\cdots\downarrow\uparrow\rangle$. (b) Initial state is three interacting strings $\sigma^-_3\sigma^+_6\sigma^+_8\sigma^-_{11}\sigma^-_{13}\sigma^+_{15}|\downarrow\uparrow\cdots\downarrow\uparrow\rangle$. (c) Initial state is a single long string $\sigma^-_5\sigma^+_{14}|\downarrow\uparrow\cdots\downarrow\uparrow\rangle$.

for all the training sets. Fig. 5.18 shows the behaviour of the measured chiral condensate as a function of T, m, and the filling fraction $\nu := \frac{N}{L}$ where $N = \sum_{i=0}^{L-1}\sigma^z_i$ is the net particle number. The

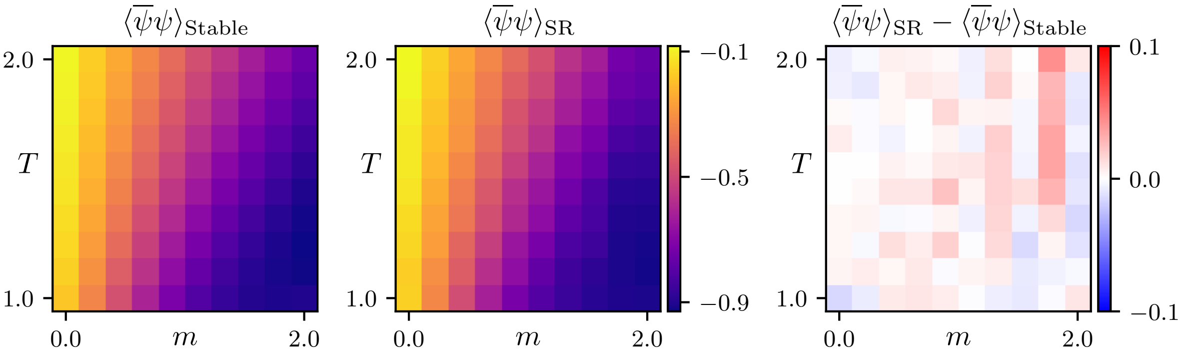

Figure 5.17: Comparison between the exact chiral condensate of the steady state (left), with the chiral condensate computed by the Stochastic Reconfiguration algorithm (center) as a function of temperature T and mass m. The unnormalised difference between the two is shown in the right figure.

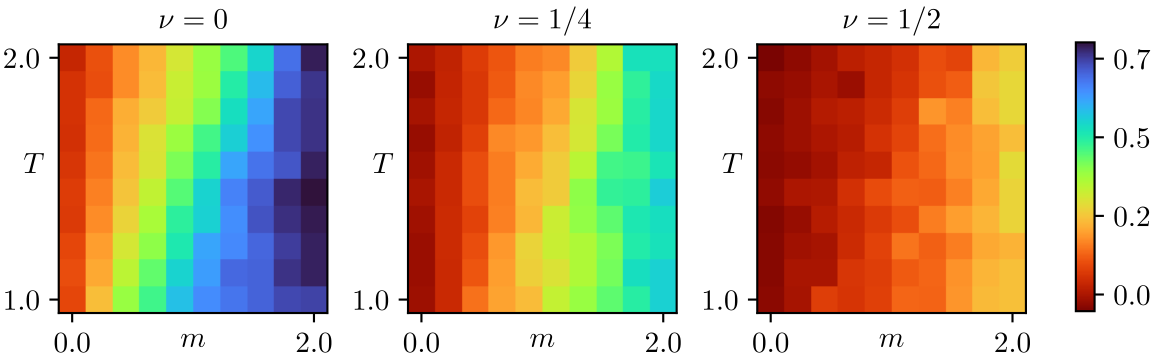

Figure 5.18: Measurement of the chiral condensate of the learned steady state solution on a $L = 32$ lattice size. The three different columns show the system at different filling fractions $\nu = \frac{N}{L}$.

filling fraction ν varies in the range $\nu \in [-1, 1]$. By CP-symmetry, the measured chiral condensate is symmetric about $\nu = \frac{1}{2}$ when all other bare parameters are held fixed.

BIBLIOGRAPHY

[1] Georges Aad et al. Production of Υ(nS) mesons in Pb+Pb and pp collisions at 5.02 TeV. *Phys. Rev. C*, 107(5): 054912, 2023. doi: 10.1103/PhysRevC.107.054912.

[2] T. Matsui and H. Satz. J/ψ Suppression by Quark-Gluon Plasma Formation. *Phys. Lett. B*, 178:416–422, 1986. doi: 10.1016/0370-2693(86)91404-8.

[3] Xiaojun Yao. Open quantum systems for quarkonia. *Int. J. Mod. Phys. A*, 36(20):2130010, 2021. doi: 10.1142/S0217751X21300106.

[4] Nora Brambilla, Tom Magorsch, Michael Strickland, Antonio Vairo, and Peter Vander Griend. Bottomonium suppression from the three-loop QCD potential. *Phys. Rev. D*, 109(11):114016, 2024. doi: 10.1103/PhysRevD.109.114016.

[5] Matteo Cacciari, Mario Greco, and Paolo Nason. The p_T spectrum in heavy-flavour hadroproduction. *JHEP*, 05:007, 1998. doi: 10.1088/1126-6708/1998/05/007.

[6] Heinz-Peter Breuer and Francesco Petruccione. *The Theory of Open Quantum Systems*, chapter 6. Oxford University Press, 01 2007. ISBN 9780199213900. doi: 10.1093/acprof:oso/9780199213900.001.0001. URL `https://doi.org/10.1093/acprof:oso/9780199213900.001.0001`.

[7] Hisham Ba Omar, Miguel Ángel Escobedo, Ajaharul Islam, Michael Strickland, Sabin Thapa, Peter Vander Griend, and Johannes Heinrich Weber. QTRAJ 1.0: A Lindblad equation solver for heavy-quarkonium dynamics. *Comput. Phys. Commun.*, 273:108266, 2022. doi: 10.1016/j.cpc.2021.108266.

[8] Andrew J. Daley. Quantum trajectories and open many-body quantum systems. *Adv. Phys.*, 63(2):77–149, 2014. doi: 10.1080/00018732.2014.933502.

[9] Giacomo Torlai and Roger G. Melko. Latent space purification via neural density operators. *Phys. Rev. Lett.*, 120:240503, Jun 2018. doi: 10.1103/PhysRevLett.120.240503. URL `https://link.aps.org/doi/10.1103/PhysRevLett.120.240503`.

[10] Joshua Lin, Di Luo, Xiaojun Yao, and Phiala E. Shanahan. Real-time dynamics of the Schwinger model as an open quantum system with Neural Density Operators. *JHEP*, 06:211, 2024. doi: 10.1007/JHEP06(2024)211.

[11] J. Eisert, M. Cramer, and M. B. Plenio. Area laws for the entanglement entropy - a review. *Rev. Mod. Phys.*, 82:277–306, 2010. doi: 10.1103/RevModPhys.82.277.

[12] Giacomo Passetti, Damian Hofmann, Pit Neitemeier, Lukas Grunwald, Michael A. Sentef, and Dante M. Kennes. Can Neural Quantum States Learn Volume-Law Ground States? *Phys. Rev. Lett.*, 131(3):036502, 2023. doi: 10.1103/PhysRevLett.131.036502.

[13] Zakari Denis, Alessandro Sinibaldi, and Giuseppe Carleo. Comment on ”Can Neural Quantum States Learn Volume-Law Ground States?”. 9 2023.

[14] Giuseppe Carleo and Matthias Troyer. Solving the quantum many-body problem with artificial neural networks. *Science*, 355(6325):602–606, 2017. doi: 10.1126/science.aag2302.

[15] John B. Kogut and Leonard Susskind. Hamiltonian Formulation of Wilson's Lattice Gauge Theories. *Phys. Rev. D*, 11:395–408, 1975. doi: 10.1103/PhysRevD.11.395.

[16] David H. Ackley, Geoffrey E. Hinton, and Terrence J. Sejnowski. A learning algorithm for boltzmann machines. *Cognitive Science*, 9(1):147–169, 1985. ISSN 0364-0213. doi: https://doi.org/10.1016/S0364-0213(85)80012-4. URL `https://www.sciencedirect.com/science/article/pii/S0364021385800124`.

[17] J. J. Hopfield. Neural networks and physical systems with emergent collective computational abilities. *Proc. Nat. Acad. Sci.*, 79:2554–2558, 1982. doi: 10.1073/pnas.79.8.2554.

[18] Nicolas Le Roux and Yoshua Bengio. Representational power of restricted boltzmann machines and deep belief networks. *Neural Computation*, 20(6):1631–1649, 2008. doi: 10.1162/neco.2008.04-07-510.

[19] Michael J. Hartmann and Giuseppe Carleo. Neural-Network Approach to Dissipative Quantum Many-Body Dynamics. *Phys. Rev. Lett.*, 122(25):250502, 2019. doi: 10.1103/physrevlett.122.250502.

[20] Filippo Vicentini, Riccardo Rossi, and Giuseppe Carleo. Positive-definite parametrization of mixed quantum states with deep neural networks. 6 2022.

[21] Filippo Vicentini, Damian Hofmann, Attila Szabó, Dian Wu, Christopher Roth, Clemens Giuliani, Gabriel Pescia, Jannes Nys, Vladimir Vargas-Calderon, Nikita Astrakhantsev, and Giuseppe Carleo. Netket 3: Machine learning toolbox for many-body quantum systems, 2021. URL `https://arxiv.org/abs/2112.10526`.

[22] Peter Kramer and Marcos Saraceno, editors. *Geometry of the Time-Dependent Variational Principle in Quantum Mechanics*. Springer Berlin Heidelberg, 1981. doi: 10.1007/3-540-10579-4. URL `https://doi.org/10.1007/3-540-10579-4`.

[23] Michael V. Berry. The Quantum Phase, Five Years After. In Alfred D. Shapere and Frank Wilczek, editors, *Geometric Phases in Physics*, 1989.

[24] Sandro Sorella. Green function monte carlo with stochastic reconfiguration. *Physical Review Letters*, 80(20):4558–4561, may 1998. doi: 10.1103/physrevlett.80.4558. URL `https://doi.org/10.1103%2Fphysrevlett.80.4558`.

[25] Sandro Sorella, Michele Casula, and Dario Rocca. Weak binding between two aromatic rings: Feeling the van der waals attraction by quantum monte carlo methods. *The Journal of Chemical Physics*, 127(1):014105, jul 2007. doi: 10.1063/1.2746035. URL `https://doi.org/10.1063%2F1.2746035`.

[26] Alessandro Sinibaldi, Clemens Giuliani, Giuseppe Carleo, and Filippo Vicentini. Unbiasing time-dependent Variational Monte Carlo by projected quantum evolution. *Quantum*, 7:1131, 2023. doi: 10.22331/q-2023-10-10-1131.

[27] Julian Schwinger. Gauge invariance and mass. ii. *Phys. Rev.*, 128:2425–2429, Dec 1962. doi: 10.1103/PhysRev.128.2425. URL `https://link.aps.org/doi/10.1103/PhysRev.128.2425`.

[28] Wibe A. de Jong, Kyle Lee, James Mulligan, Mateusz Płoskoń, Felix Ringer, and Xiaojun Yao. Quantum simulation of nonequilibrium dynamics and thermalization in the Schwinger model. *Phys. Rev. D*, 106(5):054508, 2022. doi: 10.1103/PhysRevD.106.054508.

[29] Kyle Lee, James Mulligan, Felix Ringer, and Xiaojun Yao. Liouvillian Dynamics of the Open Schwinger Model: String Breaking and Kinetic Dissipation in a Thermal Medium. 8 2023.

[30] Pascual Jordan and Eugene P. Wigner. About the Pauli exclusion principle. *Z. Phys.*, 47:631–651, 1928. doi: 10.1007/BF01331938.

[31] Victor V. Albert and Liang Jiang. Symmetries and conserved quantities in lindblad master equations. *Phys. Rev. A*, 89:022118, Feb 2014. doi: 10.1103/PhysRevA.89.022118. URL `https://link.aps.org/doi/10.1103/PhysRevA.89.022118`.

[32] Markus Schmitt and Markus Heyl. Quantum many-body dynamics in two dimensions with artificial neural networks. *Physical Review Letters*, 125(10), sep 2020. doi: 10.1103/physrevlett.125.100503. URL `https://doi.org/10.1103%2Fphysrevlett.125.100503`.

[33] Razvan Pascanu, Tomas Mikolov, and Y. Bengio. On the difficulty of training recurrent neural networks. *30th International Conference on Machine Learning, ICML 2013*, 11 2012.

Chapter 6

Summary and Conclusion

The large scale separation between Λ_{QCD} and the masses of the heavy quarks m_Q makes their properties particularly interesting, due to effective heavy quark expansions. This thesis has presented my contributions in both developing techniques to compute heavy hadron matrix elements and the real-time dynamics of heavy quarks in a thermal medium, as well as presenting a first measurement of the Spectator Effect matrix elements using newly developed X-space renormalisation schemes. By working towards more precise measurements of these and related observables, we move closer to an understanding of inclusive/exclusive tensions of CKM matrix elements, of the Quark-Gluon-Plasma produced at heavy ion colliders, and of QCD as a whole.

- **X-space renormalisation schemes**

  In Chapter 3, a set of X-space renormalisation schemes for isospin-nonsinglet $\Delta Q = 0$ and $\Delta Q = 2$ four-quark HQET operators have been proposed, and the $O(\alpha_S)$ matching coefficients between these schemes and $\overline{\mathrm{MS}}$ in the dimensionally regulated continuum have been calculated. This allows for a gauge-invariant, nonperturbative renormalisation matrix elements calculated in lattice HQET, without the need to extract the power-divergent self-energy contribution m_{stat}. Precise computations of these matrix elements with lattice HQET will reduce theory uncertainties on lifetimes of heavy hadrons, and help constrain physics beyond the Standard Model. Note that, when implementing the X-space scheme for these four-quark operators in lattice HQET, it is convenient to use Ginsparg-Wilson discretisations of the light quarks (e.g., with the domain-wall fermion action) to avoid additional mixing between the four-quark operators of interest and operators in other chiral representations.

  Next-to-next-to-leading-order calculations of the matching coefficients presented in Eqs. (3.76) to (3.78) at $O(\alpha_S^2)$ are possible, but the computation is complicated by the fact that unlike p-type integrals that only have one external scale, the perturbative calculations shown in Sec. 3.2.3 have two external scales $x_{\mathrm{src}}, x_{\mathrm{snk}}$ corresponding to the source and sink locations of the three-point renormalisation scheme proposed. Corrections due to finite light-quark masses are more easily calculable (though they are likely smaller than the $O(\alpha_S^2)$ corrections on typical lattice-QCD ensembles), and require computation of the three-loop integrals in Sec. 3.2.3 either analytically in the light-quark mass, or by expanding in powers of the light quark mass. $O(\frac{1}{m_Q})$ corrections are in principle also calculable, but require considering mixing of the four-quark operators with dimension-7 operators that contain an additional covariant derivative, as well as considering the $O(\frac{1}{m_b})$ corrections to the static HQET Lagrangian.

The calculations and techniques used in this work can be readily applied to X-space schemes for other classes of operators. For instance, using the auxiliary-field formalism, nonlocal operators such as $\overline{q}(x)W(x,y)q(y)$, where $W(x,y)$ is a Wilson line, are transformed into products of local operators $\overline{q}Q_{y-x}(x)\overline{Q}_{y-x}q(y)$, which can be renormalized by the techniques presented in Sec. 3.2.3. The calculations of the three-loop diagrams involving gluons attached to the light-quark propagators presented in Sec. 3.2.3 can also be applied to renormalise massless four-quark operators such as the $\Delta S = 1$ four-quark operators relevant for kaon decays.

- **Spectator Effects**

  In Chapter 4, a first determination of the Spectator Effect matrix elements for a heavy-light meson are determined, using the nonperturbative X-space renormalisation schemes proposed in Chapter 3. Though the uncertainties due to lattice-artifacts have been estimated with a continuum limit fit, the calculation was performed in ensembles with an unphysically large value of the pion mass, and chiral limit fits were not attempted. The addition of ensembles with a lighter pion mass, or the use of partially quenches quark propagators, may allow these calculations to be extended to an extraction of the relevant matrix elements at the physical point. Such a determination would greatly reduce the current theoretical uncertainty on inclusive lifetime ratios $\tau(B^+)/\tau(B^0)$, and may be compared to experimentally extracted matrix elements used in the inclusive determination of the CKM matrix elements V_{cb}, V_{ub}.

  The heavy-light decay constant f_B^{HQET} is similarly determined, however note that unlike the Spectator Effect matrix elements, f_B has been calculated in a number of different lattice actions and strategies at the physical point. A detailed analysis of the window problem, and the utility of step-scaling was demonstrated for f_B^{HQET}, where $O(\alpha_S^3)$ results for the matching between X-space and $\overline{\mathrm{MS}}$ were available. The step-scaling was made slightly awkward by the fact that the available ensembles did not have lattice spacings that were even multiples of each other, leading to signficant uncertainties due to the interpolation strategies used. With the addition of further ensembles with compatible lattice spacings, it may be possible that this strategy can provide a determination of f_B^{HQET} with uncertainties that are competitive with other determinations [1].

- **Variational Approaches to simulating Open Quantum Field Theories**

  Chapter 5 presents evidence that Neural Network variational ansätze can parametrise the space of states of the Open Schwinger Model in a systematically controllable manner. This represents the first time a variational ansätz has been applied to an Open-QFT, and suggests possible extensions to more complicated theories. This setting is quite different from heavy quarks propagating in the Quark Gluon Plasma: it is *easier* because it is in less dimensions, but *harder* because the fermions were not matched to an effective field theory. The fact that the theory was not matched to a nonrelativistic theory is encouraging if the end goal is to simulate $O(100)$ $\bar{c}c$-pairs produced in a heavy ion collision. In extending such variational parametrisations of lattice discretised QFTs to higher dimensions, there a number of technical difficulties to deal with - such as a choice of Jordan-Wigner path through the higher dimensional lattice. Alternatively, continuous parametrisations of nonrelativistic density matrices are possible, which may be simpler to implement.

- **Dirac Traces and the Tutte Polynomial**

  In this thesis, a connection between dimensionally regulated Dirac traces and Tutte polynomials of corresponding graphs was proven. The connection is theoretically interesting in both directions, on the one hand giving a graph-theoretic interpretation of what dimensionally regulated traces means, and on the other hand providing a 'physical' interpretation for the Tutte polynomial $T(G; x, y)$ evaluated along $y = -1$ (at least when G is a circle graph). Preliminary investigations suggest the connection may also be practically useful, providing faster algorithms to compute Dirac traces for single traces of randomly contracted Dirac matrices. These preliminary investigations have to be taken with a grain of salt, given that the distribution of Dirac traces that actually appear in realistic multi-loop calculations is not going to be the uniformly random contracted distribution. It would however be interesting to see a complete implementation of arbitrary Dirac traces utilising the connection to Tutte polynomials developed in the future.

  The discussion in Appendix A.3 motivates one to consider a more in-depth study of the computational complexity of Tutte polynomial evaluations on the class of circle graphs (similar to what was performed for planar graphs in Ref. [2]). For instance, a natural conjecture to consider is that Theorem A.3.0.9 can be strengthened to a statement that evaluations of d-dimensional Dirac traces is #P-hard. Following the strategy outlined in Appendix A.3, this would first require showing that $\pi_{\{(1-n,0)\}}(\mathbf{Circle})$ are #P-complete, possibly by showing that the reduction in Ref. [3] can be made parsimonious. Then perhaps by finding a different transformation (other than k-stretching) that circle graphs are closed under, that allows one to interpolate the Tutte polynomial on the entire plane. In a similar vein, it would be interesting to consider the computational problem of computing the coefficient of ϵ^n in Tr_d, where $d = 4 - \epsilon$ for a fixed n (as in practical perturbative QFT calculations calculations are only performed to some fixed number of loops).

  Though a framework for handling open indices, multiple traces and the 'tHooft-Veltman γ_5 is presented in Appendix A.4, it is possible that there is a more natural framework for these objects as well. A more matroid-theoretic interpretation of products of multiple Dirac traces with indices contracted in some fashion may allow for a clean analysis of the computational complexity of this more complicated case. Graph-theoretic interpretations of γ_5, evanescent operators, and similar complications in dimensionally regulated Dirac matrices may prove fruitful in the future.

Bibliography

[1] Y. Aoki et al. FLAG Review 2024. 11 2024.

[2] Dirk Vertigan. The computational complexity of Tutte invariants for planar graphs. *SIAM Journal on Computing*, 35(3):690–712, 2005. doi: 10.1137/S0097539704446797.

[3] Walter Unger. On the k-colouring of circle-graphs. In Robert Cori and Martin Wirsing, editors, *STACS 88*, pages 61–72, Berlin, Heidelberg, 1988. Springer Berlin Heidelberg. ISBN 978-3-540-48190-4.

CHAPTER A

DIRAC TRACES AND THE TUTTE POLYNOMIAL

Content in this section has been reproduced from the following reference:

Joshua Lin. Dirac Traces and the Tutte Polynomial. JHEP, 10 2024. doi: 10.1007/JHEP05(2025)235.

Contents

This appendix contains details of the proofs of the main theorems presented in Sec. 2.1.5 linking the conventional dimensionally regulated Dirac trace to Tutte polynomial evaluations:

$$\mathrm{Tr}_d(\gamma_{\mu_{x_1}} \cdots \gamma_{\mu_{x_{2n}}}) = 4(-1)^{|E|}(-2)^{n-c(\mathrm{Gr}(x))}\, d^{\,c(\mathrm{Gr}(x))}\, T\left(\mathrm{Gr}(x); 1-\tfrac{d}{2}, -1\right) \tag{A.1}$$

A.1 MAPPING BETWEEN DIRAC TRACE AND TUTTE POLYNOMIAL

In this section, the formal connection between the dimensionally regulated Dirac trace and the Tutte polynomial is proven. Before the main theorems and proofs are presented, some groundwork is necessary to introduce key ideas and fix notation. We start by formalising the dimensionally regulated Dirac Trace. One approach to constructing the d-dimensional trace Tr_d is by exhibiting explicit infinite-dimensional representations of the d-dimensional Clifford Algebra, as discussed in Ref [1]. In this section, a formal construction of Tr_d will be presented instead by considering the defining relations

$$\{\gamma_\mu, \gamma_\nu\} \coloneqq \gamma_\mu\gamma_\nu + \gamma_\nu\gamma_\mu = g_{\mu\nu}\mathbb{1}, \qquad g_{\mu\mu} = d \tag{A.2}$$

as relations on symbols, with no reference made to matrix-like structures for the γ-objects. For the purposes of this work, no distinction will be made between lower and upper indices (all indices will be lower indices) as everything will be considered in Euclidean signature.

For concreteness, first consider the case of computing a single Dirac trace where there are no free indices. Extensions to traces with open (uncontracted) Dirac indices, and Dirac traces including γ_5 insertions are presented in Appendix A.4. Let Σ be a countable alphabet of symbols (usually labelled as $\Sigma = \{\mu_1, \mu_2, \dots\}$), and let $P(n)$ be the set of all permutations of tuples of length $2n$ with symbols from Σ, such that each symbol appears exactly twice. The map Tr_d will be defined as a map from $x = (x_1, \dots, x_{2n}) \in P(n)$ to $\mathrm{Tr}_d(x) \in \mathbb{Z}[d]$, the ring of polynomials in d with integer coefficients, with the interpretation that $\mathrm{Tr}_d(x) = \mathrm{Tr}_d(\gamma_{x_1} \cdots \gamma_{x_{2n}})$.

Definition A.1.0.1. *A function* $\mathrm{Tr}_d : \cup_{n \in \mathbb{N}_{\geq 0}} P(n) \to \mathbb{Z}[d]$ *is called a d-dimensional trace operation if it satisfies the base case* $\mathrm{Tr}(\varnothing) = 4$ *where* $\varnothing \in P(0)$ *is the empty tuple, and for all* $n \geq 1$, $1 \leq i < 2n$ *and* $x = (x_1, \cdots, x_{2n}) \in P(n)$*, it satisfies the recursion relations:*

$$x_i \neq x_{i+1} \quad \Longrightarrow \quad \mathrm{Tr}_d(x) = -\mathrm{Tr}_d(S_{i,i+1}(x)) + 2\mathrm{Tr}_d(C_{i,i+1}(x)), \tag{A.3}$$

$$x_i = x_{i+1} \quad \Longrightarrow \quad \mathrm{Tr}_d(x) = d\ \mathrm{Tr}_d(C_{i,i+1}(x)), \tag{A.4}$$

where $S_{i,j} : P(n) \to P(n)$ *is the map that swaps the* i*-th element* x_i *with the* j*-th element* x_j *in the tuple, and* $C_{i,j} : \{x \in P(n)\} \to P(n-1)$ *is the map that removes the* i*-th and* j*-th elements in the tuple, and relabels all other occurrences of* x_j *in the tuple to* x_i*.*

Definition A.1.0.1 is a formalisation of the defining relations given in Eq. (A.2). The base case $\mathrm{Tr}_d(\varnothing) = 4$ is the conventional choice used in most calculations involving dimensional regularisation, but this condition can be changed, for instance to $\mathrm{Tr}_d(\varnothing) = 2^{\frac{d}{2}}$. This latter choice may seem more natural given that in even spacetime dimensions d, the standard representation of the Clifford Algebra has dimension $2^{\frac{d}{2}}$. However, such modifications to the base case do not affect the renormalization procedure in any meaningful way, and simply amount to a shift in the renormalization constants [1].

A graph $G = (V, E, \pi)$ refers to an undirected graph possibly with multi-edges and loops, and is specified by a vertex set V, an edge set E, and a map $\pi : E \to (V \times V)/\sim_f$ associating an edge with its endpoints, where for all $v_0, v_1 \in V$, $(v_0, v_1) \sim_f (v_1, v_0)$. The collection of all graphs is typeset as **Graph**. A circle graph is a graph formed by first drawing a collection of straight chords on a common circle, then associating each chord with a vertex of the graph, and an edge between two vertices if and only if the two corresponding chords intersect. The collection of all circle graphs is typeset as **Circle**.

Definition A.1.0.2. *The map*

$$\mathrm{Gr} : \bigcup_{n \in \mathbb{N}_{\geq 0}} P(n) \to \mathbf{Circle} \tag{A.5}$$

associates to every $x \in P(n)$ *a circle graph. The construction first places the elements of the tuple* x *in order around a circle, joining the repeated elements with straight chords. The circle graph is the intersection graph of this construction, so that the vertex set is the set of symbols appearing in the tuple* x*, and edges correspond to intersections of chords.*

As an example:

$$P(4) \ni (\mu_1, \mu_2, \mu_3, \mu_2, \mu_1, \mu_4, \mu_3, \mu_4) \mapsto$$

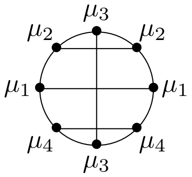

$$\mapsto$$

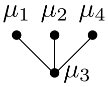

$$\in \textbf{Circle}$$

Clearly this construction satisfies a cyclic symmetry, where the same graph is associated to all cyclic shifts of a tuple in $P(n)$. This observation will be related to the property that traces are invariant under cyclic shifts. Furthermore, the associated graph is invariant under reversing the order of the tuple, which is related to invariance of traces under transposes and inverses.

In the general case, the Tutte polynomial is a polynomial defined for matroids (this will be relevant in Appendix A.3, where a brief introduction to matroids is presented). For the purposes of this section, it is simpler to restrict to the special case of undirected graphs. To define the Tutte polynomial, we first introduce some basic graph terminology:

- $c(G)$ is the number of connected components of the graph.
- $b(G)$ is the number of bridges of the graph, where a bridge is an edge that if removed from G, the number of connected components increases by one.
- $l(G)$ is the number of loops of the graph G, where a loop is an edge that has both of it's endpoints as the same vertex.
- $G - e$ is the graph obtained by deleting the edge e from the graph G
- G/e is the graph obtained by contracting the edge e (deleting e, and merging it's two endpoints).

Definition A.1.0.3. [2] *The Tutte polynomial is the unique function* $T : \textbf{Graph} \to \mathbb{Z}[x, y]$ *satisfying the base case* $T(G) = x^{|b(G)|} y^{|l(G)|}$ *if* G *has no edges that are not bridges or loops, and for any edge* e *that is not a bridge or a loop, the deletion-contraction relation holds:*

$$T(G) = T(G - e) + T(G/e). \tag{A.6}$$

The main observation of this work is that the anticommutation relations of the Dirac algebra can be reinterpreted as a deletion-contraction relation for the Tutte polynomial computed on the associated circle graph. To see this, it is simplest to make some technical detours. Firstly, the 'recipe theorem' for the Tutte polynomial for graphs which was originally stated and proved in Ref [3] is given below in the form presented in Ref [4]:

Proposition A.1.0.4. [3, Thm. 1] *Suppose the function* $\overline{T} : \textbf{Graph} \to \mathbb{Z}[x, y, \alpha, \sigma, \tau]$ *satisfies the base case* $\overline{T}(G) = x^{|b(G)|} y^{|l(G)|} \alpha^{|V|}$ *if* G *has no edges that are not bridges or loops, and satisfies a modified recurrence relation*

$$\overline{T}(G) = \sigma \overline{T}(G - e) + \tau \overline{T}(G/e). \tag{A.7}$$

Then $\overline{T}$ *is given by a transformation of variables of the Tutte polynomial:*

$$\overline{T}(G;x,y,\alpha,\sigma,\tau) = \alpha^{c(G)}\sigma^{|E|-|V|+c(G)}\tau^{|V|-c(G)}T\left(G;\frac{\alpha x}{\tau},\frac{y}{\sigma}\right). \tag{A.8}$$

In the following proofs, it is easiest to utilise an alternative parametrisation of the Tutte polynomial:

Definition A.1.0.5. *For a graph* G*, let* $f : V \to \{1,\cdots,n\}$ *be an arbitrary function. Assigning an arbitrary direction to each edge of the graph, where* $\mathrm{src},\mathrm{dest} : E \to V$ *are functions associating an edge with its source vertex and its destination vertex, then the number of collisions is defined by*

$$\mathrm{coll}(f) = \sum_{e\in E} \delta_{f(\mathrm{src}(e)),f(\mathrm{dest}(e))} \tag{A.9}$$

where δ_{ab} *is the kronecker-delta. The generalised chromatic-polynomial is a function* $\chi : \mathbf{Graph} \to \mathbb{Z}[q,n]$ *given by*

$$\chi(G;q,n) = \sum_{f:V\to\{1,\cdots,n\}} q^{\mathrm{coll}(f)} \tag{A.10}$$

Note that $\chi(G;0,n)$ is the chromatic polynomial of the graph G, that counts the number of proper colourings of the graph G with n-colours (where the endpoints of every edge must be coloured different colours). The generalised chromatic-polynomial satisfies a deletion-contraction relation, which allows us to prove that it can be written as an evaluation of the Tutte polynomial:

Proposition A.1.0.6.

$$\chi(G;q,n) = \overline{T}\left(G;1+\frac{q-1}{n},q,n,1,q-1\right) = n^{c(G)}(q-1)^{|V|-c(G)}T\left(G;1+\frac{n}{q-1},q\right) \tag{A.11}$$

Proof. Note that if G has no edges, then $\chi(G;q,n) = n^{|V|}$ as there can be no collisions. If e is a bridge, then $\chi(G;q,n)$ is composed of a contribution corresponding to the endpoints of e being colored the same $\left(\frac{q}{n}\right)\chi(G-e;q,n)$, and a contribution corresponding to the endpoints of e being colored differently $\left(\frac{n-1}{n}\right)\chi(G-e;q,n)$, giving a relationship $\chi(G;q,n) = \left(1+\frac{q-1}{n}\right)\chi(G-e;q,n)$. If e is a loop, then $\chi(G;q,n) = q\chi(G-e;q,n)$ as the loop always gives a collision. Finally, for any other edge e there is a deletion-contraction relation, described pictorially in an example:

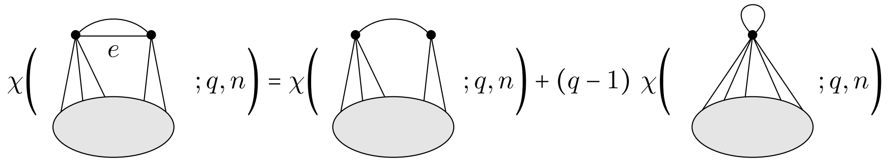

(A.12)

where the grey blob represents the rest of the unshown graph that has arbitrary structure. The first term on the right hand side of Eq. (A.12) correctly counts the contributions from the sum where the two vertices connected by e are coloured differently, and the second term corrects for the behaviour when the two vertices are coloured the same (in order to generate the factor of q due to the collision). Eq. (A.11) follows from the above observations and an application of Proposition A.1.0.4. ☐

Proposition A.1.0.7. *There is a unique function* Tr_d *satisfying the postulates outlined in Definition A.1.0.1, and it is given by:*

$$\mathrm{Tr}_d(x) = 4(-1)^{|E|}\ \chi(\mathrm{Gr}(x);-1,d) \tag{A.13}$$

Proof. For positive integer values of d, the right hand side of Eq. (A.13) (RHS) can be expanded using Definition A.1.0.5 as

$$\begin{aligned}\mathrm{RHS}(\mathrm{Gr}(x)) &= 4(-1)^{|E|} \sum_{f:V(\mathrm{Gr}(x))\to\{1,\ldots,d\}} (-1)^{\mathrm{coll}(f)} && \text{(A.14)}\\ &= 4 \sum_{f:V(\mathrm{Gr}(x))\to\{1,\ldots,d\}} \prod_{e\in E} (-1)^{1-\delta_{f(\mathrm{src}(e)),f(\mathrm{dest}(e))}} && \text{(A.15)}\end{aligned}$$

We will now proceed to show that RHS satisfies the defining postulates of Tr_d. Since $\mathrm{Gr}(\varnothing)$ is the empty graph, $\mathrm{RHS}(\mathrm{Gr}(x)) = 4$, thus the base condition is satisfied. Now suppose that $x = (x_1,\ldots,x_{2n}), 1 \le i < 2n$, and $x_i = x_{i+1}$. The vertex corresponding to (x_i, x_{i+1}) in $\mathrm{Gr}(x)$ is an isolated vertex, and $\mathrm{RHS}(\mathrm{Gr}(x)) = d \cdot \mathrm{RHS}(\mathrm{Gr}(C_{i,i+1}(x)))$ as the isolated vertex can be coloured in d ways and there are no associated collisions. Hence the condition corresponding to $\gamma_\mu\gamma_\mu = d\cdot\mathbb{1}$ is satisfied.

Suppose instead that $x_i \neq x_{i+1}$. Then x_i and x_{i+1} correspond to two different vertices in $\mathrm{Gr}(x)$, which are either connected by a single edge, or not connected by any edges. Suppose j, k are chosen such that $i, i+1, j, k$ are four different integers. Then, the following equation holds regardless of the structure of the chords connecting the regions ①,② and ③ (not shown below):

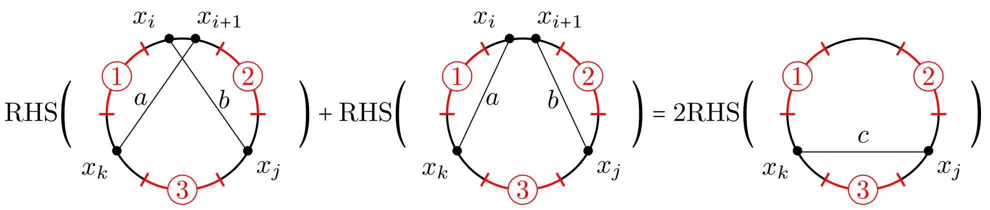

(A.16)

where it is understood that RHS is acting on the corresponding intersection graphs of the circle graphs depicted in Eq. (A.16). To prove Eq. (A.16), first notice that for a particular coloring of the chords, if chord a is colored differently to chord b, then the contribution from that coloring vanishes on the left hand side of Eq. (A.16) as the first circle diagram has a relative factor of (-1) compared to the second circle diagram due to the color collision. So, the only colorings that contribute on the left hand side are colorings in which both chords a and b are colored the same, which are in bijective correspondence with colorings of the chords on the right hand side diagram, where chord c is coloured the same as the chords a and b. Note that any chords that connect region ① to ③, or region ② to ③ will cross exactly one of either chord a or chord b for the left hand diagrams, and will cross chord c on the right hand diagram. Thus, any such chord will contribute the same factor to the sum on either side of Eq. (A.16). And if a chord connects region ① to ②, it crosses both chords a and b on the left hand side, but since a and b are colored the same, it is equivalent to not crossing either (as it picks up two minus signs if it is colored differently to a and b), as in the right diagram. Hence Eq. (A.16) is true, proving that RHS satisfies the recurrence relation corresponding to $\{\gamma_\mu, \gamma_\nu\} = 2g_{\mu\nu}$, for positive integer values of d.

The observations above show that RHS satisfies the recurrence relations defining Tr_d for all positive integer values of d. Since RHS are finite degree polynomials in d, by lagrange interpolation in fact RHS satisfies the recurrence relations for all values of d. It is the unique valid definition, as the value of Tr_d on any particular value of x is uniquely determined by the recurrence relations, which can always simplify $\mathrm{Gr}(x)$ to graphs with no edges.

□

The proof above is formalising the intuition that d-dimensional traces of Dirac matrices behave as if there were d-different anticommuting matrices for positive integer values of d. With this proposition, the main theorem follows:

Theorem A.1.0.8. *The unique map* Tr_d *satisfying the defining properties in Definition A.1.0.1 is given by:*

$$\mathrm{Tr}_d(x) = 4(-1)^{|E|}(-2)^{|V|-c(\mathrm{Gr}(x))}\ d^c\ T\left(\mathrm{Gr}(x), 1 - \tfrac{d}{2}, -1\right) \tag{A.17}$$

where $c(\mathrm{Gr}(x))$ *is the number of connected components of* $\mathrm{Gr}(x)$*,* V *is the set of vertices of* $\mathrm{Gr}(x)$*,* E *is the set of edges of* $\mathrm{Gr}(x)$*.*

Proof. Eq. (A.17) follows from Proposition A.1.0.7 and Proposition A.1.0.6. □

An immediate observation from Theorem A.1.0.8 is that traces in $d = 4$ correspond to evaluating the Tutte polynomial $T(G; -1, -1)$ for appropriately constructed graphs G. This point $(x, y) = (-1, -1)$ is one of the special points in the Tutte plane where the Tutte polynomial is known to be calculable in polynomial time. Following the definitions in [5], consider $2^V, 2^E$ as the free vector spaces over $\mathbb{Z}/2\mathbb{Z}$ with basis given by the set of vertices V, and the set of edges E respectively for a graph $G = (V, E)$. There are boundary ∂ and coboundary δ maps defined between the two vector spaces:

$$\begin{tikzcd} 2^V \arrow[r, shift left, "\delta"] & 2^E \arrow[l, shift left, "\partial"] \end{tikzcd} \tag{A.18}$$

where $\partial(e)$ is the sum of the two endpoints of edge e, $\delta(v)$ is the sum over all edges incident to v (loops are counted twice, thus they don't appear in the result as the base field is $\mathbb{Z}/2\mathbb{Z}$), and the maps are extended by linearity to be well defined on all of 2^V and 2^E. The subspace $\ker(\partial) \cap \mathrm{im}(\delta) \subseteq 2^E$ is the space of bicycles.

Theorem A.1.0.9 ([5], Thm. 9.1)**.** *If a graph* G *has* $|E|$ *edges and the dimension of the bicycle space of* G *is* $\dim(B(G))$*, then*

$$T(G; -1, -1) = (-1)^{|E|}(-2)^{\dim(B(G))} \tag{A.19}$$

Theorem A.1.0.10. *For $x \in P(n)$, the 4-dimensional trace is given by*

$$\mathrm{Tr}_4(x) = 4(-2)^{|V|+c(\mathrm{Gr}(x))+\dim(B(\mathrm{Gr}(x)))} \tag{A.20}$$

where $c(\mathrm{Gr}(x))$ is the number of connected components of $\mathrm{Gr}(x)$, V is the set of vertices of $\mathrm{Gr}(x)$, and $\dim(B(G))$ is the dimension of the bicycle space of G.

Proof. Follows from Theorems A.1.0.8 and A.1.0.9. □

A.2 COMPARISONS TO TRADITIONAL ALGORITHMS

In light of the connection between Dirac traces and Tutte polynomial evaluations, standard identities used to simplify Dirac traces can be reinterpreted as identities for Tutte polynomials. This exercise can be instructive in understanding the structure and nature of currently used algorithms. For instance, both TRACER [6] and FORM [7] make use of variations of the following identity to simplify d-dimensional traces:

$$\gamma_\mu \gamma_{\nu_1} \cdots \gamma_{\nu_n} \gamma_\mu = (-1)^n d\ \gamma_{\nu_1} \cdots \gamma_{\nu_n} + 2\sum_{j=1}^{n} (-1)^{n-j} \gamma_{\nu_j} \gamma_{\nu_1} \cdots \gamma_{\nu_{j-1}} \gamma_{\nu_{j+1}} \cdots \gamma_{\nu_n} \tag{A.21}$$

where the γ_μ at the right end of the chain on the left hand side of the equation is anticommuted through the chain all the way to the left side. This can be interpreted as an identity for Tutte polynomials:

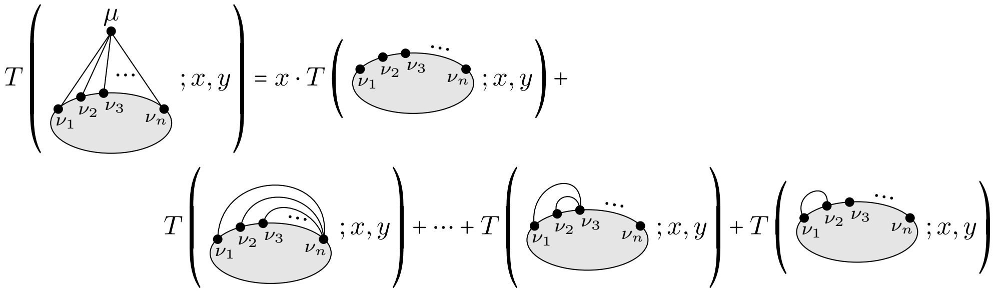

(A.22)

where the grey blob represents the rest of the graph, with possible edges between the nodes labelled $\nu_1, \ldots, \nu_n$. The identity is proven by repeatedly applying the deletion-contraction formula to the edges connected to μ, starting with the edge connected to ν_n. For traces in four-dimensions, there is a Chisholm identity for odd values of n [8]:

$$\mathrm{Tr}_4(\gamma_\mu \gamma_{\nu_1} \cdots \gamma_{\nu_n} \gamma_\mu) = -2\mathrm{Tr}_4(\gamma_{\nu_n} \cdots \gamma_{\nu_1}) \tag{A.23}$$

which translates into a theorem concerning the bicycle number:

Theorem A.2.0.1. *For a graph G with nodes μ, $\nu_1, \dots, \nu_n$ where n is odd and the only edges connected to μ are single edges to each of the nodes $\nu_1, \dots, \nu_n$, then there is a natural isomorphism between the bicycle space $B(G)$ of G, and the bicycle space $B((G - \mu) \star K_n)$ of a modified graph where the vertex μ has been removed, and edges have been attached between every pair of distinct vertices in the list $\nu_1, \dots, \nu_n$ (equivalently, a copy of the complete graph on n nodes K_n is glued onto the vertices $\{\nu_1, \dots, \nu_n\}$).*

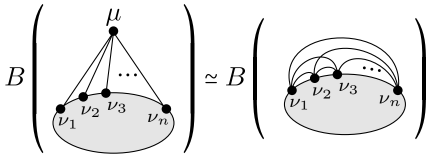

(A.24)

Proof. It is possible to utilise the Chisholm identity as well as Theorem A.1.0.10 to conclude at the very least that the dimensions of the respective bicycle spaces are the same. The following purely graph-theoretic proof presents more geometric intuition for the theorem, as well as providing an explicit isomorphism $f : B(G) \to B((G - \mu) \star K_n)$ between the two bicycle spaces.

For any $X \in B(G)$, $X \in \mathrm{im}(\delta)$, so choose a representative $Y \in \delta^{-1}(X)$. The collection of all vertices in Y that are not μ forms a subset of vertices Y' in $(G - \mu) \star K_n$, define $f(X) \coloneqq \delta(Y')$. For this map to be well defined, $\delta(Y')$ must first be invariant under the choice of $Y \in \delta^{-1}(X)$. To see this, first note that because X is a bicycle, $X \in \ker(\partial)$ and hence there must be an even number of edges connected to μ, corresponding to an even cardinality subset $N \subseteq \{\nu_1, \dots, \nu_n\}$ of neighbors of μ in the subgraph defined by X. If $\mu \notin Y$, then $Y \cap \{\nu_1, \dots, \nu_n\} = N$, conversely if $\mu \in Y$ then $Y \cap \{\nu_1, \dots, \nu_n\} = \{\nu_1, \dots, \nu_n\} - N$ owing to the fact that $\delta(Y) = X$. In either situation, $\delta(Y') \cap K_n$ is given by the complete bipartite graph $K_{|N|, n-|N|}$ which contains exactly every edge connecting vertices in N to vertices outside of N in the subset $\{\nu_1, \dots, \nu_n\}$. Hence, $\delta(Y')$ is invariant under your choice of $Y \in \delta^{-1}(X)$. Note that it is precisely because n is odd that $\partial(\delta(Y')) = 0$, as the vertices in N have an odd number of K_n edges $(n - |N|)$ connected to them.

The above remarks have demonstrated a map $f : B(G) \to B((G - \mu) \star K_n)$. The inverse map can be constructed completely analogously, where for any $X \in B((G - \mu) \star K_n)$, pick a $Y \in \delta^{-1}(X)$, and set $f^{-1}(X) = \delta(Y)$ (where the vertices in Y are now considered as vertices of G). □

For even values of n the corresponding statement about bicycle spaces does not hold (a counterexample is given by the four-cycle $G = C_4$, where $\dim(B(G)) = 1$ but $\dim(B((G - \mu) \star K_2)) = 0$ for any vertex $\mu \in C_4$). Instead, for even n there is a different relation:

$$\gamma_\mu \gamma_{\nu_1} \cdots \gamma_{\nu_n} \gamma_\mu = 2\gamma_{\nu_n} \gamma_{\nu_1} \cdots \gamma_{\nu_{n-1}} + 2\gamma_{\nu_{n-1}} \cdots \gamma_{\nu_1} \gamma_{\nu_n} \tag{A.25}$$

which can be proven by applying the anticommutation relation to γ_μ on the right once, and then applying the Chisholm identity Eq. (A.23). Naively, the number of terms generated by applications of the d-dimensional recurrence relation Eq. (A.21) and the 4-dimensional recurrence relations

Eqs. (A.23) and (A.25) in order to simplify a string of γ-matrices is exponential in the length of the string. A natural question to ask is what computational complexity classes evaluations of d-dimensional and 4-dimensional traces belongs to, and this is discussed in Appendix A.3.

A simple reason that dedicated Tutte polynomial algorithms might be asymptotically faster than currently used Tr_d algorithms is that being able to use the Tutte polynomial deletion-contraction relation on graphs can relate Dirac traces to Tutte polynomial evaluations of graphs that are *not* Circle graphs. To understand this in more detail, first we introduce the notion of local equivalence of graphs in order to understand the classification of Circle graphs. To locally complement a graph G at a vertex v is to replace the induced subgraph on all the neighbors of v with the complement graph (to be precise, neighbors w_i, w_j of v are connected by an edge in the new graph if and only if they were not connected by an edge in the original graph) . If a graph G_1 can by a series of local complementations turn into a graph G_2 then they are said to be locally equivalent.

Theorem A.2.0.2 ([9])**.** *A simple graph G is a circle graph if and only if no graph locally equivalent to G has an induced subgraph isomorphic to one of the graphs depicted below:*

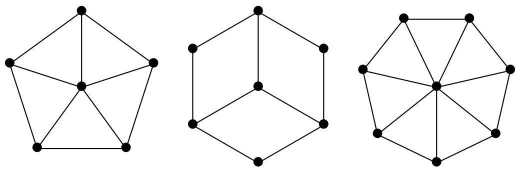

(a) (b) (c)

Figure A.1: Key examples of graphs that are not circle graphs.

With this classification of Circle graphs, it is possible to construct relationships between an evaluation of Tr_d and Tutte polynomial evaluations that *cannot* be written as d-dimensional traces, for example in the evaluation of the trace of the following product of 12 γ-matrices:

$$\mathrm{Tr}_d(\gamma_{\mu_1}\gamma_{\mu_3}\gamma_{\mu_2}\gamma_{\mu_5}\gamma_{\mu_4}\gamma_{\mu_6}\gamma_{\mu_5}\gamma_{\mu_3}\gamma_{\mu_4}\gamma_{\mu_1}\gamma_{\mu_2}\gamma_{\mu_6}) = 128d \cdot T\Bigg($$

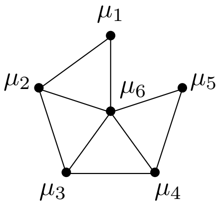

$$;1 - \frac{d}{2}, -1\Bigg)$$

$$= 128d\Bigg(T\Bigg($$

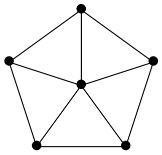

$$;1 - \frac{d}{2}, -1\Bigg) - T\Bigg($$

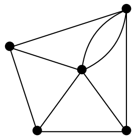

$$;1 - \frac{d}{2}, -1\Bigg)\Bigg) \tag{A.26}$$

derived by applying the deletion-contraction formula to the graph Fig. A.1(a). This formula however cannot be written as a relation on single dirac traces, as the first graph appearing in the final line of Eq. (A.26) is not a circle graph. Such relations open the door to potentially faster algorithms for computing Tr_d. For example, a generic algorithm is to specify certain special classes of graphs where the answer is known and use the deletion-contraction relation to recursively travel towards these special cases. All current algorithms for Tr_d rely on this idea where the special case are graphs with no edges, however (as described in Ref [10] for chromatic polynomial computations) a trivial improvement is to include the complete graphs as a special case as well. In the case of Eq. (A.26), it would require adding 6 edges to complete the graph, but require taking away 9 edges to reduce it to the empty graph. For this idea to be useful, an explicit formula is required for the Tutte polynomial evaluated on the complete graph, which is provided below:

Theorem A.2.0.3.

$$\begin{aligned}\mathrm{Tr}_d\left(\gamma_{\mu_1}\cdots\gamma_{\mu_n}\gamma_{\mu_1}\cdots\gamma_{\mu_n}\right) &= (-1)^{1+\lceil\frac{n}{2}\rceil}2^{1+n}d\ T\left(K_n;1-\frac{d}{2},-1\right) \\ &= 4\sum_{\lambda\vdash n}(-1)^{\sum_{i<j}\lambda_i\lambda_j}\frac{1}{c_1!\cdots c_k!}\left(\prod_{i=0}^{l-1}(d-i)\right)\frac{n!}{\lambda_1!\cdots\lambda_l!}\end{aligned} \tag{A.27}$$

where the sum is performed over all distinct partitions $\lambda = (\lambda_1,\ldots,\lambda_l)$ of n (such that $i<j$ implies $\lambda_i \le \lambda_j$, and $\sum_{i=1}^{l}\lambda_i = n$), and $c_1,\ldots,c_k$ are the multiplicities of the distinct numbers in the partition.

Proof. The proof follows from considering the representation $\mathrm{Tr}_d(x) = 4(-1)^{|E|}\ \chi(\mathrm{Gr}(x);-1,d)$ proven in Proposition A.1.0.7. Each partition $\lambda = (\lambda_1,\ldots,\lambda_l)\vdash n$ corresponds to a certain partition of the n vertices into l different colours, and the factor of $(-1)^{\sum_{i<j}\lambda_i\lambda_j}$ accounts for all the colour collisions. The factor of $\prod_{i=0}^{l-1}(d-i)$ counts the number of ways of assigning colours from d choices to the different groups defined by the partition, but must be corrected by the factor of $\frac{1}{c_1!\cdots c_k!}$ to correct for overcounting. Finally, $\frac{n!}{\lambda_1!\cdots\lambda_l!}$ accounts for the different ways of distributing the colours among the vertices. □

A.3 COMPLEXITY OF EVALUATING SINGLE DIRAC TRACES

Given the connection developed between Dirac traces and computations of the Tutte polynomial, a natural question to consider is the asymptotic complexity of computing Dirac traces. The algorithms to compute Tr_d with deletion-contraction relations as in Appendix A.2 naively generate exponentially many terms, and one may wonder whether it is possible to find a polynomial time algorithm instead. As a quick review of the relevant complexity classes that will be discussed in this section,

- P is the class of decision problems that can be solved by a deterministic Turing machine in a polynomial amount of computation time with respect to the size of the input.
- NP is the class of decision problems for which any successful query is accompanied by the existence of a polynomial-length ‘certificate’, which can be verified in polynomial-time by a fixed deterministic algorithm.
- FP is the class of function problems which are computable in polynomial time.

- #P is the class of function problems corresponding to counting the number of certificates to given decision problems in NP [11].
- P^A (FP^A) for a given problem A is the class of decision (function) problems which are computable in polynomial time given access to an oracle that either decides A if A is a decision problem, or computes A if A is a function problem.

For more detailed definitions, see Ref [12]. This section will consider the problem of computing single Dirac traces with all indices contracted, and no γ_5 insertions. Because these correspond to evaluations of the Tutte polynomial for circle graphs by Theorem A.1.0.8, the computational problems we will be interested in are defined in terms of evaluations of the Tutte polynomial:

Definition A.3.0.1. *Let $\pi_X(\mathcal{C})$ be the function problem of computing the Tutte polynomial for a specified class of graphs $\mathcal{C}$ in the subset X of the Tutte plane. X can take three forms:*

- *X is either a single point $X = \{(a,b)\}$ where $(a,b) \in \mathbb{R}^2$*
- *X is a rational curve, specified by a parametrisation $f : \mathbb{R} \to \mathbb{R}^2$ where $f(s) = \left(\frac{u(s)}{v(s)}, \frac{w(s)}{z(s)}\right)$ where u, v, w, z are finite-degree polynomials in s with coefficients in $\mathbb{Q}$. In this case, the Tutte polynomial output is considered as a rational function in the parameter s.*
- *X is the entire plane $\mathbb{R}^2$, in which case the Tutte polynomial output is a polynomial in canonical variables x, y.*

Computing single Dirac traces corresponds to computing the Tutte polynomial along the line $y = -1$ for circle graphs, and is written as $\pi_{\{(s,-1):s\in\mathbb{R}\}}(\textbf{Circle})$. Mainly this section will deal with the question of whether or not $\pi_{\{(s,-1):s\in\mathbb{R}\}}(\textbf{Circle}) \in \mathsf{FP}$, the class of functions which are computable in polynomial time, or whether $\pi_{\{(s,-1):s\in\mathbb{R}\}}(\textbf{Circle})$ is contained in a complexity class believed to be distinct from FP (which would necessarily require superpolynomial time algorithms to compute), such as the class of #P-hard problems. Though it is possible that #P = FP, it would for example immediately imply that P = NP which has long been conjectured to be false [13].

It was shown that for the class of all graphs, $\pi_{\{(a,b)\}}(\textbf{Graph}) \in$ #P-hard, and $\pi_{\{f(s):s\in\mathbb{R}\}}(\textbf{Graph}) \in$ #P-hard in Ref [14] for generic rational points (a,b) and generic rational curves $f(s)$. These results were then extended to the class of planar graphs in Ref [15]. The analysis for the complexity of evaluating Dirac traces is slightly complicated by the fact that Dirac traces are associated with evaluating Tutte polynomial along the specific curve $y = -1$, and for the class of circle graphs. It is however quite natural to conjecture that Dirac traces would also be #P-hard in the absence of some special structures present only within the class of circle graphs. Towards the goal of proving this statement, we follow the strategy used in Ref [14] for the case of Tutte polynomial evaluations for the class of all graphs. The first objective is to identify specific points within the Tutte plane for which evaluations are difficult. For the class of circle graphs, deciding whether a given circle graph has a proper n-colouring for $n \geq 4$ is known to be NP-complete by reduction to 3-SAT:

Theorem A.3.0.2 ([16], Thm. 1)**.** *The problem of deciding whether a given circle graph is n-colourable is* NP*-complete for $n \geq 4$.*

Unfortunately, this does not immediately imply that the corresponding function problem of computing $T(G; 1-n, 0)$ for $n \geq 4$ and circle graphs G is #P-complete, as this would require finding a parsimonious reduction (one that preserves the number of solutions) from n-colourability to 3-SAT. It may be possible to modify the reduction in Ref [16] to become parsimonious, for now, we will be satisfied with the following corollary:

Corollary A.3.0.3. *$\pi_{\{(1-n,0)\}}(\mathbf{Circle})$ for integer $n \geq 4$ (and hence, also $\pi_{\mathbb{R}^2}(\mathbf{Circle})$) are* NP*-hard function problems.*

Proof. The only technical remark to make is that because $\pi_{\{(1-n,0)\}}(\mathbf{Circle})$ is a function problem, what is meant by NP-hard in this context is not a polynomial time many-to-one reduction of decision problems (as in Ref [17]), but rather that given access to a $\pi_{\{(1-n,0)\}}(\mathbf{Circle})$-oracle, one can solve any NP problem in polynomial time, $\mathsf{NP} \subseteq P^{\pi_{\{(1-n,0)\}}(\mathbf{Circle})}$. Corollary A.3.0.3 then follows from Theorem A.3.0.2, because deciding whether a given circle graph G is n-colourable can be done by computing the chromatic polynomial $\chi(G; 0, n) = n^{c(G)}(-1)^{|V|-c(G)}T(G; 1-n, 0)$ and checking whether or not the result equals zero.

This immediately implies $\pi_{\mathbb{R}^2}(\mathbf{Circle})$ is also NP-hard, because being able to compute the Tutte polynomial on the entire plane allows you in polynomial time to evaluate the Tutte polynomial at any specific point $(1-n, 0)$ by evaluating the polynomial at $x = 1-n, y = 0$. ☐

The strategy proceeds by utilising a general theorem proven in Ref [14] that $\pi_{\mathbb{R}^2}(\mathcal{C})$ is polynomial time reducible to $\pi_L(\mathbb{C})$ for generic rational curves L, and as long as the class of graphs $\mathcal{C}$ is 'large' enough in a technical sense. The theorems quoted below from Ref [14] are all stated in the more general case of matroids, which we now provide a brief a review of. A matroid is a pair $M = (S, \rho)$ of a ground set S and a rank function $\rho : 2^S \to \mathbb{Z}$ satisfying $0 \leq \rho(A) \leq |A|$ for all $A \subseteq S$, $\rho(X) \leq \rho(Y)$ for $X \subseteq Y \subseteq S$, and $\rho(X \cup Y) + \rho(X \cap Y) \leq \rho(X) + \rho(Y)$. Every graph $G = (V, E)$ gives rise to a 'graphic' matroid by letting the ground set be the set of edges E, and letting the rank function $\rho(X) = n - c$ where n is the number of vertices in the subgraph formed by the edges in X and c is the number of connected components of the subgraph. Instead of specifying the entire rank function ρ, a matroid can also be specified by its bases, which are the maximal independent subsets $X \subset S$, where an independent subset X is one that satisfies $\rho(X) = |X|$. In the case of graphic matroids, $\rho(X) = |X|$ if and only if X has no cycles (X is a forest).

The number $f(n)$ of non-isomorphic matroids on a set of n elements grows at least as fast as $\log_2(\log_2(f(n))) \geq n - \frac{3}{2}\log_2(n) + O(\log\log n)$[18]. As pointed out in Ref [14], this implies both the input size, and the runtime for computing the Tutte polynomial on general matroids is exponential in n, as the naive algorithm utilising deletion-recurrence relations runs in time exponential in n. The class of matroids corresponding to circle graphs can be represented more succinctly however:

Definition A.3.0.4 ([14]). *A class of matroids $\mathcal{C}$ is succinct if there is an injective mapping e of the members of $\mathcal{C}$ into strings of some finite alphabet Σ, such that if $|e(M)|$ denotes the length of $e(M)$*

$$\mathcal{C}_n := \{(S,\rho) \in \mathcal{C} : |S| = n\}, \quad e(n) := \max\{|e(M)| : M \in \mathcal{C}_n\}, \tag{A.28}$$

then there exists some polynomial p such that $e(n) \leq p(n)$ for all n.

Lemma 5. *The class of circle graphs is succinct.*

Proof. Succinctness of the class of circle graphs follows from succinctness of the class of all simple graphs. An explicit succinct encoding of simple graphs is given by writing down the adjacency matrix of a simple graph. ☐

A class of simple transformations on matroids are given by tensor products with the uniform matroid $U_{r,n}$, which has ground set of n elements and bases all subsets of size r. To define this tensor product, a few background definitions are required. A pointed matroid N_d is a matroid on a ground set with a distinguished element, the point d, which is neither a loop ($\rho(\{d\}) = 0$) nor a coloop ($\rho(S - \{d\}) = \rho(S) - 1$). If $M = (S,\rho), N = (T,\lambda)$ are two matroids with $e \in S, f \in T$, the 2-sum of M and N is the matroid $((S \cup T)\backslash\{e,f\},\sigma)$ such that for $A \subseteq S\backslash\{e\}, B \subseteq T\backslash\{f\}$

$$\sigma(A \cup B) = \rho(A) + \lambda(B) - \delta(A,B) + \delta(\varnothing,\varnothing) \tag{A.29}$$

where $\delta(A,B) = 1$ if both $\rho(A) = \rho(A \cup \{e\})$ and $\lambda(B) = \lambda(B \cup \{f\})$, else $\delta(A,B) = 0$. The tensor product $M \otimes N$ of an arbitrary matroid M and the pointed matroid N is obtained by taking the 2-sum of M with N at each point e of M and the distinguished point d of N [19]. For tensor products with the uniform matroid, it does not matter which element is chosen as the distinguished point, as the matroid is invariant under permutations of the base set.

Not all uniform matroids are graphic, however the cases of interest are. In particular, $U_{k,k+1}$ corresponds to $(k+1)$-edged cycle graph, and $U_{1,k+1}$ corresponds to the $(k+1)$-edged dipole graph ($(k+1)$ edges connecting two vertices). The tensor product of a graphic matroid with $U_{k,k+1}$ has the effect of replacing every edge with a k-stretched version, and the tensor product of a graphic matroid with $U_{1,k+1}$ with a k-thickened version, hence the naming convention. For example, 2-stretchings and 2-thickenings of K_4 are shown below:

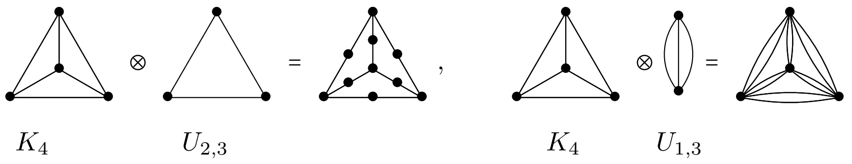

(A.30)

The utility of thinking about these tensor products is that evaluating the Tutte polynomial on the k-lengthened or k-thickened versions of a matroid at a specific point (x,y) yields the Tutte polynomial for the original matroid at a different point (x',y'). Specifically,

Theorem A.3.0.6 ([14], Eq. 4.1)**.** *For a matroid $M = (S,\rho)$ and a pointed matroid N,*

$$T(M \otimes N; x, y) = T_C(N; x, y)^{|S|-\rho(S)} T_L(N; x, y)^{\rho(S)} T(M; X, Y) \tag{A.31}$$

where for k-lengthening:

$$T_C(U_{k,k+1}; x, y) = \sum_{i=0}^{k-1} x^i, \quad T_L(U_{k,k+1}; x, y) = 1, \quad X = x^k, \quad Y = \frac{x^k + x(y-1) - y}{x^k - 1} \tag{A.32}$$

and for k-thickening:

$$T_C(U_{1,k+1}; x, y) = 1, \quad T_L(U_{k,k+1}; x, y) = \sum_{i=0}^{k-1} y^i, \quad X = \frac{y^k + x(y-1) - y}{y^k - 1}, \quad Y = y^k \tag{A.33}$$

Thus, being able to evaluate the Tutte polynomial efficiently for a class of graphs closed under k-thickening and k-lengthening allows one to take a given graph, and evaluate it's Tutte polynomial on the transformed (X, Y) coordinates, which in turn allows for an interpolation of the Tutte polynomial on the entire plane provided the curve is generic. Note that the k-thickening operation is not useful for the problem $\pi_{\{(s,-1):s\in\mathbb{R}\}}(\textbf{Circle})$ because the class of circle graphs contains only simple graphs and does not contain any k-thickened graphs. Furthermore by inspecting Eq. (A.33), it is clear that the k-thickening transformation $(x, y) \mapsto (X, Y)$ is only well-defined for the line defined by $y = -1$ by taking some limit as $y \to -1$, complicating the situation. By focusing only on the k-lengthening operation, the main theorem of Ref [14] is slightly modified:

Theorem A.3.0.7 ([14], Thm. 1 (modified))**.** *Let L be a rational curve $f(s) = (x(s), y(s)) = \left(\frac{u(s)}{v(s)}, \frac{w(s)}{z(s)}\right)$ for polynomials u, v, w, z with coefficients in $\mathbb{Q}$ such that $(x(s) - 1)(y(s) - 1)$ is not constant, and such that $x(s)$ is also not constant. Let $\mathcal{C}$ be a succinct class of matroids closed under k-stretching, where computing the k-stretch of a succinct representation of a matroid takes polynomial time both in k and the size of the matroid, yielding a succinct representation of the stretched matroid. Then $\pi_{\mathbb{R}^2}(\mathcal{C})$ is polynomial time reducible to $\pi_L(\mathcal{C})$.*

Unfortunately, the class of circle graphs is not closed under k-lengthenings.

Proposition A.3.0.8. *The class of circle graphs is not closed under lengthenings.*

Proof. An explicit example of a graph G whose 2-lengthening is not a circle graph is provided below:

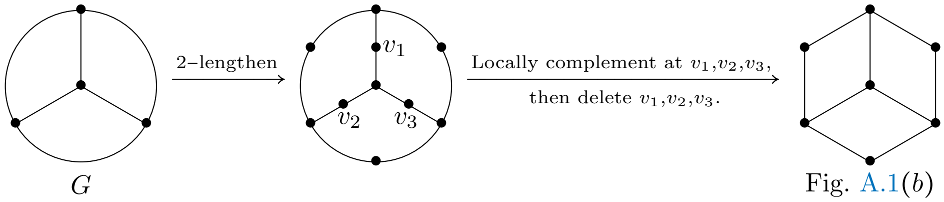

Figure A.2: Example of a circle graph G whose 2-lengthening is not a circle graph.

But G is a circle graph, since it has 4 vertices, and hence cannot be locally equivalent to a graph that contains one of the graphs in Theorem A.2.0.2 as an induced subgraph, as they all have at least 6 vertices. An explicit example is given by $\mathrm{Gr}((1,2,3,4,1,2,3,4))$. ☐

A weaker statement is of course possible to make:

Theorem A.3.0.9. *Let the class* Circle* *be the class of circle graphs and all k-lengthenings of circle graphs. Then computing* Tr_d *on this class is* NP*-hard.*

Proof. Follows from Theorem A.3.0.7 and Corollary A.3.0.3. ☐

To circumvent the issue of circle graphs not being closed under k-stretchings, it is possible to imagine that there is a subset of circle graphs closed under stretchings yet where determining whether the graph is k-colourable is still NP-hard. A candidate for such a class is the class of circle graphs that do not contain a 4-clique, as Ref [16] comments that the k-colourability problem is still NP-hard on this class. Unfortunately, this class is also not closed under lengthenings, for example the graph G' obtained from G in Fig. A.2 by taking a single edge and subdividing it into two pieces, is a circle graph with no 4-clique but whose 2-lengthening is not a circle graph.

The situation is considerably simpler for 4-dimensional traces, for which the computational problem $\pi_{\{(-1,-1)\}}(\textbf{Circle})$ corresponds to evaluating the Tutte polynomial at the special point $(-1,-1)$.

Theorem A.3.0.10. *Computing 4-dimensional traces is in* FP*.*

Proof. Let $G = (V, E)$ denote a circle graph. Note that one choice of succinct representation consists of writing down its adjacency matrix, whose size scales as $O(|V|)^2$. The bicycle space $\mathrm{im}(\delta) \cap \ker(\partial)$ can be computed in polynomial time by gaussian elimination over the field $\mathbb{Z}_2$, as pointed out in Ref [14]. Computing the 4-dimensional trace by utilising $\mathrm{Tr}_4(x) = 4(-2)^{|V|+c(\mathrm{Gr(x)})+\dim(B(\mathrm{Gr}(x)))}$ is then a polynomial in $|V|$ overhead, as the number of connected components of $\mathrm{Gr}(x)$ can be computed with breadth/depth-first search. ☐

In practice, dimensional regularisation calculations usually only require expansions of Tr_d around $d = 4$ at some finite fixed order (corresponding to the number of loops in the diagram). It may be the case that these expansions also have a graph-theoretic interpretation, and can be calculated in polynomial time. In light of these partial results, a complete understanding of the computational complexity of computing the Tutte polynomial for the class of circle graphs would be an interesting study to see.

A.4 Open indices, multiple traces and γ_5

The formalism established in Appendix A.1 deals with the case where all indices within a single Dirac trace are contracted amongst each other, and there are no γ_5 insertions. In practical calculations, these conditions are violated if there are multiple fermion loops connected by some interactions, or the theory under investigation contains chiral interactions. Formally speaking, the problem of computing products of Dirac traces with indices contracted in some arbitrary fashion can be reduced to the problem of computing single Dirac traces with some open (uncontracted) indices. Furthermore, Dirac traces with γ_5 insertions (in the 't-Hooft Veltman γ_5 scheme) can similarly be reduced to the problem of computing Dirac traces with open indices. Though it is standard knowledge about how to reduce the problem of traces with open indices to traces with all indices contracted, it seems helpful to provide a perspective on how to formalise this procedure.

To formalise the problem, it is easier to now specify a specific alphabet of symbols. Let $P(n,m)$ be the set of all tuples of length $2n + 2m$ where each symbol in $\{\mu_1, \dots, \mu_n\}$ appears twice (these are the contracted indices) and each symbol in $\{\nu_1, \dots, \nu_{2m}\}$ appears only once. Unlike in the case with all indices contracted, recursion relations of the form Eqs. (A.3) and (A.4) are not sufficient to determine Tr_d on $P(n,m)$ due to the fact that anticommuting uncontracted indices doesn't help simplify the expression. The additional physical axiom that is imposed is that the only structures that can appear in the trace $\mathrm{Tr}_d(x)$ for $x \in P(n,m)$ are metric tensors g_{ν_i,ν_j}. Let $Q(m)$ be the set of perfect matchings on the complete graph K_{2m} with labelled vertices $\{1, \dots, 2m\}$. Then the trace can be written as a linear combination:

$$\mathrm{Tr}_d(x) = \sum_{G \in Q(m)} C_G \left(\prod_{e \in G} g_{\nu_{\mathrm{src}(e)} \nu_{\mathrm{snk}(e)}} \right) \tag{A.34}$$

for some constants C_G, where for each edge e in each perfect matching G, an arbitrary orientation has been picked. This arbitrary orientation has no affect on the resulting expression, as the metric tensor is symmetric ($g_{\alpha\beta} = g_{\beta\alpha}$). The problem has thus been reduced to determining the constants C_G. What is calculable with the technology introduced thus far are traces where the uncontracted indices are contracted, in other words for some $G' \in Q(m)$,

$$\begin{aligned} \mathrm{Tr}_d \left(\prod_{e \in G'} g_{\nu_{\mathrm{src}(e)} \nu_{\mathrm{snk}(e)}} \cdot x \right) &= \sum_{G \in Q(m)} C_G \left(\prod_{e' \in G'} g_{\nu_{\mathrm{src}(e')} \nu_{\mathrm{snk}(e')}} \right) \left(\prod_{e \in G} g_{\nu_{\mathrm{src}(e)} \nu_{\mathrm{snk}(e)}} \right) \\ &= \sum_{G \in Q(m)} C_G \, d^{\,\mathrm{cyc}(G \star G')} \end{aligned} \tag{A.35}$$

where 'cyc' is the function that counts the number of undirected cycles of a graph, and $G \star G'$ is the graph obtained by gluing the labelled vertices of the two graphs together. The left-hand-side of Eq. (A.35) has no uncontracted indices, and can be computed by a Tutte polynomial evaluation of the corresponding graph, and the right hand side is a linear combination of the unknown C_G coefficients. By computing Eq. (A.35) for all $G' \in Q(m)$, enough contraints are found to constrain C_G for all $G \in Q(m)$. With the observations made above, the Dirac trace with open indices can be defined as follows:

Definition A.4.0.1. *Let A be a $|Q(m)| \times |Q(m)|$ sized matrix, whose entries are given by:*

$$A_{G_1,G_2} = d^{\,\mathrm{cyc}(G_1 \star G_2)} \tag{A.36}$$

The d*-dimensional trace is extended to* $P(n,m)$ *by defining:*

$$\mathrm{Tr}_d(x) = \sum_{G_1,G_2\in Q(m)} \mathrm{Tr}_d\left(\prod_{e\in G_1} g_{\nu_{\mathrm{src}(e)}\nu_{\mathrm{snk}(e)}} x\right)(A^{-1})_{G_1,G_2}\left(\prod_{e\in G_2} g_{\nu_{\mathrm{src}(e)}\nu_{\mathrm{snk}(e)}}\right) \tag{A.37}$$

A practical way to approach the problem is to use anticommutation relations to move all the uncontracted indices to the left of the string. The contracted indices then can be handled via a Tutte polynomial evaluation, and what's left is a trace over purely uncontracted indices $\mathrm{Tr}_d(\nu_1,\nu_2,\dots,\nu_{2m})$. There is a simple formula for this trace, which requires first a few technical definitions and statements:

Definition A.4.0.2. *The sign* $\mathrm{sign}(G)$ *of a perfect matching* $G\in Q(n)$ *on the complete graph* K_{2n} *with labelled vertices* $\{1,\dots,2n\}$ *is given by the sign of the naturally constructed involution in the symmetric group* S_{2n}*. Explicitly:*

$$\mathrm{sign}(G) := \prod_{e\in G}(-1)^{\mathrm{snk}(e)-\mathrm{src}(e)+1} \tag{A.38}$$

where an arbitrary orientation has been chosen for the edges $e\in G$*.*

Lemma 3. *For* $n\geq 0$*,*

$$\sum_{G\in Q(n)} \mathrm{sign}(G) = 1 \tag{A.39}$$

Proof. This lemma can be proven by induction on n. For the basecase, $Q(0)$ contains only the empty perfect matching, which has sign 1. For any $n\geq 1$, the node labelled by 1 is matched to some other node $i\in\{2,\dots,2n\}$. The result of summing over the signs of all such perfect matchings fixing i gives $(-1)^i\sum_{G\in Q(n-1)}\mathrm{sign}(G) = (-1)^i$ by inductive hypothesis. Finally, summing over $i\in\{2,\dots,2n\}$ proves the lemma. □

As an intermediate step, the following theorem gives an interesting alternate way of evaluating the d-dimensional trace:

Theorem A.4.0.4. *For* $x\in P(n)$*,*

$$\mathrm{Tr}_d(x) = 4\sum_{G\in Q(n)}(-1)^{\mathrm{sign}(G)} d^{\,\mathrm{cyc}(G\star\mathrm{Gr}'(x))} \tag{A.40}$$

where $\mathrm{Gr}'(x)$ *is the graph on* $2n$ *vertices where vertex* i *is connected to vertex* j *by an edge if and only if* $x_i = x_j$*.*

Proof. Fix a positive integer value of d, and consider the generalised chromatic number formula for Tr_d given in Proposition A.1.0.7:

$$\mathrm{Tr}_d(x) = 4(-1)^{|E|}\,\chi(\mathrm{Gr}(x);-1,d) \tag{A.41}$$

The RHS of Eq. (A.40) has a similar structure to the RHS of Eq. (A.41). For every graph $G\in Q(n)$, $d^{\,\mathrm{cyc}(G\star\mathrm{Gr}(x))}$ is counting the number of non-proper vertex-colourings of $\mathrm{Gr}'(x)$ if there are d colours where each cycle is coloured the same. As the cycles are colored the same, each of these colorings can be associated with a colouring appearing in $\chi(\mathrm{Gr}(x);-1,d)$. For a single term in the LHS sum (where each of the contractions is colored with a specific color), it matches correctly onto the contributions on the right, by some kind of inclusion-exclusion. ☐

Finally, traces with all uncontracted indices can be evaluated by the following formula:

Theorem A.4.0.5. *For* $x=(\nu_1,\cdots,\nu_{2m})\in P(0,m)$, *the equation:*

$$\mathrm{Tr}_d(x)=4\sum_{G\in Q(m)}(-1)^{\mathrm{sign}(G)}\left(\prod_{e\in G}g_{\nu_{\mathrm{src}(e)}\nu_{\mathrm{snk}(e)}}\right)\tag{A.42}$$

holds where $\mathrm{sign}(G)$ *indicates its sign when canonically associated to a permutation in* S_{2m}.

Proof. Follows from Definition A.4.0.1 and theorem A.4.0.4. ☐

For example for $n\in\{1,2\}$ Eq. (A.42) takes the form:

$$\begin{aligned}\mathrm{Tr}_d(\gamma_{\nu_1}\gamma_{\nu_2})&=4g_{\nu_1\nu_2}\\ \mathrm{Tr}_d(\gamma_{\nu_1}\gamma_{\nu_2}\gamma_{\nu_3}\gamma_{\nu_4})&=4g_{\nu_1\nu_2}g_{\nu_3\nu_4}-4g_{\nu_1\nu_3}g_{\nu_2\nu_4}+4g_{\nu_1\nu_4}g_{\nu_2\nu_3}\end{aligned}\tag{A.43}$$

Now that the technology is set up to treat traces including open indices, extensions to multiple traces and the ‘t-Hooft-Veltman (HV) γ_5 is not difficult. In particular, products of multiple traces where indices are possible contracted amongst the different traces can formally be handled by doing single dirac traces with open indices, and contracting the resulting metric tensors. Also, the HV γ_5 is specified by:

$$\gamma_5:=\frac{1}{4!}\tilde{\epsilon}_{\mu_1\mu_2\mu_3\mu_4}\gamma_{\mu_1}\gamma_{\mu_2}\gamma_{\mu_3}\gamma_{\mu_4}\tag{A.44}$$

where $\tilde{\epsilon}$ is the fully-antisymmetric tensor in four dimensions; hence traces involving γ_5 are performed simply as traces with open indices. The ~ emphasizes that the ϵ-tensor is a 4-dimensional object in the HV-scheme. The 4-dimensional tensors satisfy the contraction relations:

$$\tilde{\epsilon}_{\mu_1\mu_2\mu_3\mu_4}\tilde{\epsilon}_{\nu_1\nu_2\nu_3\nu_4}=\sum_{\sigma\in S_4}\mathrm{sign}(\sigma)\prod_{i=1}^{4}\tilde{g}_{\mu_i\nu_{\sigma(i)}},\tag{A.45}$$

$$g_{\nu\mu_1}\tilde{\epsilon}_{\mu_1\mu_2\mu_3\mu_4}=\tilde{g}_{\nu\mu_1}\tilde{\epsilon}_{\mu_1\mu_2\mu_3\mu_4}=\tilde{\epsilon}_{\nu\mu_2\mu_3\mu_4},\qquad \tilde{g}_{\nu\mu_1}g_{\nu\mu_2}=\tilde{g}_{\nu\mu_1}\tilde{g}_{\nu\mu_2}=\tilde{g}_{\mu_1\mu_2},\qquad \tilde{g}_{\mu\mu}=4.\tag{A.46}$$

A.5 NOTATION

$b(G)$	The number of bridges of the graph G. A bridge is an edge which, if removed, causes $c(G)$ to increase by one.
$B(G)$	The space of bicycles of the graph G.
$C_{i,j}$	Operation on $P(n)$ that contracts the i-th index with the j-th index.
$c(G)$	The number of connected components of the graph G.
$\chi(G;q,n)$	Generalised chromatic-polynomial function, where $\chi(G;0,n)$ is the regular chromatic polynomial in the variable n.
Circle	The class of circle graphs.
Circle*	The class of circle graphs, and all k-lengthenings of circle graphs.
$\mathrm{coll}(f)$	The count of the number of collisions in the coloring described by f.
d	Dimension of Euclidean spacetime, analytically continued from integer values to arbitrary complex values.
∂, δ	Boundary and coboundary maps used to define the bicycle number.
FP	Function problems which can be computed in polynomial time.
$G \star G'$	For two graphs G, G' with subsets of vertices that are labelled the same, $G \star G'$ is the graph obtained by gluing the vertex subsets together.
$\mathrm{Gr}(x)$	For $x \in P(n)$, the graph formed by placing the elements of x around a circle, connecting contracted elements by straight chords, and taking the intersection graph.
$\mathrm{Gr}'(x)$	For $x \in P(n)$, the graph formed on $2n$ labelled vertices $\{1, \dots, 2n\}$ such that i and j are connected by an edge if and only if $i \neq j$ and $x_i = x_j$.
K_n	Complete graph on n vertices.
$K_{m,n}$	Complete bipartite graph (an edge connecting every node in a set of m vertices to every node in a set of n vertices).
$l(G)$	The number of loops of the graph G. A loop is an edge which connects a vertex to itself.
NP	The class of decision problems for which a verification Turing machine can verify a given problem has a solution in polynomial time given a polynomial length certificate.
$\#\mathsf{P}$	The class of function problems corresponding to counting the number of certificates of a given NP decision problem.
P	The class of decision problems solvable in polynomial time.
ρ	The rank function of a matroid.
$\pi_X(\mathcal{C})$	Function problem corresponding to computing the Tutte polynomial on some subset $X \in \mathbb{R}^2$ for the family of graphs described by $\mathcal{C}$.

$P(n)$	Set of all permutations of tuples of length $2n$ with symbols from Σ, such that each symbol appears exactly twice.
$Q(n)$	Set of perfect matchings on the complete graph K_{2n}.
Σ	Countable alphabet of symbols, usually labelled as $\Sigma = \{\mu_1, \mu_2, \dots\}$.
$S_{i,j}$	Operation on $P(n)$ that swaps the i-th element in the tuple with the j-th element in the tuple.
S_n	Symmetric group of permutations on n elements.
$\mathrm{src}(e), \mathrm{snk}(e)$	The source and sink/destination of an oriented edge e.
$T(G; x, y)$	The Tutte polynomial of the graph G, in the variables x and y.
Tr_d	The dimensionally regulated Dirac trace in d-dimensions.
$\mathbb{Z}[x_1, \dots, x_n]$	Ring of polynomials in the variables $x_1, \dots, x_n$ with integer coefficients.

BIBLIOGRAPHY

[1] John C. Collins. *Renormalization*, volume 26 of *Cambridge Monographs on Mathematical Physics*. Cambridge University Press, Cambridge, 7 2023. ISBN 978-0-521-31177-9, 978-0-511-86739-2, 978-1-00-940180-7, 978-1-00-940176-0, 978-1-00-940179-1. doi: 10.1017/9781009401807.

[2] W. T. Tutte. A contribution to the theory of chromatic polynomials. *Canadian Journal of Mathematics*, 6: 80–91, 1954. doi: 10.4153/CJM-1954-010-9.

[3] J. G. Oxley and D. J. A. Welsh. The tutte polynomial and percolation. In J. A. Bondy and U. S. R. Murty, editors, *Graph Theory and Related Topics*, pages 329–339, 1979.

[4] Béla Bollobás. *Modern Graph Theory.* Springer New York, 1998. ISBN 9781461206194. doi: 10.1007/978-1-4612-0619-4.

[5] P. Rosenstiehl and R.C. Read. On the principal edge tripartition of a graph. In B. Bollobás, editor, *Advances in Graph Theory*, volume 3 of *Annals of Discrete Mathematics*, pages 195–226. Elsevier, 1978. doi: https://doi.org/10.1016/S0167-5060(08)70508-9.

[6] Matthias Jamin and Markus E. Lautenbacher. TRACER: Version 1.1: A Mathematica package for gamma algebra in arbitrary dimensions. *Comput. Phys. Commun.*, 74:265–288, 1993. doi: 10.1016/0010-4655(93)90097-V.

[7] J. Kuipers, T. Ueda, J. A. M. Vermaseren, and J. Vollinga. FORM version 4.0. *Comput. Phys. Commun.*, 184: 1453–1467, 2013. doi: 10.1016/j.cpc.2012.12.028.

[8] J. S. R. Chisholm. Generalisation of the kahane algorithm for scalar products of gamma-matrices. *Comput. Phys. Commun.*, 4:205–207, 1972. doi: 10.1016/0010-4655(72)90009-4.

[9] A. Bouchet. Circle graph obstructions. *Journal of Combinatorial Theory, Series B*, 60(1):107–144, 1994. ISSN 0095-8956. doi: https://doi.org/10.1006/jctb.1994.1008.

[10] Sriram Pemmaraju and Steven Skiena. *Computational Discrete Mathematics: Combinatorics and Graph Theory with Mathematica.* Cambridge University Press, 2003.

[11] L.G. Valiant. The complexity of computing the permanent. *Theoretical Computer Science*, 8(2):189–201, 1979. ISSN 0304-3975. doi: https://doi.org/10.1016/0304-3975(79)90044-6.

[12] Sanjeev Arora and Boaz Barak. *Computational Complexity: A Modern Approach.* Cambridge University Press, USA, 1st edition, 2009. ISBN 0521424267.

[13] Stephen A. Cook. The complexity of theorem-proving procedures. In *Proceedings of the Third Annual ACM Symposium on Theory of Computing*, STOC '71, page 151–158, New York, NY, USA, 1971. Association for Computing Machinery. ISBN 9781450374644. doi: 10.1145/800157.805047.

[14] F. Jaeger, D. L. Vertigan, and D. J. A. Welsh. On the computational complexity of the jones and Tutte polynomials. *Mathematical Proceedings of the Cambridge Philosophical Society*, 108(1):35–53, 1990. doi: 10.1017/S0305004100068936.

[15] Dirk Vertigan. The computational complexity of Tutte invariants for planar graphs. *SIAM Journal on Computing*, 35(3):690–712, 2005. doi: 10.1137/S0097539704446797.

[16] Walter Unger. On the k-colouring of circle-graphs. In Robert Cori and Martin Wirsing, editors, *STACS 88*, pages 61–72, Berlin, Heidelberg, 1988. Springer Berlin Heidelberg. ISBN 978-3-540-48190-4.

[17] Richard M. Karp. Reducibility among combinatorial problems. In Raymond E. Miller, James W. Thatcher, and Jean D. Bohlinger, editors, *Complexity of Computer Computations: Proceedings of a symposium on the Complexity of Computer Computations*, pages 85–103. Springer US, Boston, MA, 1972. ISBN 978-1-4684-2001-2. doi: 10.1007/978-1-4684-2001-2_9.

[18] Donald E Knuth. The asymptotic number of geometries. *Journal of Combinatorial Theory, Series A*, 16(3): 398–400, 1974. ISSN 0097-3165. doi: https://doi.org/10.1016/0097-3165(74)90063-6.

[19] Thomas Brylawski. *Matroid Theory and its Applications*. Springer Berlin Heidelberg, 2011. ISBN 9783642111105. doi: 10.1007/978-3-642-11110-5.

CHAPTER B

TABLE OF INTEGRALS FOR DIMENSIONALLY REGULATED POSITION-SPACE LOOP INTEGRALS

Contents

Different dimensionally regulated loop-integrals are introduced in various places during this thesis, some of which are related to others by boundary conditions. For convenience of reference, the important integrals are collected in this appendix. A brief overview of relevant facts about the su(3)-Lie algebra is also provided in Appendix B.0.1. Many calculations were performed in Mathematica [1], with the aid of the Tracer package [2] for Dirac traces in the 't Hooft-Veltman scheme, and HypExp [3] for expansions of hypergeometric functions.

B.0.1 COLOUR MATRICES

Due to QCD being a nonabelian gauge theory, perturbative diagrams include traces over products of colour matrices. Throughout this thesis, lowercase latin letters $a, b, c, \ldots$ are indices for either the fundamental or antifundamental representation of SU(3). An orthogonal basis of 8 traceless, hermitian matrices T^A is chosen to have the normalization $\mathrm{Tr}(T^A T^B) = \frac{1}{2}\delta^{AB}$, such that they satisfy

$$[T^A, T^B] = i f^{ABC} T^C \tag{B.1}$$

where f^{ABC} are the structure constants of SU(3). Note that this normalization *differs* from the normalization chosen for the Gell-Mann matrices λ_A, which are chosen such that $\mathrm{Tr}(\lambda_A \lambda_B) = 2\delta_{AB}$.

Note also that the conventional mathematical definition of the Lie algebra as the tangent space at the identity of SU(3) as embedded in the space of 3×3 complex matrices (in other words, the space of matrices X such that $\mathbb{1} + \epsilon X$ has determinant one and is unitary up to $O(\epsilon^2)$) is actually the space of traceless *antihermitian* matrices. Thus, iT^A in the convention adopted by this thesis forms a basis of the su(3) Lie algebra, and A can be thought of as indexing the adjoint representation of $SU(3)$.

With this choice of convention, the fundamental casimir C_F takes the form:

$$T^A_{ab}T^A_{bc} = C_F \delta_{ac} = \frac{N_c^2 - 1}{2N_c}\delta_{ac} \tag{B.2}$$

Also, the following identities are used to convert the Spectator Effect operators between Eq. (4.69) and Eq. (4.70), as well as to compute the $O(\alpha_S)$ renormalization of the operators:

$$\begin{aligned}
T^A_{ab}T^A_{cd} &= \frac{C_F}{N_c}\delta_{ad}\delta_{cb} - \frac{1}{N_c}T^A_{ad}T^A_{cb} = \frac{C_F}{1 - \frac{1}{N_c^2}}\left(\frac{1}{N_c}\delta_{ad}\delta_{cb} - \frac{1}{N_c^2}\delta_{ab}\delta_{cd}\right) && \text{(B.3)}\\
(T^A_{ab}T^B_{bc})(T^A_{de}T^B_{ef}) &= \frac{C_F}{2N_c}\delta_{ac}\delta_{df} - \frac{1}{N_c}T^A_{ac}T^A_{df} && \text{(B.4)}\\
(T^A_{ab}T^B_{bc})(T^B_{de}T^A_{ef}) &= \frac{C_F^2}{N_c}\delta_{af}\delta_{dc} + \frac{1}{2N_c^2}T^A_{af}T^A_{dc} = \frac{C_F}{2N_c}\delta_{ac}\delta_{df} + \left(C_F - \frac{1}{2N_c}\right)T^A_{ac}T^A_{df} && \text{(B.5)}\\
T^A_{ab}T^B_{bc}T^A_{cd} &= -\frac{1}{2N_c}T^B_{ad} && \text{(B.6)}\\
\epsilon_{abc}T^A_{ad}T^A_{be}\epsilon_{def} &= \frac{2C_F}{1 - N_c}\delta_{cf} && \text{(B.7)}
\end{aligned}$$

Because three-quark baryonic sources were used in defining the X-space schemes (which only exist in $N_c = 3$, and introduce an ϵ^{abc} tensor), color traces involving baryonic sources are explicitly evaluated without attempting to write in terms of N_c.

B.0.2 PROPAGATOR TYPE DIAGRAMS

Firstly, in Sec. 2.1.2 the generalized position-space propagators (with arbitrary powers of the propagator in the denominator) were introduced:

$$\begin{aligned}
D_H^{-1}(x;n) &= \int \frac{d^dp}{(2\pi)^d}\frac{e^{ipx}}{(v\cdot p)^n} = \delta^{d-1}(x_\perp)\frac{e^{-\frac{in\pi}{2}}(-x_0)^{n-1}}{\Gamma(n)}\theta(0 > x_0) \quad \text{if} \quad n > 0\\
D_S^{-1}(x;n) &= \int \frac{d^dk}{(2\pi)^d}\frac{e^{ikx}}{(-k^2)^n} = \frac{i\Gamma(\frac{d}{2} - n)}{4^n\pi^{\frac{d}{2}}\Gamma(n)}(-x^2)^{n-\frac{d}{2}} \quad \text{if} \quad n > 0
\end{aligned} \tag{B.8}$$

from which the ordinary position-space propagators can be derived by substituting in $n = 1$:

$$\begin{aligned}
D_L^{-1}(x) &= \langle T\{\psi_\alpha(0)\overline{\psi}_\beta(x)\}\rangle = \int \frac{d^dp}{(2\pi)^d}e^{ipx}\frac{i}{\not{p}} = \frac{-i\Gamma(\frac{d}{2})}{2\pi^{\frac{d}{2}}}\frac{\not{x}}{(-x^2 + i\epsilon)^{\frac{d}{2}}}\\
D_H^{-1}(x) &= \langle T\{Q(0)\overline{Q}(x)\}\rangle = \int \frac{d^dp}{(2\pi)^d}\frac{1 + \not{v}}{2}\frac{i}{v\cdot p}e^{ipx} = \delta^{d-1}(\vec{x})\frac{1 + \not{v}}{2}\theta(0 > x^0)
\end{aligned} \tag{B.9}$$

For $O(\alpha_S)$ renormalization of HQET, there are some propagator-type diagrams that are needed, drawn schematically below:

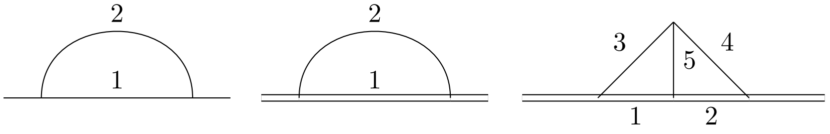

$$\tag{B.10}$$

Note that the $i\epsilon$ is implicit in all propagators. The notation $\tilde{X}, \overline{X}$ is used for a momentum-space version/a dimensionless version of X (wherever this is unambiguous). The first diagram corresponds to:

$$\begin{aligned} I_{LL}(n_1,n_2) &= (-p^2)^{\frac{d}{2}-n_1-n_2}\overline{I}_{LL}(n_1,n_2) = \int \frac{\mathrm{d}^d k}{(2\pi)^d}\frac{1}{(k^2+i\epsilon)^{n_1}((k+p)^2+i\epsilon)^{n_2}} \\ \overline{I}_{LL}(n_1,n_2) &= \frac{\Gamma(\frac{d}{2}-n_1)\Gamma(\frac{d}{2}-n_2)\Gamma(-d+2n_1+2n_2)}{2^{2n_1+2n_2}\pi^{\frac{d}{2}}\Gamma(n_1)\Gamma(n_2)} \end{aligned} \tag{B.11}$$

the second diagram corresponds to:

$$I_{HL}(n_1,n_2) = (-v\cdot p)^{d-n_1-2n_2}\overline{I}_{HL}(n_1,n_2) := \int \frac{d^d k}{(2\pi)^d}\frac{1}{(v\cdot(p+k)+i\epsilon)^{n_1}(-k^2-i\epsilon)^{n_2}} \tag{B.12}$$

$$\overline{I}_{HL}(n_1,n_2) = (-v\cdot p)^{d-n_1-2n_2}\frac{i2^{d-2n_2}(-1)^{-n_1-n_2}}{(4\pi)^{d/2}}\frac{\Gamma(2n_2+n_1-d)\Gamma(\frac{d}{2}-n_2)}{\Gamma(n_1)\Gamma(n_2)}(-v\cdot p)^{d-2n_2-n_1} \tag{B.13}$$

and the third diagram corresponds to:

$$\begin{aligned} &(-v\cdot p)^{d-n_1-n_2-3n_3-2n_4-2n_5}\overline{I}(n_1,n_2,n_3,n_4,n_5) := \\ &\quad \int \frac{d^d k_L d^d k_R}{(2\pi)^{2d}}\frac{1}{(v\cdot(p+k_L))^{n_1}(v\cdot(p+k_R))^{n_2}(-k_L^2)^{n_3}(-k_R^2)^{n_4}(-(k_L-k_R)^2)^{n_5}} \end{aligned} \tag{B.14}$$

where

$$\overline{I}(n_1,n_2,n_3,n_4,0) = \overline{I}_{HL}(n_1,n_3)\overline{I}_{HL}(n_2,n_4) \tag{B.15}$$

$$\overline{I}(0,n_2,n_3,n_4,n_5) = \overline{I}_{LL}(n_3,n_5)\overline{I}_{HL}\left(n_2,n_4+n_3+n_5-\frac{d}{2}\right) \tag{B.16}$$

$$\overline{I}(n_1,n_2,0,n_4,n_5) = \overline{I}_{HL}(n_1,n_5)\overline{I}_{HL}(n_2+n_1+2n_5-d,n_4) \tag{B.17}$$

and applying the combination $\partial_{k_3}(k_3-k_4)$ gives the integration-by-parts relation:

$$\overline{I}(n_1,n_2,n_3,n_4,n_5) = \frac{-n_1\mathbf{1}^+\mathbf{2}^- - n_3\mathbf{3}^-(\mathbf{5}^- - \mathbf{4}^-)}{d-n_1-n_3-2n_5}\overline{I}(n_1,n_2,n_3,n_4,n_5) \tag{B.18}$$

B.0.3 TRIPODS

There are a series of tripod diagrams, where the light-light diagram is given by:

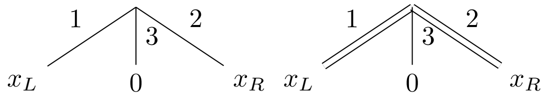

$$\tag{B.19}$$

where the first diagram corresponds to the T_{LL} (solved in Sec. 3.2.3):

$$T_{LL}(x_L, x_R; n_1, n_2, n_3) = \int \frac{d^d p_L d^d p_R}{(2\pi)^{2d}} \frac{e^{ip_L x_L} e^{-ip_R x_R}}{(-p_L^2)^{n_1}(-p_R^2)^{n_2}(-(p_L - p_R)^2)^{n_3}} \tag{B.20}$$

$$\begin{gathered} T_{\text{LL}}(x_1, x_2; n_1, n_2, n_3) = \frac{-\Gamma(\frac{d}{2} - n_1)\Gamma(d - n_1 - n_2 - n_3)}{\Gamma(n_2)\Gamma(n_3)\Gamma(\frac{d}{2})4^{n_1+n_2+n_3}\pi^d}(-x_R^2)^{-d+n_1+n_2+n_3} \\ \int_0^1 \mathrm{d}x(1 - x_1)^{-\frac{d}{2}+n_1+n_2-1} x_1^{-\frac{d}{2}+n_1+n_3-1} {}_2F_1\left(\frac{d}{2} - n_1, d - n_1 - n_2 - n_3, \frac{d}{2}, \frac{-(x_L - x_1 x_R)^2}{x_1(1 - x_1)x_R^2}\right) \end{gathered} \tag{B.21}$$

The corresponding heavy-heavy diagram was not solved in the main text, but it can also be used to provide boundary conditions for wedge diagrams containing a heavy line. This provides a cross-check for certain integrals in the method provided in the main text. T_{HH} is given by:

$$T_{HH} = \int \frac{d^d p_L d^d p_R}{(2\pi)^{2d}} \frac{e^{ip_L x_L} e^{-ip_R x_R}}{(v \cdot p_L)^{n_1}(v \cdot p_R)^{n_2}(-(p_L - p_R)^2)^{n_3}} \tag{B.22}$$

which can be solved similarly to T_{LL} by introducing Schwinger parameters:

$$\begin{gathered} T_{HH}(x_1, x_2; n_1, n_2, n_3) = \frac{i^{-n_1-n_2+n_3}}{\Gamma(n_1)\Gamma(n_2)\Gamma(n_3)} \int_0^\infty ds_1 ds_2 ds_3 \\ S(s_3)\delta_\perp^{d-1}(x_L - x_R)\delta(s_1 + s_2 + x_L^0 - x_R^0) s_1^{n_1-1} s_2^{n_2-1} s_3^{n_3-1} \exp\left(-i\frac{(vs_1 + x_L)^2}{4s_3}\right) \end{gathered} \tag{B.23}$$

and integrating over s_3, and then integrate over s_2 then s_1 (remember the δ function means the domain gets changed), to get:

$$\begin{gathered} T_{HH}(x_1, x_2; n_1, n_2, n_3) = \frac{1}{4^{n_3}\pi^{\frac{d}{2}}} \frac{\Gamma(\frac{d}{2} - n_3)}{\Gamma(n_3)\Gamma(n_1 + n_2)} {}_2F_1\left(n_1, d - 2n_3, n_1 + n_2, \frac{-\mathrm{d}x}{x_L^0}\right) \\ (-idx)^{-1+n_1+n_2}(-(x_L^0)^2)^{-\frac{d}{2}+n_3}\delta_\perp(x_L - x_R)\theta(dx > 0) \end{gathered} \tag{B.24}$$

where $\mathrm{d}x = x_R^0 - x_L^0$. Note that the δ function forces x_L, x_R to have the same spatial component, so that the entire integral has a simple functional dependence on $v \cdot x$.

B.0.4 WEDGE DIAGRAMS

There are two 'Wedge' diagrams of interest:

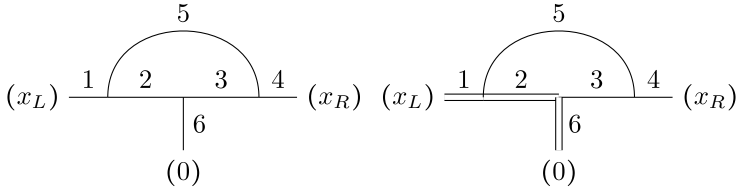

(B.25)

The first is the light-light wedge, which was considered in Sec. 3.2.3:

$$\begin{gathered} W_{LL}(x_L, x_R; n_1, n_2, n_3, n_4, n_5, n_6) := \\ \int \frac{d^d p_L d^d p_R d^d k}{(2\pi)^{3d}} \frac{e^{ip_L x_L} e^{-ip_R x_R}}{(-p_L^2)^{n_1}(-(p_L - k)^2)^{n_2}(-(p_R - k)^2)^{n_3}(-p_R^2)^{n_4}(-k^2)^{n_5}(-(p_L - p_R)^2)^{n_6}}. \end{gathered} \tag{B.26}$$

The W_{LL} master integral has base cases whenever an internal line vanishes, or when two external lines vanish:

$$\begin{aligned}
W_{LL}(n_2=0) &= I_{LL}(n_3,n_5)T_{LL}(x_L,x_R;n_1,-\frac{d}{2}+n_3+n_5+n_4,n_6)\\
W_{LL}(n_5=0) &= I_{LL}(n_2,n_3)T_{LL}(x_L,x_R;n_1,n_4,-\frac{d}{2}+n_2+n_3+n_6)\\
W_{LL}(n_3=0) &= I_{LL}(n_2,n_5)T_{LL}(x_L,x_R;-\frac{d}{2}+n_1+n_2+n_5,n_4,n_6)\\
W_{LL}(n_1=n_4=0) &= D_S^{-1}(x_L-x_R;n_5)T_{LL}(x_L,x_R;n_2,n_3,n_6)\\
W_{LL}(n_1=n_6=0) &= D_S^{-1}(x_L;n_2)T_{LL}(x_L,x_R;n_5,n_4,n_3)\\
W_{LL}(n_4=n_6=0) &= D_S^{-1}(-x_R;n_3)T_{LL}(n_1,n_5,n_2)
\end{aligned} \tag{B.27}$$

In general, W_{LL} can be reduced to these base cases by use of integration-by-parts relations (derived from inserting $\partial_k\cdot k$ in front of the integrand of Eq. (3.81)):

$$\overline{W}_{LL}(x_L,x_R;\vec{n}) = \frac{n_2\mathbf{2}^+(\mathbf{5}^- - \mathbf{1}^-) + n_3\mathbf{3}^+(\mathbf{5}^- - \mathbf{4}^-)}{d-n_2-n_3-2n_5}\overline{W}_{LL}(x_L,x_R;\vec{n}), \tag{B.28}$$

Eq. (B.28) reduces the W_{LL} master integral to base cases where either n_2, n_3 or n_5 equals zero in the argument of W_{LL}.

To solve the right diagram W_{HL},

$$\begin{aligned}
&W_{HL}(x_L,x_R;n_1,n_2,n_3,n_4,n_5,n_6) \coloneqq\\
&\quad\int\frac{d^dp_Ld^dp_Rd^dk}{(2\pi)^{3d}}\frac{e^{ip_Lx_L}e^{-ip_Rx_R}}{(v\cdot p_L)^{n_1}(v\cdot(p_L-k))^{n_2}(-(p_R-k)^2)^{n_3}(-p_R^2)^{n_4}(-k^2)^{n_5}(v\cdot(p_L-p_R))^{n_6}}.
\end{aligned} \tag{B.29}$$

one can use integration by parts by applying $(\partial_k\cdot k)$:

$$0 = (d-n_2-n_3-2n_5) + n_2\mathbf{1}^-\mathbf{2}^+ - n_3(-\mathbf{4}^- + \mathbf{5}^-)\mathbf{3}^+ \tag{B.30}$$

which can be used to lower indices until either n_1, n_4, n_5 are zero, in which case it can be evaluated with the boundary conditions:

$$\begin{aligned}
W_{HL}(x_L,x_R;n_1=n_6=0) &= D_H^{-1}(x_L;n_2)T_{LL}(x_L,x_R,n_5,n_4,n_3)\\
W_{HL}(x_L,x_R;n_4=n_6=0) &= D_S^{-1}(-x_R;n_3)T_{HH}(x_L-x_R,-x_R;n_1,n_2,n_5)\\
W_{HL}(x_L,x_R;n_5=0) &= I_{LL}(n_2,n_3)T_{HH}(x_L-x_R,-x_R;n_1,-d+n_2+2n_3+n_6,n_4)
\end{aligned} \tag{B.31}$$

B.0.5 Three Point Functions

The heavy-heavy three-point function required for the X-space position schemes are given as:

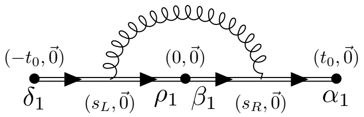

$$= \left[\frac{1+\not{v}}{2}(igv_\mu T_A)\right]_{\alpha_1\beta_1}\left[\frac{1+\not{v}}{2}(igv_\mu T_A)\right]_{\rho_1\delta_1}\cdot\int_{-t_0}^{0} ds_L \int_0^{t_0} ds_R \int \frac{d^dk}{(2\pi)^d}\frac{-ie^{is_Lk-is_Rk}}{k^2}$$
$$= [\not{v}T_A]_{\alpha_1\beta_1}[\not{v}T_A]_{\rho_1\delta_1}\left(-\frac{\alpha_S}{\pi\epsilon}-\frac{\alpha_S}{2\pi}\left(2+\log\left(-\frac{1}{4}e^{\gamma_E}\pi\mu^2t_0^2\right)\right)\right), \tag{B.32}$$

The heavy-light diagram can be evaluated in terms of tripods:

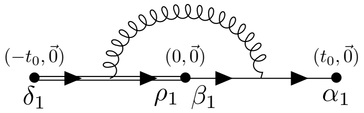

$$= \int \frac{d^dp_Ld^dp_R}{(2\pi)^{2d}}\int_{-t_0}^{0} ds_L\left[\frac{i}{\not{p}_R}(ig\gamma_\mu T_A)\frac{i}{\not{p}_R-\not{p}_L}\right]_{\alpha_1\beta_1}\left[\frac{1+\not{v}}{2}(igv_\mu T^A)\right]_{\rho_1\delta_1}\frac{-ie^{ip_L^0s_L-ip_R^0t_0}}{p_L^2}$$
$$= -ig^2\int_{-t_0}^{0} ds_L\left[\gamma_\alpha\not{v}\gamma_\beta T^A\right]_{\alpha_1\beta_1}\left[\frac{1+\not{v}}{2}T^A\right]_{\rho_1\delta_1}\frac{\partial}{\partial x_R^\alpha}\left(\frac{\partial}{\partial x_R^\beta}+\frac{\partial}{\partial x_L^\beta}\right)T(x_L,x_R;1,1,1)\Big|_{\substack{x_L\to(s_L,\vec{0})\\ x_R\to(t_0,\vec{0})}} \tag{B.33}$$

Finally, the diagram with a gluon attaching to two light lines can be reduced to the W_{LL} master integral:

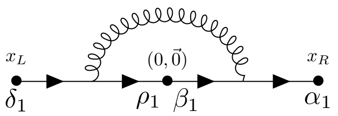

$$= -ig^2\mu^{4-d}(\gamma^\alpha\gamma^\mu\gamma^\beta T^a)_{\alpha\beta}(\gamma^\rho\gamma^\mu\gamma^\delta T^a)_{\rho\delta}$$
$$\times\int\frac{d^dp_Ld^dp_Rd^dk}{(2\pi)^{3d}}\frac{e^{ip_Lx_L-ip_Rx_R}\;p_R^\alpha(p_R-k)^\beta(p_L-k)^\rho p_L^\delta}{(-p_L^2)(-(p_L-k)^2)(-(p_R-k)^2)(-p_R^2)(-k^2)}, \tag{B.34}$$

where the factors of p_L, p_R in the numerator can be handled by differentiating with respect to x_L, x_R. Calculating Eqs. (B.32) to (B.34) at the relevant values of x_L and x_R is the main computation involved in calculating the $O(\alpha_S)$ contribution to the ratios of three-point correlation functions to two-point correlation functions presented in table 3.3.

BIBLIOGRAPHY

[1] Wolfram Research, Inc. Mathematica, Version 14.0. URL `https://www.wolfram.com/mathematica`. Champaign, IL, 2024.

[2] Matthias Jamin and Markus E. Lautenbacher. TRACER: Version 1.1: A Mathematica package for gamma algebra in arbitrary dimensions. *Comput. Phys. Commun.*, 74:265–288, 1993. doi: 10.1016/0010-4655(93)90097-V.

[3] T. Huber and Daniel Maitre. HypExp: A Mathematica package for expanding hypergeometric functions around integer-valued parameters. *Comput. Phys. Commun.*, 175:122–144, 2006. doi: 10.1016/j.cpc.2006.01.007.

Chapter C

Statistics in this Thesis

Contents

C.0.1 Usage of Statistics in this Thesis

Statistics plays a crucial role in various analyses described in this thesis. For example, as described in Sec. 2.2, Lattice-QCD calculations are traditionally performed by Monte-Carlo sampling of the space of gauge fields, for a chosen discretisation of the continuum QCD action. Furthermore, the variational ansatz used in Chapter 5 also utilised Monte-Carlo sampling from the basis states of the Hilbert space in order to estimate observables, and provide estimates for the Quantum Geometric Tensor (QGT) and forces required for Lindbladian time evolution. In these situations, various errors should be taken into account, for example:

- Statistical error due to the finite number of samples taken from either distribution. In Sec. 4.2.7, the statistical error and correlations between different correlation functions were taken into account by utilising a Bayesian framework [1]. Assuming that the number of samples is large enough that the central limit theorem can be utilised, the data set has approximately Gaussian statistics. Formally, supposing that $G(x)$ labels some correlation function data based on a discrete label x (possibly indexing over both 2-point and 3-point correlation functions), and $M(\theta;x)$ is a deterministic model for the correlation function with a finite number of parameters indexed by θ. Given a prior distribution $\rho(\theta)$ for the parameters, the posteriori distribution is given by:

  $$P(\theta|G) \propto \rho(\theta)\exp\left[-\frac{1}{2}(\overline{G(x)} - M(\theta;x))\sigma^{-2}_{x,x'}(\overline{G}(x') - M(\theta;x'))\right] \tag{C.1}$$

  where $\overline{G}(x)$ and $\sigma^{2}_{x,x'}$ are the estimated means and covariances of the correlation functions given the data. This framework allows one to include prior knowledge of the fitted parameters into the fitted parameters, though in practice the priors were taken to be relatively flat.

In Chapter 5, because both the QGT and forces are estimated with Monte-Carlo, the statistical error due to having a finite number of samples actually induces a drift into the time evolution. To assess the effect of this drift, multiple runs at the same parameters were taken (for example, in Fig. 5.13). For a given observable such as the chiral condensate, this error was added in quadrature with the estimate of the statistical uncertainty due to the MCMC sampling of the observable.

- There is also systematic error due to choosing a model to use in either situation. In the case of Sec. 4.2.7, this amounts to a choice of fitting range, and choosing a number of excited states to use in the fitting function. As discussed in Sec. 4.2.7, the Akaike information criterion is used to select the number of excited states used, and fitted results are model averaged over a wide range of fitting regions.

  For the neural network parametrisations investigated in Chapter 5, the systematic errors induced by the parametrisation were systematically investigated in Fig. 5.14. The takeaway message is that the systematic error can be controlled in the infinite volume limit by using an appropriate polynomial scaling of the number of parameters used.

- Monte-Carlo Markov Chains introduce autocorrelations between samples in the same chain, as commonly used proposal algorithms do not immediately thermalise. This is discussed briefly in Sec. 4.2.7, and the situation in the Langevin limit of Hamiltonian Monte Carlo is clarified in Appendix C.0.2.

C.0.2 AUTOCORRELONS, AND THE FATE OF LANGEVIN

Sampling from path integrals is a numeric way to obtain nonperturbative results about quantum systems. To be concrete, physical observables $\langle \mathcal{O} \rangle$ are obtained by the following formula:

$$\langle \mathcal{O} \rangle = \frac{\int D\Phi \; \mathcal{O}(\Phi) e^{-S(\Phi)}}{\int D\Phi \; e^{-S(\Phi)}} \tag{C.2}$$

where Φ are some degrees of freedom describing the physical system, and $S(\Phi)$ is the action. Because the integral $\int D\Phi$ is often very high dimensional (in the case of Lattice-QCD, 10^{10} dimensional), innovative algorithms are required to perform the calculation. The algorithm utilised to generate the ensembles described in Sec. 4.2.1 utilise a variant of the Hamiltonian Monte Carlo (HMC) algorithm [2]. To implement HMC, one can introduce conjugate momenta variables p to the field variables Φ (which are assumed to live in some compact base space $\mathcal{X}$). Notice that the probability distribution given by:

$$\exp\left[-S(\Phi) - \frac{1}{2} p^T M^{-1} p\right] \tag{C.3}$$

is the same path integral distribution as shown in Eq. (C.2) when marginilizing over p, and M is a symmetric, positive-definite mass matrix. At each step in the MCMC chain, the momenta can be directly resampled (refreshed) from the correct Gaussian distribution:

$$q \sim \exp\left(-\frac{1}{2}q^T q\right), \quad p \sim \sqrt{M}q \tag{C.4}$$

Notice that the classical Hamiltonian equations of motion:

$$H(\Phi, p) = S(\Phi) + \frac{1}{2}p^T M^{-1} p, \quad \frac{\mathrm{d}\Phi}{\mathrm{d}t} = \frac{\partial H}{\partial p} = M^{-1}p, \quad \frac{\mathrm{d}p}{\mathrm{d}t} = -\frac{\partial H}{\partial \Phi} = -\frac{\partial S(\Phi)}{\partial \Phi} \tag{C.5}$$

preserves the action Eq. (C.3) and there is a trivial jacobian term, where the action plays the role of the potential in the Hamilton equations of motion. The choice of mass matrix M cuts the total phase space $\mathcal{X} \times \mathcal{X}^*$ into surfaces of constant energy. After refreshing the momenta, the classical Hamiltonian equations of motion are integrated for a fixed amount of time t, before starting over. Note that there are integration errors in integrating the equations of motion, which require Monte Carlo accept/reject steps to account for.

In the limit that the time between momentum refreshes is taken to zero, the HMC algorithm limits towards the (overdamped) Langevin approach, which can be represented by the following stochastic differential equation:

$$d\Phi_t = -\nabla S(\Phi_t)\mathrm{d}t + \sqrt{2}\mathrm{d}W_t \tag{C.6}$$

where W_t is a standard brownian motion. The first term on the right side of Eq. (C.6) causes the sampling to be driven toward local minima of the action S, and the second term adds random brownian noise to the motion to be able to properly thermalise. An alternative way to understand Eq. (C.6) is the associated Fokker-Planck equation:

$$\frac{\mathrm{d}p}{\mathrm{d}t} = \nabla \cdot (p\nabla S) + \nabla^2 p \tag{C.7}$$

where p is a probability distribution over the Φ degrees of freedom, that approaches the distribution e^{-S} as $t \to \infty$. A practical question important for the usage of this algorithm is "how quickly does p approach e^{-S}?". The answer to this question is provided by the spectrum of Eq. (C.7); specifically when the space of fields Φ is compact, or when S is sufficiently well-behaved, there is a discrete spectrum. The steady distribution e^{-S} corresponds to the zero eigenvalue, and the larger eigenvalues (dubbed 'autocorrelons') are modes that exponentially decay under Fokker-Planck evolution.

A practical 0d-QFT example is shown in Fig. C.1, where the potential has the shape of a double-well. The blue curve corresponds to the zero eigenvalue, which is e^{-S} (the steady-state solution). The first excited state in orange is the mode that decays the slowest under Fokker-Planck evolution, and intuitively has the expected shape, it is essentially a mode that tells you which well you are living in. The second excited state (in green), is much higher up in the spectrum, and decays much faster than the orange mode.

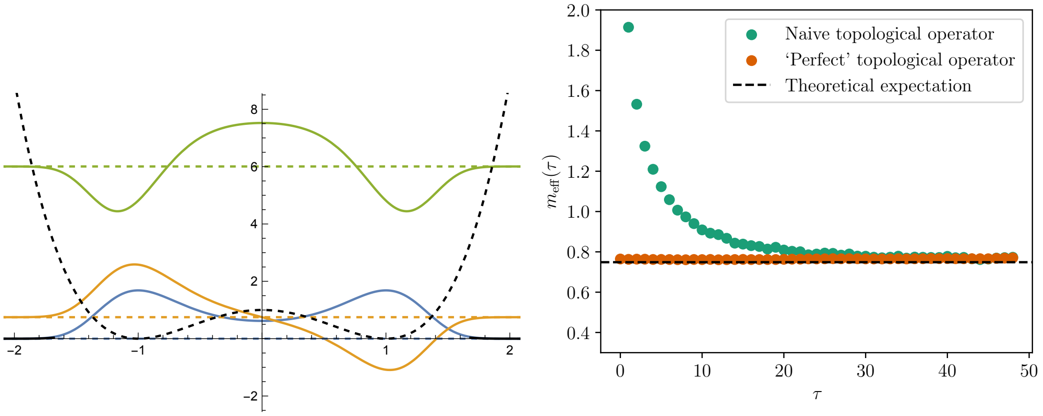

Figure C.1: A 0d-QFT example, where $S(x) = (x-1)^2(x+1)^2$. On the left: Black dashed line shows $S(x)$, colored lines show the spectrum of the Fokker-Planck operator. On the right: Effective mass plots for autocorrelation times of 'topological' operators, in blue is $\theta(x>0)$, and in orange the operator $e^{S(x)}q(x)$, where $q(x)$ is the orange curve in the left plot.

Note that each of the modes $q(x)$ of the Fokker-Planck equation corresponds to an observable $\mathcal{O}(x) = q(x)\cdot e^S$ that has an autocorrelation time given by the eigenvalue of $q(x)$ under the Fokker-Planck operator. On the right of Fig. C.1 shows effective mass plots for autocorrelation times from simulations of the Langevin equation (with $\mathrm{d}t = 0.01$). Both the naive operator $\theta(x>0)$ (that tries to detect whether the particle is in the left well or the right well), and the 'perfect' operator $q(x)e^{S(x)}$ limit to the correct exponentially decaying behaviour in the black dashed line (spectral gap of the Fokker-Planck operator). The naive operator however also has nontrivial overlap onto higher modes of the Fokker-Planck operator, and hence sees some 'excited-state contributions' from higher mass autocorrelons.

In the case of 3+1d $SU(3)$ gauge theory, it is expected that the longest autocorrelation times arise in topological observables, such as the instanton number. Extending the analysis performed in this section to $3+1$d $SU(3)$ gauge theories and solving the Fokker-Planck spectrum could confirm this belief, and rule out gauge-invariant observables with very long autocorrelation times. Furthermore, it provides a construction of a 'perfect' definition of instanton number - in the sense of constructing the operator with the longest autocorrelation time.

BIBLIOGRAPHY

[1] G.P. Lepage, B. Clark, C.T.H. Davies, K. Hornbostel, P.B. Mackenzie, C. Morningstar, and H. Trottier. Constrained curve fitting. *Nuclear Physics B - Proceedings Supplements*, 106-107:12–20, mar 2002. doi: 10.1016/s0920-5632(01)01638-3. URL `https://doi.org/10.1016%2Fs0920-5632%2801%2901638-3`.

[2] S. Duane, A. D. Kennedy, B. J. Pendleton, and D. Roweth. Hybrid Monte Carlo. *Phys. Lett. B*, 195:216–222, 1987. doi: 10.1016/0370-2693(87)91197-X.